On long-term variations in the BrO/SO_2 molar ratios in volcanic gas plumes

Dissertation
zur Erlangung des Grades
"Doktor der Naturwissenschaften"
am Fachbereich Physik, Mathematik und Informatik
der Johannes Gutenberg-Universität in Mainz

Florian Dinger
geb. in Aalen

Mainz, den 3. Juni 2019

Berichterstatter:
Prof. Dr. [redacted]
Prof. Dr. [redacted]
Prof. Dr. [redacted]
Personenbezogene Daten Dritter müssen in der elektronischer Version unkenntlich gemacht werden, siehe EU Verordnung 2016/679 (DSVGO).

Datum der mündlichen Prüfung:
9. September 2019

On long-term variations in the BrO/SO_2 molar ratios in volcanic gas plumes

Abstract

This dissertation reports, analyses, and compares multi-year time series of the sulphur dioxide (SO_2) and bromine monoxide (BrO) slant column densities and the BrO/SO_2 molar ratios in the gas plumes emitted by 6 volcanoes in Central and South America (Nevado del Ruiz, Cotopaxi, Masaya, Tungurahua, Galeras, Villarrica). The time series have been obtained from assessing remote-sensing data from the Network for Observation of Volcanic and Atmospheric Change (NOVAC) with differential optical absorption spectroscopy (DOAS). This data set exceeds 10 years of continuous data and thus provides not only a unique empirical foundation for studies on the atmospheric bromine chemistry but allows also for the first time for an investigation of long-term variations in the chemical composition in volcanic gas plumes. The observed long-term variations in the BrO/SO_2 time series range from sudden changes, linear long-term trends, annual periodicities, and a fortnightly periodicity at Cotopaxi.

For Masaya, Nevado del Ruiz, and Cotopaxi, the BrO/SO_2 time series have been compared with the meteorological conditions obtained from ECMWF simulation data. A strong anti-correlation between the BrO/SO_2 molar ratios and the specific humidity has been observed at Masaya (coefficient of $-42\,\%$, average humidity of $14\,\mathrm{g\,kg^{-1}}$). No such correlation has been observed for Nevado del Ruiz or Cotopaxi (both with an average humidity of $4\,\mathrm{g\,kg^{-1}}$). At Nevado del Ruiz, an asymptotic increase of the mean BrO/SO_2 molar ratios depending on the atmospheric age of the volcanic gas plumes has been observed; the mean BrO/SO_2 molar ratios there reached an equilibrium around 9 min after the release to the atmosphere and remained at this level for at least 60 min. In contrast, the mean BrO/SO_2 molar ratios were the same for all observed plume ages at Masaya ($2-20$ min) and Cotopaxi ($9-60$ min).

A mean long-term BrO/SO_2 molar ratio of about $4\cdot10^{-5}$ has been observed for 4 of the 5 reported low-latitude volcanoes. Decreased BrO/SO_2 molar ratios correlated with enhanced volcanic activity on several time scales, for example, persistently lower BrO/SO_2 molar ratios during multi-month phases of high activity at Nevado del Ruiz and Tungurahua and lower BrO/SO_2 molar ratios at the starts of a multi-year eruption period when compared to the long-term means.

The Earth tides have been identified as the most likely cause for the fortnightly periodicity observed at Cotopaxi (correlation coefficient of 50 %). A quantitative model has been developed to investigate a possible causal link between the Earth tides and volcanic degassing. The model describes the impact of the tide-induced gravity variations on the bubble coalescence rate in magmatic melt and suggests a tide-induced enhancement by up to a multiple of 10 %. Another novel model investigates under which conditions the mechanical interaction between gas bubbles and tilted crystals in magmatic melt could cause an erection of the crystals or an enhanced bubble coalescence rate.

Kurzzusammenfassung

Diese Dissertation veröffentlicht, analysiert und vergleicht mehrjährige Zeitreihen der schrägen Säulendichten von Schwefeldioxid (SO_2) und Brommonoxid (BrO) sowie dem BrO/SO_2 Molverhältnis in den Gasfahnen von 6 zentral- und südamerikanischen Vulkanen (Nevado del Ruiz, Cotopaxi, Masaya, Tungurahua, Galeras, Villarrica). Die Zeitreihen wurden durch die Auswertung von Fernerkundungsdaten des Network for Observation of Volcanic and Atmospheric Change (NOVAC) mittels differenzieller optischer Absorptionsspektroskopie (DOAS) ermittelt. Dieser Datensatz umfasst mehr als 10 Jahre kontinuierliche Daten und stellt damit nicht nur Studien zur atmosphärischen Bromchemie ein einzigartiges empirisches Fundament bereit sondern erlaubt zum ersten Mal auch die Untersuchung von Langzeitvariationen der chemischen Zusammensetzung von vulkanischen Gasfahnen. Die beobachteten Langzeitvariationen reichen von plötzlichen Änderungen, linearen Langzeittrends und Jahresgängen hin zu einer zweiwöchigen Periodizität am Cotopaxi.

Für Masaya, Nevado del Ruiz und Cotopaxi wurden die BrO/SO_2 Zeitreihen mit meteorologischen ECMWF Simulationsdaten verglichen. Am Masaya wurde eine starke Antikorrelation zwischen den BrO/SO_2 Molverhältnissen und der spezifischen Feuchte beobachtet (Koeffizient von $-42\,\%$, mittlere Feuchte von $14\,\mathrm{g\,kg^{-1}}$). Am Nevado del Ruiz oder Cotopaxi wurden keine solche Korrelation beobachtet (jeweils mittlere Feuchte von $4\,\mathrm{g\,kg^{-1}}$). Am Nevado del Ruiz wurde ein asymptotischer Anstieg der mittleren BrO/SO_2 Molverhältnisse in Abhängigkeit vom atmosphärischen Alter der vulkanischen Gasfahnen beobachtet; die mittleren BrO/SO_2 Molverhältnisse erreichten dort etwa 9 min nach der Freizetzung in die Atmosphäre ein Gleichgewicht und blieben für mindestens 60 min auf diesem Level. Im Gegensatz dazu waren die mittleren BrO/SO_2 Molverhältnise am Masaya ($2 - 20$ min) und Cotopaxi ($9 - 60$ min) für alle beobachteten Fahnenalter gleich.

An 4 der 5 diskutierten Vulkane niedriger Breite wurde ein mittleres Langzeit–BrO/SO_2–Molverhältnis von etwa $4 \cdot 10^{-5}$ beobachtet. Niedrige BrO/SO_2 Molverhältnisse waren auf mehreren Zeitskalen mit erhöhter vulkanischer Aktivität korreliert, zum Beispiel beständig niedrigere BrO/SO_2 Molverhältnisse während mehrmonatigen Phasen hoher Aktivität am Nevado del Ruiz und Tungurahua und niedrigere BrO/SO_2 Molverhältnisse jeweils am Anfang mehrjähriger Eruptionsperioden.

Als wahrscheinlichste Ursache für die zweiwöchige Periodizität am Cotopaxi wurde die Erdtiden identifiziert (Korrelationskoeffizient von 50 %). Zur Untersuchung eines möglichen kausalen Zusammenhangs zwischen den Erdtiden und vulkanischer Entgasung wurde ein quantitatives Modell entwickelt. Das Modell beschreibt den Einfluss der tideninduzierten Gravitationsvariationen auf die Blasenkoaleszenzrate in Magma und schlägt eine tideninduzierte Steigerung um bis zu mehrere 10 % vor. Ein weiteres Modell beschreibt unter welchen Umständen die mechanische Wechselwirkung zwischen Gasblasen und gekippten Kristallen in Magma zu einem Aufstellen der Kristalle oder zu einer erhöhten Blasenkoaleszenzrate führen kann.

List of publications

Parts of this thesis have been published in the peer-reviewed articles listed in the following. The full citations can be found in the bibliography of this thesis.

- [Dinger et al., 2018]: *Periodicity in the BrO/SO_2 molar ratios in the volcanic gas plume of Cotopaxi and its correlation with the Earth tides during the eruption in 2015*
  My contributions: I were predominantly involved in all parts of the publication. In particular, I retrieved and processes the spectroscopic results, contributed expertise on the Earth tides, lead the discussion, and wrote the manuscript.

- [Dinger et al., 2019]: *On the link between the Earth tides and volcanic degassing*
  My contributions: I were predominantly involved in all parts of the publication. In particular, I conceptualised the model, contributed expertise on the Earth tides and bubble coalescence and volcanic degassing, assessed the physical consistency of the model, and wrote the manuscript.

- [Lübcke et al., 2016]: *Retrieval of absolute SO_2 column amounts from scattered-light spectra: implications for the evaluation of data from automated DOAS networks*
  My contributions: I double-checked the algorithm and were involved in the interpretation of the results.

- [Hidalgo et al., 2018]: *Evolution of the 2015 Cotopaxi Eruption Revealed by Combined Geochemical & Seismic Observations*
  My contributions: I contributed the BrO/SO_2 data and were involved in its comparison with the other data sets.

- [Warnach et al., 2019]: *Variation of the BrO/SO_2 molar ratio in the plume of Tungurahua volcano between 2007 and 2017 and its relationship to volcanic activity*
  My contributions: I co-evaluated the BrO/SO_2 time series and were involved in its interpretation.

In addition, I contributed during this thesis to a not yet submitted manuscript and another publication which is unrelated to the actual topic of the thesis but has relevance for in-situ measurement of volcanic gas emissions.

- Rüdiger, Dinger, et al., 2018: *Halogen activation in the plume of Masaya volcano: field observations and box model investigations*, in preparation
  My contributions: I contribute the BrO/SO_2 data and am involved in its comparison with the other data sets.

- [Hoheisel et al., 2019]: *An improved method for mobile characterisation of $\delta^{13}CH_4$ source signatures and its application in Germany*
  My contributions: I set up and characterised the instrument and were involved in the interpretation of the data.

Self-citation

My two first author publications are in large parts literally incorporated into this thesis in order to keep the high level of readability conducted during the peer-review processes. Namely, Chapter 6 incorporates the content of [Dinger et al., 2018] and Chapter 9 incorporates the content of [Dinger et al., 2019]. Furthermore, some paragraphs of these two publications are incorporated in the first 4 chapters of this thesis. In these cases no further reference to these two publications is given.

Contents

1 Introduction

Structure of this thesis This thesis is ordered in three parts: *Part I: Methods (Chapters 2-4)* gives a motivation for and an introduction in the presented field of research, recapitulates the theoretical background on volcanic degassing, discusses the measurement principle and setup, and reports the data processing algorithms. *Part II: Observations (Chapters 5-8)* presents, discusses, and compares the time series of the gas emissions of six South and Central American volcanoes. The studies on three volcanoes Nevado del Ruiz, Cotopaxi, and Masaya are discussed in greater detail in separate chapters. *Part III: Models (Chapters 9-10)* derives analytical models which seek to understand some of the reported empirical findings. *Chapter 9* elucidates a possible link between the Earth tidal potential and variations in volcanic degassing, an empirical link observed e.g. in the Cotopaxi data presented in this thesis. *Chapter 10* discusses the mechanical interaction between gas bubbles and tilted crystals in magmatic melt. *Chapter 11* concludes the overall findings and proposes a roadmap for future advances.

Why study volcanoes? Volcanoes have ever attracted and threatened mankind alike. Settlements close to volcanoes often benefit from fertile soils and rich ore-deposits but also suffer from occasional volcanic disasters. The destruction of Pompeii and Herculaneum in 79 BC by an eruption of Mt. Vesuvius (Italy) is probably the best known volcanic disaster, however, the lethal threat of volcanoes is unbroken, e.g., the eruption of Nevado del Ruiz (Colombia) in 1985 caused 23 000 causalities [Voight, 1990]. The life with volcanoes thus still asks for a good understanding when and how volcanic eruptions will appear. Today, monitoring of volcanic activity allows in parts for a prediction of volcanic eruptions. Accurate predictions of volcanic activity are also valuable for societies which are not directly affected by volcanic hazards, e.g., because volcanic eruptions often cause a shut down of international air transport in the vicinity of the volcano [e.g. Ulfarsson and Unger, 2011].

A second motivation to study volcanoes is their impact on the local and global environment. On geological time scales, the volcanic recycling of sedimented and subducted carbon is the origin and keeper of Earth's hospitable climate and life. Although today's volcanic carbon dioxide (CO_2) emissions are dwarfed by the recent anthropogenic CO_2 emissions by at least a factor of 100 [Gerlach, 2011] — an important finding for the recent climate change debate! — understanding the Earth's climate history thus goes hand in hand with understanding the volcanic CO_2 emission history. On human time scales, extremely strong volcanic eruptions which input material in the stratosphere

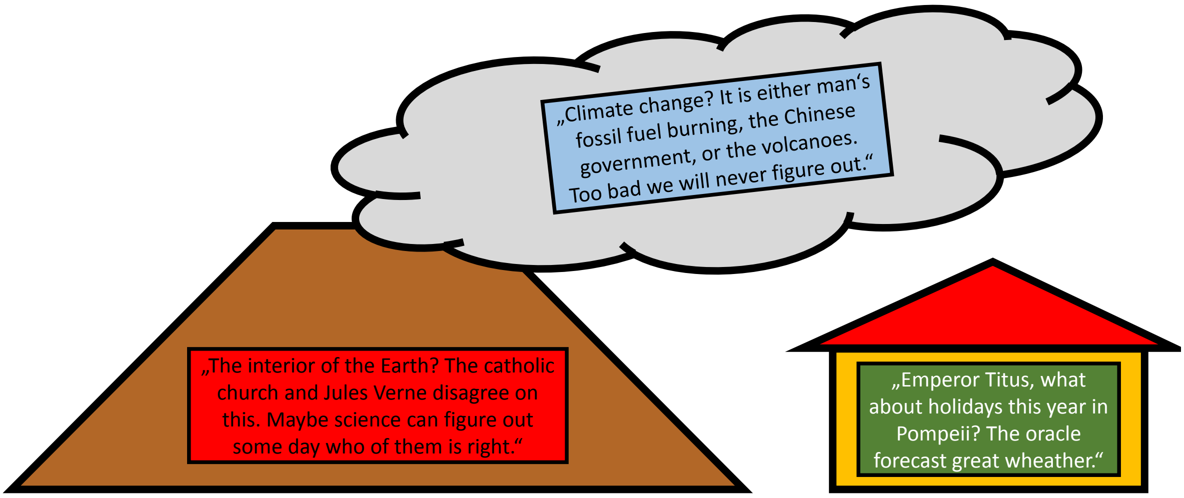

Figure 1.1: Just three out of many motivations why studying volcanic degassing is smart.

can cause volcanic winters resulting in global temperature drops by several Kelvin for several years [Timmreck, 2018], e.g., the extreme weather events of 535/536 have been caused by an unidentified volcanic source [Larsen et al., 2007], the "year without summer" in 1816 by Tambora [Oppenheimer, 2003], in 1883 by Krakatau [Rampino and Self, 1982], in 1991 by Pinatubo [Minnis et al., 1993]. On a local level, volcanic gas emissions have an impact on the atmospheric chemistry and can, e.g., cause a tropospheric ozone destruction. Furthermore, volcanic sulphur and halogen emissions and their subsequent products such as acid rain are burdens for life. For example, the environmental pollution caused by the eruption of Laki volcano (Iceland) in 1783/84 killed several hundred thousand heads of livestock in Iceland, with subsequent 9000 human causalities mostly due to starvation [Jackson, 1982]. Also the more distant Europe suffered the sulphurous air pollution caused by this eruption resulting in an increase of mortality by 10 % in England and by even up to 38 % in parts of France [Gudmundsson, 2010].

Third, secured knowledge on the interior of our planet is rather scarce. Drilling measurements end at a depth of about 10 km. Besides seismic experiments, and magnetic and geothermal observations, volcanoes — and in particular their gas and ash emissions — thus pose one of the rare telegrams from deep below our feet. Understanding the processes within volcanic systems as well as those which feed those systems may grant mankind important insights in the inner of our planet, its past, and its future.

Why measure volcanic gas emissions? Magmatic melts are reservoirs of dissolved volatile species. Typically, the dominant part of those volatiles is water vapour (H_2O) followed by CO_2 and sulphur compounds but also by a large number of trace gases such as halogen compounds [Oppenheimer et al., 2014]. The solubility of volatiles in magmatic melts is primarily pressure dependent with secondary dependencies on temperature, melt composition, and volatile speciation [Gonnermann and Manga, 2013]. Volcanic gas emissions are caused by the ascent of volatile-rich magmatic melt from a deep magma reservoir to a shallow magma chamber [Oppenheimer et al., 2014]. During ascent, the magmatic melt usually exhibits a decreasing hydrostatic pressure and thus a decreasing volatile solubility which causes volatiles to partition in the gas phase and ultimately to degas from the volcanic system. Monitoring the magnitude and chemical composition of volcanic gas emissions has thus not only value for the atmospheric and environmental sciences but also the potential to give insight in those geological processes which vary the volatile solubility within a volcanic system.
Volcanic sulphur dioxide (SO_2) emission fluxes have been monitored by remote sensing since the 1970s [Moffat and Millan, 1971, Malinconico and Lawrence, 1979] and are nowadays a central parameter in the interpretation of volcanic degassing behaviour. Variations in the SO_2 emissions fluxes can however lead to ambiguous volcanological interpretations, e.g., a decrease in SO_2 emission fluxes could be caused either by a slower magma ascent — thus a precursor of decreasing volcanic threat — or by a partial plumbing of the volcanic system which can result in an increasing pressure causing a future eruption — thus a precursor for increasing volcanic threat.
Because the pressure dependency of the volatile solubility in the magmatic melt is different for each particular volatile species, molar ratios of major gas constituents in volcanic gas plumes are discussed as accessible and less ambiguous proxies for the magma pressure and degassing depth. The molar ratios are typically interpreted with respect to SO_2. In particular carbon to sulphur and halogen to sulphur ratios turned out to be powerful tools enabling to detect events of magma influx at depth, and respectively the arrival of magma in shallow zones of the magmatic system [e.g. Edmonds et al., 2001, Métrich et al., 2004, Allard et al., 2005, Aiuppa et al., 2005a, Burton et al., 2007, Bobrowski and Giuffrida, 2012].
Furthermore, the volcanic emission flux of a gas species X, which is hard to access by a direct measurement, can be estimated by multiplying the SO_2 emissions flux estimates with the molar X to sulphur ratio, a common approach to access volcanic CO_2 emission fluxes [Gerlach et al., 1998, Conde et al., 2014, Carn et al., 2017] or volcanic halogen emission fluxes [Aiuppa et al., 2005a, Theys et al., 2009, Hörmann et al., 2013, Bobrowski and Platt, 2015].

How to measure volcanic gas emissions? Traditionally, measurements of volcanic gas emissions have been conducted by in-situ sampling and subsequent sample analysis in the laboratory. These methods enable to detect a vast number of different gas species and their isotopologues in the volcanic gas emissions, thus allow for a well constraint interpretation of the ongoing volcanic conditions and changes. These methods are however work intensive and risky, have a rather low temporal resolution, and are locally limited to the gas emitted at the sampling sites. More recently, automatised in-situ "Multi-Gas" sensors are installed in the field which measure and transmit the concentration of volcanic trace gases in the ambient atmosphere with an hourly to daily resolution [e.g. Aiuppa et al., 2005b, Roberts et al., 2017]. A major drawback of these in-situ sensors is however their vulnerability to destruction by a volcanic explosion or due to permanent contact with the corrosive volcanic gases. Another limitation of in-situ measurements is that they might not be representative for the bulk gas emissions. In conclusion, the routinely application of the different in-situ methods for near-real time monitoring faces several serious limitations.

The development of passive remote sensing techniques such as Correlation Spectrocopy (COSPEC) [Newcomb and Millan, 1970, Moffat and Millan, 1971, Elias et al., 2006] and Differential Optical Absorption Spectroscopy (DOAS) [Platt et al., 1980, Platt and Stutz, 2008, Kern, 2009] allows for recording semi-continuous (only during daytime) long-term time series of the emission magnitudes of several volcanic gas species as well as analyses of the shape and transport of volcanic gas plumes. Since the early 2000s, the costs of performing such measurements have been drastically reduced due to the installation of automatic remote sensing networks at an increasing number of volcanoes, e.g. Soufriere Hills [Edmonds et al., 2003], Stromboli and Mt. Etna (FLAME network) [Burton et al., 2009, Salerno et al., 2009], Kilauea (FLYSPEC) [Businger et al., 2015], or White Island [Miller et al., 2006]. Most prominently, the Network for Observation of Volcanic and Atmospheric Change (NOVAC) [Galle et al., 2010], funded by the European Union in 2005, encompasses today about 100 automatically measuring optical UV-spectrometers at 42 volcanoes which are predominately located in South and Central America. The NOVAC data are recorded by UV-spectrometers which scan across the sky from horizon to horizon in steps of 3.6° by means of a small field-of-view telescope yielding a mean temporal resolution of about 10 min per scan. In its current state, NOVAC data allows for an automatised retrieval of the volcanic trace gas concentrations of SO_2 [Galle et al., 2010] and bromine monoxide (BrO) [Lübcke et al., 2014] in the volcanic gas plumes.

In addition, volcanic SO_2 emissions can be routinely retrieved also via satellite-based remote sensing since the 1990s [e.g. Eisinger and Burrows, 1998, Carn et al., 2017]. In contrast, BrO in volcanic gas plumes has been detected by satellites only after major volcanic explosions [Theys et al., 2009] or by at least monthly averaging [Hörmann et al., 2013]. The launch of the Sentinel-5P satellite (with the TROPOMI instrument onboard) in 2017 has heralded a new era of satellite-based UV-spectroscopy due to the strongly enhanced spatial ground pixel resolution of down to $3.5 \times 7\,km^2$. As one consequence, it is expected that TROPOMI measurements allow for a satellite-based retrieval of daily means of volcanic BrO/SO_2 molar ratio in passively (but sufficiently strongly) degassing volcanoes [Seo et al., 2018, Warnach et al., 2018, Theys et al., 2019].

Why study BrO/SO_2 molar ratios? As motivated above, the remote sensing of the gas composition is highly desirable in order to establish an additional near-real time monitoring tool which further constrains and supports the volcanological interpretation based on SO_2 emission fluxes. With SO_2 already at hand, at least one other volcanic gas species has to be retrieved via remote sensing. The heavily desired candidates are H_2O or CO_2, however, it has not yet been possible to retrieve their volcanic contributions by remote sensing routinely due to their rather high atmospheric backgrounds [although some recent developments succeeded for special conditions, e.g. Kern et al., 2017, Butz et al., 2017]. The next desired candidates are chlorine and fluorine compounds. Hydrogen chloride (HCl), hydrogen fluorine (HF) [both via Fourier Transform InfraRed (FTIR) spectroscopy, e.g. Mori and Notsu, 1997, Mori et al., 2002] and chlorine dioxide (OClO) [via UV-DOAS, e.g. Gliß et al., 2015] in volcanic plumes can be accessed by measurement campaigns using state-of-the-art remote sensing instruments.
Except the remote-controlled FTIR scanner system installed on Stromboli volcano since 2009 [La Spina et al., 2013], no robust, autarkic, and in particular inexpensive instruments such like the NOVAC instruments are yet developed for chlorine and fluorine compounds. In contrast, BrO can be retrieved from the same UV-spectra which are recorded by the already widely-spread low maintenance UV-spectrometer monitoring the SO_2 emission fluxes. Accordingly, a vast remote sensing data set of BrO/SO_2 time series is already available. Thus, although BrO is not on the list of the most desired plume constituent species, BrO/SO_2 molar ratios are the best accessible remotely sensed gas proxy for volcanic processes so far.

Opportunities and challenges of the BrO/SO_2 molar ratios The release of volcanic bromine is poorly understood and much work is still required in order to use the BrO/SO_2 molar ratio as a fully reliable proxy for volcanic activity variations. The challenge is the interplay of the manifold physical and chemical behaviour of bromine causing the relative Br/S abundance ratio to be significantly altered by virtually any involved compartment of the volcanic system (see Figure 1.2 and Chapters $2-4$). On the one hand, these omnipresent links pose the opportunity to use the Br/S molar ratio to study any of the involved compartments provided that the thermodynamic and chemical constraints of the subsequent compartments are sufficiently known. On the other hand, knowledge on these constraints is usually rather fragmented what makes it hard to look deep in the system because each additional compartment further decreases the precision and the accuracy of the Br/S ratio estimates in forgoing compartments. The greater motivation for this thesis lies in the better understanding of the link between varying volcanic activity and the ultimately observed variations in BrO/SO_2 molar ratios. The measurement and interpretation of BrO/SO_2 molar ratios faces four particular challenges (going along the inverted direction of the black arrows in Figure 1.2):
(1) The BrO concentrations in volcanic gas plumes are most of the time below the detection limit of the NOVAC instruments and only advanced spectroscopic methods

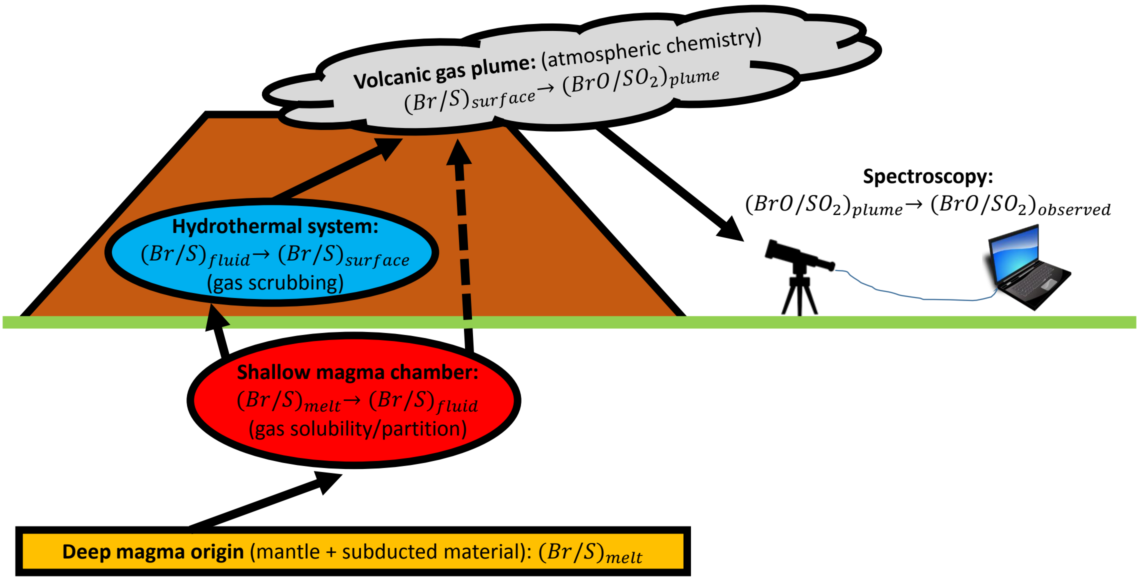

Figure 1.2: Sketch of several compartments and processes which can change the bromine to sulphur molar ratio during the way from great depth to the finally retrieved measurement output.

and sophisticated data filtering allows for a retrieval of continuous BrO/SO_2 time series. The BrO retrieval used in this thesis is based on the algorithm developed by Lübcke et al. [2014]. Several algorithm advances are introduced and applied in Chapter 4 of this thesis.

(2) Volcanic bromine is assumed to be emitted predominately as hydrogen bromine (HBr) and only subsequently converted to BrO in the atmosphere via the reaction with O_3. This so called "bromine explosion" is studied in lab experiments, empirical observations, and theoretical simulations. The bromine explosion apparently reaches an equilibrium in BrO/SO_2 molar ratios for atmospheric plume ages of $2 - 10$ minutes and therefore a sophisticated choice of the measurement location presumably constraints the atmospheric effects to a relative (and thus simple to interpret) offset between Br_{total}/SO_2 and BrO/SO_2. The details on this equilibrium are, however, not yet fully understood, thus the atmospheric bromine chemistry remains a source of uncertainty when interpreting the variations in the BrO/SO_2 time series as volcanological signals. This thesis does not focus on an investigation of the atmospheric bromine chemistry, however, the reported observations are discussed with respect to empirical manifestations of the bromine explosion. Furthermore, Rüdiger et al. [2019] have used the BrO/SO_2 data from Masaya volcano reported in this thesis as an input parameter for their atmospheric chemistry model.

(3) Volcanoes often host hydrothermal systems which are in contact with the volcanic

gas flows. Because bromine is more hydrophilic than sulphur the Br/S molar ratios in the gas decreases when passing a hydrothermal system. The magnitude of this scrubbing effect depends on parameters such as the volume of the hydrothermal system, its pH-value, and its degree of saturation in the particular gas species. On the one hand, an analysis of the magmatic system therefore requires sufficient knowledge on the state of the hydrothermal system. On the other hand the Br/S molar ratios may be a powerful proxy for the variations of the conditions in the hydrothermal system.
(4) While the sulphur solubility in magmatic melt is relatively well constrained, the bromine partition from the magmatic melt to the fluid water phase or the gas phase is rather complex. Furthermore, theoretical and empirical findings indicate that the pressure dependency of the solubility of sulphur and bromine in magmatic melt is relatively close to each other. In consequence, it is not yet known which gas species starts to partition to the gas phase at greater depth and thus degasses earlier from the volcanic systems. Accordingly, an increasing BrO/SO_2 molar ratio can be yet interpreted ambiguously as a rise or a decrease of magma and thus volcanic activity.

Within this thesis, empirical evidence is collected and interpreted which links the variations of the BrO/SO_2 molar ratios to variations in the meteorological conditions, in the hydrothermal system, and in the magmatic system.

Part I: Methods

2 Volcanic degassing

This chapter aims to sketch the way and processes which volcanic volatiles undergo from great depth until they are ready to be measured in the atmosphere. A comprehensive introduction in the geophysics of the Earth is given by Clauser [2014]. A detailed description of the manifestations of volcanism can be found in Schmincke [2014] and manifestations of volcanic degassing are discussed by Oppenheimer et al. [2014]. Mathematical approaches on several volcanological processes are discussed by Fagents et al. [2013], including the contribution from Gonnermann and Manga [2013] on the processes of volcanic degassing. If not cited otherwise, the following chapter refers to these four textbooks.

2.1 Volcanism

Origin of volcanism The interior of the Earth is a reservoir of thermal energy, originating from the release of gravitational potential energy and radioactive decay. Seismic observations imply that large parts of the Earth's mantle consists of molten material called magmatic melt or in short magma [Clauser, 2014]. The outer $0 - 100\,\text{km}$ of the Earth are called lithosphere which is mostly solid but also rather fragile consisting of tectonic plates which are exposed to forces from below [Clauser, 2014, Kanamori and Press, 1970, Conrad and Lithgow-Bertelloni, 2002]. Local temperature inhomogeneities in the lower crust can lead to a partial melting of the lithosphere, allowing material transport from the Earth's mantle and the lower crust to the Earth's surface. Those locations are called volcanoes [Schmincke, 2014]. The origin of volcanism can be distinguished in three different mechanism depending on the location of the volcano with respect to the tectonic plates: convergent "subduction" zones, divergent zones, or hot spots.

At subduction zones a tectonic plate slides below another tectonic plate what causes a melting of the two plates at the contact boundaries (Figure 2.1). At divergent zones two (typically oceanic) plates diverge and the resulting gap is filled by molten mantle material. Hot spots are apparently randomly distributed over the Earth's surface. While still under debate, hot spot volcanism is assumed to be independent from tectonic mechanisms but originates from hotter temperature anomalies at the outer core of the Earth which cause a persistent melting of material in the overlying lithosphere [Morgan, 1971].

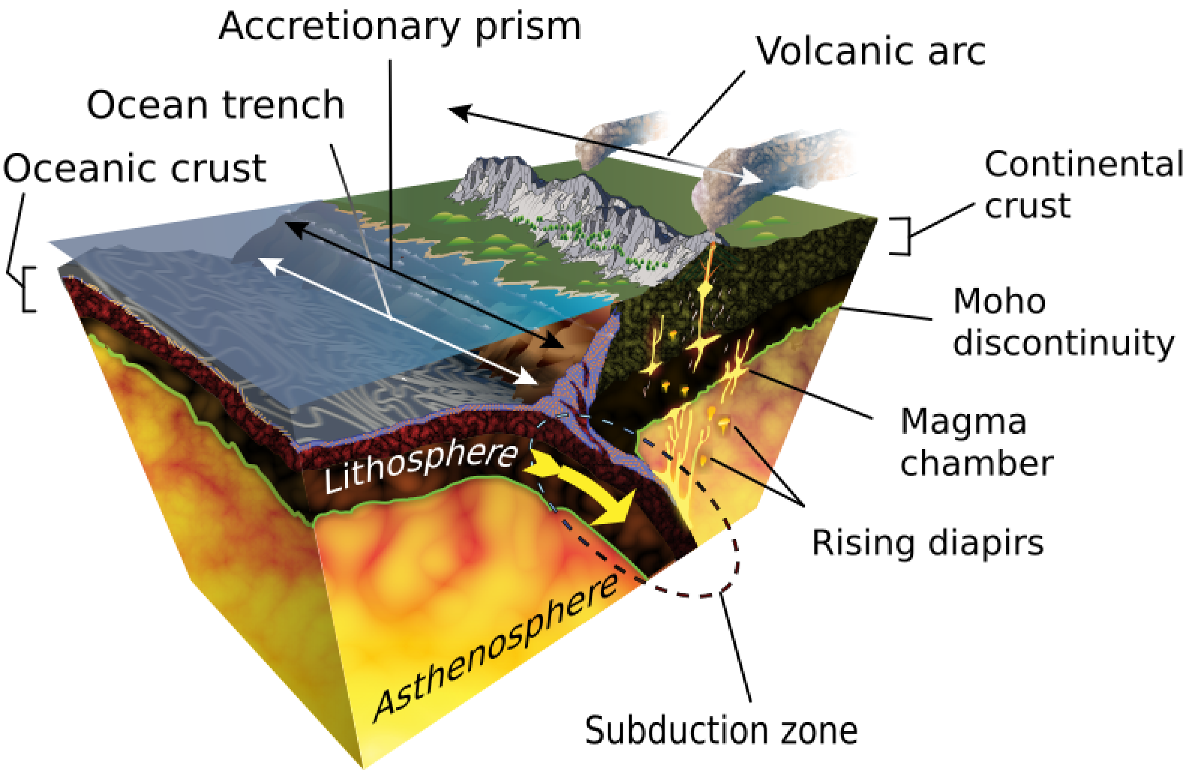

Figure 2.1: Schematic of subduction zone volcanism at an ocean–continent boundary. Provided by K. D. Schroeder under a Creative Commons Attribution-ShareAlike 4.0 licence at https://commons.wikimedia.org/wiki/File:Subduction-en.svg.

Chemical composition of magmatic melt The chemical composition of the magmatic melt is generally a manifestation of the overall relative abundance of the chemical elements in the crust and the upper mantle. Accordingly, quartz (SiO_2) is the predominant contribution ranging from below 40 to above 70 weight percent (wt%) followed by typically large contribution of the oxides of aluminium, iron, magnesium, calcium, sodium, and potassium (not mandatorily in this order) [e.g. Watson and Harrison, 1983, McKenzie and Bickle, 1988], and by traces of virtually all other chemical elements. In particular, magmatic melts also host volatiles. Typically, the dominant part of the volatiles is H_2O (up to 7 wt%) followed by CO_2 (up to 0.7 wt%) and sulphur compounds (up to 0.3 wt% sulphur) as well as by a large number of trace gases such as halogen compounds [e.g. Giggenbach, 1996, Aiuppa et al., 2009, Oppenheimer et al., 2014, Bobrowski et al., 2015].
While the magmatic melt in divergent zones consists predominately of pristine mantle material, the magmatic melt in subduction zones consists predominately of molten material of the local crust. Magmatic melts in subduction zones are therefore enriched in elements associated with the ocean and marine sediments. This first of all results

in relative large contribution of H_2O ($3 - 7$ wt%) to the magmatic melt but also in an enrichment in halogens [Oppenheimer et al., 2014, Kendrick et al., 2014, Pagé and Hattori, 2017]. This thesis reports the volcanic gas emissions of six subduction zone volcanoes (exclusively), therefore the following qualitative and quantitative processes are discussed with respect to subduction zone volcanism.

The lower density of molten magma with respect to its solidified counterpart can cause magma to ascent from its deep origin to a shallow magma chamber located less than 10 km below the surface. During the ascent the decrease in pressure and temperature causes a separation from the initial mono-phase magmatic melt to a multi-phase system consisting of a remaining SiO_2-dominated melt phase, a solid phase consisting of individual crystals of several species, a gas phase typically initiated by the exsolution of CO_2 from the melt phase at $10 - 15$ km depth [e.g. Lowenstern, 2001], and a hydrous fluid phase caused by the exsolution of H_2O from the melt phase starting at $4 - 8$ km depth [e.g. Chiodini et al., 2016].

Effusive and explosive volcanic manifestations Ascent of juvenile volatile-rich magma from the depth to a shallow magma chamber results in volatile degassing. The subsequent expansion of the gas phase causes a pressurisation of the shallow system. When the overpressure in the magmatic system exceeds the yield strength of the solid surroundings, the host rock bursts at its weakest point and the volcanic explosion ejects material until the overpressure is neutralised.

At some rare locations (while writing namely at seven locations: Ambrym in Vanuatu, Erta Ale in Ethiopia, Kilauea on Hawaii/USA, Erebus in Antarctica, Masaya in Nicaragua, Nyiragongo in D.R. Congo, Villarrica in Chile), the magmatic melt — which is for ancient reasons called “lava” once you can see it — is in direct contact with the atmosphere in the form of a lava lake. At these locations the volcanic volatiles can leave the magma with relatively little resistance. In consequence, the pressurisation of the magmatic system typically remains uncritical and magmatic activity is manifested by continuous effusive (= non-explosive) volcanic degassing with occasional but weak ejection of lava or solid material in the atmosphere.

For the vast number of volcanoes, the volcanic conduit is, however, plugged with solid material which limits the chemical and thermodynamic interaction between the magma and the atmosphere. The end-members of these filled volcanic systems are called “open” when volcanic gas emissions can nevertheless leave the system although with some resistance due to the dynamic pressure within the plug material and “closed” when the gas emissions are virtually inhibited. The more closed a system is the more overpressure is possible until the yield strength of the plug material is exceeded and thus the more energy can get released by a sudden volcanic explosion [e.g. Bebbington, 2014, Cassidy et al., 2018].

Hydrothermal system At most volcanoes, the magma is in direct or indirect chemical and thermodynamic contact with environmental water, e.g., the ground water or melt water from a glacier topping the volcanic edifice.

The thermodynamic contact can cause boiling in parts of the hydrothermal system. Depending on the geometry and thermodynamic properties (such as the heat conductivity and porosity of the host rock) of the overall volcanic system, this can result in superficial manifestations such as hydrothermal springs, in a virtually instantaneous expansion of the hydrothermal system causing a phreatic (from greek *phrear* meaning "well/spring") explosion [Germanovich and Lowell, 1995], or in the sudden mixing and interaction of hydrothermal water and magma potentially causing a phreatomagmatic explosion [Wohletz, 1986, Büttner et al., 1999].

The chemical contact between the magma and the hydrothermal system can cause a change in the composition of the different magma phases. In particular, gas flows which have eventually already separated from the magma can get completely or partially re-dissolved in the hydrothermal system. Thus, gas flows which passed through a hydrothermal system are not only reduced in their magnitude but can also change their relative chemical composition because the hydrothermal scrubbing efficiency is different for each particular gas species and also depends on the ambient conditions [Symonds et al., 2001, Di Napoli et al., 2016].

2.2 Partition of volcanic volatiles

Volatile partition in magmatic melts At great depth, all volatiles are dissolved in the magmatic melt phase. With decreasing depth, the volatile solubility of magmatic melts generally decreases following a predominant pressure dependency with secondary dependencies on temperature, melt composition, and volatile speciation [Gonnermann and Manga, 2013]. This pressure dependency can be modelled with high accuracy for H_2O and CO_2 [see Gonnermann and Manga, 2013, and referred literature therein] and is also relatively well constrained under diverse and variable conditions for sulphur [e.g., Scaillet and Pichavant, 2005, Moretti and Ottonello, 2005, Lesne et al., 2011, Witham et al., 2012]. In contrast, it is more challenging to constrain the halogen behaviour in the melt–fluid phase because of their low abundances in magmatic melt but also because halogens (except fluorine) strongly prefer to partition in the hydrous fluid phase [Bureau et al., 2000]. For water-poor magmas, the knowledge is yet limited to the qualitative observation that halogens typically reach saturation, if at all, at low pressure [Edmonds et al., 2009, who studied Kilauea volcano].
For water-rich magmas (which is the typical case for subduction zone volcanoes), the quantitative pressure dependency of the chlorine solubility in the melt–fluid phase is relatively well constrained [e.g., Carroll, 2005, Balcone-Boissard et al., 2016] and also some insights in the behaviour of the other halogens have been gathered by the experimental [e.g., Bureau and Métrich, 2003, Bureau et al., 2010, 2016, Cadoux et al., 2018] or empirical [e.g., Villemant et al., 2005, Kutterolf et al., 2015] derivation of their melt-fluid partition coefficients. Sulphur and H_2O, and thus also the hydrophilic halogens, degas predominately after CO_2. Sulphur degasses prior to chlorine [e.g., Aiuppa, 2009]. Bromine has a larger partition coefficient than chlorine, thus it is reasonable to assume that bromine degasses prior to chlorine.
It is however not yet clear whether sulphur is predominately degassing prior or after bromine. On the one hand, it is reasonable that despite of the different partition coefficients bromine and chlorine are rather simultaneously partitioning in the hydrous fluid phase once this phase is established. And thus bromine degasses together with water and chlorine and after sulphur. Cadoux et al. [2018] backed this hypothesis by a simple model applied on new experimental data of the halogen partition coefficients. On the other hand, Bobrowski and Giuffrida [2012] reported empirical data from Mt. Etna which indicate that bromine degasses earlier than sulphur. As today, there is no evidence that the one or the other hypothesis is predominately valid. In particular, it appears to be possible that the bromine–sulphur degassing order differs between volcanoes.

Molar ratios in volcanic gas emissions as proxy for volcanic activity The volatile solubility of the magmatic melt varies differently (and non-linearly) with varying pressure for each individual volatile species, and thus also the relative chemical com-

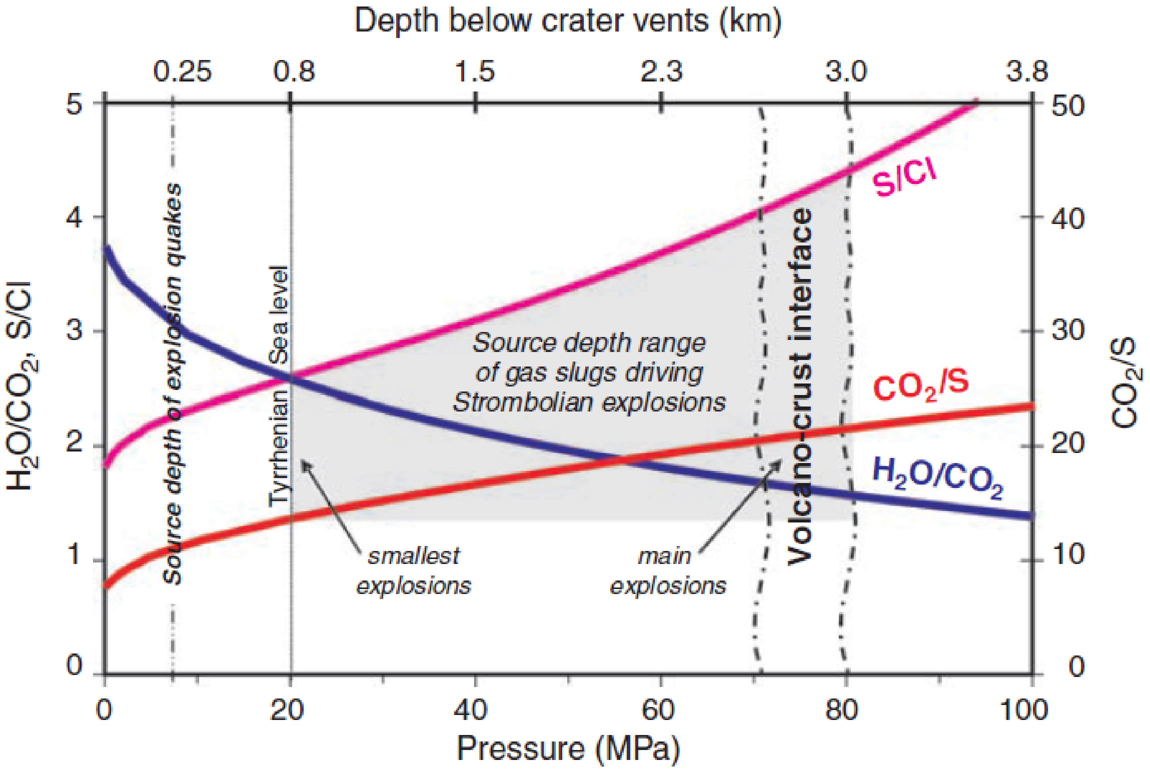

Figure 2.2: Modelled pressure dependency of the molar ratios of various volatiles in the magmatic gas phase. Based on data from Stromboli volcano (Italy). Figure reprinted from [Burton et al., 2007] with the kind permission from AAAS.

position of the magmatic gas phase is pressure dependent. This pressure dependency of the chemical composition is backed theoretically and empirically for the H_2O/CO_2 molar ratio and empirically for several molar ratios with respect to sulphur (see e.g. Figure 2.2). Given a particular pair of volatile species, the relation between their current molar ratio in the gas phase and the current surrounding pressure depends on the other thermodynamic parameters such as the temperature, the magma composition, and state of the hydrothermal system (e.g., its size, its pH-value, and its degree of saturation in the particular gas species). Measuring several different molar ratios would allow to constrain these minor dependencies empirically.

As sketched above, the interpretation of Br/S molar ratios still lacks a theoretical foundation first of all because the degassing order of the two species may depend sensibly on the ambient conditions [Aiuppa et al., 2005a, Cadoux et al., 2018]. Also an empirical derivation of their degassing order by correlating BrO/SO_2 molar ratios in volcanic gas plumes with other volcanological parameters such as seismic records have not yet been successful, not least due to of the ambiguous interpretation options of the still limited BrO/SO_2 data sets available [Bobrowski and Giuffrida, 2012, Lübcke et al., 2014].

In the absence of an explicit interpretation of the Br/S molar ratios, at least the reasoning that a change in Br/S molar ratios is probably caused by a significant change in magmatic conditions appears to be nevertheless a reasonable hypothesis. Several studies on BrO/SO_2 molar ratios in volcanic gas plumes revealed that the ratios generally follow the same typical pattern: the ratios are relatively low prior and during an eruption but are higher at the end of the eruption or during quiescent degassing periods, as observed, e.g., at Mt. Etna [Bobrowski and Giuffrida, 2012], Nevado del Ruiz [Lübcke et al., 2014], Tungurahua [Warnach et al., 2019], Cotopaxi [Dinger et al., 2018], and the conclusions of this thesis.

2.3 Volcanic gas emissions of sulphur and bromine

Sulphur emission fluxes Volcanic sulphur emissions are predominately emitted as SO_2 and hydrogen sulfide (H_2S). Total emitted volcanic sulphur is virtually always dominated by the SO_2 contribution while the H_2S contribution ranging from the same order of magnitude as SO_2 to two orders of magnitude lower [Gerlach, 2004, Oppenheimer et al., 2011]. With an increasing amount of measured volcanic sources, the lower estimate constraint of the global annual volcanic SO_2 emission flux has been updated to higher values from 13 Tg/yr [Andres and Kasgnoc, 1998] to $15 - 21$ Tg/yr [Halmer et al., 2002] to (23 ± 2) Tg/yr [Carn et al., 2017]. The large uncertainties in the H_2S measurements make it difficult to report accurate volcanic emission fluxes for total sulphur. After the emission to the troposphere, the atmospheric lifetime of SO_2 is estimated to be in the order of hours to days [Beirle et al., 2014, Fioletov et al., 2015]. The SO_2 background mixing ratio is usually below 1 ppb in the atmospheric background but can easily achieve levels of 1 ppm in volcanic gas plumes.

The negligible background values together with the chemical stability and the relatively strong UV absorption structures make SO_2 an easily accessible tracer for volcanic gas emissions. SO_2 emission flux estimates are nowadays routine parameter in volcanic monitoring. The accuracy of ground-based SO_2 emission flux estimates may experience high uncertainties due to the atmospheric radiative transport [e.g., Mori et al., 2006, Kern et al., 2010], relies on the quality of wind data used to approximate plume speed, and requires additional information on the plume altitude. Satellite-based SO_2 emission flux estimates are furthermore limited to one observation per day (and per satellite) and are thus intrinsically blind for diurnal variations of the SO_2 emissions fluxes.

Bromine emissions and atmospheric bromine chemistry Volcanic bromine is considered to be emitted predominately as hydrogen bromine (HBr) which is then converted in the atmosphere by photochemistry to several bromine species by the so called bromine explosion process [Platt and Lehrer, 1997, Wennberg, 1999, von Glasow, 2010, and Figure 2.3]. One of these secondary species is bromine monoxide (BrO) which is the only bromine species routinely accessible by today's remote sensing techniques. In order to quantify the total volcanic bromine emissions, it is therefore crucial to establish a robust understanding of the quantitative link between the emitted HBr and the observed BrO. This link has been studied by empirical observations [von Glasow et al., 2009, Lübcke et al., 2014, Gliß et al., 2015, Roberts, 2018, Rüdiger et al., 2019], theoretical models and simulations [Bobrowski et al., 2007, Roberts et al., 2009, 2014, von Glasow, 2010], and lab experiments [Rüdiger et al., 2018]. Gutmann et al. [2018] concluded the current state of the art a their review article.

Based on empirical observations, the equilibrium of the conversion $HBr \rightleftharpoons BrO$ is typically reached within the first $2 - 10$ min after the release of HBr to the atmosphere and remains constant for the next at least 30 min [Bobrowski and Giuffrida, 2012, Lübcke et al., 2014, Platt and Bobrowski, 2015, Gliß et al., 2015]. Accordingly, BrO measurements should only be conducted at gas plumes with plume ages of at least $2-10\,\mathrm{min}$ because otherwise the equilibrium BrO concentration can be underestimated. Assuming typical wind speeds of $5-10\,\frac{\mathrm{m}}{\mathrm{s}}$ this implies a minimum distance to the volcanic vent of $1.5-3.0\,\mathrm{km}$. Model simulations have proposed a BrO fraction relative to total Br of $40-50\,\%$ for a "medium" relative bromine abundance of $\mathrm{Br_{total}/SO_2} = 7.4\cdot10^{-4}$ and $10-20\,\%$ for a "high" relative bromine abundance of $\mathrm{Br_{total}/SO_2} = 24\cdot10^{-4}$ peaking roughly at minute 10 after the HBr release following by a decrease to about the half of the maximum values until minute 35 [Roberts et al., 2014].

The HBr $\rightleftharpoons$ BrO conversion rate or even the stationary equilibrium HBr/BrO ratio may depend on the chemical plume composition, on the atmospheric conditions (meteorology) such as the solar irradiance, the specific humidity, and/or relative humidity, and on the tropospheric background ozone level. The HBr $\rightleftharpoons$ BrO conversion in a volcanic gas plume is expected to be more efficient for high concentrations of bromide ions ($\mathrm{Br^-}$) and/or protons ($\mathrm{H^+}$) in the aerosol phase [e.g. Bobrowski et al., 2007]. A higher humidity level causes smaller $\mathrm{Br^-}$ and/or $\mathrm{H^+}$ concentrations and thus a slower BrO genesis, as confirmed by model simulations and experimental results [Rüdiger et al., 2018, and pers. comm. with Stefan Schmitt]. The tropospheric background ozone variations appear to have a seasonal cycle in the near-surface layers [Vukovich et al., 1997, Pochanart et al., 2003] and the free troposphere [Brönnimann et al., 2000, Monks, 2000, Cooper et al., 2014, Katragkou et al., 2015] with maxima between March and July in the northern hemisphere and maxima between September and November in the southern hemisphere. If the reaction rate of the bromine explosion is ozone-limited, more background ozone implies a faster and possibly stronger BrO genesis.

Access to meteorological data The atmospheric chemistry and meteorological conditions may have an impact on the $\mathrm{BrO/SO_2}$ molar ratios observed in volcanic gas plumes and therefore a routine comparison of the $\mathrm{BrO/SO_2}$ time series with the meteorological variations appears to be mandatory to rule out (or likewise investigate) systematic $\mathrm{BrO/SO_2}$ offsets cause by meteorological variations. Unfortunately, direct measurements of the meteorological conditions at volcanoes, and in particular at the altitudes of volcanic plumes, are scarcely available.

A quantification of the sky cloudiness or the aerosol load in a volcanic plume may be retrieved directly from the spectroscopic data by well-established methods such as an analysis of variations in the oxygen dimer ($\mathrm{O_4}$) absorption or an analysis of the so-called colour index [Wagner et al., 2014, 2016]. However, the spectra recorded by NOVAC do not allow for an application of the the validated versions of those methods because the spectral properties are optimised for a retrieval of $\mathrm{SO_2}$ and BrO, thus for a wavelength range below $360\,\mathrm{nm}$. In contrast, the $\mathrm{O_4}$ analysis requires spectra of good quality also at longer wavelengths. First investigations with modified versions of those methods applied on NOVAC data did not succeed in a reliable retrieval of the sky cloudiness (see Section 4.5).

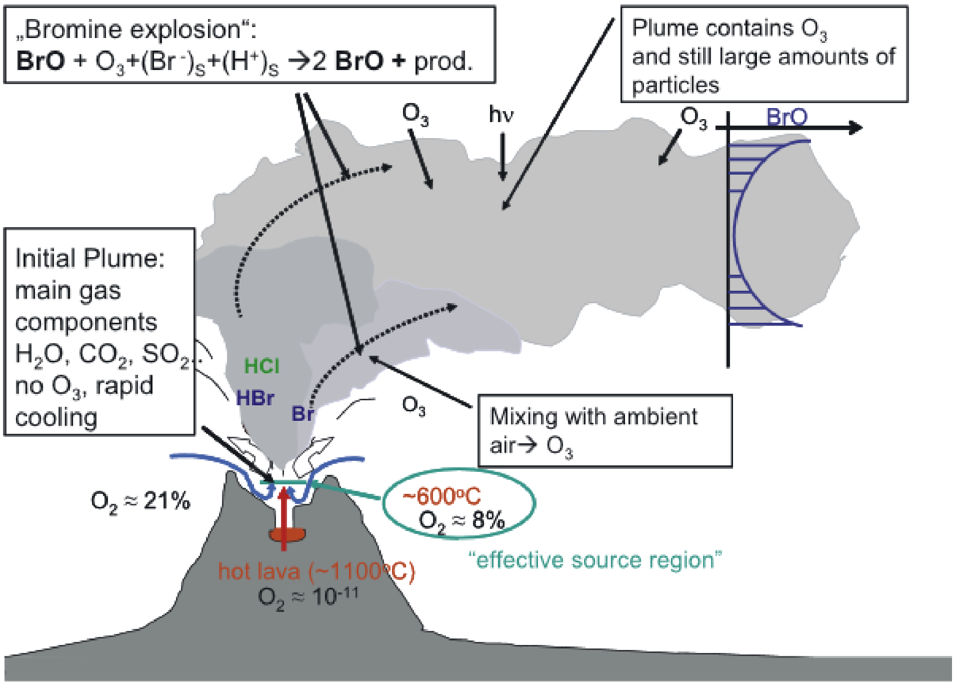

Figure 2.3: Sketch of the conditions and the bromine conversion process inside a volcanic gas plume. Figure reprinted from [Bobrowski et al., 2007].

Weather forecast models pose the best available proxy for the meteorological conditions around the volcanic gas plume. Therefore, in this thesis the meteorological conditions are accessed by the operational analysis data from ECMWF (on a Gaussian Grid N640 and with a T1279 truncation) with a spatial resolution of 0.14° x 0.14° and a temporal resolution of 6 h (0:00, 6:00, 12:00, and 18:00 UTC) calculated for 137 discrete altitude layers with exponentially increasing vertical distance from ground to an altitude of 60 km. The ECMWF results are subsequently interpolated to the manually chosen altitude. The following model parameters are presented and discussed in this thesis: (1) the air temperature, (2) the air pressure, (3) the specific humidity, and (4) relative humidity in order to investigate their possible influence on plume chemistry, (5) the wind speed and (6) the wind direction in order to reconstruct the plume transport (and therefore the plume age), and (7) the total cloud cover as a poor but the still most suited proxy for the radiative conditions. The total cloud cover gives a relative value (from 0 to 1) for the cloud thickness above a pixel integrated from ground up to an altitude of 60 km. A total cloud cover of 1 does not necessarily indicate the presence of an optical dense cloud cover, but rather indicates whether significant light scattering within clouds has occurred somewhere above the ground pixel.
The evalution of the NOVAC data from Nevado del Ruiz (Chapter 5) and Masaya (Chapter 7) use additional meteorological ground-based records for comparison.

2.4 The Earth tidal potential

The spectroscopic results retrieved at Cotopaxi will be compared with the signal generated by the Earth tidal forcing (Chapter 6). Subsequently, a model which links the Earth tides to volcanic degassing is developed (Chapter 9). This section provides a summary on the Earth tides.

Astronomic origin and characteristics of the tidal potential Residual gravitational forces of the Moon and the Sun deform the Earth's surface and interior periodically and thus lead to the so-called Earth tides. The tidal potential can be modelled as the result of the interference of an infinite number of sinusoidal tidal harmonics with precisely known frequencies and amplitudes [Darwin, 1883, Doodson, 1921, see Table 2.1]. At the Equator, the tidal potential varies predominantly with a semi-diurnal periodicity. The amplitude of the semi-diurnal cycle is modulated within the so called spring–neap tide cycle with a periodicity of 14.8 days caused by the interference of the lunar semi-diurnal tide and the solar semi-diurnal tide. The peak-to-peak amplitude of the associated semi-diurnal gravity variations is $a^{st}_{astro} = 2.4\,\mu\mathrm{m\,s^{-2}}$ during spring tide and $a^{nt}_{astro} = 0.9\,\mu\mathrm{m\,s^{-2}}$ during neap tide and is at an intermediate level at other times of the cycle. At mid latitudes, the tidal potential varies predominantly with diurnal periodicity and at other latitudes both periodicities mix. The spring–neap tide cycle is, however, manifested everywhere and has maximum variability at the Equator [Agnew, 2007]. The tidal potential firstly gives rise to a periodical elevation of the Earth's crust with a semi-diurnal peak-to-peak variation of up to about 50 cm (maximum at the Equator), and secondly all crustal compartments exhibit an additional semi-diurnal gravity variation by up to $1.16 \cdot a^{st}_{astro}$ [Harrison et al., 1963, Baker, 1984]. This gravity variation typically has no effect on the rigid solid crust but can cause fluid movement, e.g. prominently manifested in the form of ocean tides [Ponchaut et al., 2001].

Volcanological manifestations of the tidal potential Evidence for tidal impacts on volcanism has been gathered by numerous empirical studies which detected a temporal proximity between tidal extrema and volcanic eruptions [Johnston and Mauk, 1972, Hamilton, 1973, Dzurisin, 1980] or seismic events [McNutt and Beavan, 1981, 1984, Rydelek et al., 1988, McNutt, 1999, Custodio et al., 2003, Ide et al., 2016, Petrosino et al., 2018], or found a correlation between the spring–neap tide cycle and variations in volcanic deformation [De Mendoca Dias, 1962, Berrino and Corrado, 1991] or variations in the volcanic gas emissions.

The tide-induced stress variations ($\sim 0.1 - 10\,\mathrm{kPa}$) appear to be negligibly small in comparison to tectonic stresses ($\sim 1 - 100\,\mathrm{MPa}$) or stresses caused by pressure and temperature gradients within a shallow magmatic system ($\sim 1\,\mathrm{MPa}$). The rate of tidal

Table 2.1: Strongest tidal harmonics [Agnew, 2007]. The tide species are divided by the horizontal bars in the semi-diurnal, diurnal, and long-term harmonics (see text for details). The Darwin Symbols are a set of conventional notation, the amplitude gives the theoretical amplitude of the periodical vertical displacement of the Earth's surface which would be caused by this particular tidal harmonic alone. The frequency is given in cycles per day and the length of the period is given in days.

Tide species	Darwin Symbol	Amplitude [metre]	Frequency [day^{-1}]	Length of Period [day]
semi-diurnal	M2	0.63221	1.9322736	0.5175251
	S2	0.29411	2.0000000	0.5000000
	N2	0.12105	1.8959820	0.5274312
	K2	0.07991	2.0054758	0.4986348
diurnal	K1	0.36864	1.0027379	0.9972696
	O1	0.26223	0.9295357	1.075806
	S1	0.12199	0.9972621	1.002745
long-term	Mf	0.06661	0.0732022	13.66079
	Mm	0.03518	0.0362916	27.55459
	Ssa	0.03099	0.0054758	182.6217

stress change can, however, be around 1 kPa h^{-1} and thus potentially exceeds stress rates of the other processes by 1 to 2 orders of magnitude [Sparks, 1981, Emter, 1997, Sottili et al., 2007]. Furthermore, these subtle stress variations may cause an amplified volcanic reaction, when, for example, the tidal variations cause a widening of tectonic structures [Patanè et al., 1994], a periodic decompression of the host rock [Sottili et al., 2007, Sottili and Palladino, 2012], a variation in the host rock permeability [Bower, 1983, Elkhoury et al., 2006, Manga et al., 2012], self-sealing of hydrothermal fractures [Cigolini et al., 2009], or a mechanical excitation of the uppermost magmatic gas phase [Girona et al., 2018].

Studies on the tidal manifestation in volcanic degassing First studies on the co-variations in tidal pattern and volcanic gas emissions hypothesised a possible tidal impact on the observed sulphur dioxide (SO_2) emission fluxes at Masaya [Stoiber et al., 1986] and Kilauea [Connor et al., 1988]. Since the 2000s, automatic scanning networks based on UV-spectrometers [e.g. Galle et al., 2010] have provide multi-year time series of volcanic gas emissions of SO_2 and bromine monoxide (BrO). The availability of such data sets enabled extensive investigation of long-term degassing variations. Correlation with the long-term tidal patterns has been reported for the SO_2 emission fluxes of Villarrica and Llaima [Bredemeyer and Hansteen, 2014], and the BrO/SO_2 molar ratios in the gas plume of Cotopaxi [Dinger et al., 2018]. Another possible but less significant correlation has been reported for the SO_2 emission fluxes of Turrialba [with a periodicity somewhere between 9.1 d and 16.7 d, Conde et al., 2014]. Furthermore, Lopez et al. [2013] reported a periodicity of roughly 16 d in the SO_2 emission fluxes of Redoubt retrieved from the satellite-based Ozone Monitoring Instrument (OMI) — the authors proposed that this periodicity is, however, an artefact of the satellite orbit rather than a tidal signal. In addition, correlation with the long-term tidal patterns have been reported for the diffuse radon degassing of Terceira [Aumento, 2002] and Stromboli [Cigolini et al., 2009].

Cycles in volcanic degassing patterns are not unique to periodicities which match the tidal potential. Many studies reported periodic volcanic degassing patterns with periods of minutes [e.g. Fischer et al., 2002, Boichu et al., 2010, Campion et al., 2012, 2018, Tamburello et al., 2013, Pering et al., 2014, Ilanko et al., 2015, Moussallam et al., 2017, Bani et al., 2017]. In contrast, observations of long-term periodicities are rare. Besides the above mentioned about biweekly periodicities, periodic long-term pattern with periodicities of 50 days and 55 days have been observed in the SO_2 emission flux of Soufrière Hills [Nicholson et al., 2013] and Plosky Tolbachik [Telling et al., 2015], respectively.

3 Remote sensing of volcanic gases

This chapter gives a recapitulation of the most important concepts which are required to follow the applied measurement strategy and evaluation. A comprehensive discussion of the quantum-mechanical interaction between light and matter can be found in most textbooks on optical spectroscopy [e.g. Platt and Stutz, 2008]. Kern [2009] gives a comprehensive summary tailored to the spectroscopic retrieval of volcanic SO_2 and Lübcke [2014] introduces the retrieval of volcanic BrO/SO_2 molar ratios applied in the thesis. Oppenheimer et al. [2014] and Platt et al. [2018] give a broader comparison of several further remote sensing techniques used in volcanology.

3.1 MAX-DOAS measurement of volcanic gas plumes

Measurement strategy In a Multi-AXis-Differential Optical Absorption Spectroscopy (MAX-DOAS) set-up, spectra of scattered solar radiation from different viewing directions are collected by a small field-of-view telescope and subsequently recorded by a spectrometer (Figure 3.1). The attenuation of solar radiation in the atmosphere depends on the chemical composition of the air along the light path and the effective light path length. All solar radiation which reaches the local troposphere has been exposed to basically the same stratospheric attenuation effects and therefore variations in the observed intensity spectra are caused predominantly either by inhomogeneities in the chemical composition of the local troposphere or different tropospheric light paths. A comparison of the spectra from the different viewing direction thus reveals the angular distribution of the local tropospheric inhomogeneities and effective light path lengths. A volcanic gas plume is a strong local inhomogeneity and in addition the atmospheric background is typically negligible for most volcanic trace gases. In consequence, this inhomogeneity in the chemical composition can be distinguished spectroscopically from a variation of the light path lengths. Accordingly, MAX-DOAS is able to retrieve the attenuation effect caused by a volcanic gas plume by comparing two light spectra which are recorded in the viewing direction of the volcanic gas plume and in a reference viewing direction which is not affected by the volcanic pollution, respectively (see I_{plume} and I_{ref} in Figure 3.1). By a careful spectroscopic evaluation it is furthermore possible to retrieve the concentration distribution (or rather the slant column density distribution, see Section 3.3) of several volcanic trace gases within the volcanic gas plume.

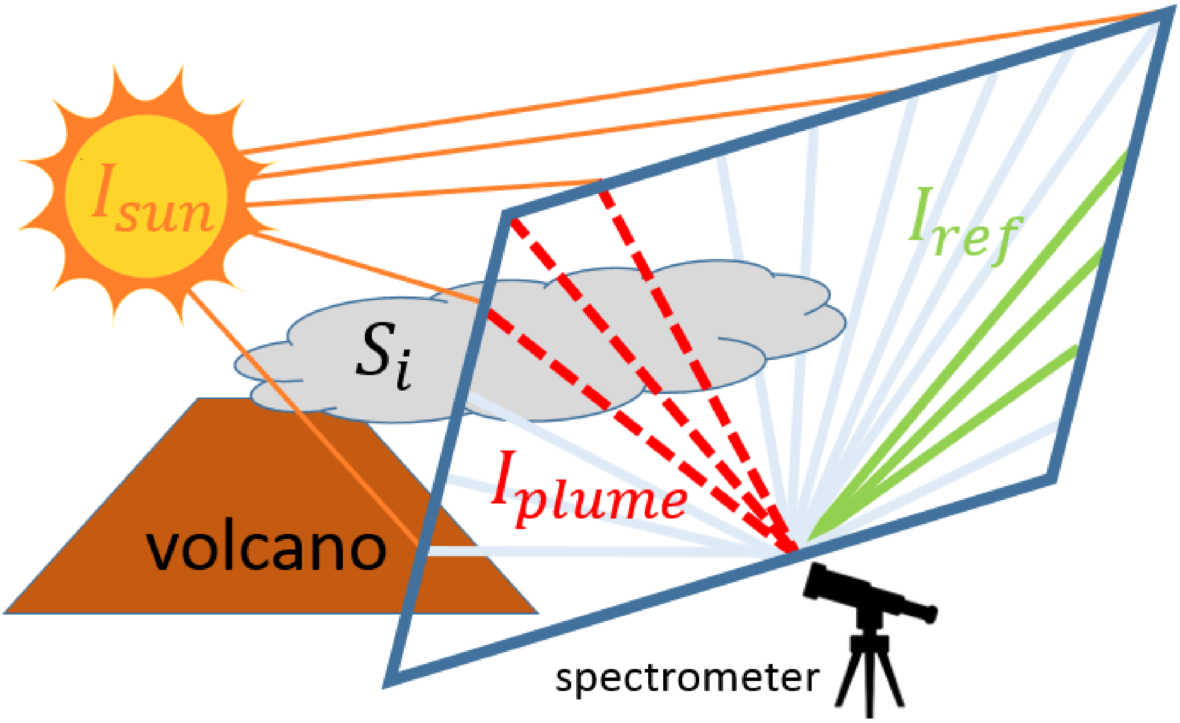

Figure 3.1: MAX-DOAS measurement of a volcanic gas plume: A spectrometer records the scattered solar radiation which is collected by a small-field-of-view telescope. The telescope looks in different viewing directions scanning through the volcanic gas plume and through a reference region which is assumed to be not contaminated by any volcanic gas. The measurement output is the angular distribution of the scattered solar radiation.

Theoretical recipe for optical absorption spectroscopy A reliable interpretation of the MAX-DOAS results requires a theoretical understanding for the different light attenuation processes which can cause the variation in the angular intensity distribution. The theoretical starting point of DOAS (see Section 3.3) is the Lambert–Beer law generalised for light extinction in a narrow beam:

A narrow light beam with an initial intensity spectrum I_0*(photon wavelengths* λ*) propagates through an optical medium with the local light extinction coefficient* $\varepsilon_{ext}(s) > 0$*, where* $s \geq 0$ *indicates the spatial position along the actual light path. Then the beam intensity* $I(\lambda, s)$ *continuously decreases due to the interaction of the light beam with the matter of the optical medium whereat the loss rate is proportional to the local beam intensity, that is*

$$\frac{dI(\lambda,s)}{ds} = -\varepsilon_{ext}(s) \cdot I(\lambda,s) \tag{3.1}$$

The extinction coefficient summarises the beam attenuation effects of all possible interaction mechanisms between photons and the matter of the optical medium. These are predominantly photon absorption by the matter and photon scattering from the beam

to the environment. In contrast, the magnitude of effective photon sources such as photon emission of the matter in the beam or photon scattering from the environment in the beam are typically negligible compared to the magnitude of the beam attenuation processes - at least for measurements in the UV/visible wavelength range. Light extinction is in general actually sub-linearly dependent on the local beam intensity due to, e.g., saturation effects in the photon absorption [Condon, 1964]. A detailed quantum-mechanical investigation of the absorption and scattering processes nevertheless theoretically confirms the validation of the assumed linearity in the empirical Lambert–Beer law for sufficiently small light intensities such as the typical light conditions observed in the Earth's atmosphere.
An integration of the Lambert–Beer law along the actual light path L gives the recipe for optical absorption spectroscopy

$$\tau(\lambda; L) = \underbrace{\ln\left[\frac{I_0(\lambda)}{I(\lambda, L)}\right]}_{\text{measurement}} \overset{!}{=} \underbrace{\int_0^L \varepsilon_{ext}(s)\, ds}_{\text{model}} \tag{3.2}$$

with the optical depth $\tau(\lambda; L)$ associated to the light path L. Hereby, the optical depth $\tau(\lambda; L)$ on the left-hand side of eq. 3.2 is deduced from the MAX-DOAS measurement (whereat $I_0(\lambda)$ is sometimes instead taken from literature [e.g. Chance and Kurucz, 2010]) and the wanted physical parameters are retrieved by a sophisticated model of the involved attenuation processes stated on the right-hand side of eq. 3.2.

3.2 Radiative transport in the troposphere

For MAX-DOAS measurements, the radiative transport of the scatted solar radiation through the troposphere has to be modelled (right-hand side of eq. 3.2). A high-resolution spectrum of the solar irradiance (in the following called the "solar atlas spectrum") is shown in Figure 3.2a+b. The solar atlas spectrum is highly structured with intensity variations by more than 100 % within a range of a nanometre.

The troposphere consists predominantly of air molecules but often also holds a significant aerosol load. Volcanic gas plumes are a mixture of atmospheric air, volcanic gases, and typically a relatively large aerosol load. Aerosol particles are accumulations of many molecules such as water droplets, dust, soot, or volcanic ash.

Four light attenuation processes are quantitatively relevant to model the right-hand side of eq. 3.2 for MAX-DOAS measurements: (1) light absorption by molecules, (2) quasi-elastic Rayleigh photon scattering by molecules, (3) Mie scattering and absorption of photons by aerosol particles, and (4) inelastic Raman photon scattering by molecules.

(1) Light absorption Molecules are quantum-mechanical objects which consist of several spatially separated hadronic nuclei and an electron shell whose electron number equals the total electronic charge of the nuclei. Molecules can absorb photons causing an excitation of their electron shell to a higher electronic energy state or an excitation of their hadronic system to a higher vibrational or rotational energy state. The transition probability from one energy state to another energy state differs between the possible transitions by orders of magnitudes due to quantum-mechanical effects. Therefore, light absorption is extremely sensitive for the absorbed photon energy and thus for the photon wavelength λ. Further, the transition probabilities depend (slightly but differently for each transition) on the ambient conditions, in particular on the ambient temperature T and ambient pressure p.

The absorption cross section $\sigma_i(\lambda, T, p)$ of a vast number of gas species i have been obtained by lab experiments and quantum theoretical calculations for several sets of temperature and pressure conditions. Each gas species has its own unique absorption footprint which allows for a high spectroscopic selectivity between different species (see the high-resolution absorption cross sections of SO_2, O_3, and BrO in Figure 3.3). Given the local number density $\rho_i(s)$ of the particular gas species i, the local absorption coefficient of the particular trace gas species is given by

$$\varepsilon_{absorption,i}(\lambda, s) = \sigma_i(\lambda, T(s), p(s)) \cdot \rho_i(s) \tag{3.3}$$

The excited molecules relax back to the electronic ground state — typically within the next nanoseconds after the photon absorption — and re-emits one or more photons. Photon absorption nevertheless results in an attenuation of the narrow light beam intensity due to two reasons: First, for most eigenstates the re-emission is dominated by

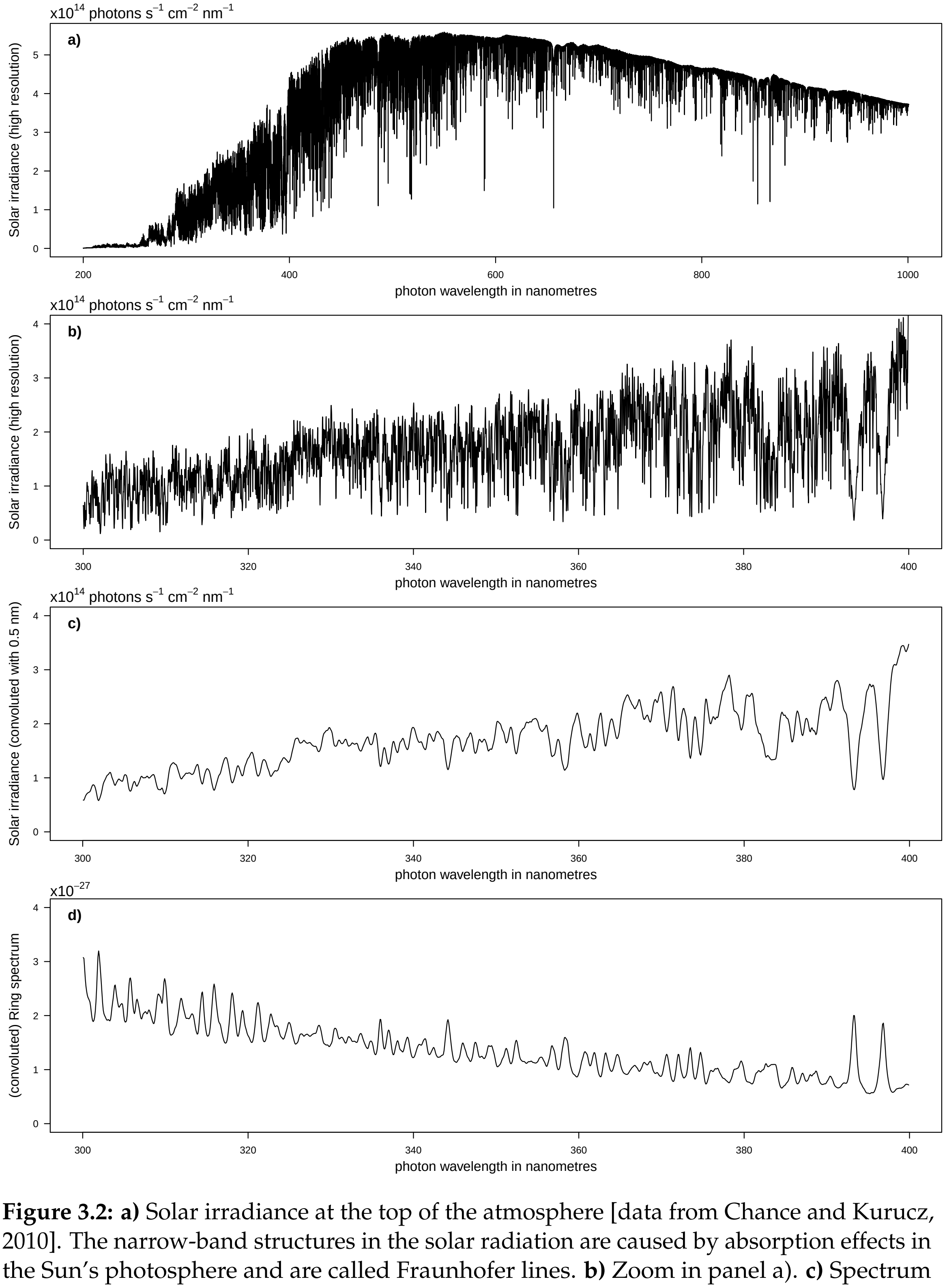

Figure 3.2: **a)** Solar irradiance at the top of the atmosphere [data from Chance and Kurucz, 2010]. The narrow-band structures in the solar radiation are caused by absorption effects in the Sun's photosphere and are called Fraunhofer lines. **b)** Zoom in panel a). **c)** Spectrum from b) convoluted with a Gaussian shaped instrument line function with a FHWM of 0.5 nm. **d)** Calculated Ring spectrum (see text).

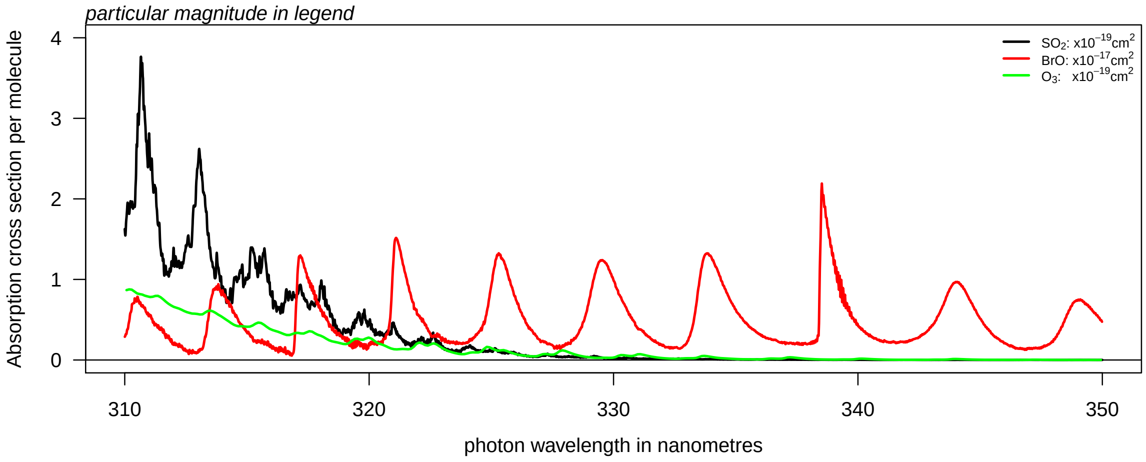

Figure 3.3: High-resolution absorption cross sections of SO_2, O_3, and BrO [Vandaele et al., 2009, Burrows et al., 1999, Fleischmann et al., 2004].

collision-induced relaxation which causes the emission of several photons with much longer wavelengths compared to the absorbed wavelength. Second, the propagation direction of the re-emitted photon(s) does in general not coincide with the initial light beam direction.

(2) Rayleigh scattering Quasi-elastic (i.e. the change of the photon wavelength is negligible) scattering of photons on molecules is called Rayleigh scattering. The Rayleigh extinction coefficient of an air parcel with pressure p and temperature T is given by [e.g. Platt and Stutz, 2008]

$$\varepsilon_{Ray}(\lambda; p, T) = \frac{24 \cdot \pi^3}{\rho_{air}(p, T)} \cdot \left[\frac{n_{air}(\lambda; p, T)^2 - 1}{n_{air}(\lambda; p, T)^2 + 2}\right]^2 \cdot F_K^{air}(\lambda) \cdot \lambda^{-4} \tag{3.4}$$

with the molecular number density of air $\rho_{air}(p, T)$, the refractive index of air $n_{air}(\lambda; p, T)$, and the King depolarisation correction factor of air $F_K^{air}(\lambda) \approx 1.05$. The strong but continuous wavelength dependency of the Rayleigh scattering [approximately $\sim \lambda^{-4.04}$, Nicolet, 1984] can be observed in everyday life: it causes the sky to be blue and the dawn to be red. The phase function of the Rayleigh scattering is approximately given by $\Phi(\theta) = \frac{3}{4} \cdot [1 + \cos^2(\theta)]$ where $\theta = 0°$ indicates the initial photon propagation direction (thus perfect forward-scattering) and $\theta = 180°$ indicates perfect back-scattering. Accordingly, there is a high probability that the propagation direction of the photon significantly changes during the scattering process.

(3) Mie scattering The interaction between photons and spherical aerosol particles whose size is in a the same order of magnitude as the photon wavelength is more complicated to access. Mie [1908] presented an exact quantitative and geometrical solution for the scattering of photons on spherical particles of a given fixed size. Natural aerosol particles - and in particular ash particles - are however neither spherical not all of the same size. Therefore, the Mie extinction coefficient of real aerosols are typically derived by numerical models [e.g., Fu and Sun, 2001] or empirically as

$$\varepsilon_{Mie}(\lambda) \approx \varepsilon_{Mie,0} \cdot \lambda^{-\alpha} \tag{3.5}$$

with the Angström exponent $\alpha \in (0, 4)$ which is inversely related to the size of the aerosol particles [Ångström, 1929]. The Angström exponents of the aerosols in volcanic ash and gas plumes typically range by (1 ± 1) [e.g. Spinetti and Buongiorno, 2007, Hervo et al., 2012, Sellitto et al., 2018]. The Mie phase function depends on the relative size of the particle compared to the photon wavelength. For particles with a size similar or larger than the photon wavelength, the Mie scattering is predominantly forward-scattering with a maximum at 0°.

(4) Raman scattering Inelastic scattering processes of photons on molecules which additionally change the vibrational or rotational energy eigenstate of the molecule are called Raman scattering. Raman scattering can either cause an energy transfer from the photon to the molecule (Stokes process) or an energy transfer from the molecule to the photon if the molecule is already in an excited energy state (anti-Stokes process). The Raman scattering cross section $\sigma^{air}_{Raman}(\lambda; p, T)$ is orders of magnitudes smaller than the Rayleigh scattering cross section [Platt and Stutz, 2008]. Grainer and Ring [1962] nevertheless observed a spectroscopically significant decrease of the optical depths of the Fraunhofer lines in the solar irradiance spectrum caused by atmospheric Raman scattering. This effect is nowadays called the "Ring effect".

The Ring effect can be corrected by considering the atmospheric Raman scattering as a pseudo-absorber and treat it in the spectroscopic retrieval analogously to the absorbing trace gases. For this purpose, the "Ring spectrum" (Figure 3.2d)

$$\sigma_{Ring}(\lambda) = \frac{\sigma^{air}_{Raman} * I_{ref}(\lambda)}{I_{ref}(\lambda)} \tag{3.6}$$

is retrieved by a convolution of the reference spectrum $I_{ref}(\lambda)$ with the Raman scattering cross section [e.g. Solomon et al., 1987, Bussemer, 1993].

For the MAX-DOAS measurement, the differential Ring effect between the viewing directions of the volcanic gas plume and of the reference has to be retrieved/corrected. The Ring spectrum may however differ significantly between the viewing directions of the volcanic gas plume and of the reference if the broadband structure of the intensity spectra $I_{ref}(\lambda)$ and $I_{plume}(\lambda)$ differ. In particular, enhanced Mie scattering in one viewing direction can cause the sky to be "more white" in that direction. This can be caused, e.g., by a (partially) cloudy sky or by a volcanic gas and ash plume which hosts a large aerosol load. The wavelength dependency of the scattering polynomial can typically vary from λ^{-4} to λ^{0}. The reference region typically hosts less aerosols thus the original Ring spectrum (eq. 3.6) is calculated rather for the lower end-member case of λ^{-4}. The upper end-member can be approximated by adding a second pseudo-absorber

$$\sigma_{Ring\lambda 4}(\lambda) = \lambda^{4} \cdot \sigma_{Ring}(\lambda) \tag{3.7}$$

to the fit scenario. While this "linear interpolation" of the two end-members can not perfectly retrieve the actual differential Ring effect, it is a sufficient correction as long as the optical depth of the analysed process is above 10^{-4} [Wagner et al., 2009].

Angular distribution of differential optical depths The MAX-DOAS measurement does not output a single optical depth with respect to the extraterrestrial light intensity I_0 but an angular distribution of differential optical depths with respect to the light intensity I_{ref} recorded at an arbitrary but fixed telescope elevation angle α_0 (a-priori usually zenith looking and a-posteriori picked for the then determined reference direction, see Figure 3.1). The differential optical depth in dependency of the elevation angle α is then calculated by $\tau(\lambda;\alpha) = I_{ref}(\lambda;\alpha_0)/I(\lambda;\alpha)$. With the parametrisations of the four relevant tropospheric attenuation processes, for a chosen set of i significantly absorbing trace gas species, and $j = \{i, Ring, Ring\lambda 4\}$ considering absorption and Raman scattering, eq. 3.2 can be specified for MAX-DOAS measurements as

$$\tau(\lambda;\alpha) = \int_{0}^{L(\alpha)} \left[\sum_{j} \sigma_j(\lambda, T(s), p(s)) \cdot \rho_j(s) + \varepsilon_{Ray}(\lambda, s) + \varepsilon_{Mie}(\lambda, s) \right] ds \tag{3.8}$$

3.3 Differential Optical Absorption Spectroscopy

This thesis seeks to retrieve the ratio of two gas concentrations ρ_i (or more precisely the ratio of two column densities S_i, see below) in the volcanic plume from remote sensing observations and the radiative transport model stated in eq. 3.8. For this purpose a spectroscopic retrieval algorithm is required which reduces the number of unknown parameters on the right-hand side of eq. 3.8 such that the desired quantities can be obtained by a robust fit on the data set. This is realised by applying differential optical absorption spectroscopy (DOAS) [Platt et al., 1980, Stutz and Platt, 1996, Platt and Stutz, 2008, Kern, 2009] which reduces the level of unknown parameters by assuming several simplifications as discussed in the following.

First, the pressure and the temperature in the local troposphere are approximately constant. Thus, the variations of the absorption cross sections during a measurement due to pressure or temperature variations are rather negligible. Therefore, it is appropriate to use a set of absorption cross sections with fixed temperature and pressure for the retrieval which allow to simplify eq. 3.8 to

$$\tau(\lambda;\alpha) \approx \sum_j \left[\sigma_j(\lambda) \cdot \int_0^{L(\alpha)} \rho_j(s)\, ds \right] + \int_0^{L(\alpha)} \left[\varepsilon_{Ray}(\lambda,s) + \varepsilon_{Mie}(\lambda,s) \right] ds \tag{3.9}$$

where the summation index $j = i + 2$ includes all relevant absorbing trace gas species i plus the two Ring cross sections.

Second, the integrals of the trace gas densities along the actual light path are identified for convenience as the slant column density $S_j(\alpha) = \int_0^{L(\alpha)} \rho_j(s)\, ds$ of the particular trace gas species (in the later text abbreviated as SCD) and eq. 3.9 simplifies to

$$\tau(\lambda;\alpha) \approx \sum_j \left[\sigma_j(\lambda) \cdot S_j(\alpha) \right] + \int_0^{L(\alpha)} \left[\varepsilon_{Ray}(\lambda,s) + \varepsilon_{Mie}(\lambda,s) \right] ds \tag{3.10}$$

Third, the effects of the Rayleigh scattering and the Mie scattering vary rather smoothly with the wavelength while the absorption cross sections (and the Ring cross sections) are typically highly structured. DOAS utilises this qualitative discrimination criterion via a parametrisation of the broadband scattering effects by a polynomial $P(\lambda;n)$ of suitable order $n \in [1,10]$. The ultimate model used by DOAS is accordingly

$$\tau(\lambda;\alpha) \approx \sum_j \left[\sigma_j(\lambda) \cdot S_j(\alpha) \right] + P(\lambda;\alpha;n) \tag{3.11}$$

with $j + n = i + 2 + n$ unknown parameters remaining (for a particular elevation angle α). Typical spectrometers record the intensity spectra (and thus optical depths $\tau(\lambda)$) simultaneously in 512 to 2048 wavelength channels with a channel width of, e.g., about

0.08 nm for NOVAC instruments. The unknown parameters can therefore be retrieved by a multi-dimensional least-squares fit using the set of observed $\tau(\lambda)$. Instead of using the total set of $\tau(\lambda)$, better spectroscopic results can often be achieved when the evaluated wavelength range is limited to the $10 - 25$ nm (thus about $100 - 300$ wavelength channels) were the particular trace gas of interest has suitable absorption features, i.e. where it is maximum selective. That is because limiting the wavelength range reduces the set of significantly contributing gas species to, e.g., $i = 2$ for SO_2 in the UV and $i = 6$ for BrO in the UV, and enhances the validity of the polynomial approximation of the scattering processes for a fixed polynomial order n.
Thus about 10 unknown parameters have to be estimated by a least-squares DOAS fit applied on about $100 - 300$ simultaneously measured $\tau(\lambda)$. In principle, a DOAS fit can simultaneously retrieve the SCDs of all gas species whose absorption cross sections are included in the DOAS fit scenario. It is nevertheless recommended to use for each gas species of central interest an own DOAS fit scenario which maximises the accuracy and precision of the retrieved SCD of the particular gas species.

3.4 Technical application of DOAS

The theory described above presumes an ideal instrument. For real measurements, the electronic and optical set-up adds further sources of uncertainties which have to be corrected prior to or assessed by the spectroscopic analysis. This section gives a summary of the most relevant effects and applied corrections. See Platt et al. [1997], Platt and Stutz [2008], and Kern [2009] for more details.

Optical system

Instrument line function The instrument has a limited spectral resolution. Therefore, the spectrum of a monochromatic photon beam with wavelength λ_{mc} would be altered from its initial delta-peak distribution to the instrument line function (ILF) $\delta(\lambda_{mc}) \rightarrow H(\lambda;\lambda_{mc})$ after passing the optical system. The instrument line function is usually roughly of Gaussian shape. In general, most ILFs can be modelled in good approximation by an asymmetric super-Gaussian line shape

$$H(\lambda) = A \cdot \exp\left[-\left|\frac{\lambda-\lambda_0}{\sigma\cdot[1+\mathrm{sign}(\lambda-\lambda_0)\cdot a_\sigma]}\right|^{k\cdot[1+\mathrm{sign}(\lambda-\lambda_0)\cdot a_k]}\right] \tag{3.12}$$

with the normalised amplitude A, the line width parameter σ, the super-Gaussian exponent k, and the asymmetry parameters a_σ and a_k. The parameter λ_0 gives the maximum of the line shape which is for a symmetric line shape close to (but not necessarily exactly) the initial monochromatic line at λ_{mc} but which is less meaningful for an asymmetric line shape. The full width half maximum (FWHM) of such a line shape is

$$\mathrm{FWHM} = \sigma\cdot\sqrt[k]{\ln(2)}\cdot\underbrace{\left[(1-a_\sigma)\cdot\left(\sqrt[k]{\ln(2)}\right)^{\frac{-a_k}{1+a_k}} + (1+a_\sigma)\cdot\left(\sqrt[k]{\ln(2)}\right)^{\frac{a_k}{1-a_k}}\right]}_{\text{for a symmetric line shape } (a_\sigma=0,\ a_k=0):\ \Rightarrow 2} \tag{3.13}$$

The ILF can be accessed by recording the emission lines of elementary lamps (e.g. mercury) because their spectra virtually consists of monochromatic delta-peaks and the ILF is then the shape of the actually measured emission lines. Another possibility lies in the retrieval of the broadening of the measured Fraunhofer lines compared to their pendants in a solar atlas spectrum (see Section 4.4).
The ILF is in general dependent on λ_{mc}. For the limited wavelength range of the DOAS retrieval of the particular gas species of interest, the assumption of a fixed ILF independent on λ_{mc} is usually considered to be to be sufficiently accurate. This assumption is applied in the spectroscopic retrieval used in this thesis and also in the following theoretical discussion. Any incident radiation spectrum $I(\lambda, L)$ can be

considered to be fundamentally a collection of monochromatic delta-peaks, thus after the passing the optical system the convoluted radiation spectrum

$$I^*(\lambda, L) = I(\lambda, L) * H(\lambda) = \int I(\lambda - \lambda') \cdot H(\lambda, \lambda')\, d\lambda' \tag{3.14}$$

hits the detector (Figure 3.4). Analogously also the absorption signal of a gas species i is recorded by the instrument as $\sigma_i(\lambda)^* = \sigma_i(\lambda)^{high\,resolution} * H(\lambda)$. An accurate spectroscopic retrieval therefore requires accurate knowledge on the ILF at the particular measurement time of the spectrum.

Convolution with a symmetric ILF with wrong line width Lübcke [2014] investigated the effect of a convolution of the high resolution absorption cross sections with a slightly wrong ILF line width on the accuracy of the SO_2 and BrO SCDs retrieved by DOAS. For this purpose, he prepared two synthetic Fraunhofer spectra (a reference spectrum and a measurement spectrum which is the reference plus additional absorption signals) by a convolution with a Gaussian-shaped ILF with a chosen "true" full width half maximum (FWHM). In contrast, the convoluted absorption cross sections of the SO_2 and BrO DOAS fit scenarios are calculated by a convolution of the high resolution absorption cross sections with a Gaussian-shaped ILF with another "applied" (thus not the "true") FWHM. His study implies a relative systematic offset of the retrieved SO_2 SCDs by $-1.5\,\%$ per $+0.01\,\mathrm{nm}$ difference in the FWHM of the applied ILF minus the true ILF. For BrO, the relative systematic offset has been smaller and depends on the absolute SCD, e.g., $-0.5\,\%/0.01\,\mathrm{nm}$ for $S_{\mathrm{BrO}} = 1.5 \cdot 10^{14} \frac{\mathrm{molec}}{\mathrm{cm}^2}$ but only $-0.35\,\%/0.01\,\mathrm{nm}$ for $S_{\mathrm{BrO}} = 3 \cdot 10^{14} \frac{\mathrm{molec}}{\mathrm{cm}^2}$. The relative systematic offset in the BrO/SO_2 molar ratios lies between the offset of the relative effect on the SO_2 SCDs and the BrO SCDs, e.g., $+1.1\,\%/0.01\,\mathrm{nm}$ for $S_{\mathrm{SO_2}} = 1 \cdot 10^{18} \frac{\mathrm{molec}}{\mathrm{cm}^2}$ and $S_{\mathrm{BrO}} = 1.5 \cdot 10^{14} \frac{\mathrm{molec}}{\mathrm{cm}^2}$. These quantitative simulation results should not be understood to hold in general but are useful to estimate the upper limit of the systematic error caused by unknown deviations of the applied ILF from the true ILF during the actual measurement.

Convolution with an asymmetric ILF with wrong asymmetry If the asymmetry of the ILF is wrongly estimated, the convoluted absorption cross section is in general shifted in its wavelength calibration. As long as the centre of mass location and the line width of the ILF correctly estimated, these shifts can be expected to be lower than $\pm 0.1\,\mathrm{nm}$ for any realistic misestimation of the asymmetry of the ILF (Figure 3.5). The ILFs of the NOVAC instruments evaluated in this thesis roughly vary between a symmetric and a right-heavy asymmetric Gaussian shape (green and red ILF in Figure 3.5). This implies that also temperature-driven diurnal variations of the ILFs can be expected to vary the ILF in the range between the green and the red ILF, although presumably by much less than the illustrated range. The shifts depend on the particular

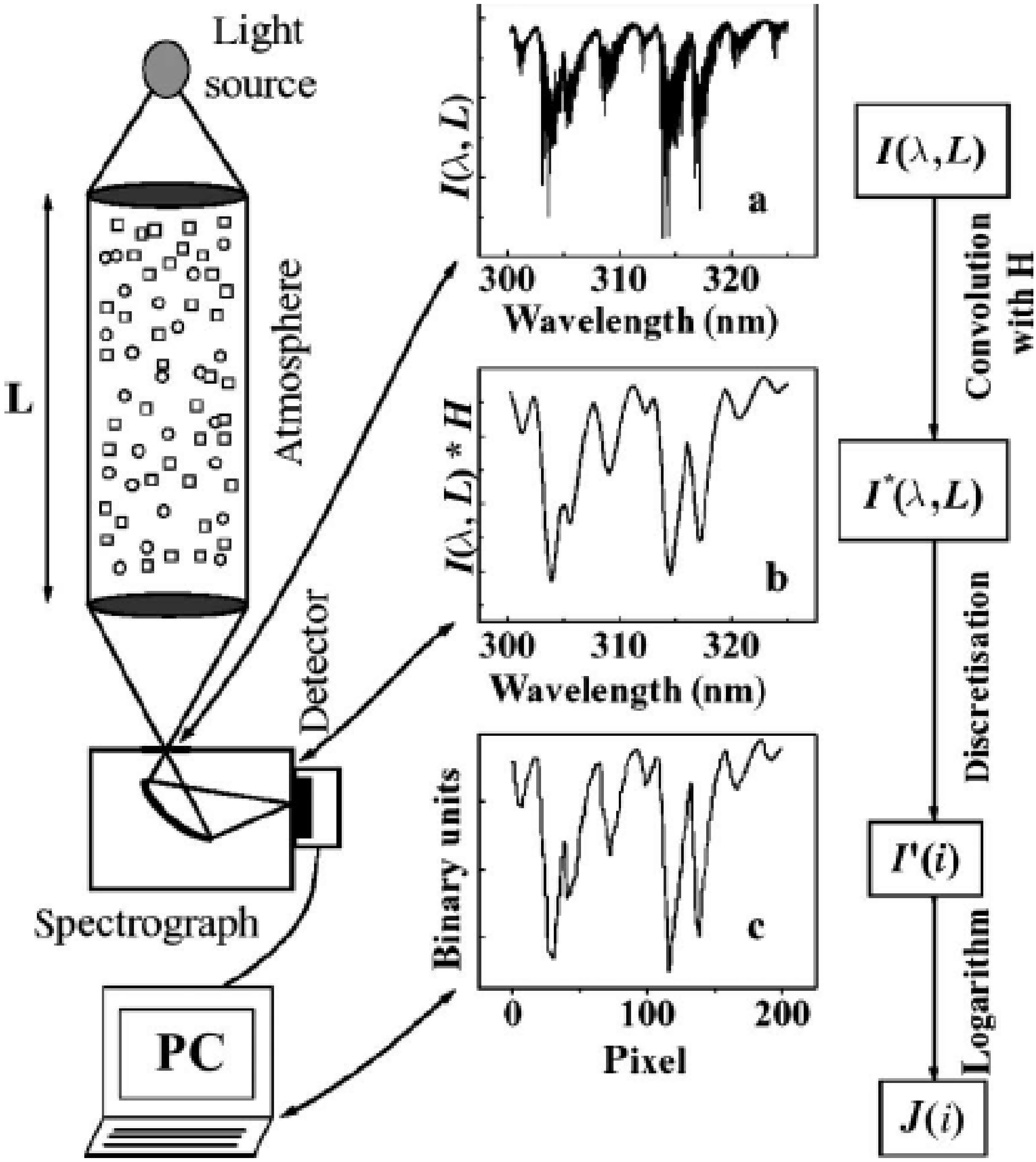

Figure 3.4: Sketch of a DOAS measurement. Light from a source propagates through the atmosphere and its residual spectrum is recorded by a spectrometer. Figure reprinted from [Stutz and Platt, 1996] with a Fair Use permission from OSA.

absorption cross section and thus have a different magnitude for different trace gas species, e.g. Figure 3.5 proposes that BrO is less affected by a wrongly estimated asymmetry of the ILF than SO_2. As a remark, the shifts may exceed ± 0.1 nm if the centre of mass location is wrongly estimated (e.g. the calibration has been applied on the maximum location instead, see Figure 3.6).
On the one hand, these ILF-driven wavelength shifts could be sufficiently corrected automatically during the DOAS fit by allowing the Levenberg–Marquardt part of the DOAS fit (see below) to shift each convoluted absorption cross section by a dynamically retrieved effective wavelength shift (and squeeze). On the other hand, such a procedure would add more degrees of freedom to the fit scenario and thus could reduce the reliability of the fit results. An often applied compromise is to link all absorption cross sections together and optimise for one shared effective wavelength shift and wavelength squeeze (see below).

Validity of the DOAS algorithm The step from the Lambert–Beer law (eq. 3.1) to the optical depth τ (eq. 3.2) requires the mathematical operation of the logarithm. For a non-high-resolution measurement, this step is not strictly valid because the mathematical operations of a logarithm and a convolution do not commute. Nevertheless, as long as the absorption signals are small compared to the overall intensity of the measured spectrum the logarithm can be approximated by the linear function $\log(1+x) \approx x$ and thus eq. 3.2 regains approximate validity. In the context of MAX-DOAS tomography, small means an optical depth of $S_i \cdot \sigma_i(\lambda) \leq 0.1$. A practical way to circumvent this limitation lies in the shift of the analysed wavelength interval to an interval where the maximum magnitude of $\sigma_i(\lambda)$ is sufficiently small for a given S_i. As a remark, this limitation only holds for the absorption signals and the Ring effect but not for the broad-band scattering signals.

Undersampling: the I_0 effect and the tilt effect In a non-high resolution measurement, the Fraunhofer lines in the highly structured solar radiation spectrum cause two significant effects on the spectral retrieval of MAX-DOAS tomography called collectively the I_0 effect. As discussed in the last paragraph, the DOAS retrieval is only a good approximation when the optical depth of a particular absorption signal is small compared to the intensity in the (high-resolution) spectrum. While comparatively large intensities may have been recorded at the position of the measured, i.e. convoluted, Fraunhofer lines, there is only little intensity at the bottom of the actual Fraunhofer lines. The DOAS retrieval is thus intrinsically inaccurate at the Fraunhofer lines even when the average absorption signals do not exceed the optical depth threshold of 0.1. In addition and more subtle, the spectral absorption structures interfere with the Fraunhofer lines such that the step from eq. 3.1 to eq. 3.2 is invalid in this case because the ratioing and the convolution do not commute. The I_0 effect can be approximately

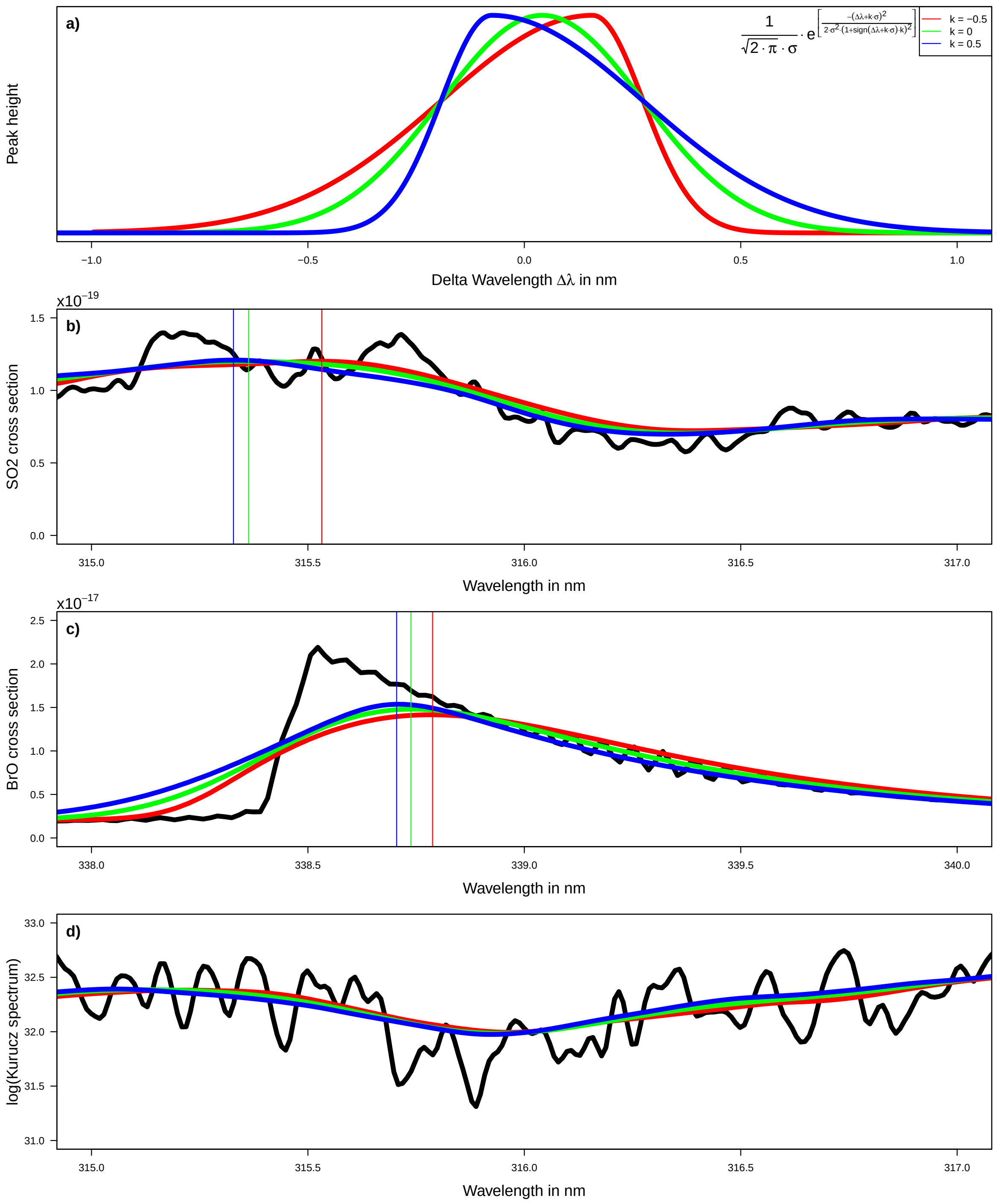

Figure 3.5: a) Three ILFs with the centre of mass at the same location but different asymmetry (the shift between maximum and centre of mass is actually $k \cdot \sigma - \mathcal{O}(\sigma^3)$). **b)** Zoom in the SO_2 absorption cross section from [Vandaele et al., 2009, @298 K] convoluted with the three ILFs. **c)** Zoom in the BrO absorption cross section from [Fleischmann et al., 2004, @298 K] convoluted with the three ILFs. **d)** Zoom in the Solar Atlas from Chance and Kurucz [2010] convoluted with the three ILFs (logarithmised). The local maxima of the convoluted absorption cross sections are indicated by the vertical lines.

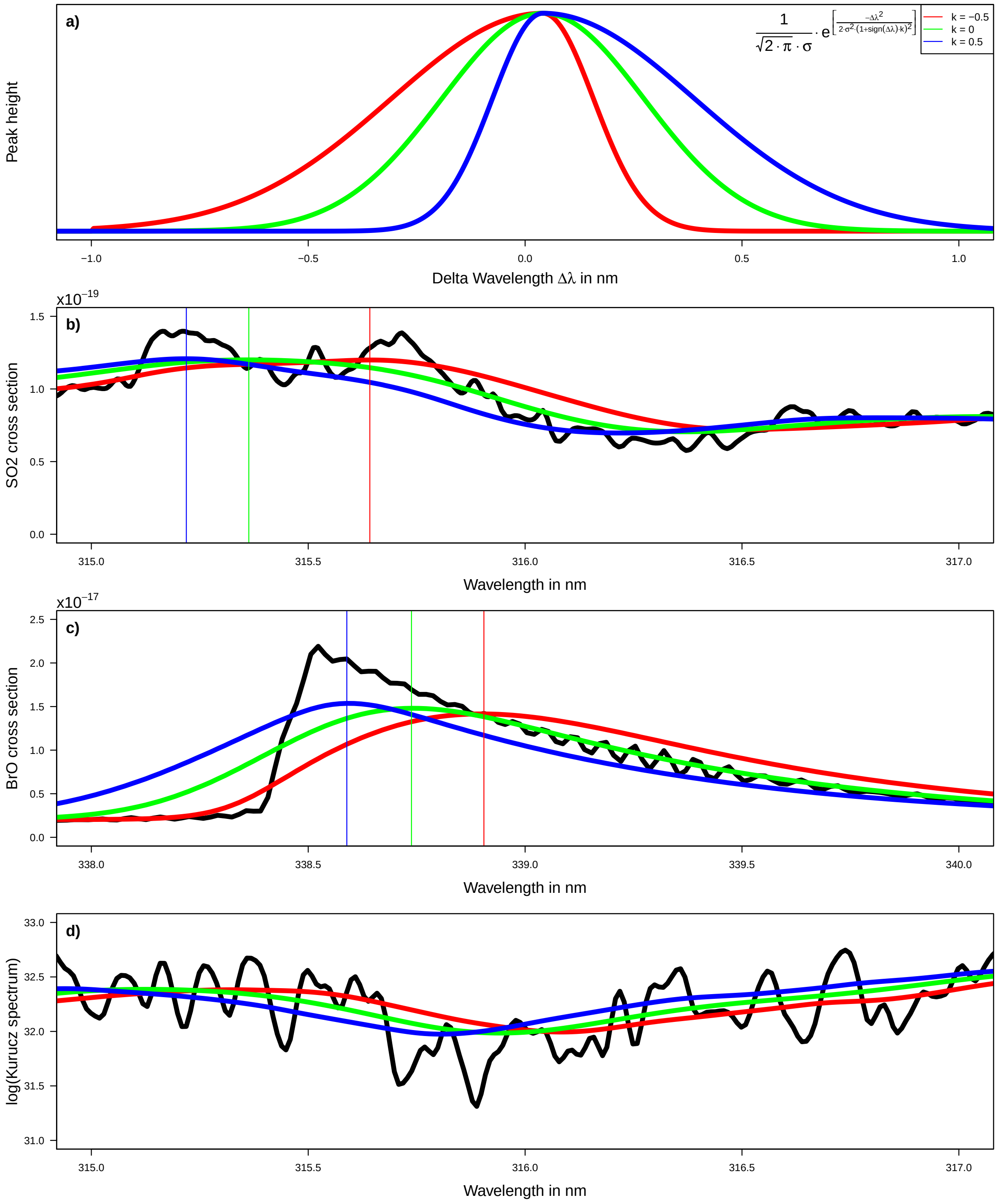

Figure 3.6: a) Three ILFs with different asymmetry and the same maximum location but thus different centre of mass locations. **b)** Zoom in the SO_2 absorption cross section from [Vandaele et al., 2009, @298 K] convoluted with the three ILFs. **c)** Zoom in the BrO absorption cross section from [Fleischmann et al., 2004, @298 K] convoluted with the three ILFs. **d)** Zoom in the Solar Atlas from Chance and Kurucz [2010] convoluted with the three ILFs (logarithmised). The local maxima of the convoluted absorption cross sections are indicated by the vertical lines.

corrected by re-calculating the effective absorption cross section $\sigma_i^{I_0}(\lambda, S_i)$ given a particular S_i by [Aliwell et al., 2002, Wagner et al., 2002]

$$\sigma_i^{I_0}(\lambda, S_i) = \frac{1}{S_i} \cdot \ln \left[\frac{I_{hr}(\lambda) * H(\lambda)}{[I_{hr}(\lambda) \cdot \exp(-\sigma_i(\lambda) \cdot S_i)] * H(\lambda)} \right] \tag{3.15}$$

with a high-resolution solar atlas spectrum $I_{hr}(\lambda)$, e.g., in this thesis the spectrum from Chance and Kurucz [2010] has been used.

Further, the interference of broad-band scattering structures with the Fraunhofer lines causes a variation of the relative depths of the Fraunhofer lines. These variations systematically shift the centre of mass of the intensity spectrum towards the direction where the differential broad-band structures between reference spectrum and plume spectrum are weaker. The convolution of the highly resolved structures by the instruments manifests this spectral shift in the convoluted spectrum by up to 1 pm for typical instruments, the so-called tilt effect [e.g. Lampel et al., 2017]. This shift is nevertheless rather small compared to the typical resolution of the spectrometer (of about 80 pm for the NOVAC instruments) and can thus be corrected in very good approximation by the Levenberg–Marquardt shift parameter in the DOAS fit (see below).

Detector effects

Electronics: offset and dark current The charge-coupled device detector records the scattered solar radiation spectrum by adding several subsequent exposures to an average spectrum in order to obtain a high signal-to-noise ratio while avoiding spectral saturation. The analogue-to-digital converter of the detector can not handle negative voltages. Therefore a low positive voltage offset is added to any detector signal in order to avoid negative signals caused by electronic noise. This offset slightly varies with temperature and also between channels. The actual offset spectrum can be accessed by covering the telescope, and recording and averaging several thousand individual exposures (at the minimum exposure time of about 3 ms). This offset spectrum then has to be subtracted from all recorded scan spectra. For the subtraction the offset spectrum has to be rescaled such that it matches the same number of individual exposures used to record the particular scan spectrum.

The detector exhibits a dark current caused by the thermal excitation of electrons in the detector. The dark current signal increases nearly linearly with increasing exposure times and exponentially with increasing temperatures. The actual dark current spectrum can be accessed by covering the telescope and recording a spectrum with rather large exposure time (but avoiding any saturation effects in the spectrum) of about 10 s. The dark current effect can then be corrected in good approximation by a subtraction of the offset-corrected dark current spectrum from the already offset-corrected scan spectra whereby the dark current spectrum has to be rescaled in order to match the total exposure time of the particular scan spectrum. Furthermore, the dark current and the scan spectrum have to be recorded by similar temperatures. Accordingly an active cooling control helps not only to reduce the dark current exponentially but also improves the dark current correction.

Wavelength-to-pixel mapping The detector records different wavelength intervals of the convoluted spectrum by (usually) 2048 channels (or "pixels"). The spectroscopic analysis requires the translation back from the channel/pixel space to the wavelength space. Because the detector is planar and due to non-linear dispersion in the optical system, the wavelength-to-pixel mapping (WPM) is non-linear and furthermore temperature dependent. The WPM can be accessed by calibrating either the peaks of the emission spectrum of an elementary lamp or the Fraunhofer lines in a recorded atmospheric spectrum, respectively, to their literature positions. For the limited wavelength ranges used in a typical DOAS fit, the WPM can then be derived in good approximation as a polynomial of second order

$$WPM_{ref}(\lambda) = a_0 + a_1 \cdot \lambda + a_2 \cdot \lambda^2 \tag{3.16}$$

fitted on the previously determined calibration points.

Stray light Some incident radiation leaks through the optical system due to the finite optical quality of the involved optical components. Parts of the stray light are then reflected in an usually unknown way on the detector causing enhanced signals independent on the actual wavelength of the incoming stray light photons. The stray light signals add arguably almost identically to the reference spectrum and the measurement spectrum, such that the measured optical density spectrum reads $\tau = \log[(I_{ref} + I_{stray})/(I_{meas} + I_{stray})]$. The stray light effect can be partially corrected by allowing the DOAS fit to retrieve I_{stray} spectroscopically. This is realised by adding a stray light polynomial — typically of 0th or 1st order — in the intensity space to the DOAS fit scenario.

DOAS fit scenarios

Levenberg–Marquardt fit The WPM of two recorded solar radiation spectra differs due to temperature effects and due to the tilt effect. The temperature effect can be minimised either by an active temperature control and/or by recording both spectra in fast succession and thus at approximately the same ambient temperature. The tilt effect is however an unavoidable systematic uncertainty. The DOAS algorithm retrieves these effects by combining the least-squares fit with a Levenberg–Marquardt fit. The Levenberg-Marquart fit starts with the same WPM for the reference spectrum and the measurement spectrum and then iteratively varies the WPM_{ref} of the reference by adding a shift (in this thesis limited to $a_{shift} \in \pm 0.2\,\mathrm{nm}$, but with retrieved values predominantly within $\pm 0.3\,\mathrm{pm}$) and squeeze (in this thesis limited to $a_{squeeze} \in 1 \pm 0.02$, but with retrieved values predominantly within 1 ± 0.0005) of the WPM such that

$$WPM_{meas}(\lambda) = WPM_{ref}(\lambda) + a_{shift} + (a_{squeeze} - 1) \cdot (\lambda - \lambda_0) \tag{3.17}$$

with a fixed reference wavelength λ_0, e.g. the wavelength of the first channel of the chosen fit range.

The WPM of the convoluted absorption cross section could also differ from the WMP of the recorded spectra. The most obvious origins of such deviations could be (1) a slight mis-calibration of the high-resolution absorption cross sections, (2) a convolution of the high-resolution absorption cross sections with a ILF which slightly deviates from the ILF of the currently evaluated intensity spectra, (3) a mis-calibration of the recorded spectra, (4) a (partial) saturation of the strongest absorption lines, or (5) a wavelength shift analogously to the above mentioned tilt effect. The first origin could be avoided by a proper preparation of the absorption cross sections. The second origin could be avoided by a routinely measurement or retrieval of the ILF. This is not the case for NOVAC measurements where the same ILF is used for a large range of ambient conditions. but is unavoidable when knowledge on the ILF is limited. The third origin has to be basically avoided by a reliable calibration of the recorded spectra. Nevertheless, the precision of a Fraunhofer calibration is limited at the effective lower limit of the solar spectrum ($\sim 300\,\mathrm{nm}$, see Figure 3.2). The fourth and fifth origin are real variations of the effective absorption cross section, i.e. the validity of the applied high-resolution cross section has slightly decreased for such measurement scenario with strong absorption signals.

On the on hand, the WPM of every individual absorption cross sections could deviate differently from the WPM of the recorded spectra. On the other hand, a DOAS fit scenario is typically tailored to one absorbing species whose absorption signal dominates the other absorption signals. It has been empirically observed that this misalignment can be partially corrected by including a further set of two Levenberg–Marquardt parameters which are shifting and squeezing the WMP of all convoluted absorption cross sections simultaneously. Section 4.4 discusses whether and how these additional parameters could improve the retrieval of NOVAC data.

For the NOVAC retrieval, the fit ingredients are grouped in three blocks of shared WPM: (1) the measurement spectrum, (2) the reference spectrum and the 2 Ring spectra, and (3) all absorption cross sections. The DOAS fit is then allowed to optimise the relative positions of these three blocks by shifting and squeezing their WPM accordingly, thus there are 4 Levenberg–Marquardt fit parameters (2 shift and 2 squeeze parameters).

As a remark: The actual implementation in the DOASIS software (Section 4.2) copies the WPM of the reference spectrum to the measurement spectrum and then applies shift and squeeze on the reference spectrum (+ identical modifications applied of the Ring spectra). This is a mathematically identical algorithm.

Table 3.1: DOAS fit scenarios as applied in this thesis. The two lowest lines give the parameter ranges of the Levenberg–Marquardt fit routine.

	SO_2 fit	BrO fit
Fit range	$314.8 - 326.8$ nm (standard) $326.5 - 335.3$ nm (alternative)	$330.6 - 352.75$ nm
(Pseudo-)Absorption cross sections:		
SO_2	Vandaele et al. [2009], @298 K	(same)
O_3	Burrows et al. [1999], @221 K	(same)
BrO		Fleischmann et al. [2004], @298 K
O_4		Hermans et al. [2003]
NO_2		Vandaele et al. [1998], @294 K
CH_2O		Meller and Moortgat [2000], @298 K
2 Ring spectra calculated from the particular reference spectrum		
Further DOAS fit parameters:		
Polynomial of order $n = 3$ in the optical depth space		
Stray light polynomial of order $n = 0$ in the intensity space		
Reference spectrum (+ 2 Ring spectra): $a_{shift} \in \pm 0.2$ nm and $a_{squeeze} \in 1 \pm 0.02$		
Absorption cross sections (linked together): $a_{shift} \in \pm 0.2$ nm and $a_{squeeze} \in 1 \pm 0.02$		

DOAS fit of SO_2 and BrO Finding the optimal DOAS fit scenario is cumbersome and differs between instruments. In this thesis, the NOVAC spectra are evaluated with the fit scenarios given in Table 3.1 which are based on the proposals by Vogel [2011], Vogel et al. [2013], Hörmann et al. [2013], and Lübcke [2014].

The SO_2 absorption cross section contains several wavelengths intervals with strong absorption peaks. Particularly well suited for passive remote sensing is the electronic state spreading from 260 nm to about 330 nm (Figure 3.3) or rather the wavelength range from $300 - 330$ nm because hardly any solar radiation below 300 nm reaches the troposphere (Figure 3.2a). Within this wavelength interval only O_3 contributes significantly to the overall absorption signal allowing for a high sensitivity for SO_2 due to the limited possibilities of interfering gas species. SO_2 SCDs in volcanic plumes observed by NOVAC occasionally exceed $1 \cdot 10^{18} \frac{\text{molec}}{\text{cm}^2}$ resulting in optical densities potentially exceeding the DOAS validity threshold of ~ 0.1. Vogel [2011] proposes a "standard" SO_2 fit range from $314.8 - 326.8$ nm which is valid in good approximation for SO_2 SCDs of up to $1 \cdot 10^{18} \frac{\text{molec}}{\text{cm}^2}$. For the accurate retrieval of extremely strong SO_2 signals (typically exceeding $3 \cdot 10^{18} \frac{\text{molec}}{\text{cm}^2}$), Hörmann et al. [2013] proposes an "alternative" SO_2 fit range from $326.5 - 335.3$ nm which is valid in good approximation SO_2 SCDs of up to $10 \cdot 10^{18} \frac{\mathrm{molec}}{\mathrm{cm}^2}$. As drawback, the SO_2 measurement error of the alternative SO_2 fit is drastically increased with relative values of about 10 %, i.e. about $1 \cdot 10^{18} \frac{\mathrm{molec}}{\mathrm{cm}^2}$ for the most extreme SO_2 SCDs. Within this thesis, the SO_2 retrieval uses at every evaluation step the standard fit range by default. The finally processed high-level data are subsequently evaluated with the alternative fit range and final results are picked according to an algorithm which tries to find a best compromise between potential systematic inaccuracy and reduced precision (Section 4.4).

Besides the measurement spectrum and the reference spectrum, the SO_2 fit scenario contains the two Ring spectra and the absorption cross sections of SO_2 [Vandaele et al., 2009, @298 K] and O_3 [Burrows et al., 1999, @221 K]. The broadband features are modelled by a polynomial of 3rd order. Further, a constant intensity offset included in order to correct for stay light. The BrO fit scenario is similar but with a fit range from $330.6 - 352.75$ nm [Vogel, 2011, Vogel et al., 2013] and the absorption cross sections of BrO [Fleischmann et al., 2004, @298 K], SO_2, O_3, O_4 [Hermans et al., 2003], NO_2 [Vandaele et al., 1998, @294 K], and CH_2O [Meller and Moortgat, 2000, @298 K].

Measurement error and detection limit A DOAS fit gives for every SCD of the included gas species an associated fit error which results exclusively from the least-square fit. The least-squares fit method presumes that all 2048 channel measurements are completely independent. In a real measurement the channels are however not completely independent. Accordingly, these fit errors in general underestimate the real measurement error because they (1) do not correct for the inter-correlation of the individual pixels and (2) additionally also do not incorporate the uncertainties of the Levenberg–Marquardt fit. Early investigations by Stutz and Platt [1996] indicated correction factors from the fit errors to the measurement errors of roughly $2 - 3$. Lampel [2014] has however shown by a detailed modelling of his spectrometers that the conversion factors are often below 2.

One way to estimate the correction factor from fit errors to the measurement error lies in analysing the noise of data free of influence from the trace gas of interest. The correction factor can then be estimated as the ratio of the standard deviation of the SCDs divided by the mean fit error of the SCDs. Within this thesis, the correction factors for BrO are determined in that way separately for each instrument with correction factors varying from $1.09 - 1.92$ (except for two outlier instrument with factors of 2.60 and 2.88, see Table 4.3). For SO_2, it was not possible to obtain sufficiently gas free data causing fro some instruments unreliable results. For consistence, a fixed correction factor of 2 has been used to calculate SO_2 measurement errors for the SO_2 fit errors. The detection limits are reported as two times the mean measurement error of the gas free data.

For the BrO/SO_2 molar ratios, the measurement errors are calculated by Gaussian error propagation and the detection limit is given by the mean BrO detection limit of the particular instrument divided by the simultaneously retrieved/recorded SO_2 SCD.

4 Retrieval of BrO/SO_2 molar ratios from NOVAC data

4.1 Network for Observation of Volcanic and Atmospheric Change (NOVAC)

Remote sensing networks The development of passive remote sensing techniques such as DOAS allows for recording semi-continuous (only during daytime) long-term time series of the magnitudes of volcanic gas emissions as well as analyses of the shape and transport of volcanic gas plumes. Since the early 2000s, the costs of performing such measurements have been drastically reduced due to the installation of automatic remote sensing networks at an increasing number of volcanoes, e.g. Soufriere Hills [Edmonds et al., 2003], Stromboli and Mt. Etna [FLAME network Burton et al., 2009, Salerno et al., 2009], Kilauea [FLYSPEC, Businger et al., 2015], or White Island [Miller et al., 2006]. Most prominently, the Network for Observation of Volcanic and Atmospheric Change (NOVAC), funded by the European Union from 2005 − 2010, encompasses today more than 100 automatically measuring optical UV-spectrometers permanently installed at 42 volcanoes predominantly located in South and Central America (see Figure 4.1, https://novac-community.org/, and [Galle et al., 2010]).

NOVAC instruments The NOVAC instruments are designed in an autarkic and simple set-up in order to match the harsh conditions and remote locations of volcanoes [Galle et al., 2003, Kern, 2009, Galle et al., 2010]. As a drawback, NOVAC instruments do not have an active temperature control as the power supply by solar panels is limited. The NOVAC data are recorded by UV-spectrometers which scan across the sky from horizon to horizon in steps of 3.6° by means of a small-field-of-view telescope yielding a mean temporal resolution of about 10 min per scan. The usable wavelength of the recorded spectra range from 280 nm to 360 nm, which allows — in its current state — for an automatised retrieval of the slant column densities of SO_2 [Galle et al., 2010] and BrO [Lübcke et al., 2014] in the volcanic gas plumes.

Figure 4.1: Map listing the volcanoes monitored within the Network for Observation of Volcanic and Atmospheric Change (NOVAC) asof June 2018. Courtesy of Santiago Arellano, see http://www.novac-project.eu/images/Map2018.png.

Raw data recorded by the NOVAC instruments Prior to each scan (every 5 − 15 min), the measurement routine adjusts the exposure time to the meteorological conditions. This adjustment is determined by recording a set of zenith spectra with varying numbers of consecutive exposures. Because the main goal of NOVAC is the monitoring of volcanic SO_2 emission rates, this try-and-error algorithm stops once the number of consecutive exposures is sufficiently close to the exposition conditions which have been fixed manually as the best compromise between precision and temporal resolution of the SO_2 measurement. While this leads typically to a precision of the SO_2 retrieval in the percent range, the setting is not optimal for the BrO retrieval.
The latest zenith spectrum is saved as the the first spectrum associated with the new scan. Next, the telescope looks downwards where a plate inhibits any light accessing the telescope and a dark current spectrum is recorded and saved as the second spectrum associated with the scan. No additional offset spectrum is recorded, following the pragmatic and measurement time saving approach that the subtraction of a non-offset corrected dark current spectrum from the measurement spectra is sufficient to correct simultaneously for offset and dark current. Subsequently, the telescope scans from horizon to horizon in 3.6° steps adding another 51 spectra to the scan, totalling in 53 spectra per scan.
The NOVAC stations transmit the recorded spectra via radiocommunication to the

local observatories. The transmission rate depends on the meteorological conditions and may have a delay of days. The observatories then regularly upload the raw data on the NOVAC server located at the Chalmers University of Technology in Gothenburg, Sweden. A weekly updated mirror of the Gothenburg server is stored on a server located at the Institute of Environmental Physics at the University of Heidelberg, Germany. A single NOVAC instrument typically records $150 - 200\,\mathrm{MB}$ of data per day, leading to up to $300\,\mathrm{GB}$ of unpacked data per volcano and year. Therefore, the 53 spectra of one scan are compactly saved as one pak-file per scan, reducing the required storage by a factor of 13. During the packing process, the software checks the data and labels "incomplete" scans by a corresponding extension of their file names. The scan data can be unpacked by the PAK2STD.exe program (available on the NOVAC server) which outputs the 53 spectra of a particular scan in 53 individual std-files (DOASIS input file format). Besides the pak-files, the settings of each particular scan are available in a txt-file per scan. Furthermore, for some volcanoes pre-evaluated time series of the SO_2 emission fluxes are available as one or two txt-files per day.

4.2 Processing of NOVAC BrO/SO_2 data

This thesis adopted the spectroscopic retrieval routine described by Lübcke [2014] and Lübcke et al. [2014]. In particular, the DOAS fit scenarios of all spectroscopic retrievals of SO_2 and BrO are applied identically. Also most evaluation steps were applied identically and explicit modifications of their evaluation routine are highlighted in the text. Nevertheless, the architecture of the routine has been fundamentally re-worked during this thesis in order to enhance the extensibility, flexibility, and user-friendliness. Furthermore, the subsequent evaluation (Section 4.3) has been extended during this thesis. This evaluation is automatised by a massive and comprehensive set of GNU R scripts written during this thesis.

Architecture of the retrieval routine The NOVAC spectra are evaluated using the DOASIS software package [Kraus, 2006]. DOASIS comes with a graphical user interface (GUI) and a command console. The DOASIS-GUI enables to display and manipulate spectra, to apply DOAS by means of DOAS fits, and also to run retrieval routines written in jscript (in the form of jscript project jsp-files). A console-based evaluation saves run time and storage and is thus recommended for evaluating large data sets such as the NOVAC data. Console-based evaluations are using for convenience batch files including large lists of jsp-files instead of calling the numerous jsp-files manually. The jsp-files look always similar calling four specific js-files:

1. *Variable_(instrument name).js* lists the path to the data associated to the particular instrument and contains specific settings associated with the instrument and how its data should be evaluated.

2. *GlobalSettings.js* is the header of the project. It loads libraries, defines variables (although some are defined in the main part for convenience/due to DOASIS issues), and loads all globally used data such as the high-resolution absorption cross sections.

3. *Functions.js* lists a large set of functions used in the main part.

4. *(Evaluation.js)*: The main part which is loaded from a set of different fixed evaluation routines (with different names). See below.

The routine *(Evaluation.js)* operates at different levels of data processing, namely: (1) Quality check of the individual scan spectra, (2) a retrieval of the angular distribution of the SO_2 SCDs during the particular scan, (3) spectral adding of spectra form a particular scan, (4) spectral adding of spectra from consecutively recorded scans.

Preparation of the raw data Some preparations and pre-processing is required before the NOVAC data can be input in the evaluation routine, in particular when a large amount of data should be evaluated automatically. In order to evaluate a particular data set, the desired amount of raw data (i.e. the corresponding pak-files) has to be downloaded from the NOVAC server to the local computer. The set of raw data can then be assessed by *PrepareFiles.R*, an automatised and user-friendly routine written and executed in GNU R.
This routine, first, loads the file names of the (sub-)set (which volcano and which time interval) of the downloaded pak-files manually chosen for the subsequent evaluation. Second, the routine rejects data already labelled by the packing-routine as "incomplete" scans and data with unreliable time stamps such as from the future (with respect to the upload time) or apparently delayed by more than a year (what is presumable rather caused by an erroneous GPS signal and not by a delayed upload). Third, it retrieves the names of all instruments which contribute to the final set of passing scans (i.e. of the pak-files) and creates for each of these instruments a set of jsp-files (differing just in their *Evaluation.js*) as well as a default *Variable_(instrument name).js*-file. Fourth, it creates a set of batch files for each particular instrument. The most important batch file (per instrument) loads the scans one by one by means of pak-files, only then unpacks the individual spectra, runs the scan evaluation routine, and finally deletes all individual spectra. These batch files allow not only for efficiently small storage requirements but also allow for a flexible updating or reprocessing of the data. The additionally created batch files allow for subsequent advanced retrievals or analyses.
When *PrepareFiles.R* has performed properly, the user can read off the involved NOVAC instruments, e.g., by checking the list of created *Variable_(instrument name).js*. Before the batch files can be run, the geo-coordinates of the instruments (accessible e.g. via the txt-files stored on the NOVAC server) have to be added manually to the particular *Variable_(instrument name).js* files and also other instrument specific settings may be changed manually. Furthermore, for each instrument the mercury emission spectrum has to be downloaded from the NOVAC server and has to be prepared such that it includes directly accessible information on the initial wavelength-to-pixel mapping of the spectrometer and the instrument line function (Section 3.4).

Preceding quality checks of the individual spectra Prior to the actual DOAS evaluation, the spectra of each particular scan are checked for several conditions. Only if the scan passes all conditions, it is assessed in the subsequent analysis. The quality conditions are applied in order to filter out spectroscopically unreliable spectra as well as scans whose number of passing reliable spectra are considered insufficient for a reliable spatial analysis. The quality check consists of 4 levels:

1. Check the zenith spectrum for over- and under-exposition: Although the number of consecutive exposures is adapted prior to each scan to the current ambient conditions, the zenith spectrum can be nevertheless over- or under-exposed. The

zenith spectrum is checked for over-exposition at any part of the spectrum (i.e. in particular at the intensity maximum at around 480 nm). If the zenith spectrum is too close to the saturation limit of 3550 counts (88 % of maximum counts, manually fixed), the total scan gets rejected. If not, the zenith spectrum gets dark current-corrected and subsequently checked for under-exposition (checked at the maximum). If the maximum is below 500 counts (12 % of maximum counts, manually fixed) the total scan gets rejected.

2. All spectra recorded at viewing zenith angles beyond $\pm 75^\circ$ are rejected in order to avoid artefacts from nearby obstacles or long light paths. This condition limits the maximum number of spectra per scan to 41.

3. Each particular spectrum of the scan gets checked analogously for over- and under-exposition. The procedure is identical as for the zenith spectrum. If a particular spectrum fails a check, this spectrum is excluded from the further evaluation.

4. After performing the check for all spectra of the scan, the number of passing scan spectra is counted. The scan is rejected if less than 20 spectra have passed the checks. The number of passing spectra is saved in output file, what gives the flexibility to subsequently adjust the required number of passing spectra considered acceptable for the analysis.

Typically less than 10 % of all scans are rejected due to an under-exposition of the zenith spectrum. These spectra a predominately recorded in the early and late hours of the day when the sun light intensity can be relatively low. For Nevado del Ruiz about 25 % of all scans are rejected based on the zenith spectrum reflecting the often particularly cloudy conditions at Nevado del Ruiz. Subsequently, $12 - 40$ % of all scans pass the "≥ 20 spectra" filter (Table 4.1).

Retrieval of the spatial SO$_2$ distribution If the scan passed all quality checks, its spectra are evaluated with the DOAS technique in order to retrieve the angular distribution of the SO$_2$ SCDs during this scan. The actual preparation and settings discussed in this section holds analogously for all DOAS evaluations within this thesis.

1. Wavelength-to-pixel calibration: The calibration is done in two steps. First, the zenith spectrum gets calibrated by coping the initial mercury calibration. The calibration has, however, in general changed since the recording of the mercury spectrum. Therefore, the mercury-calibrated zenith spectrum is compared to the calibrated solar atlas spectrum from Chance and Kurucz [2010]. This routine identifies the Fraunhofer lines in the zenith spectrum and manipulates (by a linear shift and a linear squeeze) the wavelength-to-pixel mapping such that the recorded Fraunhofer lines match with their theoretical wavelengths. The calibration is subsequently copied to all other spectra of the particular scan.

2. Two Ring spectra are calculated by DOASIS with respect to the zenith spectrum.
3. The SO_2 SCDs of each scan spectra are retrieved separately by applying a SO_2 DOAS fit which uses the zenith spectrum as the reference spectrum and the standard fit range from $314.8 - 326.8$ nm (see Section 3.4 for details). As a remark, no I_0-effect correction or additional retrieval with the alternative fit range is applied yet in order to save run time.
4. The resulting angular distribution of SO_2 SCDs is saved in one std-file per scan. This distribution is not absolutely calibrated because the zenith spectrum may contain absorption signals from the volcanic gas plume.
5. If the final set of passing scan spectra is lower than 20, the whole scan is rejected from the further analysis (but the angular SO_2 distribution is nevertheless saved).

The precision of the SO_2 data allows for a spatial analysis of the volcanic plume (Figure 4.2). The integral of this distribution allows to retrieve the SO_2 emission fluxes if and only (1) if it is assured that the SO_2 SCDs are absolutely calibrated, (2) if the wind speed and the wind direction are known, and (3) if the plume height is known [Galle et al., 2010]. The first condition is typically assured and can be checked spectroscopically (Section 4.5). The second and third condition could be retrieved by a tomography if two NOVAC instrument simultaneously observe the gas plume (Section 7.3), but in general these two conditions are estimated and can cause major inaccuracies.

This thesis does not focus on a retrieval of the SO_2 emission fluxes but utilises the angular SO_2 SCD distribution for the evaluation of the BrO/SO_2 molar ratios in the volcanic gas plume.

Spectral adding of scan spectra The optical density of BrO in a volcanic gas plume is at least one order of magnitude smaller than for SO_2 and thus a higher photon statistic is required for sufficiently precise BrO results beyond the detection limit. At manually controlled measurements, this is realised by a sufficiently large number of consecutive exposures (and besides, typical state-of-the-art campaign instruments are much more precise than NOVAC instruments due better spectrometers and an active temperature stabilisation). For NOVAC data optimised with respect to the SO_2 retrieval requirements, the required larger number of exposures per spectrum can be realised by a subsequent spectral adding of spectra which are recorded in the temporal proximity and in the same or at least similar viewing direction.

For this purpose, the evaluation routine utilises in a next step the retrieved SO_2 SCD angle distribution to identify all spectra which are predominantly part of the volcanic plume, i.e. with only little dilution, and add these spectra in order to get one "added-plume-spectrum" per scan. The drawback of this method is the loss of spatial information as the retrieval derives only one mean plume value for the BrO SCDs and thus for the BrO/SO_2 molar ratios. A volcanic gas plume can be assumed to have an

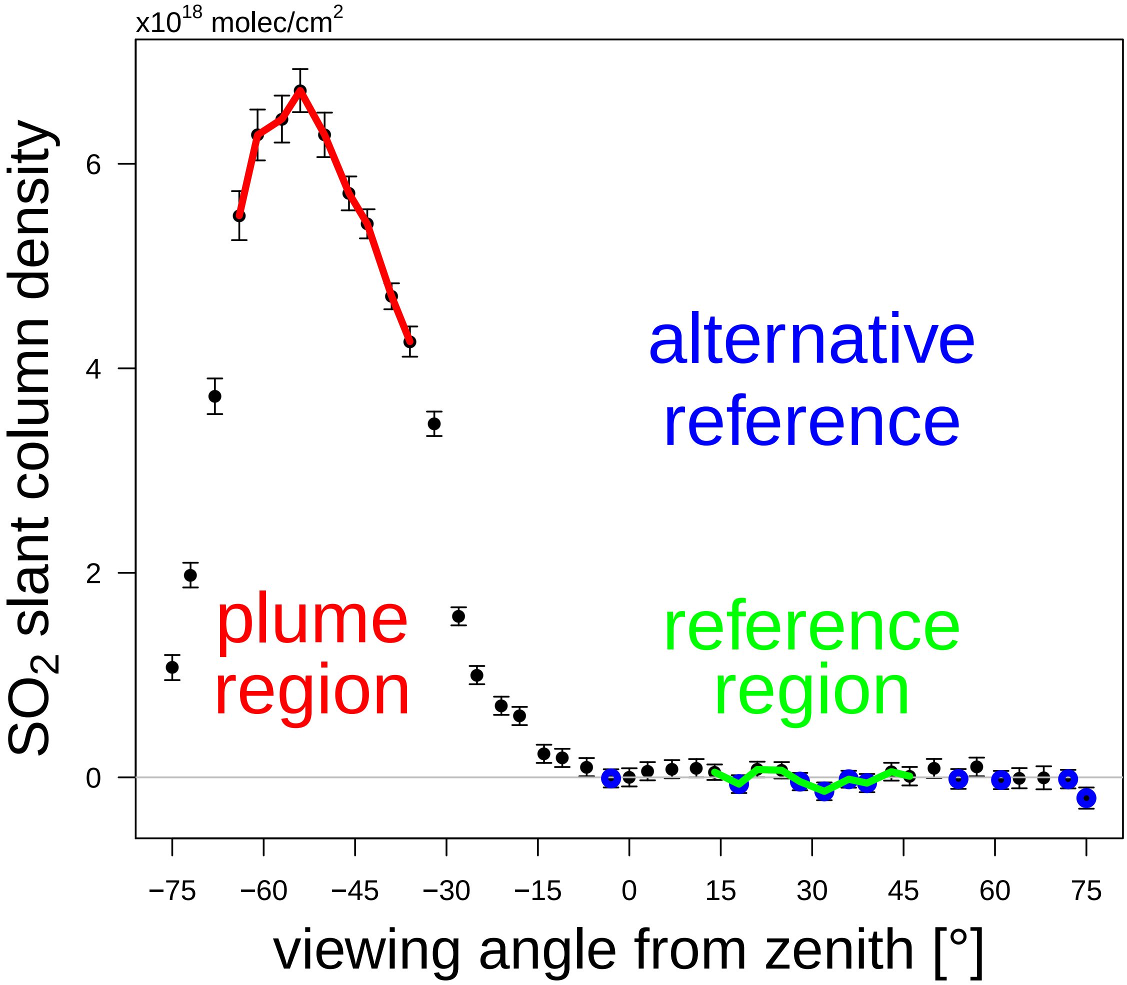

Figure 4.2: Real example results of the preliminary SO$_2$ retrieval as it could be observed by the measurement conditions sketched in Figure 3.1. The spectra of the plume (red) get spectroscopically added and re-evaluated. The original routine from Lübcke et al. [2014] would include an additional tenth data point in the plume region resulting in a smaller mean plume SO$_2$ SCD. The effective reference spectrum could be retrieved by spectroscopic adding of the reference region (green), however, instead the ten spectra with the lowest preliminary SO$_2$ SCD (blue) are added in order to ensure a more flexible algorithm (see text for explanation).

about Gaussian shaped angular gas distribution embedded in a flat, gas free reference region. (The reference region might be differing from zero SO_2 as the arbitrary picked reference spectrum might contain gas. However, on this stage only the angle-dependent shape but not the quantitative value is of interest.)

For their prove of concept, Lübcke et al. [2014] ignored this reasonable assumption of the plume shape and simply defined the plume region as the angle region with the highest running mean value over 10 spectra for the SO_2 SCDs, that is at least an angle region of 33°. This plume region could however include also viewing directions where the volcanic plume has been significantly diluted or when the plume has not yet dispersed to a larger angle region. In consequence, the added-plume-spectrum would then underestimate the SO_2 (and any else) SCD in the actual plume. In this thesis, the plume region is instead automatically retrieved by a Gaussian distribution fitted on the angular SO_2 SCD distribution. The standard deviation range of the Gaussian distribution (peak position $\pm\,\sigma_{Gauss}$) is then defined as the plume region. The Gaussian fit is also used as a quality filter which checks whether a reliable plume region has been found at all: The scan is rejected from the further analysis if no or only a partial plume is detected, i.e. (1) if the Gaussian fit fails to converge, or (2) if $\sigma_{Gauss} < 5°$. Furthermore, if the plume region is rather large it may overlap with the reference region. To avoid this inconsistency, the plume region is defined as proposed by Lübcke et al. [2014] if the (Gaussian) plume region exceeds $2\,\sigma_{Gauss} > 33°$. Empirically, the efficiency of the Gaussian fit filters varies between the volcanoes and rejects between $20-40\,\%$ of the scans which have passed the preceding filters. Masaya is an exception where just 9 % of the data are neglected reflecting the particularly close proximity of the NOVAC station to the volcanic vent of just 1.5 km which does not allow for a major plume dispersion. The switch for $2\,\sigma_{Gauss} > 33°$ has been applied for about two thirds of the scans presented in thus thesis.

In accordance with Lübcke et al. [2014], the 10 spectra of the scan with the lowest SO_2 SCDs are considered as gas-free background spectra and are added up to one "added-reference-spectrum" per scan. Alternatively, the added reference spectrum could be calculated analogous to the added plume spectrum by adding the 10 consecutive spectra with the lowest running mean value. This approach is however problematic when the plume is centred in the zenith of the scan plane and the reference region is separated in a left and a right part (not illustrated in Figure 4.2).

The accuracy of this plume retrieval can be further improved, e.g., by considering the deviations from a Gaussian plume profile due to differential angle dependent projections in the scan plane or the differential plume dilution in lateral and vertical direction. Nevertheless, the Gaussian plume profile arguably correctly detects (or rejects) most of the real shapes and the real but marginal effect would be whether to add one more or one less spectrum to the plume region.

In the next step, for each scan an SO_2 and a BrO DOAS fit (see Section 3.4 for details) are performed based on the added-plume-spectrum and added-reference-spectrum. Subsequently, the SCDs retrieved by the SO_2 and BrO DOAS fits, respectively, are used to calculate I_0-corrected absorption cross sections. For low SCDs, the I_0-effect correc-

Table 4.1: List of the efficiency of the data quality filter in percent of the total number of scans. The filters are consecutively applied from left to right. For Villarrica, the *bad* χ^2_{BrO} filter statistics also includes scans neglected due to the additional $|\text{Shift}_{BrO}| > 0.19$ filter. Number of scans as for the time intervals of the time series presented in the subsequent chapters. Statistics have not been logged for Tungurahua and Galeras.

	# scans	spectra quality		Gauss fit		passing	
		zenith	< 20 spec.	failed	$\sigma < 5°$	total	bad χ^2_{BrO}
N. del Ruiz	660000	25	12	24	4	**36**	3
Cotopaxi	170000	4	12	36	7	**41**	4
Masaya	130000	5	33	9	<1	**53**	12
Villarrica	320000	10	40	18	4	**28**	8

tion can harm more than it helps because it may introduce artefacts. Accordingly, the I_0-effect correction is only applied on the absorption cross sections of those gas species which exceeded the following manually chosen threshold: $S_{SO_2} \geq 1.5 \cdot 10^{18} \frac{\text{molec}}{\text{cm}^2}$, $S_{O_3} \geq 7.5 \cdot 10^{17} \frac{\text{molec}}{\text{cm}^2}$, $S_{BrO} \geq 1 \cdot 10^{14} \frac{\text{molec}}{\text{cm}^2}$, $S_{O_4} \geq 2 \cdot 10^{42} \frac{\text{molec}}{\text{cm}^2}$, $S_{NO_2} \geq 5 \cdot 10^{15} \frac{\text{molec}}{\text{cm}^2}$, $S_{CH_2O} \geq 1.5 \cdot 10^{16} \frac{\text{molec}}{\text{cm}^2}$ [see Lübcke, 2014]. Subsequently, I_0-corrected SO$_2$ and BrO DOAS fits are performed.

Spectral adding of consecutively recorded scans The detection limit of the resulting mean BrO SCD per scan is in the order of $(7 \pm 1) \cdot 10^{13} \frac{\text{molec}}{\text{cm}^2}$ (varying between the different instruments). The BrO SCDs exceed this limit typically only for the very strong degassing prior or after an eruption. This detection limit can be lowered by adding the data of consecutive scans. The adding can be done either by a subsequent averaging of the DOAS results retrieved for the individual scans or by a spectral adding of the single-scan added-plume/reference-spectra of consecutively recorded scans to "multi-scan-plume/reference-spectra" which are then evaluated by a second DOAS retrieval. Both methods should in principle result in the same signal-to-noise ratio enhancement and Lübcke [2014] also confirmed this for SO$_2$ SCDs retrieved from NOVAC data. The latter method is considered to be more robust not least because it allows to inspect the spectroscopic results "by eye" (of the human or computer alike) on the basis of optical depth spectra rather than trusting that non-obvious but significant signals are hidden in the noise.

Accordingly, in this thesis the added-plume-spectra and the added-reference-spectra of four consecutive scans are added, however, only those scans with a goodness of the fit of $\chi^2_{BrO} < 2 \cdot 10^{-3}$ ($\approx 90\,\%$ of all suitable scans, see Table 4.1) are considered in order to avoid the influence of relatively bad scans. Multi-scan reference spectra are obtained analogously. For periods with significant BrO degassing, the final BrO data have a mean temporal resolution of 10 (and up to $\sim$ 30) data points per day and a standard deviation of about $(4 \pm 1) \cdot 10^{13} \frac{\text{molec}}{\text{cm}^2}$ for the different instruments (see Table 4.3). The SO_2 detection limit of the final data is in the order of $1 \cdot 10^{16} \frac{\text{molec}}{\text{cm}^2}$, i.e. the relative precision of the SO_2 data is about a factor of 100 better than for BrO and thus — within the scope of BrO/SO_2 molar ratio calculation — SO_2 can be considered to be measured exactly.

The multi-scan added data is additionally routinely evaluated also with the alternative SO_2 fit range and these alternative SO_2 retrieval results are saved for a later comparison with the standard SO_2 retrieval results.

4.3 Calculation and statistics of the BrO/SO$_2$ molar ratios

The output of the DOASIS evaluation are lists of the SCDs of the different gas species. This output is then evaluated with the statistic software GNU R. The aim of the evaluation is to find a good compromise between the accuracy and precision of the final BrO/SO$_2$ results and their temporal resolution. The first quality control applied prior to each DOAS retrieval has aimed primary on run time efficiency but a further subsequent quality control sorts out further outliers. The settings reported in the following are found empirically for the set of volcanoes evaluated in this thesis.

Accuracy of the SO$_2$ data: comparison of standard and alternative SO$_2$ retrieval results For the multi-scan added results two sets of results are retrieved, the standard retrieval outputted highly precise SO$_2$ SCDs whose accuracy can however be effected by a systematic underestimation for SCDs exceeding about $1 \cdot 10^{18}\,\frac{\text{molec}}{\text{cm}^2}$ and the alternative retrieval outputted more accurate SO$_2$ SCDs for the SCD range between about $(1-10) \cdot 10^{18}\,\frac{\text{molec}}{\text{cm}^2}$ but with strongly increased relative measurement errors of about 10 %, i.e. up to $1 \cdot 10^{18}\,\frac{\text{molec}}{\text{cm}^2}$ (Section 3.4). While the SO$_2$ SCDs retrieved from NOVAC data are most of the time below $1 \cdot 10^{18}\,\frac{\text{molec}}{\text{cm}^2}$, the threshold is exceeded episodically in particular at periods of high volcanic activity. Nevado del Ruiz and Masaya are exceptions where the SO$_2$ SCDs are virtually always above this threshold. In order to find the best compromise between a potential systematic accuracy offset and a reduce precision, the final SO$_2$ time series records by default the results of the standard SO$_2$ fit but exchanges the particular data point by the result of the alternative SO$_2$ fit when the discrepancy between both fit results is larger than two times the alternative SO$_2$ measurement error. The main effect of this rather conservative picking algorithm is a correction of the underestimation of the already quite strong "outliers". In contrast, SO$_2$ SCDs up to $3 \cdot 10^{18}\,\frac{\text{molec}}{\text{cm}^2}$ are only rarely exchanged.

Filter data for relatively small χ^2 The multi-scan adding considers only scans with relatively good fit results with $\chi^2_{BrO} \leq 2 \cdot 10^{-3}$, thus most bad fit results are already filtered out during the DOAS retrieval. Nevertheless, the adding of individually "good" scans results occasionally (< 1 ‰ of multi-scan fits) in a worse multi-scan fit quality up to a multitude of the former χ^2_{BrO} threshold. Two subsequent filters discard these particularly bad outliers but also other just comparably worse data points data independently on their absolute precision (Figure 4.3). The first filter statically discards all multi-scan results whose $\chi^2_{SO_2}$ exceeds

$$\chi^2_{SO_2} = 0.005 + \left[S_{SO_2} \cdot 10^{-20}\, \frac{\text{cm}^2}{\text{molec}} \right]^2 \tag{4.1}$$

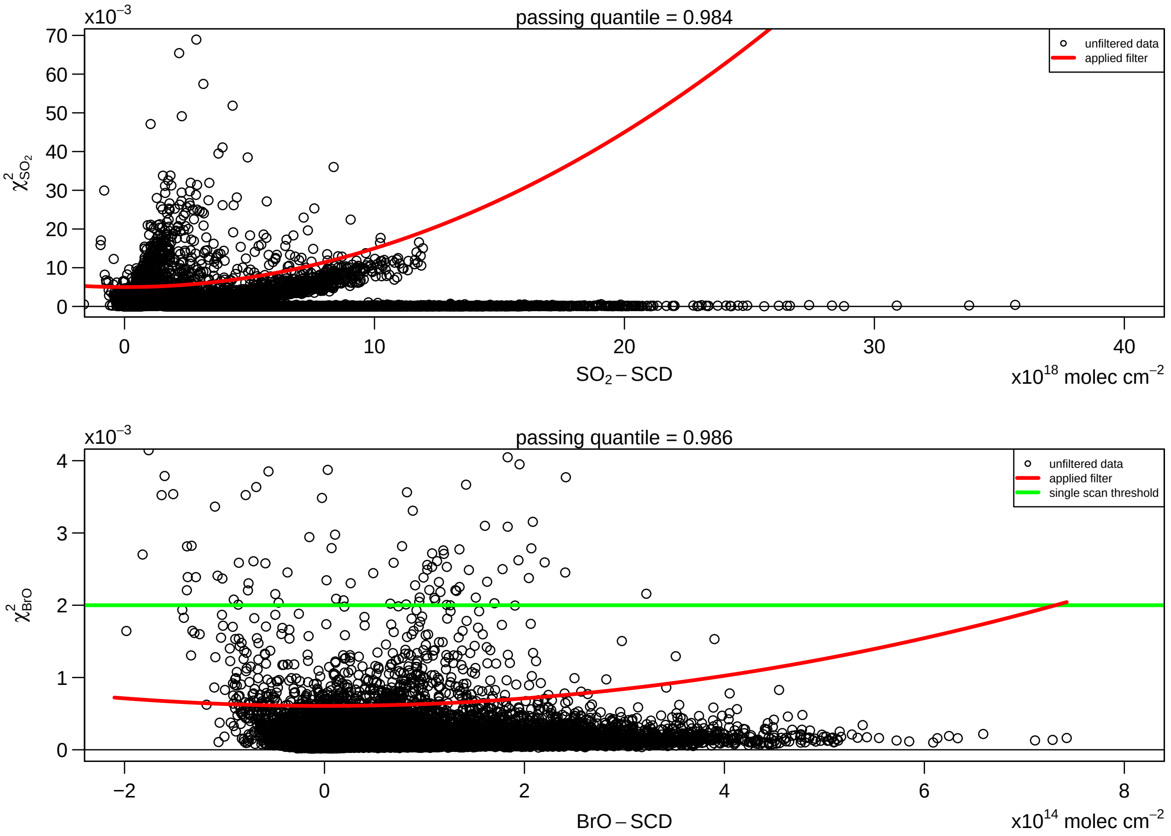

Figure 4.3: Applied χ^2 filters (red lines) exemplified for data from Nevado del Ruiz. For both filters, more than 98 % of the data pass the filter. Some multi-added results exceeds the threshold filter (green line) applied beforehand on the single scan results (here: 0.2 ‰). The two branches in the SO$_2$ plot distinguish whether the data have been retrieved with the standard or alternative SO$_2$ fit, where the fit with the alternative fit range results in much lower $\chi^2_{SO_2}$.

The second filter consists of two steps. As the first step, a quadratic fit (without linear term) of the goodness of the DOAS BrO fit χ^2_{BrO} versus the retrieved BrO SCDs S_{BrO} is performed, $\chi^2_{BrO} = \hat{a}_{0,BrO} + \hat{a}_{2,BrO} \cdot (S_{BrO})^2$. In the second step, the filter discards all data whose χ^2_{BrO} exceeds

$$\chi^2_{BrO} = \left[\hat{a}_{0,BrO} + 2 \cdot \sigma(\chi^2_{BrO})\right] + \hat{a}_{2,BrO} \cdot \left[1.5 \cdot S_{BrO}\right]^2 \tag{4.2}$$

where an additional offset of twice the standard deviation $\sigma(\chi^2_{BrO})$ and an additional relative precision error of 0.5 ensures all reasonable BrO data pass. The empirical values are listed in Table 4.2 and the results shown in Figure 4.3. The passing data set contains about 97 % of the initial data and the mean χ^2_{BrO} has reduced relatively by about 14 %,

Table 4.2: Empirical retrieved parameters for the χ^2_{BrO} filter for the different volcanoes.

	$\left[\hat{a}_{0,BrO} + 2 \cdot \sigma(\chi^2_{BrO})\right]$ 10^{-4}	$\hat{a}_{2,BrO}$ 10^{-33}
Nevado del Ruiz	6.1	2.6
Cotopaxi	5.3	2.0
Masaya	4.3	0.5
Tungurahua	2.9	5.7
Galeras	8.1	111
Villarrica	2.7	6.7

indicating that mostly strong χ^2_{BrO} outliers got neglected.

No filter for extreme DOAS shift and squeeze parameters In the DOAS fits, the absorption cross sections are allowed to be shifted by up to ±0.2 nm and squeezed by $0.98 - 1.01$ (all by the same shift and squeeze) in order to compensate for the effects of a convolution with a potentially slightly wrong ILF (Section 3.4). The shift and squeeze parameters in the SO$_2$ and BrO DOAS fit vary typically both with an about normal distributed variation (Section 4.4). A significant amount of DOAS fits - and in particular of BrO DOAS fits - however proposed shift and squeeze parameters close to the edge of the allowed parameter ranges. The origin for such extreme parameter values could be first of all twofold: (1) the fit is just by chance optimal for this extreme shift value, that is the deviations from more moderate parameter values are caused by statistical noise rather than a systematic ILF effect, or (2) the ILF is relatively badly estimated and the extreme shift value is just the least evil, that is an even larger shift value would be required for a maximum compensation of the wrongly estimated ILF. On the one hand, the latter scenario should be avoided because it may result in significantly wrongly retrieved SCDs. On the other hand, on this stage of the evaluation only fit results with a rather reliable fit quality have passed. Accordingly, the ILF can arguably not been matched too badly and thus a conservative filter for these extreme values may unnecessarily reduce the amount of final data. Furthermore and more importantly, such a filter would over-proportionally neglect small BrO SCDs and thus systematically shift the final BrO/SO$_2$ molar ratios towards large values. Therefore, no such filter is applied. A detailed analysis of the ILF variations and a possible approach to circumvent this issue without a filter is discussed in Section 4.4.

Retrieval of the measurement errors and the detection limits The measurement errors can be estimated as the DOAS fit error multiplied with a constant correction factor $\mathrm{CF}_{i\in\{\mathrm{SO_2},\mathrm{BrO}\}}$, e.g., $(\Delta S_{BrO})_{meas} = \mathrm{CF_{BrO}} \cdot (\Delta S_{BrO})_{fit}$. The correction factor can be derived as the ratio of the standard deviation of the gas free data divided by the mean fit error of the gas free data. The detection limit is here defined as two times the measurement error which is identical with two times the standard deviation of the gas free data (Section 3.4). For the following instrument-wise empirical derivation, the subsets of data with $S_{SO_2} < 3 \cdot 10^{17}\,\frac{\mathrm{molec}}{\mathrm{cm}^2}$ is assumed to be free of any volcanic gases.
The BrO SCDs of these subset centre very close to zero and are in generally normally distributed, indicating that the subsets are indeed sufficiently free of BrO. The retrieved correction factors $\mathrm{CF_{BrO}}$ varied between $1.06 - 1.92$ (except for two outlier instruments with correction factors of 2.58 and 3.05, see Table 4.3). The detection limit varied between between $3 - 5 \cdot 10^{13}\,\frac{\mathrm{molec}}{\mathrm{cm}^2}$. In contrast, the SO$_2$ SCDs of these "gas free" subsets typically peak close to the threshold of $3 \cdot 10^{17}\,\frac{\mathrm{molec}}{\mathrm{cm}^2}$, remain roughly at the same level between $0 - 3 \cdot 10^{17}\,\frac{\mathrm{molec}}{\mathrm{cm}^2}$, and only few negative SCDs are retrieved. This finding indicates that the subsets are not sufficiently free of SO$_2$. In consequence the standard deviation of these "actually not gas free" data overestimates the detection limit because this standard deviation includes both the instrumental noise but also the natural variability of low level SO$_2$ degassing. The $\mathrm{CF_{SO_2}}$ retrieved in that way span between the instruments from $1 - 7$, indicating that probably in general and analogously to BrO also $\mathrm{CF_{SO_2}} \leq 2$ holds true.
These empirical findings motivated the following approach on how the measurement errors and thus detection limits are derived in this thesis: (1) for BrO both values are taken from the empirical retrieval but (2) for SO$_2$ a fixed correction factor of $\mathrm{CF_{SO_2}} = 2$ is applied for all instruments and the detection limit of a particular instrument is thus just 4 times the mean fit error of the "gas free" data set. The fixing of the SO$_2$ values has actually hardly an effect on the ultimate (error-weighted) BrO/SO$_2$ molar ratios because their errors are dominated by the BrO error.
Furthermore, for one NOVAC instruments (D2J2375_0) the final time series did not contain any gas free data. In order to run the evaluation algorithm unchanged some plausible but conservatively high values have been applied: $\mathrm{CF_{SO_2}} = 2$, $\mathrm{CF_{BrO}} = 2$, $\mathrm{DT_{SO_2}} = 7 \cdot 10^{16}\,\frac{\mathrm{molec}}{\mathrm{cm}^2}$, $\mathrm{DT_{BrO}} = 7 \cdot 10^{13}\,\frac{\mathrm{molec}}{\mathrm{cm}^2}$.

Calculation of daily averages of BrO/SO$_2$ molar ratios In periods of relatively low volcanic activity, still only few multi-scan BrO SCDs exceed the typical detection limits of $3 - 4 \cdot 10^{13}\frac{\mathrm{molec}}{\mathrm{cm}^2}$. Calculating daily averages allows to reduce the detection limit down to $\mathrm{DT_{BrO}} = \frac{3}{\sqrt{n}} \cdot 10^{13}\,\frac{\mathrm{molec}}{\mathrm{cm}^2} \approx 1 \cdot 10^{13}\,\frac{\mathrm{molec}}{\mathrm{cm}^2}$, with n the number of "multi-scan" data points per day. Most retrieved daily BrO averages are nevertheless yet below this smaller detection limit. A blindfold rejection of all data with BrO SCDs below the detection limit would, however, not only drastically reduce the number of available data but would also select those scans when the BrO SCDs are particularly high. The

Table 4.3: Mean detection limits DT_i and correction factors CF_i (from fit error to measurement error) for the instruments evaluated in this thesis. The detection limits are given in $\frac{molec}{cm^2}$. The two last instruments at Villarrica show extraordinary large values for BrO but also otherwise suspicious behaviour, presumably caused by a bad ILF estimation (further investigations are required). For D2J2375_0 the values have been fixed manually as $CF_{SO_2} = 2$, $CF_{BrO} = 2$, $DT_{SO_2} = 7 \cdot 10^{16} \frac{molec}{cm^2}$, $DT_{BrO} = 7 \cdot 10^{13} \frac{molec}{cm^2}$.

Volcano	Instrument	DT_{SO_2}	CF_{SO_2}	DT_{BrO}	CF_{BrO}
Masaya	D2J2124_0	$13 \cdot 10^{16}$	2	$6.7 \cdot 10^{13}$	1.61
	D2J2375_0		*no gas free data*		
Nevado del Ruiz	D2J2200_0	$9.5 \cdot 10^{16}$	2	$4.2 \cdot 10^{13}$	1.31
	D2J2201_0	$4.7 \cdot 10^{16}$	2	$3.6 \cdot 10^{13}$	1.51
	D2J2813_0	$4.0 \cdot 10^{16}$	2	$4.2 \cdot 10^{13}$	1.66
	D2J2825_0	$4.6 \cdot 10^{16}$	2	$4.2 \cdot 10^{13}$	1.65
	D2J2828_0	$4.1 \cdot 10^{16}$	2	$3.3 \cdot 10^{13}$	1.56
	D2J2830_0	$3.9 \cdot 10^{16}$	2	$3.2 \cdot 10^{13}$	1.49
Galeras	I2J8553_0	$6.5 \cdot 10^{16}$	2	$3.7 \cdot 10^{13}$	1.14
	ADU6559_0	$6.2 \cdot 10^{16}$	2	$4.1 \cdot 10^{13}$	1.12
	D2J2139_0	$9.4 \cdot 10^{16}$	2	$4.8 \cdot 10^{13}$	1.09
Cotopaxi	D2J2160_0	$6.0 \cdot 10^{16}$	2	$4.0 \cdot 10^{13}$	1.19
	D2J2160_1	$6.0 \cdot 10^{16}$	2	$3.9 \cdot 10^{13}$	1.17
	I2J4969_0	$6.6 \cdot 10^{16}$	2	$4.6 \cdot 10^{13}$	1.19
	D2J2815_0	$4.2 \cdot 10^{16}$	2	$4.5 \cdot 10^{13}$	1.92
	D2J2835_0	$4.3 \cdot 10^{16}$	2	$3.7 \cdot 10^{13}$	1.55
Tungurahua	D2J2140_0	$7.4 \cdot 10^{16}$	2	$3.5 \cdot 10^{13}$	1.32
	I2J8548_0	$5.3 \cdot 10^{16}$	2	$3.9 \cdot 10^{13}$	1.50
	D2J2235_0	$4.3 \cdot 10^{16}$	2	$3.0 \cdot 10^{13}$	1.26
	D2J2235_1	$6.0 \cdot 10^{16}$	2	$3.8 \cdot 10^{13}$	1.24
	I2J8546_0	$5.6 \cdot 10^{16}$	2	$3.4 \cdot 10^{13}$	1.25
	D2J2236_0	$6.1 \cdot 10^{16}$	2	$4.5 \cdot 10^{13}$	1.27
	D2J2237_0	$11 \cdot 10^{16}$	2	$6.0 \cdot 10^{13}$	1.70
	D2J2239_0	$4.9 \cdot 10^{16}$	2	$3.7 \cdot 10^{13}$	1.37
Villarrica	D2J2197_0	$4.8 \cdot 10^{16}$	2	$3.1 \cdot 10^{13}$	1.32
	D2J2198_0	$4.8 \cdot 10^{16}$	2	$4.0 \cdot 10^{13}$	1.73
	D2J2199_0	$4.1 \cdot 10^{16}$	2	$2.8 \cdot 10^{13}$	1.20
	I2J7740_0	$5.2 \cdot 10^{16}$	2	$2.7 \cdot 10^{13}$	1.10
	D2J2562_0	$6.1 \cdot 10^{16}$	2	$7.7 \cdot 10^{13}$	2.60
	D2J2563_0	$4.7 \cdot 10^{16}$	2	$8.2 \cdot 10^{13}$	2.88

consequence of such a selection would be systematically overestimated BrO/SO$_2$ molar ratios.
Lübcke [2014] proposed to use only data with sufficiently strong $S_{SO_2} > \mathrm{SO}_2^{thres}$ as a more careful selection criterium for the calculation of the BrO/SO$_2$ molar ratios. The SO$_2$ SCD threshold SO_2^{thres} should be chosen as the best compromise between a low BrO/SO$_2$ detection limit and sufficient amount of data passing the criterium. Lübcke [2014] found a value of $\mathrm{SO}_2^{thres} = 7 \cdot 10^{17}\ \frac{\mathrm{molec}}{\mathrm{cm}^2}$ for the first instruments at Nevado del Ruiz and this thesis confirms and applies this value as an appropriate choice for all here presented NOVAC instruments. Using only data above this threshold, the detection limit of the BrO/SO$_2$ molar ratios is at most $\mathrm{DT}_{\mathrm{BrO/SO_2}} = \frac{\mathrm{DT}_{\mathrm{BrO}}}{\mathrm{SO}_2^{thres}} = \frac{5}{\sqrt{n}} \cdot 10^{-5} \approx 1.5 \cdot 10^{-5}$ but gets reciprocally smaller the further the particular observed SO$_2$ SCD is above the threshold. As consequence, also some BrO/SO$_2$ data which fluctuate around zero can pass the selection criterium (i.e. whose BrO SCD is below the BrO detection limit). For the preceding reasoning, these data (or at least their long-term averages) are nevertheless considered as reliable observations of rather low BrO/SO$_2$ molar ratios.

Reject instrument-days with small data basis On sunny days, more than 100 individual scans can be expected (e.g., a scan every 6 min for a measurement time of 10 hours). For the presented time series as many as 156 scans per day have been recorded for a day with particularly good measurement conditions. The distributions of the number of scans per day peak at $20 - 36$ scans per day (or corresponding to $5 - 9$ multi-scan spectra) for instruments installed in the main plume propagation direction. In contrast, days with less than 12 scans (i.e. less than 3 multi-scan spectra) are considered to be outliers which are potentially less accurate. Accordingly, only days with at least 3 multi-scan spectra (at least 12 single scans passed the overall spectroscopic quality control) are considered for the calculation of the daily means, other days are rejected. For these days with at least 3 multi-scan spectra, the weighted daily means of the BrO/SO$_2$ molar ratios are calculated weighted by the reciprocal BrO/SO$_2$ variance of the particular day. The remaining data set gets separated with respect to the different NOVAC stations rather than the different instruments. Time series analyses are nevertheless applied on the non-separated data set if not stated differently. As a remark, Lübcke [2014] set the minimum number of required multi-scan spectra to 5.

Statistical methods applied on the BrO/SO$_2$ data The retrieved BrO/SO$_2$ time series are evaluated for long-term pattern such as instantaneous step increases, linear or higher order trends, and periodical pattern. The retrieved BrO/SO$_2$ time series have an irregular sampling rate with time intervals with data for each day, time intervals with only few data per week, and entire data gaps spanning over months. Some periodical pattern can be detected already “by eye” or a running mean. The reliability of such periodical signals in the BrO/SO$_2$ time series are quantified by two statistical methods: (1) a Lomb–Scargle frequency component analysis [Lomb, 1976, Scargle, 1982, Press

Table 4.4: Filters applied on the DOAS results. All numbers are given in %. The "Filters" have been applied subsequently, i.e. the numbers give the fraction of data which got discarded by the particular filter w.r.t. the data which passed all previous filters. "SO_2^{thres}" refers to the fraction of data whose SO_2 SCDs are above the chosen threshold $SO_2^{thres} = 7 \cdot 10^{17}\,\frac{\text{molec}}{\text{cm}^2}$. However, the SO_2 SCDs observed at the three later volcanoes are comparably low such that this standard threshold discards much more than 90 % of the data. Therefore, the threshold SO_2^{thres} has been lowered to $5 \cdot 10^{17}\,\frac{\text{molec}}{\text{cm}^2}$ for Tungurahua and Galeras and to $3 \cdot 10^{17}\,\frac{\text{molec}}{\text{cm}^2}$ for Villarrica (still discarding $87 - 89$ % of the data!). "Passing data": "Data" gives the fraction of multi-added scan results which passed all five previous filters. "Days" gives the fraction of days in the finally retrieved time series compared to the initial number of days in the unfiltered time series. "$\text{Data}_{\text{multiadd}}^{\text{min}}$" gives the fraction of days compared to the initial number of days which passes also the requirement of at least 3 multiadd results.

Volcanoes	Filters			Passing data		
	$\chi^2_{SO_2}$	χ^2_{BrO}	SO_2^{thres}	Data	Days	$\text{Data}_{\text{multiadd}}^{\text{min}}$
Nevado del Ruiz	1.6	1.4	63.7	35.2	79.4	69.0
Cotopaxi	0.0	2.6	75.4	24.0	58.1	46.3
Masaya	0.0	4.5	0.8	94.6	97.5	88.1
Tungurahua	0.9	2.0	*89.0*	10.7	24.6	16.1
Galeras	0.2	2.0	*86.6*	13.1	14.9	7.7
Villarrica	4.4	3.6	*87.8*	11.2	16.0	7.4

et al., 1992, in the following just called Lomb–Scargle analysis] and (2) a time-lag auto-correlation analysis. Compared to a Fourier transform analysis, these two methods can more appropriately handle time series with irregular sampling intervals, in particular no interpolation of the BrO/SO_2 time series for missing days is required.

The Lomb–Scargle analysis is a set of least-square fits which fit a function with a sinusoidal term and a linear term on the data. Thereby, the periodicity of the sinusoidal (and the phase shift) is varied resulting in a periodigram showing the probability that a given periodicity is within the given time series. In contrast to the Fourier transform analysis, the proposed periodicities are however not strictly independent, i.e. after correcting for the dominant periodic pattern further proposed minor periodicities may get insignificant. The time-lag auto-correlation analysis shifts the time series in one day steps against itself and calculates the correlation coefficient between the initial and shifted time series. Shifted data points which match to days where no original data is available are excluded from the correlation calculation. Pattern in the time series of the correlation coefficients can then be interpreted as persistent long-term pattern hidden in the time series. Both methods were applied to the daily BrO/SO_2 data of the arithmetical averages of data from all instruments.

4.4 Instrumental drifts of the NOVAC instruments

The NOVAC spectrometer D2J2200_0 operates since late 2009 at Nevado del Ruiz. In the following, the variabilities of its WPM and its ILF are estimated in order to get a feeling for the quantitative scale and impact of the instrumental drifts on the measurement accuracy and precision. The ILF and its variability vary significantly between the different NOVAC instruments (Figure 4.4). The ILF variability of the here analysed D2J2200_0 is rather stable. The ILF-related effects may be in general stronger for other NOVAC instruments.

No experimental data on the variability of the ILF Prior to the installation in the field, the spectroscopic properties of each spectrometer are determined by a lab measurement of a mercury emission spectrum (at not further specified room temperature). These mercury emission spectra are stored on the NOVAC server(s), however the mercury emission spectra of some installed instruments are missing there. The intended simple design of the NOVAC instruments does not allow for an automatised experimental record of the spectroscopic properties. Further, the remote locations of the NOVAC station makes a regular manual measurement of the mercury spectrum too work-intensive and in addition the automatised measurement routine makes it not straight-forward to perform such a non-routinely measurement. Accordingly, the initially recorded mercury emission spectrum is usually the only available experimental data for the particular spectrometer. Therefore, the shape of the recorded mercury emission line centred at 334.14 nm is recorded at room temperature used as a best guess of the ILF of the particular spectrometer per default in the DOAS retrieval.

This choice is in particular plausible for the chosen BrO fit range from $330 - 352.8$ nm and the chosen alternative SO_2 fit range from $326.5 - 335.3$ nm. For the chosen standard SO_2, an interpolation of the shapes of the mercury emissions line centred at 302 nm and 334 nm can be expected to be a better estimate for the ILF in the chosen fit range from $314.8 - 326.8$ nm. Nevertheless, when the ILF is sufficiently wavelength-independent between 314 nm and 334 nm it appears to be more robust and consistent to convolute the absorption cross sections included in the standard SO_2 fit rage (that is SO_2 and O_3) with recorded shape of the 334 nm line rather than an interpolated line shape which may cause some artefacts. For instance, the ILF of the D2J2200_0 instrument appears to be sufficiently wavelength-independent as a comparison of the SO_2 absorption cross section convoluted with the recorded mercury emission lines centred at 302 nm and at 334 nm line indicates (Figure 4.5). Within this thesis the recorded 334 nm mercury line is used for all standard SO_2 fits.

It is well documented that the ILF of the spectrometers used in NOVAC changes with temperature [Galle, 2008]. Because the NOVAC instruments are not temperature controlled, the variation of the ILF follows the variation of the ambient air temperature which typically varies throughout the day and the year between $10 - 35\,^\circ$C. These

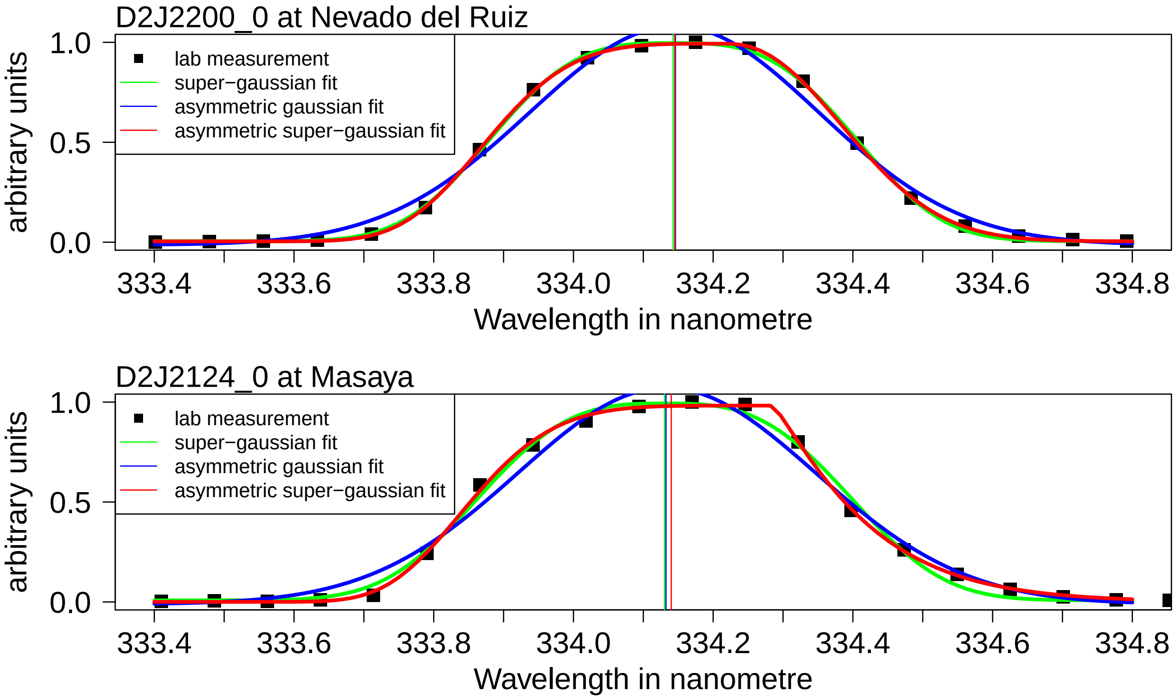

Figure 4.4: Measured instrument line function (ILF) at 334.14 nm of the two main NOVAC instruments at Nevado del Ruiz and Masaya.

experimental temperature dependencies of the ILF are however usually not retrieved in the lab and are thus not available on the NOVAC server.

ILF of D2J2200_0 measured in the lab The ILF of D2J2200_0 can be modelled in very good approximation by a symmetric super-Gaussian line shape ($a_\sigma = 0, a_k = 0$), at least for the wavelength range from $289 - 334$ nm (Figure 4.11a). The measured mercury emission lines at [289.34, 296.72, 302.18, 334.14] nm can be parametrised with width parameters $\sigma = [0.313, 0.310, 0.327, 0.299]$ nm and exponents $k = [2.64, 2.69, 2.35, 3.17]$ implying FWHM = [0.545, 0.541, 0.559, 0.532] nm. Furthermore, FWMH = 0.54 nm has been retrieved manually for the two weak mercury emission lines at 354.4 nm and 356.0 nm. These measurement results indicate a wavelength-independent FWHM of the ILF for the range of $300 - 360$ nm and hints an increase of the exponent with increasing wavelength (Figure 4.11b+c).

Wavelength-to-pixel mapping The NOVAC algorithm routinely retrieves the WPM of any reference spectrum by a calibration with a high-resolution solar atlas. The WPM is estimated in good agreement as a polynomial of 2nd order. The retrieved WPM is subsequently used for the wavelength calibration of both the reference spectrum and the plume spectrum under consideration. This calibration of the plume spectrum can

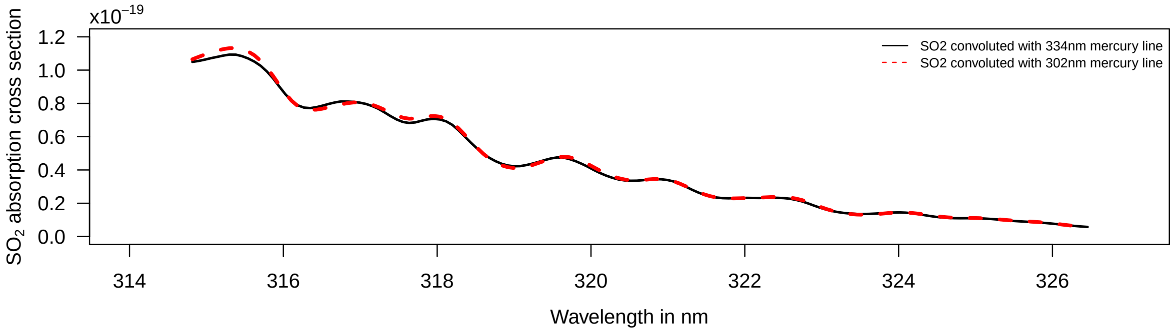

Figure 4.5: SO_2 absorption cross section from [Vandaele et al., 2009, @298 K] convoluted with the 334.14 nm and the 302.18 nm mercury emission line as recorded by the D2J2200_0 instrument. A "DOAS like" fit of the two convoluted SO_2 absorption cross section against each other proposes an insignificant linear Levenberg–Marquardt shift of (4 ± 5) pm only.

be expected to hold in very good agreement because plume spectrum and reference spectrum are recorded in close temporal proximity. Furthermore, the DOAS fit can automatically correct for small residual deviations between the such retrieved WPM of the plume spectrum and its actual WPM. Therefore, instrumental WPM drifts are expected to have hardly any direct effect on the spectroscopic results. Variations in the WPM may however be an indicator for unknown instrumental drifts which cannot be detected directly.

The WPM of D2J2200_0 has varied significantly between $2009 - 2019$ (Figure 4.6). After the (re-)installation of the instrument in the field in late 2009 and late 2014, the WMP exhibited each time an adjustment interval which lasted about half a year. Subsequently, time intervals of great stability followed over several years. During these stable time intervals the multi-year peak-to-peak variation has been in the order of 0.05 nm for the pixels associated to a wavelength range from $304 - 358$ nm. No annual periodicity or linear trend has been observed during the stable time intervals. Remarkably, while the effective WPM has been rather stable for the individual pixels, the polynomial parameters of the WPM exhibited linear drifts during both stable time intervals. Thereby, the trend in the constant and quadratic term were opposite to the trend in the linear term and furthermore the signs of the trends have been opposite for the two stable periods. A time interval of enhanced instability has started directly after the phreatomagmatic explosions on June 30 2012 and ended in June 2013 when the instrument stopped operation. During this time interval in particular pixels associated with wavelengths of about 304 nm have exhibited peak-to-peak variations of up to 0.25 nm.

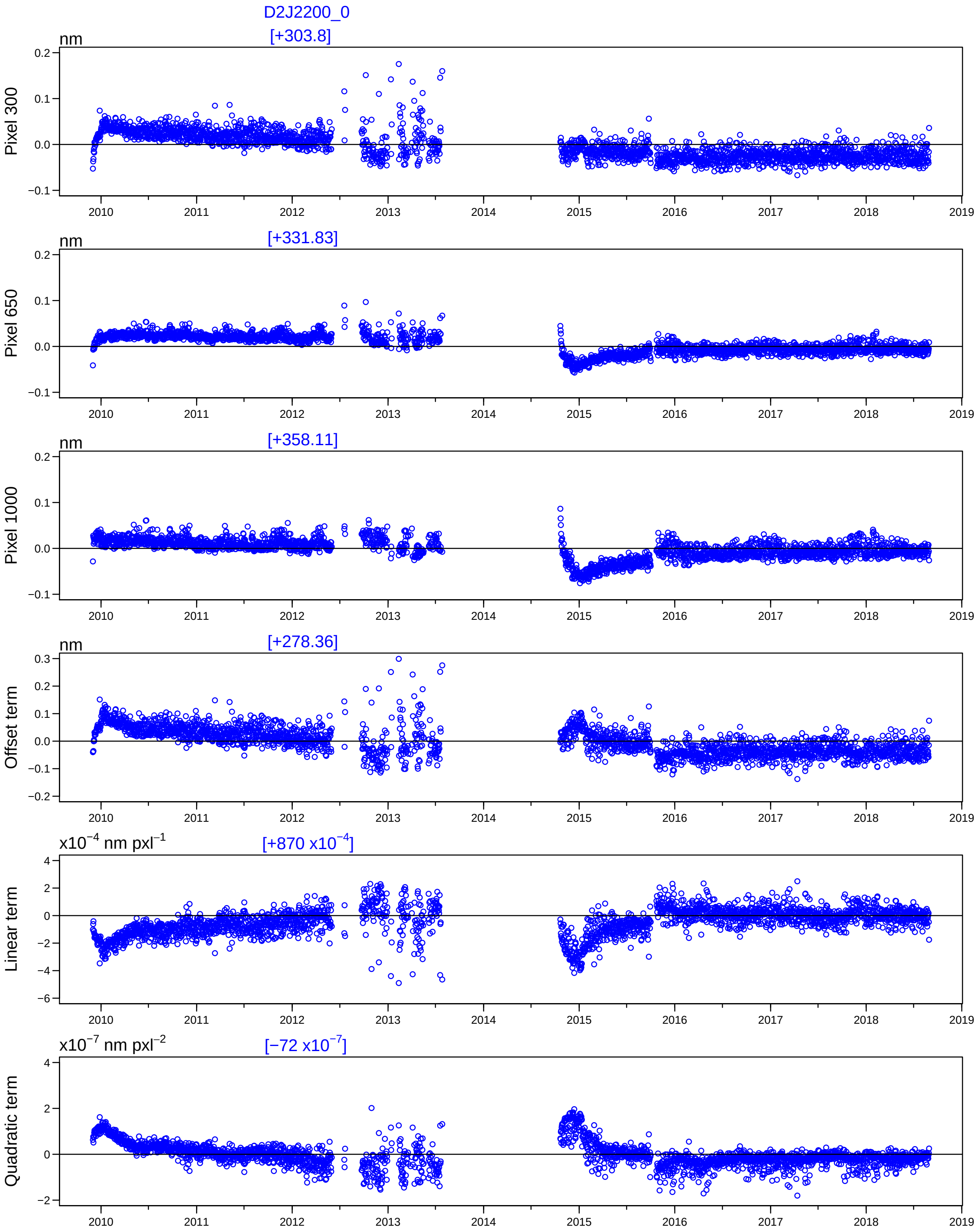

Figure 4.6: Variations of the wavelength-to-pixel mapping (WPM) of the instrument D2J2200_0. The panels show the absolute deviation with respect to the value given in the particular legend. **a-c:** Variations of the wavelengths which are associated to the pixels 300, 560, and 1000, respectively. **d-f**: Variations of the parameter of the WPM when modelled as a polynomial of 2nd order.

ILF variability accessed via Levenberg–Marquardt parameters

The additional Levenberg–Marquardt shift and squeeze parameters on the wavelength calibration of the linked absorption cross sections had been motivated as a correction of a potential ILF-induced wavelength shift and squeeze of the convoluted absorption cross sections (Section 3.4). Accordingly, the variability in the ILF should manifest in the retrieved Levenberg–Marquardt parameters. This is checked in the following paragraphs for the 9-year time series from the D2J2200_0 instrument. The D2J2200_0 instrument regularly observed SO_2 SCD of up to a multiple of $1 \cdot 10^{19} \frac{\mathrm{molec}}{\mathrm{cm}^2}$, thus large parts of the finally presented SO_2 SCDs are retrieved with the alternative SO_2 fit.

Strong variability in the shift and squeeze parameters for low SCDs For D2J2200_0, the shift and squeeze parameters are approximately normally distributed around a maximum whose position may be different from a mean shift of 0 nm or a mean squeeze factor of 1. For small SO_2 SCDs or BrO SCDs (here small is chosen as $S_{SO_2} < 1 \cdot 10^{18} \frac{\mathrm{molec}}{\mathrm{cm}^2}$ and $S_{BrO} < 1 \cdot 10^{14} \frac{\mathrm{molec}}{\mathrm{cm}^2}$, see also grey data in the Figures 4.7, 4.8, 4.9), the histograms of the squeeze parameters shows two additional accumulation for squeeze values close to the edges of the allowed parameter range, that is in the bins from 0.98 to 0.982 and from 1.018 to 1.02 (panel d in the Figures 4.7, 4.8, 4.9). Such additional accumulations are also observed for the shift parameters, however, at a lower quantitative level (panel b in the Figures 4.7, 4.8, 4.9).

The DOAS fit is expected to be particularly prone to statistical fluctuations for SCDs below the detection limit. Accordingly, the origin of these accumulations of extreme squeeze and shift parameters lies most likely in a strong impact of the statistical instrumental noise. This is further supported by the observation that these accumulations are relatively small for the standard SO_2 fit (which has a rather low detection limit) when compared with the alternative SO_2 fit or the BrO fit.

Anti-correlation between shift and squeeze The additional Levenberg–Marquardt fit causes a total wavelength shift at the initial wavelength position λ of $\Delta\lambda_{shift}(\lambda) = a_{shift} + (a_{squeeze} - 1) \cdot (\lambda - \lambda_0)$, with the minimum wavelength λ_0 of the DOAS fit range. Now presume that the convolution of the absorption cross sections with a wrong ILF resulted in a wrong line width of the absorption lines but not in an effective wavelength shift. Then the shift parameter has to correct for the squeeze-induced wavelength shift and thus the squeeze parameter and the shift parameter are anti-correlated. This anti-correlation has been observed for D2J2200_0, at least when excluding low SCDs (panel e in the Figures 4.7, 4.8, 4.9). The correlation is strong for the standard SO_2 fit (coefficient of -0.70) and still significant for the alternative SO_2 fit and the BrO Fit (coefficients of -0.44 and -0.35).

In contrast, neither the SO_2 and BrO shift parameter nor the SO_2 and BrO squeeze

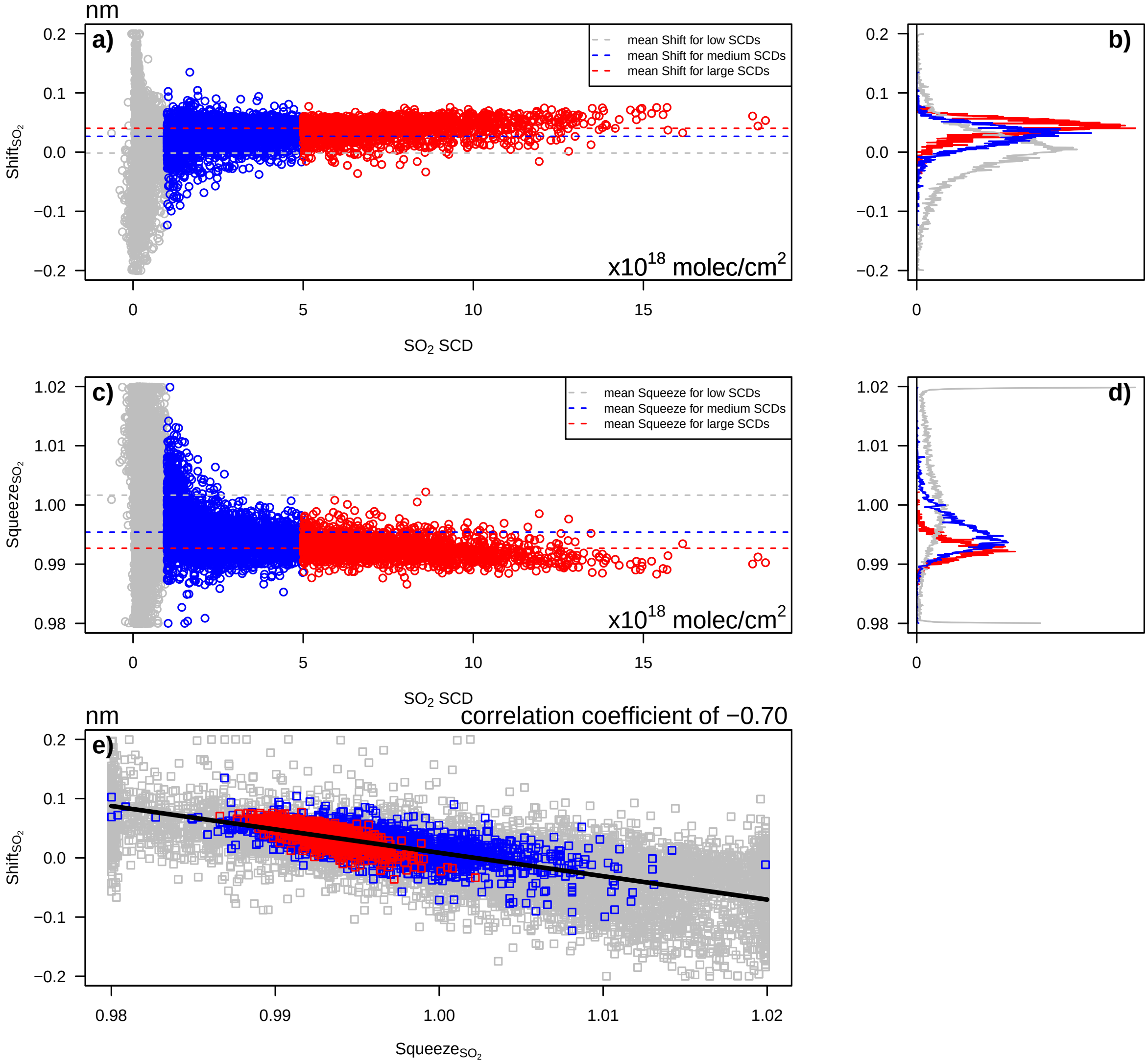

Figure 4.7: Additional Levenberg–Marquardt parameters in the standard SO$_2$ DOAS fit. **a and c:** Scatter plots of the shift and squeeze parameters as a function of the retrieved SO$_2$ SCD. The scatter plot is separated in three SCD ranges as indicated by the different colours. **b and d:** Histograms of the shift and squeeze parameters shown in panel a and c, respectively. Three histograms are shown for each of the three SCD ranges. **e:** Scatter plot of the shift parameter as a function of the squeeze parameter and for the three colour-coded SCD ranges. The plot is not transparent, that is, a part of the grey and blue data is covered by the overlying blue and red data. The linear regression applied on the combined blue and red data is given by the black line.

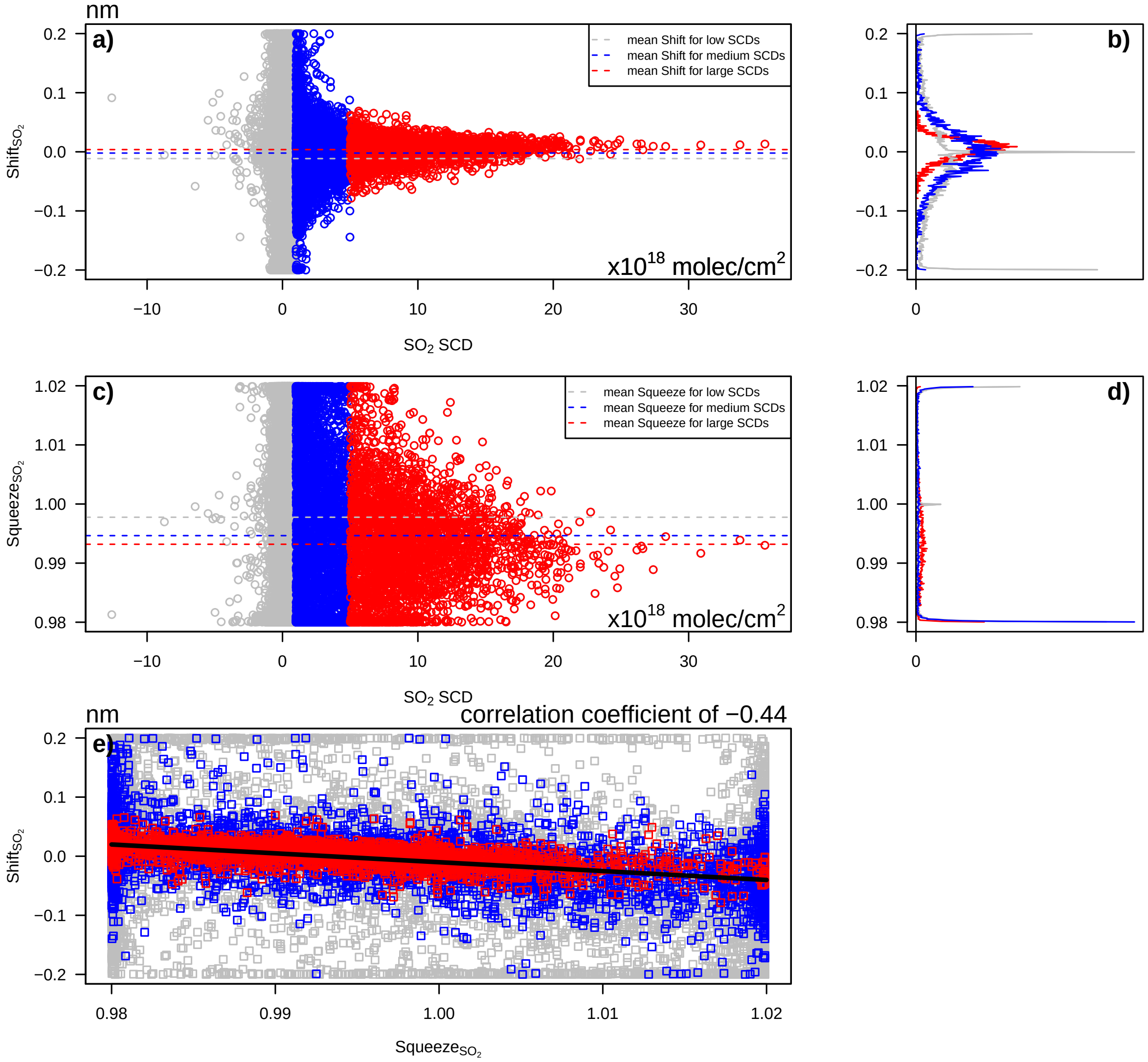

Figure 4.8: Additional Levenberg–Marquardt parameters in the alternative SO_2 DOAS fit. **a and c:** Scatter plots of the shift and squeeze parameters as a function of the retrieved SO_2 SCD. The scatter plot is separated in three SCD ranges as indicated by the different colours. **b and d:** Histograms of the shift and squeeze parameters shown in panel a and c, respectively. Three histograms are shown for each of the three SCD ranges. **e:** Scatter plot of the shift parameter as a function of the squeeze parameter and for the three colour-coded SCD ranges. The plot is not transparent, that is, a part of the grey and blue data is covered by the overlying blue and red data. The linear regression applied on the combined blue and red data is given by the black line.

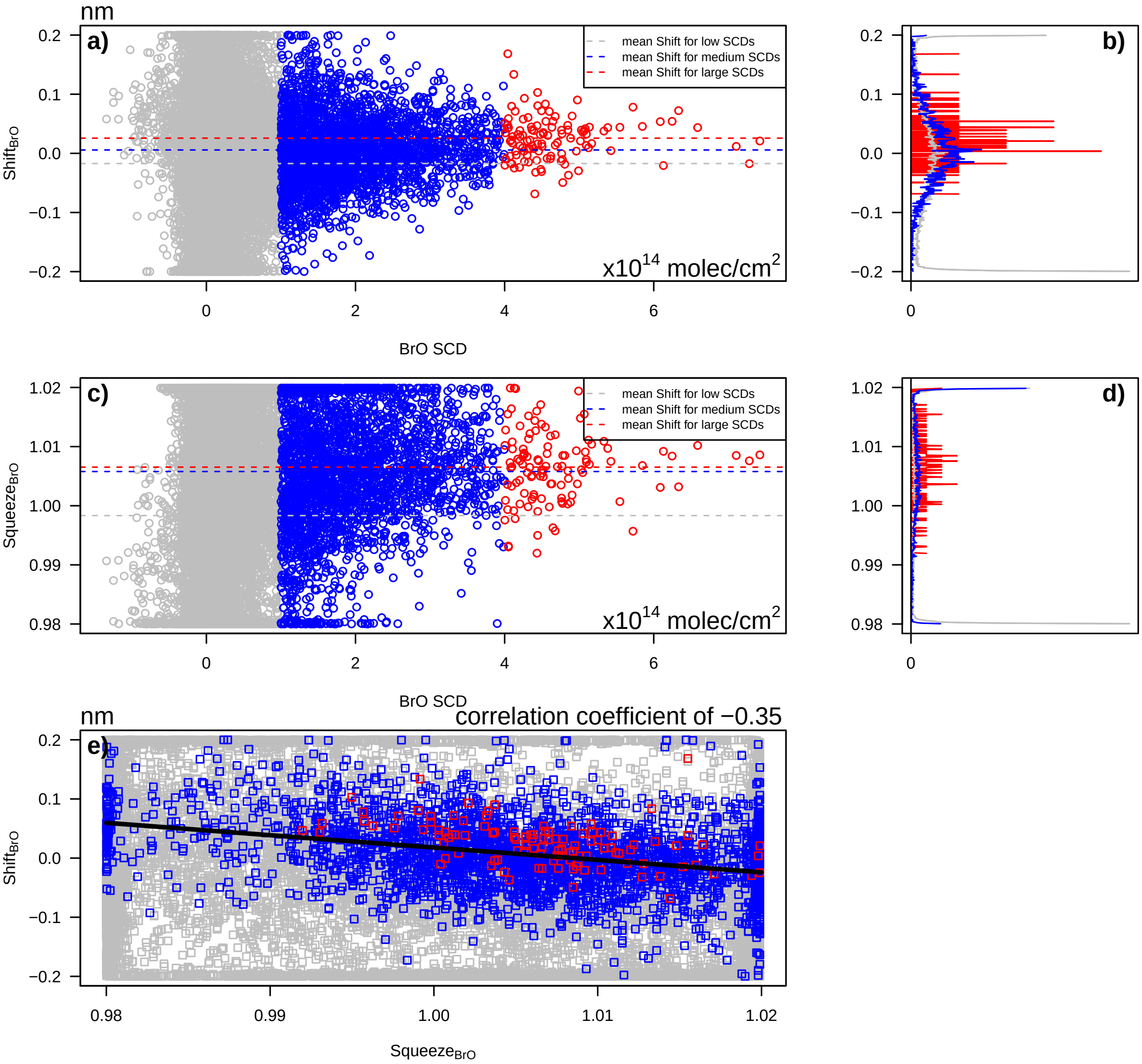

Figure 4.9: Additional Levenberg–Marquardt parameters in the BrO DOAS fit. **a and c:** Scatter plots of the shift and squeeze parameters as a function of the retrieved BrO SCD. The scatter plot is separated in three SCD ranges as indicated by the different colours. **b and d:** Histograms of the shift and squeeze parameters shown in panel a and c, respectively. Three histograms are shown for each of the three SCD ranges. **e:** Scatter plot of the shift parameter as a function of the squeeze parameter and for the three colour-coded SCD ranges. The plot is not transparent, that is, a part of the grey and blue data is covered by the overlying blue and red data. The linear regression applied on the combined blue and red data is given by the black line.

parameters are correlated when both fits are directly compared. Further, no significant correlation (i.e. with a coefficient above ±20 %) has been observed between any of the Levenberg–Marquardt shift or squeeze parameter and the time of the day or the date; neither for the total time series nor for the time series of only large SCDs.

Non-vanishing mean shifts and squeezes for large SCDs In contrast to the behaviour for low SCDs, there are in general a non-vanishing mean shifts and squeezes retrieved by all three DOAS fit scenarios. Furthermore, the mean shifts and squeezes correlate with the magnitude of the SCD (Figures 4.7, 4.8, 4.9).

For the SO_2 fit, the variability of the shift parameter only 25 % of the total variance are caused by the proposed linear correlation between the shift parameter and the SO_2 SCD while the predominant part of 75 % is presumably caused as well by the white noise fluctuations. The origin of the correlation between the SO_2 shifts and the strong SO_2 SCDs could either imply a causal impact of large real SO_2 SCDs on the DOAS fit, or a causal impact of an erroneous shift on the retrieved SO_2 SCDs, or no direct causal link between both parameters but possibly individual causal links induced by a third parameter. In the first scenario, a larger weight of the SO_2 signal — compared to the O_3 signal and the noise — forcing the shift towards the average trend would imply a systematic artefact in the SO_2 absorption signal. Presuming that I_0-effect is sufficiently corrected by the the previous spectroscopic treatment (see Section 4.2), this would first of all imply a significantly wrong convolution of the SO_2 absorption cross section (Section 3.4). Though the lab measurement indicated a rather wavelength-independent ILF, this may have changed one-time during the transportation and installation of the instrument causing this persistent shift which is rather independent on the temperature. The second scenario can be ruled out because an erroneous shift is presumably more likely for the smaller the SO_2 SCD is (see previous paragraph). No evidence for the third scenario has been found, in particular no correlation between the shifts and the squeezes on the time of the day, the seasonal cycle, or the date have been found.

Comparison with a DOAS fit without the additional parameters The debate whether the additional Levenberg–Marquardt parameters should be included in the DOAS fit at all can be condensed on the comparison of the expected systematic errors of both approaches. The underlying assumption is that the absorption cross sections are not perfectly convoluted with the ILF. The additional parameters could partially correct for this mis-convolution. On the other hand, if the absorption cross sections are almost perfectly convoluted, the additional parameters allow for a for a noise-driven overestimation of the retrieved SCDs.

The DJ2200_0 data has been re-evaluated with analogous fit scenarios but without an additional shift and squeeze parameter (fixed to 0 and 1, respectively). For the standard SO_2 fit, the mean deviation (and the standard deviation of this deviation) is $(-1.4 \pm 2.5) \cdot 10^{16} \frac{\text{molec}}{\text{cm}^2}$. These values but also almost all of the individual data points

Table 4.5: Linear regressions on the data shown in the Figures 4.7, 4.8, 4.9, performed for the subset of medium or large SCDs. The slope parameters are with respect to the SCD steps $\Delta S_{SO_2} = 1 \cdot 10^{18} \frac{\text{molec}}{\text{cm}^2}$ or $\Delta S_{BrO} = 1 \cdot 10^{14} \frac{\text{molec}}{\text{cm}^2}$. The lower part of the table lists the total shifts at the wavelength position λ_{peak} of the strongest absorption line in the specified fit scenario, see Figure 3.3.

	Unit	standard SO$_2$	alternative SO$_2$	BrO
λ_{peak}	nm	315.4	327.2	338.7
medium SCDs: $S_{SO_2} = (1-5) \cdot 10^{18} \frac{\text{molec}}{\text{cm}^2}$ and $S_{BrO} = (1-4) \cdot 10^{14} \frac{\text{molec}}{\text{cm}^2}$				
$[a_{shift}]_0$	pm	12.2 ± 0.6	-4.6 ± 1.6	-8.1 ± 3.1
$\Delta a_{shift}(S_i)$	pm/ΔS_i	6.1 ± 0.2	1.1 ± 0.6	7.3 ± 1.5
$[a_{squeeze} - 1]_0$	10^{-3}	-1.5 ± 0.1	-4.3 ± 0.5	3.3 ± 0.5
$\Delta a_{squeeze}(S_i)$	$10^{-4}/\Delta S_i$	-12.9 ± 0.4	-4.8 ± 1.9	13.1 ± 2.6
$[\Delta\lambda(\lambda_{peak})]_0$	pm	12.2 ± 1.0	-4.6 ± 1.7	-8.1 ± 3.3
$\Delta[\Delta\lambda(\lambda_{peak})]$	pm/ΔS_i	6.1 ± 0.3	1.1 ± 1.0	7.3 ± 2.1
large SCDs: $S_{SO_2} > 5 \cdot 10^{18} \frac{\text{molec}}{\text{cm}^2}$ and $S_{BrO} > 4 \cdot 10^{14} \frac{\text{molec}}{\text{cm}^2}$				
$[a_{shift}]_0$	pm	27.3 ± 1.2	-1.5 ± 0.9	24.5 ± 24.3
$\Delta a_{shift}(S_i)$	pm/ΔS_i	1.7 ± 0.2	0.6 ± 0.1	0.3 ± 5.1
$[a_{squeeze} - 1]_0$	10^{-3}	-5.3 ± 0.1	-5.9 ± 0.4	5.2 ± 3.9
$\Delta a_{squeeze}(S_i)$	$10^{-4}/\Delta S_i$	-2.7 ± 0.2	-1.0 ± 0.4	2.7 ± 8.2
$[\Delta\lambda(\lambda_{peak})]_0$	pm	27.2 ± 1.3	-1.5 ± 1.0	-24.5 ± 30.5
$\Delta[\Delta\lambda(\lambda_{peak})]$	pm/ΔS_i	1.7 ± 0.2	0.6 ± 0.3	0.3 ± 5.2

are smaller than the mean SO$_2$ fit errors of $\pm(1.6 \cdot 10^{16} \frac{\text{molec}}{\text{cm}^2} + 0.018 \cdot S_{SO_2})$. The precision of the mean results is basically identical (see orange and green dashed lines in Figure 4.10). For the alternative SO$_2$ fit, the mean deviation is $(-1.6 \pm 8.9) \cdot 10^{16} \frac{\text{molec}}{\text{cm}^2}$. Below the mean fit error of $\pm(0.4 \cdot 10^{18} \frac{\text{molec}}{\text{cm}^2} + 0.013 \cdot S_{SO_2})$. For the BrO fit, the mean deviation is $(-0.9 \pm 1.3) \cdot 10^{13} \frac{\text{molec}}{\text{cm}^2}$. For BrO SCDs above about $4 \cdot 10^{14} \frac{\text{molec}}{\text{cm}^2}$, the mean deviation is even $(-1.8 \pm 1.1) \cdot 10^{13} \frac{\text{molec}}{\text{cm}^2}$. A fraction of 18 % of the individual data is above the mean (and rather SCD-independent) fit error of $2.2 \cdot 10^{13} \frac{\text{molec}}{\text{cm}^2}$.
Accordingly, applying the additional Levenberg–Marquardt parameters on the SO$_2$ fits has hardly any impact on the accuracy and the precision of the SO$_2$ results. In contrast, the accuracy of the BrO results is significantly affected by the additional parameters. The observation that this deviation remains and even increases for strong BrO SCDs indicates that the Levenberg-Marquart parameters indeed correct a systematic effect, which is superimposed by predominant random noise effects for small BrO SCDs. An application of the additional Levenberg–Marquardt parameters is thus confirmed from empirical observations.

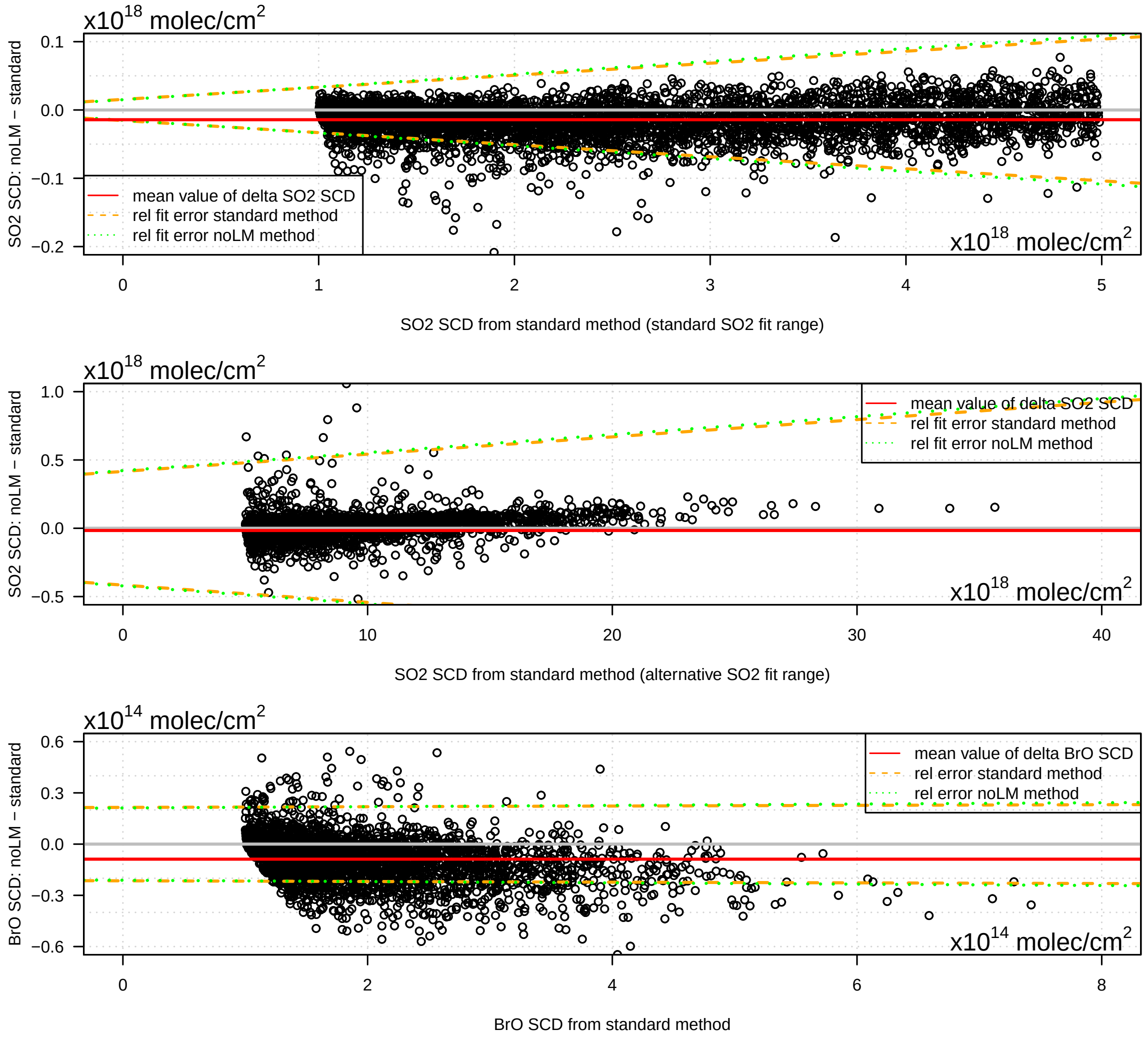

Figure 4.10: Comparison of the SO_2 and BrO SCDs when retrieved by a DOAS fit with and without additional Levenberg–Marquardt shift and squeeze parameters.

Comparison with other NOVAC instruments and conclusions The ILF of other NOVAC instruments can deviate strongly from the here analysed symmetric ILF of D2J2200_0. For example, the main instrument D2J2124_0. No detailed analysis of the ILF changes has been performed for other NOVAC instruments. Some checks have nevertheless confirmed that the behaviour of the shift and squeeze parameters vary significantly between the instrument. For example, the sign of the mean shift and squeeze (minus 1) parameter between the instrument. This confirms that the observed mean shifts and squeezes are not caused by a systematic slight mis-calibration of the high-resolution absorption cross sections but particular instrument effects.

ILF variability analysis accessed via QDOAS retrieval

ILF of D2J2200_0 retrieved from recorded spectra Missing regularly updated experimental data for the ILF, the temporal variations of the ILF could be investigated indirectly by a retrieval of the ILF from spectra of scattered sun light recorded at the particular times. Such a retrieval is implemented neither in DOASIS (the software package used for the retrievals in this thesis, see Section 4.2) nor in the official NOVAC software (https://github.com/NOVACProject) but in the QDOAS software (http://uv-vis.aeronomie.be/software/QDOAS/). The QDOAS software, however, does not allow for an automatised retrieval but only for a cumbersome manual retrieval which requires at least a minute per retrieval.

The QDOAS retrieval compares a reference spectrum recorded by the particular spectrometer with a spectrum which is derived by the convolution of a high resolution solar atlas spectrum with a parametrised model of the ILF. The algorithm then seeks to minimise the residual between the two spectra by varying the ILF parameters and outputs the optimal set of parameters. The QDOAS retrieval allows at most either for an asymmetric standard Gaussian line shaped ($k = 2$, $a_k = 0$) or for a symmetric super-Gaussian line shaped ($a_\sigma = 0, a_k = 0$) parametrisation of the ILF but not for a more general asymmetric super-Gaussian line shape. Furthermore, the atmospheric extinction processes have to be included in the QDOAS fit. For this study, the Rayleigh and Mie scattering have been estimated as usual by a polynomial of third order. Furthermore, an O_3 absorption cross section has been included in the QDOAS fit in order to correct for the strong O_3 absorption below 330 nm. An O_3 absorption cross section has been included which has been convoluted previously with the ILF measured at 334.14 nm because the QDOAS fit became unstable when including a high resolution O_3 absorption cross section. No Ring spectrum has been included in the QDOAS fit because its inclusion resulted in obviously unreliable fit results. The ILF parameters have been retrieved for 5 fit windows ($310 - 320$ nm, $320 - 330$ nm, $330 - 340$ nm, $340 - 350$ nm, $350 - 360$ nm). Hereby and for any evaluated recorded spectrum, the results of the four fit windows from $320 - 360$ nm show a consistent wavelength dependence while the first fit window from $310 - 320$ nm deviates extremely from this shared wavelength dependence by proposing inconsistently large FWMH and super-Gaussian exponents. Furthermore, the results of the latter four fit windows are in relative good agreement with the measurement results. The inconsistency of the first fit window is probably caused by the low solar light intensity between $310 - 320$ nm which makes the QDOAS retrieval in this wavelength range much more error-prone. The results of the first fit window are ignored in the following when not explicitly stated.

The QDOAS retrieval has been applied on three sets of multi-added reference spectra recorded by the NOVAC station in order to asses the diurnal, the seasonal and the inter-annual variations of the ILF.

Diurnal variations On July 1 2010, the ambient temperature monotonously increases from the 11°C at 07:37 local time (UTC-5) to 28°C at 13:16, and remained constant at 30°C from 14:12 to 17:20 (end of presented NOVAC data). For the fit window $330-340$ nm, the QDOAS retrieval proposes a strong diurnal cycle of the ILF, with a rather large FWHM and a rather small exponent at 7:37 followed by a monotonous converging of the ILF towards the lab ILF. The ILF has been stable from 12:14 to 15:34 and ambient temperatures of $25-30$°C, respectively, when the modelled super-Gaussian exponent fits almost perfectly with the lab value of 3.17 and the modelled FWHM levelled at 0.58 nm (Figure 4.11d+e). The two last data points deviate from the stable level with the model parameters significantly decreasing such that the exponent fits worse with the lab value but the FWHM fits better with the lab value. The reason for this deviation has not been found. A possible explanation may be the low light intensity at these times resulting in non-reliable QDOAS retrieval results.
The monotonous change of the ILF parameters until 12:14 are most likely caused by the temperature dependence of the ILF which indicates that the room temperature in the lab had been between $25-30$ °C. The persistent residual offset between the retrieved and measured FWHM of the ILF could be caused by both estimates of the ILF. On the one hand, the instrument and thus the ILF may have changed during the transport from Sweden to Colombia. On the other hand, the QDOAS retrieval algorithm is per construction systematically biased because some crucial components such as the Ring effect are neglected.
The monotonous diurnal variations of both model parameters are similar for all (five) fit windows. Ignoring the two first and two last time periods, the retrieved FWHM spans by (0.58 ± 0.02) nm (subject to typical standard fit error of the QDOAS retrieval of $\sigma_{\mathrm{FWHM}} = 0.02 - 0.04$ nm). The super-Gaussian exponents retrieved for the stable conditions from 12:14 to 15:34 increases linearly with wavelength from 2.6 at 325 nm to 3.8 at 355 nm (subject to typical standard fit errors of $\sigma_k = 0.01 - 0.03$). Both, the wavelength-independence of the FWHM and the wavelength-dependence of the exponent are in qualitative accordance with the lab results. For the first fit window, strongly varying FWHMs spanning from $0.61 - 0.79$ nm and exponents (3.5 ± 0.2) are strongly deviating from the results of the other fit windows and the lab results.

Seasonal and inter-annual variations The seasonal variations of the ILF are assessed by a comparison of the ILFs retrieved by QDOAS from spectra recorded at January 1, April 1, July 1, and October 1 of the years 2010, 2011, and 2012, respectively. No significant deviation has been observed for the different seasons (Figure 4.12).
The inter-annual variations of the ILF are assessed by a comparison of the ILFs retrieved by QDOAS from spectra recorded around noon time on January 1 of the years 2010, 2011, 2012, 2015, 2017, and 2018 (Figure 4.13). The inter-annual variation of the FWHM has been lower than 0.03 nm for each fit window and thus smaller than the typical diurnal variability. Also the wavelength-independence of the FWHM is confirmed by the inter-annual comparison of the four fit windows. For all years also a linearly increasing

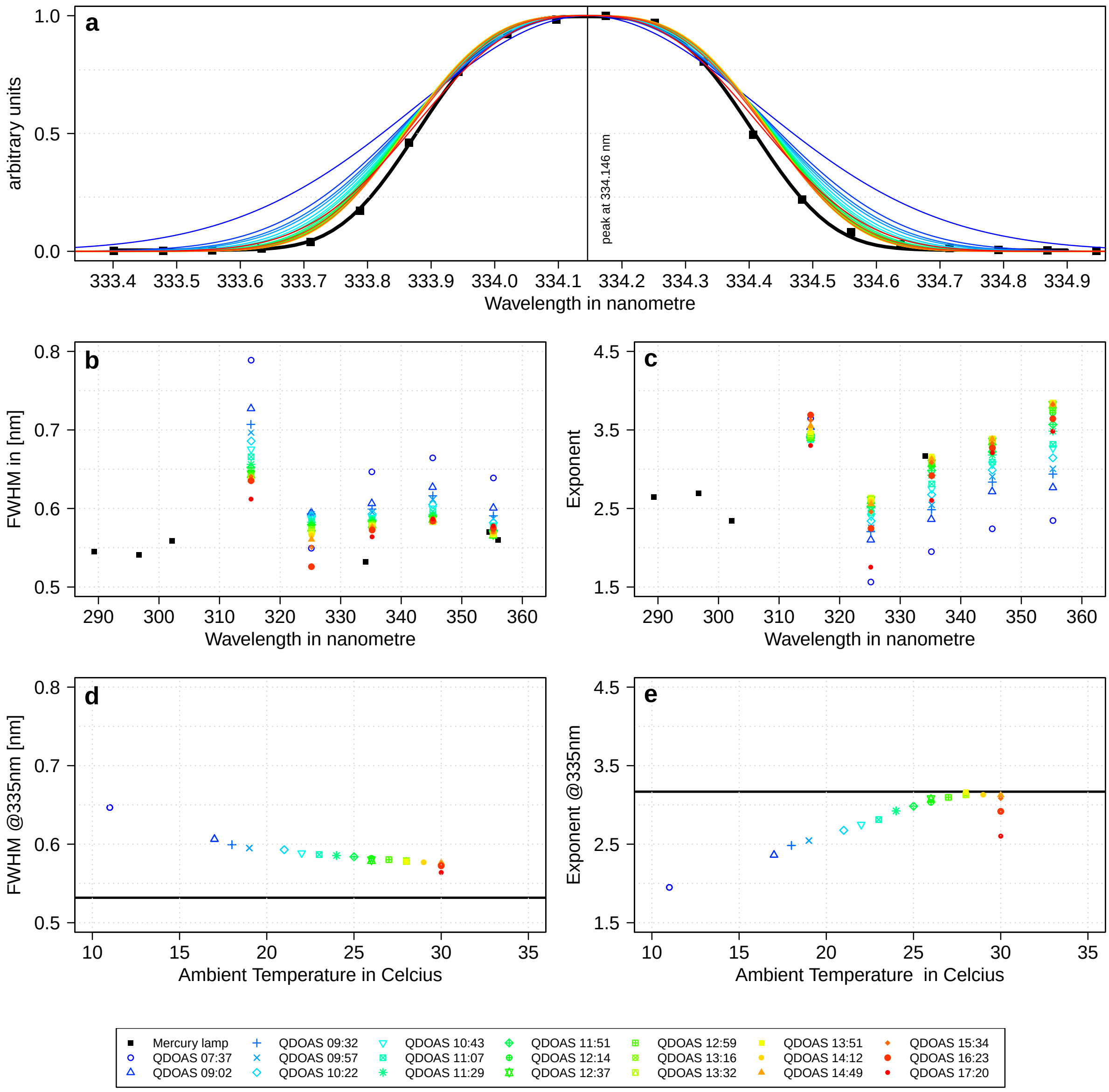

Figure 4.11: Diurnal variations of the instrument line function (ILF) of the NOVAC spectrometer with the serial number D2J2200_0 (which operates since late 2009 at Nevado del Ruiz) retrieved from spectra recorded on July 1 2010. **a)** The measurement results of the mercury emission line at 334.14 nm (black squares, measured somewhen in 2009 in a laboratory in Gothenburg, Sweden) and its super-Gaussian parametrisation (black line) are compared with super-Gaussian line shapes retrieved with QDOAS for different times of the day. **b)+c)** Measurement results (black squares) and QDOAS fit results for the five fit windows for the FWHM and super-Gaussian exponent. **d)+e)** Comparison of the results for the $330 - 340$ nm fit window with the measured 334 nm mercury line (black lines) as a function of the ambient temperature.

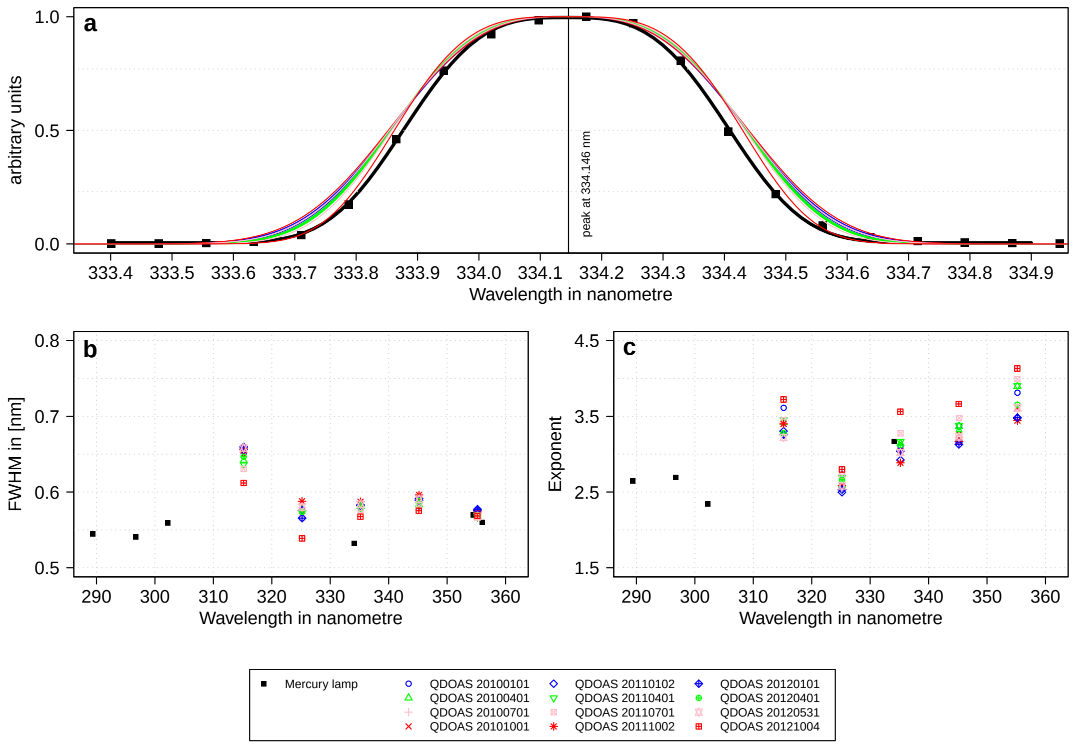

Figure 4.12: Seasonal variations of the instrument line function of the NOVAC spectrometer D2J2200_0 operating at Nevado del Ruiz. **a)** The measurement results of the mercury emission line at 334.14 nm (black squares, measured somewhen in 2009 in a laboratory in Gothenburg, Sweden) and its super-Gaussian parametrisation (black line) are compared with super-Gaussian line shapes retrieved with QDOAS for different times of the day. **b)+c)** Measurement results (black squares) and QDOAS fit results for the five fit windows for the FWHM and super-Gaussian exponent.

wavelength-dependence of the super-Gaussian exponent has been confirmed, slope and offset of this linear trend however deviate between the years and span, e.g., for the fit window from 330 − 340 nm from 2.6 in 2015 to 3.4 in 2017. The exponents retrieved for January 1 2010 matches best with the exponents retrieved for January 7 2017 and January 1 2018. The ILF results retrieved for January 1 2015 deviates the most from the inter-annual mean results. This is in line with the operation history of D2J2200_0 which stopped operation in July 2013, has been re-installed in the field in October 2014, but required a rather long period of time until March 2015 to fully re-adjust to the field conditions (Figure 4.6).

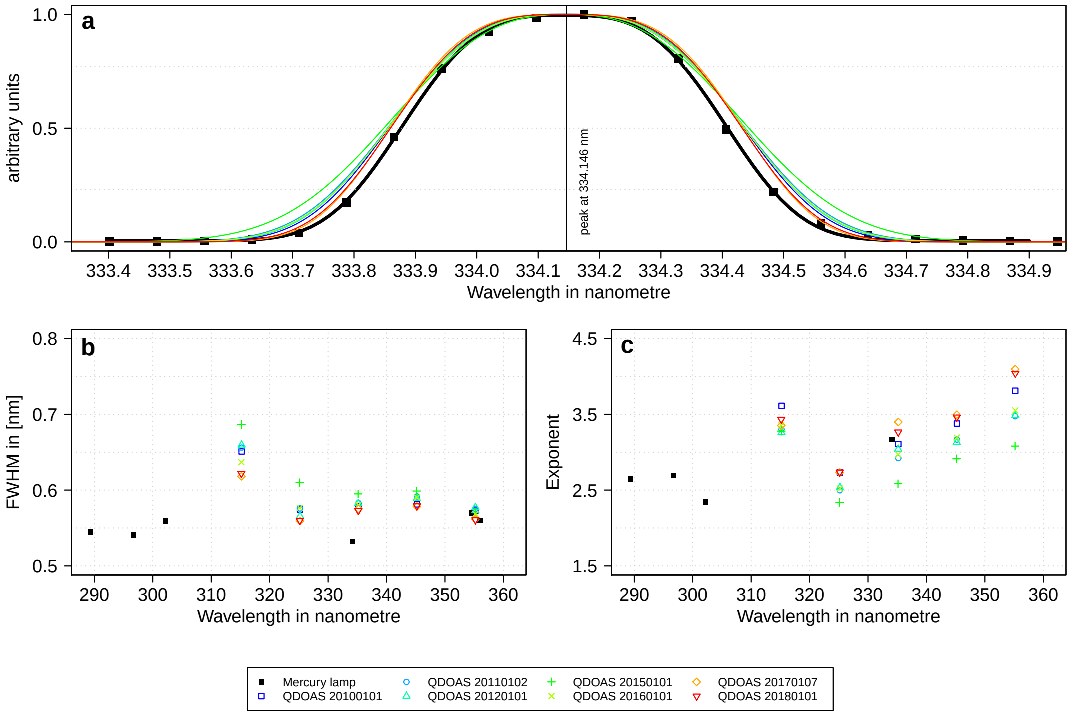

Figure 4.13: a) Comparison of the instrument line function the spectrometer D2J2200_0 retrieved from spectra recorded on January 1 (or as close as available) for 7 different years.

Implication for the accuracy of the NOVAC data The two most important results of the comparison of the measured and retrieved ILFs are (1) a persistent offset in the FWHM of 0.03 nm and (2) a diurnal trend of the FWHM causing an additional offset of up to another 0.04 nm. The diurnal trend is most likely caused by the variation of the ambient temperature. The origin of the persistent offset is not clear, but it is likely that it is just an artefact of the QDOAS retrieval. Applying the estimates from Lübcke [2014], the ignorance of the actual ILF means a systematic offset of the retrieved SO$_2$ SCDs (and thus SO$_2$ emission fluxes) by $-5\,\%$ and of the retrieved BrO/SO$_2$ molar ratios by $+4\,\%$. Further, both quantities vary by up to the same amount during the diurnal variations. Considering that most data points are recorded during the stable conditions after noon time, calculated daily means of the BrO/SO$_2$ molar ratios have a ILF-induced systematic offset of at most $+5\,\%$.

Conclusions

Levenberg–Marquardt parameters For small SO_2 and BrO SCDs, the shift and squeeze parameters are significantly affected by the statistical noise. For large SO_2 and BrO SCDs, the shift and squeeze parameters are found to apparently correct for systematic effects. These differential mean shifts and squeezes for large SCD differ between the NOVAC instruments. This implies that the systematic effects are not introduced by a slightly wrong calibration of the high-resolution absorption cross section but by instrumental drifts. It has been found that including these additional parameters to the DOAS fit scenarios results in basically the same retrieved SO_2 SCDs but significantly higher retrieved BrO SCD of in average $+0.9 \cdot 10^{13} \frac{\text{molec}}{\text{cm}^2}$. In conclusion, the use of the additional Levenberg–Marquardt parameters is recommended based on the presented empirical findings in order to enhance the accuracy for large SO_2 and BrO SCDs.

QDOAS retrieval The QDOAS retrieval indicates that the ILF-induced inaccuracy in the BrO/SO_2 molar ratios are an order of magnitude smaller than the typical measurement error (for large BrO SCDs). and has thus presumably only little impact on the final accuracy. This holds in particular true when only the variability in the BrO/SO_2 molar ratios around a mean value is examined as this is hardly influenced by a persistent ILF-induced offsets.

Possible improvements The ILF effects can be expected to be the major origin of systematic instrumental effects on the spectroscopic data. Thus it is of primary importance to provide as good as available information on the ILF for the convolution of the high-resolution absorption cross sections. This task can be done by two future adaptions: (1) by an enhanced amount of experimental data and (2) by an automatised ILF retrieval algorithm. The first approach strongly recommends that the ILF gets measured in the field or at least in the laboratory in the particular country (i.e. after the long distance transportation) and that the temperature dependency of the ILF is recorded for a range from at least $10 - 35°$C. For the second approach, a new retrieval has to be written and validated for DOASIS because QDOAS can not be automatised (and it takes several minutes to perform one retrieval manually). An automatically retrieved and thus larger data set of retrieved ILFs may furthermore help to optimise the ILF retrieval in order to learn about the origin of the persistent offset. A third approach lies in the combination of the two approaches; for example, the performance of the retrieval algorithm can be routinely checked by a comparison of the measured and retrieved temperature dependency.

Besides these fundamental improvements, the performance of the subsequent Levenberg–Marquardt correction approach could be enhanced by an iterative approach: In a first step the mean shifts and squeezes for large SCDs are retrieved by an analysis of the overall time series of a particular instrument with rather large or even unconstrained parameter ranges, i.e. exceeding $a_{shift} \in \pm 0.2\,\mathrm{nm}$ and $a_{squeeze} \in 1 \pm 0.02$. In a second step, the time series is analogously retrieved however with the shift and squeeze parameters set fixed to the mean values retrieved in the first step. With this procedure, the ILF-induced artefacts can be mostly compensated while the final time series is not altered by noise-induced shifts. The merits of such an iterative approach have been developed only at the end of this thesis. Thus the DOAS fit results presented in this thesis are retrieved with the parameter ranges of $a_{shift} \in \pm 0.2\,\mathrm{nm}$ and $a_{squeeze} \in 1 \pm 0.02$ inherited from the previous studies by Lübcke et al. [2014] rather than by the just proposed iterative approach.

4.5 Further evaluation advances

The massive NOVAC data set gives potential access to a large set of volcanological and atmospheric parameters. On the one hand, still not all available spectroscopic resources have been investigated or incorporated in order to further optimise the accuracy and temporal resolution of the NOVAC SO_2 and BrO time series. On the other hand, further parameters such as other volcanological or atmospheric trace gases or the cloud cover may be extracted from the NOVAC data and then either used as auxiliary information for improving the SO_2 and BrO evaluation or used as independent data product. The following section sketches three advances which could be incorporated in near future in the NOVAC retrieval routine. A fourth advance lies in a robust and automatised retrieval of the instrument line function from recorded NOVAC spectra as already discussed in Section 4.4.

Absolute SO_2 retrieval by using a Solar Atlas as reference Volcanic gas plumes occasionally (at some volcanoes relatively often) hoover down the volcanic slope, particularly at low wind speeds. When such a hoovering gas plume approaches the NOVAC instrument, the overall scan range of the telescope can be contaminated by near-ground volcanic trace gases. In general, such a background contamination adds different additional absorption signals of volcanic trace gases to the spectra recorded at different viewing angles. For example, a horizontally homogeneous contamination layer with constant vertically extension adds absorption signals whose magnitude is proportional to the length of the light path through the contamination layer which is the smallest for the zenith direction. Thus, such a widespread contamination causes a miscalculation (typically an underestimation) of the current volcanic gas emission flux. And this holds for a whole list of contamination scenarios where the two most obvious are: (1) the contamination layer is the current gas plume, then a part of the actual plume region is falsely interpreted as the reference region causing an underestimation due to how passive DOAS tomography works or (2) the contamination layer is an old (and therefore already significantly diluted) plume from, e.g., the previous day and there is another younger plume in higher altitude, then contamination layer varies the contrast between the younger plume region and the reference region.

Lübcke et al. [2016] presented an algorithm which can detect a possible SO_2 contamination in the reference region by using the semi-theoretical solar atlas spectrum from Chance and Kurucz [2010] as the reference spectrum in their SO_2 DOAS fit. This spectrum is assumed to be free of any SO_2 absorption signal and thus allows for an retrieval of absolute SO_2 SCDs. As a drawback, the rejection of a recorded reference spectrum makes it mandatory to simulate the instrument characteristics by, e.g., a principal component analysis (PCA) [Pearson, 1901]. Thereby, the first principal component reproduces the constant detector inhomogeneities and the second principal component is found to reproduce the temperature-dependency of the detector inhomogeneities

[Lübcke, 2014, Warnach, 2015, Lübcke et al., 2016]. For the NOVAC instruments, the contribution of the further principle components to the overall variance is too low to reliably assign them to external parameters. The two first principal components are then added as pseudo-absorbers to the SO_2 fit scenario following the reasoning that the solar atlas spectrum plus these two principal components approximately represent a volcanic-gas-free Fraunhofer spectrum as it would be recorded by the particular instrument. This approach can however cause a large drop in the precision of the SO_2 SCDs. Thus although this approach has been proven to produce results of acceptable SO_2 precision, it is recommended to use a reference spectrum recorded by the same instrument whenever no contamination is detected.
The functionality of the contamination detection algorithm is already implemented in the retrieval algorithm described in this chapter, however not yet called by the main functions for two reasons. First, this approach requires the output of a preceding PCA. This means a preceding retrieval run ignorant to the contamination in order to retrieve the input data for the PCA. An automatised simultaneous retrieval of the principle components has not yet been developed/validated. On the one hand, this is run time consuming. On the other hand and more crucial, this requires a better understanding for the temporal evolution of the principle components (e.g. random long-term trends due to ageing) in order to avoid artefacts in the spectroscopic results when using an averaged principle component which does not represent the current detector conditions.
Second, while the findings from Lübcke et al. [2016] appear to be mandatory for the accurate SO_2 emission flux estimates, this thesis and the above described retrieval algorithm focus on the BrO/SO_2 molar ratios. A contamination in SO_2 indicates also a potential contamination in other volcanic gas species such as BrO. A one-sided correction of the SO_2 SCDs could therefore potentially falsely change the BrO/SO_2 molar ratio. Lacking knowledge on the effect of such contaminations on the BrO/SO_2 molar ratio, three alternative strategies appear: (1) All data contaminated in SO_2 are rejected from the further evaluation. (2) The contamination is assumed to have no significant effect on the BrO/SO_2 molar ratios. With respect to the first strategy, this has the advantage of a higher temporal resolution and the drawback of potential systematic offsets in parts of the time series, in particular at low wind speeds. This thesis follows this strategy. (3) The contamination gets corrected as well for BrO. This approach has been examined by the Master thesis from Wilken [2018] summarised in the following paragraph.

Correction algorithm for contaminations of the BrO/SO_2 molar ratios The PCA has to use spectra virtually free of volcanic gases. The volcanic SO_2 absorption signal is that strong that virtually SO_2 free spectra can be detected by a DOAS fit which uses solely the solar atlas as the reference spectrum, i.e. without adding the (not yet determined) principle components. In contrast, such a procedure has not yet succeeded for BrO due to the weaker BrO absorption signal in volcanic gas plumes when compared to

SO_2. Accordingly, a PCA of the the detector range which spans the BrO fit range is only possible for data which has been proven to be free of SO_2 but which potentially can include some BrO absorption signal. Further, the BrO fit using the solar atlas and the two first principle components has a decreased precision compared with the standard BrO retrieval. Both effects independently do not allow for such a PCA based retrieval of BrO from NOVAC data (and up to know from any data).

An alternative BrO contamination correction approach lies in replacing the contaminated reference spectrum by another reference spectrum (recorded e.g. on the day before) which has been validated to be free of contamination and which has approximately the same detector characteristics (i.e. recorded at similar ambient conditions). Thereby, any PCA artefacts can be avoided and the drop in precision can be kept at a minimum, in particular the precision should be virtually the same when the ambient conditions are similar. The overall strategy is then first to check/detect a contamination based on the SO_2 retrieval from Lübcke et al. [2016], second to pick a suitable reference recorded by the same instrument, and third to re-evaluate BrO but also SO_2 with this alternative reference spectrum. Wilken [2018] examined this approach for several years of data from Nevado del Ruiz and Tungurahua and concluded that only slightly worse BrO precisions are retrieved when a reference spectrum recorded at approximately the same temperature and time of day and with a maximum temporal distance of about a week is used. As expected the algorithm retrieved higher SO_2 and BrO SCDs, which means besides the increase in accuracy because more data points exceeded the strong plume filter threshold of $SO_2^{thres} = 7 \cdot 10^{17} \frac{\text{molec}}{\text{cm}^2}$. Many aspects of the contamination scenarios are however not yet determined in particular about the impact in the BrO/SO_2 molar ratios. In particular, using gas free reference spectrum in general cause an overestimation of the current emission fluxes because the spectra recorded in the plume region still contain the additional contamination signal. The "true" uncontaminated signal therefore rather lies somewhere between the (over-)corrected and uncorrected value.

Wilken [2018] further concluded that the BrO/SO_2 molar ratios only slightly decreases implying that the relative contamination is slightly larger for SO_2 than for BrO. Many aspects of the contamination scenarios are not yet understood, e.g. the impact of the age of the contamination layer and thus the atmospheric life times of SO_2 and BrO. While the approach from Wilken [2018] appears to be useful to retrieve auxiliary informations on the contamination scenario, the study first of all supports the tacit assumption in this thesis that a contamination has approximately no effect on the BrO/SO_2 molar ratios. The functionality of this approach is already incorporated in overall retrieval algorithm architecture but has not yet been called when producing the data presented in this thesis. Further, Wilken [2018] found the empirical results by a manual investigation. A tool which automatically and on-line proposes and performs the correction is still under development.

Retrieval of the oxygen dimer O_4 and the Colour Index from NOVAC The DOAS approach retrieves a set of SCDs of the gas species. Roughly speaking, the SCDs give the product of the average gas concentrations times the actual light path length. Multiple photon scattering in optically dense (either due to a large ash load or condensed water emissions) volcanic plumes in general cause an enhancement of the actual light path and thus an overestimation of the gas concentrations when retrieved from the SCDs. But also an extended and/or fractional background cloud cover can cause an systematic error when interpreting the spectroscopic data, e.g., due to multiple plume transition caused by photon ping-ponging between two cloud layers [Pfeilsticker et al., 1998]. Volcanic gas plumes are often condensed and typically also exposed to a background cloud cover, in particular at low latitudes. Therefore a detection of time intervals with particularly problematic cloud scenarios may help either to reject bad data from the further evaluation or to empirically rule out a significant impact of clouds on the BrO/SO_2 molar ratios. At the location of the remote volcanoes, independent meteorological data on the cloud conditions is typically not available, in particular not with a high temporal resolution. For this purpose, Dinger et al. [2018] examined for their Cotopaxi study (Chapter 6 in this thesis) whether it is possible to retrieve the cloud cover directly from the NOVAC data and checked for meaningful correlations with the retrieved BrO/SO_2 data. The following paragraph is a literal reproduction of their appendix, except for some minor editorial changes.

Established cloud detection algorithms base on the absorption of the oxygen dimer O_4 at 360 nm or the relative intensity ratio of the intensity of the backscattered solar radiation at 320 nm and 440 nm [the so-called Colour Index, see e.g. Wagner et al., 2014]. The application of those or similar algorithms on NOVAC data faces at least three challenges: (1) The effectively detected wavelengths range from 280 nm to 400 nm, however, with a linear decrease in transmittance already from 370 nm to 400 nm due to the HOYA U330 UV bandpass filter. Accordingly, the standard colour index pair is not applicable. (2) The measurement routine automatically optimises the integration time of the spectra with respect to the wavelength range of the SO_2 retrieval ($\sim 310 - 335$ nm). As drawback, spectra are often, in particular at cloud free days, over-saturated starting a 365 nm but sometimes even already at 359 nm. Accordingly, the standard O_4 retrieval is typically not applicable on NOVAC data when the sky is cloud free. On the other hand, the absorption signal of the O_4 line at 344 nm is not significant for a spatial analysis. (3) Many NOVAC instruments (at Cotopaxi three of four) use a conical scan geometry thus never record zenith spectra. Missing the zenith value for O_4 or the colour index makes the interpretation of the analysis results more challenging.
We anyway tested both methods on the NOVAC data retrieved from the Cami station at Cotopaxi volcano (because there zenith information is available). For the colour index analysis, we compared the mean intensity of the wavelength ranges at $329 - 329.7$ nm and at $381 - 381.6$ nm [each the average of 10 detector channels, see also Lübcke, 2014]. We applied the analysis on the zenith spectra of each particular scan. The resulting time series of the colour index has not shown any periodic pattern and most long-term

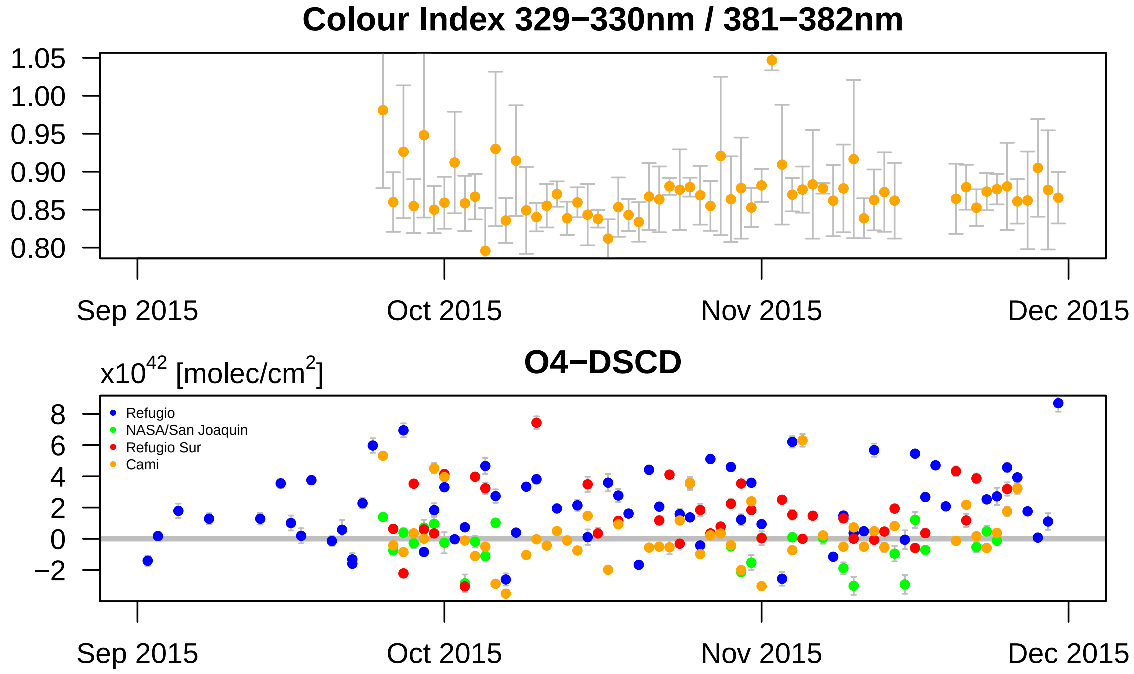

Figure 4.14: Upper panel: Colour Index (here: mean intensity of the wavelength ranges at 329 − 329.7 nm and at 381 − 381.6 nm) retrieved from Cami station. The analysis based on the single scans, shown are the daily means and the error bars indicate the standard deviations of the daily variations. **Lower panel:** Difference of the O_4 SCDs in the plume region and in the reference region (both as found by the SO_2 analysis). The O_4 enhancement observed by the stations Refugio and Refugio Sur is probably just due to the dependency of the background O_4 SCD on the elevation angle. Figure reprinted from [Dinger et al., 2018].

variations were small compared to the mean daily variations (see Figure 4.14 upper panel). For the O_4 retrieval, we applied a fit scenario with the same absorbers as for BrO [see Lübcke et al., 2014] but with a fit range from 338 nm to 365 nm. We applied the analysis on the individual spectra within each scan and used the particular zenith spectrum as reference spectrum. A comparison with the results of the SO_2 retrieval showed no correlation, i.e. no systematic enhancement or reduction of O_4 absorption signal has been observed within the volcanic plume.

As additional approach, we applied the same O_4 analysis on the multi-scan plume spectra recorded by all NOVAC stations at Cotopaxi and used the particular multi-scan reference spectrum as reference spectrum. The resulting time series neither contained periodic patterns nor showed a significant correlation with the BrO/SO_2. On the other hand, the stations Refugio and Refugio Sur, where the plume is typically passing at lower elevation angles, found O_4 enhancements by about $2 \cdot 10^{42} \frac{\text{molec}}{\text{cm}^2}$ in the plume while the stations Cami and San Joaquin, where the plume is typically passing in about zenith direction, found no O_4 enhancement in the plume (see Figure 4.14 lower panel).

This enhancement is probably solely due to the dependency of the background O_4 slant column density on the elevation angle, illustrating the difficulty to interpret the O_4 results. We want to highlight that more sophisticated and well validated studies which e.g. make use of massive filtering of the data may indeed retrieve information of the aerosol load from the NOVAC data, however, the development of such a sophisticated cloud classification algorithm is beyond the scope of this study.

Part II: Observations

5 Nevado del Ruiz

A first investigation of BrO/SO_2 time series at Nevado del Ruiz has been conducted by Lübcke et al. [2014] for the period from 2010 to early 2014. In this chapter, the extended time series until 2018 is presented and discussed.

5.1 Volcanology and Meteorology

Volcanology Nevado del Ruiz (4.9°N, 75.3°W, 5321 m a.s.l.) is a glacier-capped stratovolcano located in the Cordillera Central of the Andes of Colombia. The Smithonian Institution (http://volcano.si.edu/) lists 12 historically confirmed eruptions since 1570, typically with an Volcanic Explosivity Index (VEI) of 2 [Newhall and Self, 1982]. On November 13 1985, a phreatomagmatic explosion with VEI3 (or VEI4, [Londono and Galvis, 2018]) produced lahars which caused the Armero tragedy, one of the deadliest volcanic catastrophe in history with a death toll of 25000 causalities [Naranjo et al., 1986, Voight, 1990]. Londoño and Kumagai [2018] give an overview on the volcanic activity at Nevado del Ruiz from 1985 to 2017, primarily based on their seismic tomography data but compiled with other volcanological data. After a smaller phreatomagmatic explosion on September 1 1989, the magmatic activity stopped in 1990 and Nevado del Ruiz remained relatively quiet until 2007 with only phreatic activity. The upcoming of a new period of unrest at Nevado del Ruiz has been indicated by seismic and deformation signals since 2007, and enhanced CO_2 and Radon emissions in 2008 [Londono, 2016, Londoño and Kumagai, 2018]. The current period of unrest then started in 2010 with increased and ongoing seismicity. Since February 2010, Nevado del Ruiz emits frequently ash and continuously large amounts of SO_2. On June 30 2012, a phreatomagmatic explosions occurred emitting ash with the same chemical compositions as the ash from the 1985 and 1989 explosions. From early 2012 until (at least) early 2015, a volcanic inflation of over $3-4$ cm per year has been observed, presumably caused by a magma source at a depth of 10 km b.s.l. centred 10 km southwest of Nevado del Ruiz [Lundgren et al., 2015]. Between 2013 and 2014 some strong volcano-tectonic earthquakes with local magnitudes in Manizales city (30 km away from Navado del Ruiz) of up to 5.0 were recorded. Another volcanic crisis occurred in November 2014 with increased seismic tremor, thermal anomalies, and small vulcanian explosions [Global Volcanism Program, 2017]. Since September 2015, a small dome is growing at the bottom of the active crater [Londono and Galvis, 2018, De Paolo et al., 2019]. Seismicity and the number of vulcanian explosions were on a high level in 2015 and 2016 but decreased both after mid 2017.

Vargas et al. [2017] retrieved the evolution of the permeability of the shallow magmatic system by a seismic tomography and propose a temporal classification of the recent eruption in four phases between 1998 and 2016 (the span of their time series): (1) a predominantly gas-tight system until 2010 (2) influx of magma in the shallow system and magma degassing due to decompression in $2011-2012$, (3) magma degassing due to decompression, however, without further magma influx in $2013-2014$, and (4) influx of magma and evolution of a lava dome in $2015-2016$.

Nevado del Ruiz has currently a magma chamber at a depth $0-3$ km a.s.l. ($2-5$ km below the surface) [Londono, 2016, Vargas et al., 2017] fed by a deeper magma source. The source depth has not (yet) been well constrained with estimates varying from $20-40$ km b.s.l. [Londono, 2016], to 10 km b.s.l. [Lundgren et al., 2015], to 7 km b.s.l. [Londoño and Kumagai, 2018].

Meteorology The meteorological conditions at Nevado del Ruiz are accessed by ECMWF model data for an altitude of 5600 m (Figure 5.1) and by ground-based data for the time interval from $2014-2017$ (Figure 5.2) from meteorological stations on the western slope of Nevado del Ruiz (near the Olleta NOVAC station, see Figure 5.3). The ECMWF time series indicates annual cycles in several meteorological parameters but with different timing of their extrema. The quantitative spans given in the following refer to the running means (2 weeks window) of the about noon ECMWF values (red lines in Figure 5.1). The barometric pressure varied between $516-520$ mbar with maxima between February and June and minima between October and December. The ambient air temperature varied between $267-273$ K but without a persistent pattern. The specific humidity varied from down to $1\,\frac{\mathrm{g\,H_2O}}{\mathrm{kg\,air}}$ in January/February to mean values of $4-6\,\frac{\mathrm{g\,H_2O}}{\mathrm{kg\,air}}$ in the rest of the year. The relative humidity varied from down to 20 % in January/February to mean values of $75-100$ % in the rest of the year. This perfectly matches the average precipitation patterns at Manizales (the major city closest to Nevado del Ruiz) where the rain season spans from April to November with a maximum precipitation column of 380 mm in August and minimum 37 mm in January [IDEAM, 2018]. The cloud cover has been almost exclusively above 0.8 for most of each year and with significant deviations down to 0.3 only in January. The mean wind speeds varied between $2-15\,\frac{\mathrm{m}}{\mathrm{s}}$ with maxima in July, values typically below $5\,\frac{\mathrm{m}}{\mathrm{s}}$ from October to May, but with further secondary maxima of up $9\,\frac{\mathrm{m}}{\mathrm{s}}$ to in January/February. The wind blew all the year for most of the time from East–Southeast with the long-term mean of $(103\pm16)^\circ$ (clockwise w.r.t. northerly winds). An annual cycle can be observed in the variability of the wind direction with $(110\pm14)^\circ$ from May to October and $(101\pm19)^\circ$ from November to April.

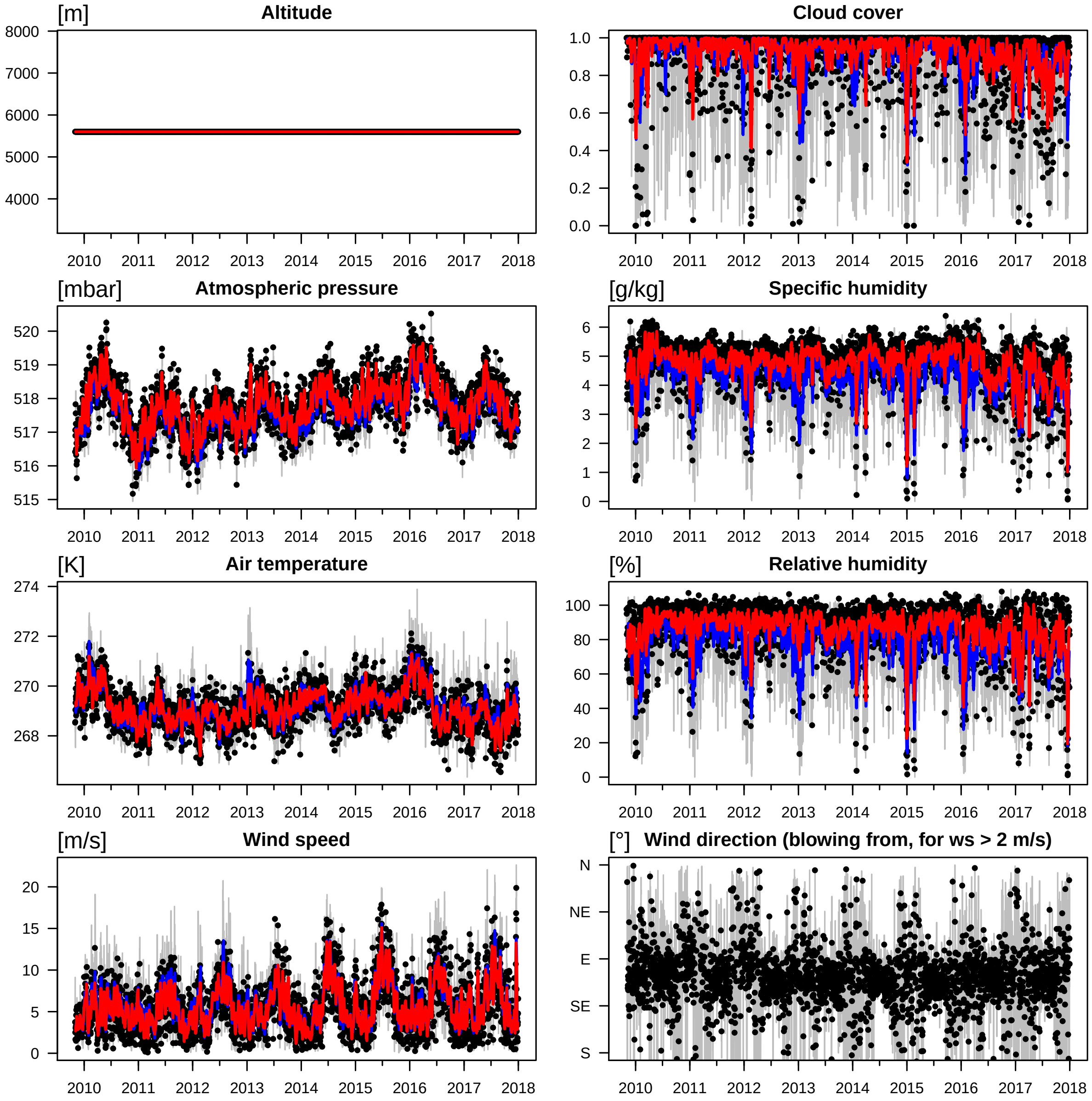

Figure 5.1: Meteorological conditions at Nevado del Ruiz volcano retrieved from ECMWF data with resolutions of 6 h and 0.14° x 0.14° and interpolated to an altitude of 5600 m a.s.l. **Grey lines:** 6-hourly data. **Blue lines:** weekly rolling average over the 6-hourly data (±3 days window). **Black dots:** around noon (18:00 UTC) data. **Red lines:** same rolling average but over the around noon data. Absolute variations are almost the same for the full data set and the around noon data only. The exception is the air temperature and the relative humidity. As expected, the air temperature is larger around noon which thus causes a smaller relative humidity around noon.

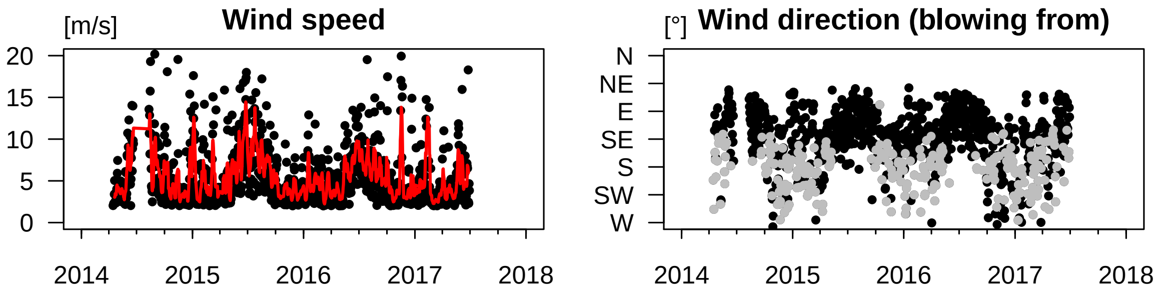

Figure 5.2: Ground-based wind data at Nevado del Ruiz recorded close to the Olleta NOVAC station (4.8957°N, 75.3575°W, at 567 mbar, personal communication from Zoraida Chacon, Servico Geologico Colombiano, Manizales, Colombia): Daily means (black/grey dots) and the running mean of a 2 weeks window (red line). Division of the wind direction: black dots for wind speeds larger than $\geq 3\,\frac{\mathrm{m}}{\mathrm{s}}$ and grey dots for wind speeds $< 3\,\frac{\mathrm{m}}{\mathrm{s}}$.

The ground-based wind data mostly confirms the wind data retrieved from the ECMWF data. Both datasets agree in (1) the semi-annual variations in the wind speed, with maximum in July and secondary maxima in January/February, (2) an annual cycle in the wind fields with larger variability in the wind direction from November to April, and (3) the wind is blowing from East-Southeast from May to October. A major discrepancy can be observed for the mean wind direction from November to April, when the ground-based data imply the wind blowing in average from South rather then from East-Southeast. When filtered for wind speeds $\geq 3\,\frac{\mathrm{m}}{\mathrm{s}}$ this discrepancy mostly vanishes. The following analysis refers to the ECMWF data.

5.2 DOAS measurements of SO_2 and BrO

NOVAC stations at Nevado del Ruiz The number of active NOVAC stations has varied between 1 and 6 stations at a time (Figure 5.3 and Table 5.1). In total 8 instruments (with the serial numbers D2J2200_0, D2J2201_0, D2J2811_0, D2J2813_0, D2J2814_0, D2J2825_0, D2J2828_0, D2J2830_0) have been installed for at least one year at the NOVAC stations, some instruments have been installed subsequently on different NOVAC stations. The stations Bruma (initial instrument: D2J2200_0) and Alfombrales (D2J2201_0) operate since December 2009. In early 2012, the Azufrado station (I2J5897_0) has been installed, however, the I2J5897_0 data could not been evaluated during this thesis as no information on the instrument line function is available. Since late 2014 three additional stations (Olleta, Recio_3, and El Camion) have been installed. Since 2017, only the four stations Bruma, Alfombrales, Recio_3, and El Camion have been operating.

SO_2 and BrO time series since 2009 Since late 2010, Nevado del Ruiz is emitting extremely large amounts of SO_2 with SO_2 SCDs exceeding several $10^{18}\,\frac{\text{molec}}{\text{cm}^2}$ almost daily (Figure 5.4 and Table 5.2). The observed SCDs of the same plume can differ between the stations because of their different distances to the volcanic vent (Section 7.3). Until October 2014, the following quantitative discussion of the time series focusses on the Bruma station in order to keep the quantitative comparisons clear. The Alfombrales station observed in this time interval similar SO_2 variations but differs to some extend in BrO as will be discussed later. The time series since October 2014 are discussed for all stations at once.

From September 2010 to February 2012, the daily maximum of the SO_2 SCDs was rather constant at about $3 \cdot 10^{18}\,\frac{\text{molec}}{\text{cm}^2}$ and the BrO SCDs varied between $1 - 2 \cdot 10^{14}\,\frac{\text{molec}}{\text{cm}^2}$ resulting in average BrO/SO_2 molar ratios of $3 \cdot 10^{-5}$. Between February 2012 and June 2012, the SO_2 SCDs exceeded $25 \cdot 10^{18}\,\frac{\text{molec}}{\text{cm}^2}$ and the BrO SCDs varied between $1 - 3 \cdot 10^{14}\,\frac{\text{molec}}{\text{cm}^2}$ resulting in average BrO/SO_2 molar ratios of $1 \cdot 10^{-5}$. On June 30 2012, several large phreatomagmatic explosions occurred. The SO_2 SCDs dropped to $15 \cdot 10^{18}\,\frac{\text{molec}}{\text{cm}^2}$ and remained on this level until July 2013. In June/July 2013, the SO_2 SCDs enhanced to $20 \cdot 10^{18}\,\frac{\text{molec}}{\text{cm}^2}$ but dropped to $10 \cdot 10^{18}\,\frac{\text{molec}}{\text{cm}^2}$ between August 2013 and November 2014. In contrast, the BrO SCDs increase after the explosions on June 30 2012 and stayed at a level of up to $4 \cdot 10^{14}\,\frac{\text{molec}}{\text{cm}^2}$ until May 2014 but dropped to $1 \cdot 10^{14}\,\frac{\text{molec}}{\text{cm}^2}$ between May and November 2014. The strong thermal anomalies and seismic activity in November 2014 have been accompanied by SO_2 SCDs exceeding $20 \cdot 10^{18}\,\frac{\text{molec}}{\text{cm}^2}$ and BrO SCDs exceeding $4 \cdot 10^{14}\,\frac{\text{molec}}{\text{cm}^2}$. Since February 2015 no Bruma data are available on the NOVAC server. The other stations (and in particular the Alfombrales station) observed persistent SO_2 SCDs of up to $15 \cdot 10^{18}\,\frac{\text{molec}}{\text{cm}^2}$ until May 2017. Since May 2017, the SO_2 SCDs typically varied between $2 - 5 \cdot 10^{18}\,\frac{\text{molec}}{\text{cm}^2}$ except

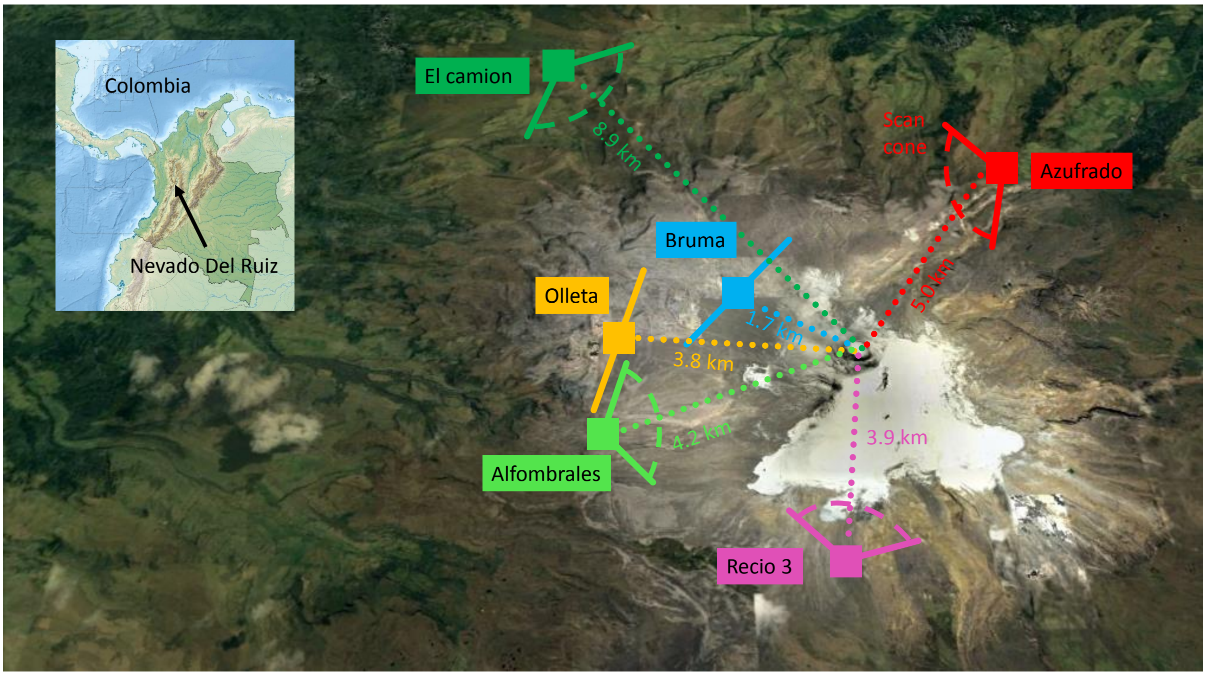

Figure 5.3: Location and scan geometries [see details in Galle et al., 2010] of the six NOVAC stations at Nevado del Ruiz, the colours match to the time series in Figure 5.4. The map was created with graphical material from Google Earth and https://commons.wikimedia.org/wiki/File:Colombia_relief_location_map.jpg.

Table 5.1: Geometric properties of the NOVAC stations at Nevado del Ruiz. All properties are taken from the official records at the NOVAC server. The distance is the horizontal distance. The angular position and scan plane angle refer to the direction from the volcanic vent to the NOVAC station and perpendicular to the scan plane, respectively, and are defined like wind directions (0° means strictly south of the vent, 90° means strictly west of the vent, etc.). The scan plane angles may have changed (undocumented) when an instrument has been repaired or reinstalled at the same station.

NOVAC station	coordinates	altitude	distance	angular position	scan plane angle	cone angle
		A	D	σ	β	
Bruma	4.90, -75.33	4864 m	1.9 km	120°	135°	90°
Alfrombrales	4.88, -75.35	4488 m	4.2 km	65°	80°	60°
Azufrado	4.92, -75.29	4218 m	5.0 km	215°	250°	60°
Olleta	4.90, -75.52	2233 m	3.8 km	90°	90°	90°
Recio_3	4.86, -75.33	4665 m	3.9 km	10°	10°	60°
El camion	4.96, -75.37	4184 m	8.9 km	145°	145°	60°

Table 5.2: Typical SO_2 SCDs and BrO SCDs in the gas plume of Nevado del Ruiz. Except for the first time period, the mean values refer to the data which are filtered for the strong plume threshold SO_2 SCD $\geq 7 \cdot 10^{17}\ \frac{\text{molec}}{\text{cm}^2}$. SCDs are reported in $\frac{\text{molec}}{\text{cm}^2}$. "Max SCDs" refers to typical upper values excluding single outliers. Since February 2015, basically no data from Bruma station are uploaded on the NOVAC server. The SCDs can therefore not be quantitatively compared with the time intervals before 2015.

Time period	mean SO_2	max SO_2	mean BrO	max BrO	mean BrO/SO_2
Based on Bruma station					
Jan '10 - Sep '10	$0.3 \cdot 10^{18}$	$0.6 \cdot 10^{18}$	*(below det.)*	$6 \cdot 10^{13}$	*(below det.)*
Sep '10 - Feb '12	$1 \cdot 10^{18}$	$3 \cdot 10^{18}$	$4 \cdot 10^{13}$	$15 \cdot 10^{13}$	$3.2 \pm 2.7 \cdot 10^{-5}$
Feb '12 - May '12	$6 \cdot 10^{18}$	$22 \cdot 10^{18}$	$5 \cdot 10^{13}$	$25 \cdot 10^{13}$	$1.1 \pm 1.3 \cdot 10^{-5}$
May '12 - Jun '12	$11 \cdot 10^{18}$	$25 \cdot 10^{18}$	$4 \cdot 10^{13}$	$15 \cdot 10^{13}$	$0.4 \pm 0.4 \cdot 10^{-5}$
Jun '12 - Oct '12			*(data gap)*		
Oct '12 - Jul '13	$8 \cdot 10^{18}$	$20 \cdot 10^{18}$	$12 \cdot 10^{13}$	$40 \cdot 10^{13}$	$1.9 \pm 1.4 \cdot 10^{-5}$
Jul '13 - Oct '13			*(data gap)*		
Oct '13 - Apr '14	$5 \cdot 10^{18}$	$10 \cdot 10^{18}$	$13 \cdot 10^{13}$	$30 \cdot 10^{13}$	$3.0 \pm 1.8 \cdot 10^{-5}$
Apr '14 - Sep '14	$5 \cdot 10^{18}$	$10 \cdot 10^{18}$	$9 \cdot 10^{13}$	$25 \cdot 10^{13}$	$1.9 \pm 1.7 \cdot 10^{-5}$
Sep '14 - Feb '15	$8 \cdot 10^{18}$	$20 \cdot 10^{18}$	$14 \cdot 10^{13}$	$50 \cdot 10^{13}$	$1.9 \pm 1.4 \cdot 10^{-5}$
Based on Alfombrales station					
Feb '15 - Sep '18	$4 \cdot 10^{18}$	$15 \cdot 10^{18}$	$14 \cdot 10^{13}$	$40 \cdot 10^{13}$	$4.2 \pm 2.3 \cdot 10^{-5}$
Based on all stations					
Feb '15 - Sep '18	$3 \cdot 10^{18}$	$15 \cdot 10^{18}$	$11 \cdot 10^{13}$	$40 \cdot 10^{13}$	$4.6 \pm 2.8 \cdot 10^{-5}$

for two peak of up to $10 \cdot 10^{18}\ \frac{\text{molec}}{\text{cm}^2}$ in October 2017 and March 2018, respectively. In contrast, the maximum BrO SCDs remained rather constant at the level of $4 \cdot 10^{14}\ \frac{\text{molec}}{\text{cm}^2}$ from November 2014 to August 2018 (the end of the presented time series).

Statistical pattern in the BrO/SO_2 time series The evolution of the BrO/SO_2 molar ratios shows a decreasing long-term trend from the beginning of the time series in December 2010 until early 2012, no significant long-term trend from early 2012 until early 2015, and an increasing long-term trend from early 2015 until August 2018. This observation of three significantly different time intervals agrees perfectly with the division of the general volcanic activity of Nevado del Ruiz during the recorded time series in (at least) three periods: (1) prior to the phreatomagmatic explosions on June 30 2012, (2) between the phreatomagmatic explosions on June 30 2012 and enhanced general volcanic activity starting on November 1 2014, and (3) since November 1 2014. Such a clear distinction of the turning points is not obvious in the BrO/SO_2 time series.

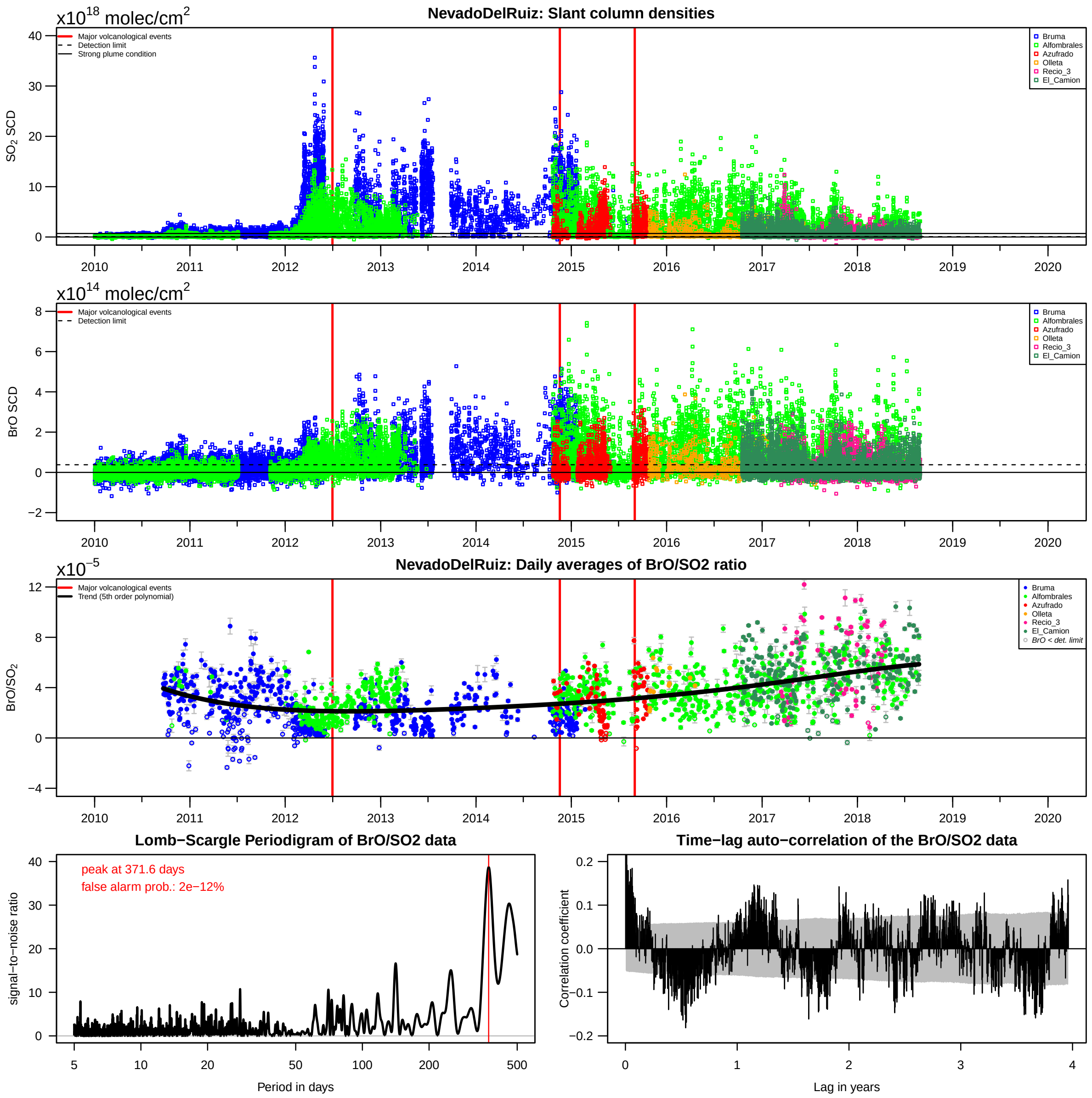

Figure 5.4: Three upper panels: Time series of the slant column densities of SO_2 and BrO and calculated BrO/SO_2 molar ratios in the gas plume emitted from Nevado del Ruiz (tick marks indicate first day of the particular year). The NOVAC stations are indicated by the different colours. BrO data below the detection limit of two standard deviations are highlighted by open circles. BrO/SO_2 molar ratios: the trend is calculated by a running mean over 45 days. **Lowest panels:** Lomb–Scargle frequency component analysis and time-lag auto-correlation coefficients (the grey area gives the 90 % confidence levels) of the BrO/SO_2 molar ratio variations.

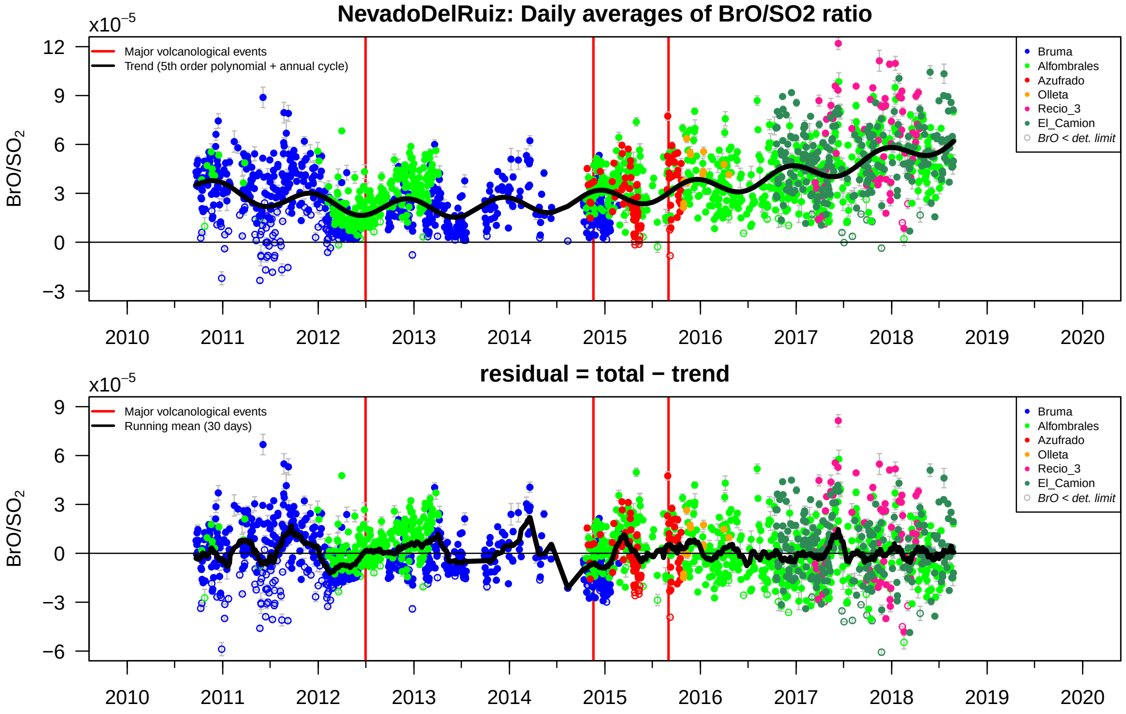

Figure 5.5: Pattern in the BrO/SO_2 time series of Nevado del Ruiz. **Upper panel:** Original BrO/SO_2 data and the best matching fit model with a polynomial term of 5th order plus an annual periodicity (black line). **Lower panel:** Residual time series after the subtraction of the best matching fit from the original data. The running mean of the residual data is given given by the black line.

A division of the BrO/SO_2 time series in these three sharp time intervals separated at June 30 2012 and November 1 2014 indicates linear annual trends in the BrO/SO_2 molar ratios of $(-1.38 \pm 0.16) \cdot 10^{-5}$ in the first period, of $(-0.10 \pm 0.13) \cdot 10^{-5}$ in the second period, and of $(0.87 \pm 0.05) \cdot 10^{-5}$ in the third period. Instead of considering these three linear trends separately, in the following statistical analyses the long-term trend is modelled as a polynomial of 5th order which matches the data more smoothly (see the third panel in Figure 5.4).

Superimposed on this long-term trend, the BrO/SO_2 time series hosts a set of dips which appear to be periodic. A Lomb–Scargle analysis indicates with extremely high confidence a sinusoidal signal with a periodicity between $350 - 400$ days, with maximum likelihood for a period of 371.6 days (false alarm probability of $3 \cdot 10^{-14}$). This is most likely a detection of a strictly annual periodicity with a period of 365.25 days. Furthermore, a Lomb–Scargle analysis indicates an (additional) periodicity of 460 days. In contrast, the time-lag auto-correlation analysis indicates a periodicity of 420 days.

Based on the empirical findings of the Lomb–Scargle analysis and also because it appears to be plausible, the model of the long-term trend has been extended for the subsequent analysis to a polynomial of 5th order plus a sinusoidal annual cycle. A

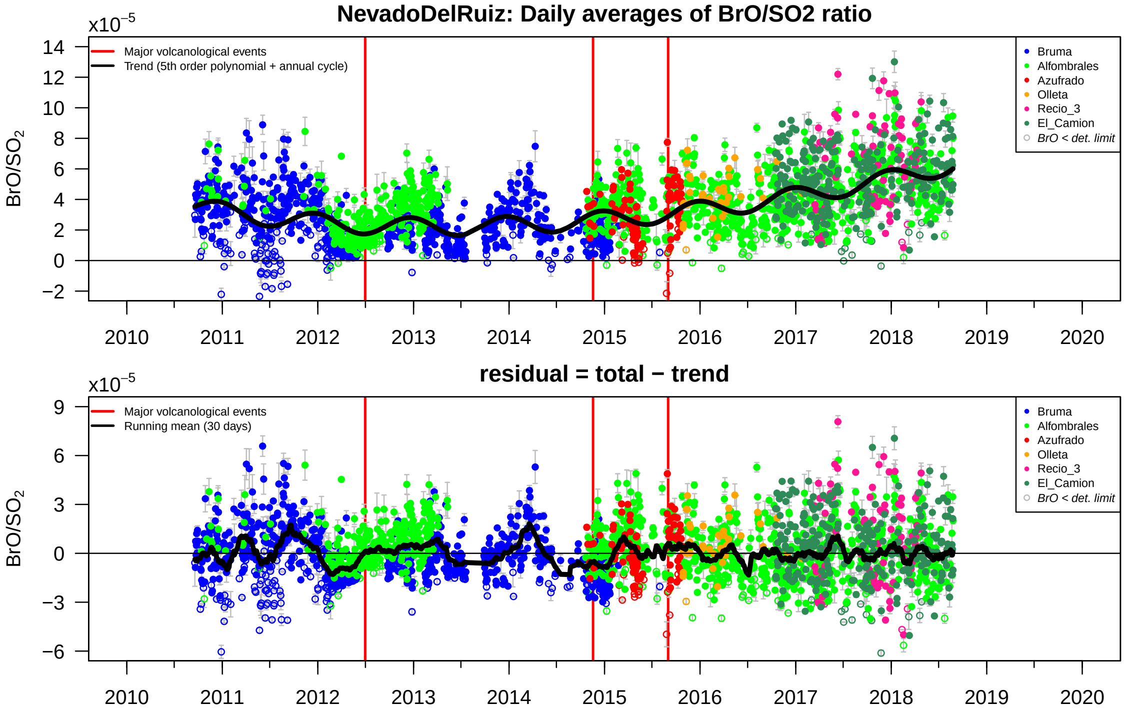

Figure 5.6: Like Figure 5.5, but including also days when only two data points are available. Besides the increase in noise, this affects in particular time intervals where data is scarce, such as the time period from July to November 2014.

subtraction of this long-term trend from the original data reveals residual patterns in the BrO/SO$_2$ time series (Figure 5.5). The residual time series shows several significant peaks and drops in the BrO/SO$_2$ molar ratios. Most prominently is an apparently semi-annual modulation at the beginning of residual time series (from late 2010 to late 2011) and three phases of at least half a year (first half of January–June 2012, May–November 2013, June 2014 to February 2015) with persistently low BrO/SO$_2$ molar ratios w.r.t. the long-term trend. The evidence for the last pattern is increased when including also days with only 2 multi-scan data points to the analysis (Figure 5.6). The semi-annual modulation is caused by a significant number of negative BrO/SO$_2$ molar ratios from June to September 2011 (already in the total time series). Without this period, the polynomial long-term trend would have smoothed the first 1.5 years of the residual time series, i.e. the semi-annual pattern would be insignificant. It remains the question on the origin of these negative BrO/SO$_2$ molar ratios. One possible interpretation is given by a background contamination with BrO as will be discussed in Section 5.3.

Two of the three periods of persistently low BrO/SO$_2$ molar ratios coincided with the two major volcanological event of the discussed time span: the first phase can been interpreted as a precursor of the phreatomagmatic explosion on June 30 2012 and the third phase can been interpreted as a precursor (and this time also coinciding pattern) of the period of enhanced volcanic activity in November 2014. No general

Table 5.3: Observed pattern in the BrO/SO_2 time series of Nevado del Ruiz.

General statistics of total time series	
Total standard deviation (of daily means)	$2.01 \cdot 10^{-5}$
Mean diurnal standard deviation	$1.72 \cdot 10^{-5}$
Mean measurement error (of daily means)	$0.35 \cdot 10^{-5}$
Observed long-term pattern	
Linear trend until Jul 12	$(-1.38 \pm 0.16) \cdot 10^{-5}$ year^{-1}
Linear trend from Jul 12 to Nov 14	$(-0.10 \pm 0.13) \cdot 10^{-5}$ year^{-1}
Linear trend from Nov 14 to Sep 18	$(0.87 \pm 0.05) \cdot 10^{-5}$ year^{-1}
Amplitude of annual component	$(0.57 \pm 0.06) \cdot 10^{-5}$
Phase shift of annual component	maximum on December 17
General statistics of the residual time series	
Standard deviation of (total - trend)	$1.66 \cdot 10^{-5}$
Standard deviation of (total - trend - annual)	$1.61 \cdot 10^{-5}$
Significant residual patterns	
Mean relative drop Feb 12 - May 12	$-0.95 \cdot 10^{-5}$
Mean relative drop May 13 - Dec 13	$-0.42 \cdot 10^{-5}$
Mean relative drop Apr 14 - Jan 15	$-0.76 \cdot 10^{-5}$

volcanological cause has been yet found for the second phase. Furthermore, the mean dates of these three phases of reduced BrO/SO_2 molar ratios are spaced approximately equidistantly by about 440-460 days (a spacing which is also shared by the phase of relatively low BrO/SO_2 molar ratios in late 2010). In consequence, these 3 or 4 phases could be the origin for the indicated periodicity with a period of 460 days. In fact, this periodicity is not proposed when the statistical analyses are restricted to the time interval from $2015 - 2018$. This raises the question whether the equidistant spacing of these 3 or 4 phases happened just by chance or whether it is a manifestation of an eigenfrequency of the current shallow system of Nevado del Ruiz, at least until early 2015. Remarkably, when restricted to the time interval from $2015 - 2018$ also the auto-correlation analysis propose an annual periodicity. The indicated 420 days periodicity may thus be an interference of an annual and an 460 days periodicity.

5.3 Origin of the observed long-term BrO/SO_2 pattern

This section lists and compares five possible origins of the observed patterns, namely (1) instrument drifts, (2) variation of the meteorology and the atmospheric chemistry altering the BrO conversion rate, (3) the melting glacier, (4) response of the hydrothermal system, (5) magmatic/geological processes.

Possible origin (1): instrumental drifts

The NOVAC instruments are not temperature-controlled. Variations in the ambient temperature may thus cause variations in the accuracy and precision of the spectroscopic results. The ambient temperature variations can in particular influence the wavelength to pixel mapping (WMP) and the instrument line function (ILF). The time series at Nevado del Ruiz is dominated by the instrument D2J2200_0 which operated from December 2009 to July 2013 at Bruma station and since November 2014 at Alfombrales station. The general discussion on the variability of the ILF of this instrument D2J2200_0 has already been discussed in detail in Section 4.4.

Wavelength-to-pixel mapping The general discussion did not observe long-term pattern in the WPM. A comparison of the BrO/SO_2 molar ratios with the variations of the WPM (based on the individual pixels) nevertheless indicates a weak correlation with correlation coefficients of up to −32 % (Figure 5.7). The correlation is relatively strong for the pixels 300 and 650 which are associated with wavelengths of about 304 nm and 332 nm but there is no correlation for pixel 1000 which is associated to 358 nm. Accordingly, the two pixels which are embracing the SO_2 DOAS fit range are affected while this is not clear for the two pixels which embrace the BrO DOAS fit range. Thus, the correlation with the BrO/SO_2 molar ratios may be caused by an inaccurate SO_2 DOAS fit rather than an inaccurate BrO DOAS fit.

Instrument line function Applied on the total time series, no significant correlation (i.e. with a coefficient above ±20 %) has been observed between the BrO/SO_2 molar ratios and any of the Levenberg–Marquardt parameters. Applied in the subset of only large SO_2 and BrO SCDs ($S_{SO_2} \geq 1 \cdot 10^{18}\,\frac{\mathrm{molec}}{\mathrm{cm}^2}$ and $S_{BrO} \geq 1 \cdot 10^{14}\,\frac{\mathrm{molec}}{\mathrm{cm}^2}$), weak correlations have been found between the BrO/SO_2 molar ratios and the SO_2 shift parameter (coefficient of −26 %), the SO_2 squeeze parameter (22 %), and the BrO shift parameter (27 %), but not for the BrO squeeze parameter (−3 %). The QDOAS approach indicated a maximum variation in the ILF shape parameters which corresponds to possible underestimations of the BrO/SO_2 molar ratios of at most +5 %. Further, neither a seasonal pattern nor a monotonous long-term trend has been observed for the ILF of

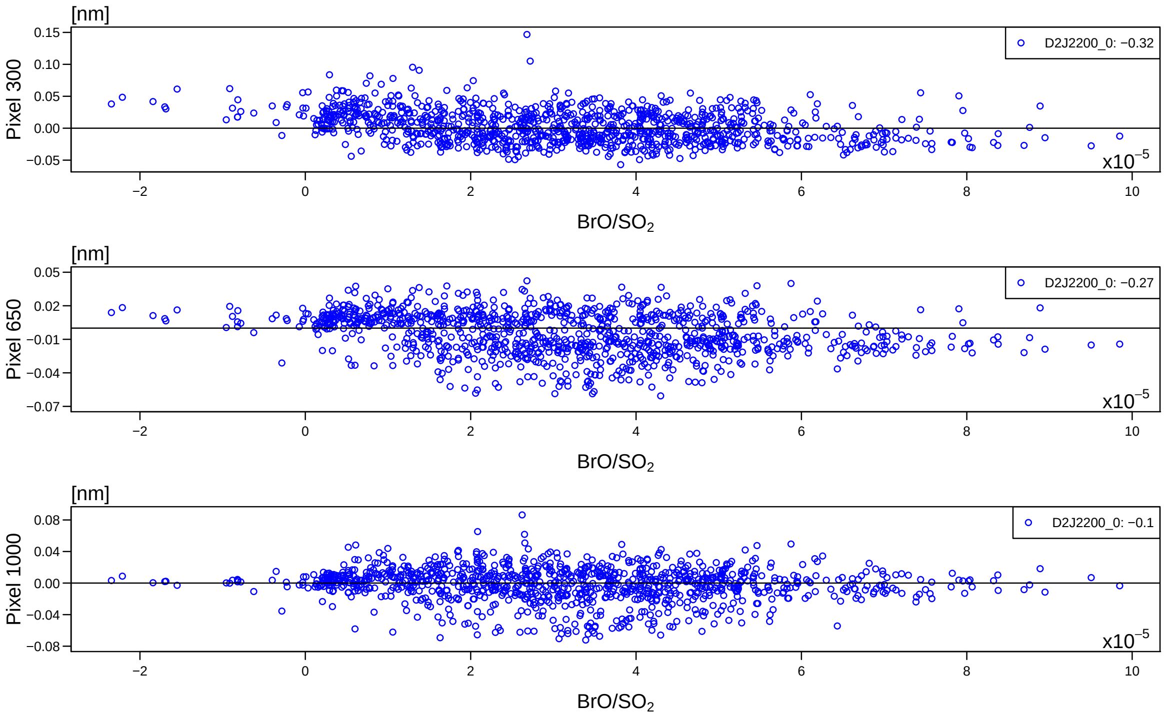

Figure 5.7: Correlation plots of the WPM variations versus the BrO/SO$_2$ molar ratios. The correlation coefficients are given in the legends.

D2J2200_0. These findings indicate that the periodic pattern and long-term trend in the BrO/SO$_2$ molar ratios are not caused by possible variation in the ILF.

Possible origin (2): meteorology and atmospheric chemistry

Estimation of the observed plume age The wind conditions control the time (in the following called "plume age") which passes until the volcanic gas plume is detected by a NOVAC instrument. The wind direction determines which particular NOVAC station observes the plume and furthermore also alters the covered distance between the volcanic vent and the point where the plume transacts the scan plane of the particular NOVAC station. This distance multiplied with the wind speed gives the plume age. In good approximation the plume age T_{plume} is given by

$$T_{plume} = \frac{D}{v_{wind}} \cdot \frac{1}{\cos(\omega - \sigma) - \sin(\omega - \sigma) \cdot \tan(\sigma - \beta)} \tag{5.1}$$

with the wind speed v_{wind}, the wind direction ω, the angular position σ of the instrument w.r.t. the volcanic vent, and the scan plane orientation β (see Table 5.1 and Figure 5.8). This estimate holds for scan geometries with a flat scan plane but overestimates the plume age for conical scan planes. The predominant Bruma station has a flat scan plane and for the sake of simplicity the plume ages are calculated for all instruments assuming a flat scan plane in the following.

Variations of the wind conditions and the observed plume age Volcanic SO_2 has an atmospheric lifetime of at least 1 day and is thus effectively conserved within the first hours after its release. The partial conversion of HBr to BrO is assumed to reach the chemical equilibrium $2 - 10$ min after the release to the atmosphere (Chapter 2). Accordingly, the wind conditions can alter the observed BrO SCDs and the derived BrO/SO_2 molar ratios. The direct distance to the volcanic vent is 1.9 km for the nearby Bruma station and at least 3.8 km for the other NOVAC stations. The typical wind speeds of $2 - 12\,\frac{\mathrm{m}}{\mathrm{s}}$ thus imply mean plume ages of $3 - 16$ min when detected by Bruma station and of at least $6 - 33$ min for the other stations. A comparison of the retrieved BrO/SO_2 molar ratios and the approximated plume ages indicate that the chemical equilibrium is reached at Nevado del Ruiz in average after 9 min (Figure 5.9a). A linear model $BrO(t \leq 9\,\mathrm{min}) = BrO_{equil} \cdot \alpha \cdot t$ proposes a BrO genesis rate of $\alpha = 0.11\,\mathrm{min}^{-1}$ of the equilibrium level per minute within the first 9 min. An exponential model $BrO(t) = BrO_{equil} \cdot (1 - e^{-\alpha \cdot (t - t_0)})$ proposes a reaction rate parameter $\alpha = 0.2 - 0.4\,\mathrm{min}^{-1}$ and a delay parameter $t_0 = 2.3 - 3.1$ min. The range of parameter estimates reflects the model output when applied on different subsets of the time interval or instruments (Table 5.4). A part of the scatter in this multi-year comparison can be explained by the increasing trend in the BrO/SO_2 molar ratios (Figure 5.9b). The extraordinary drop in mid of 2013 coincides almost exclusively with young plume ages. In contrast, all plume ages contribute to the extraordinary drops in 2012 and 2014. Furthermore, negative BrO/SO_2 molar ratios coincide exclusively with young plume ages (Figure 5.9a+c). This observation may ultimately give a physical interpretation for

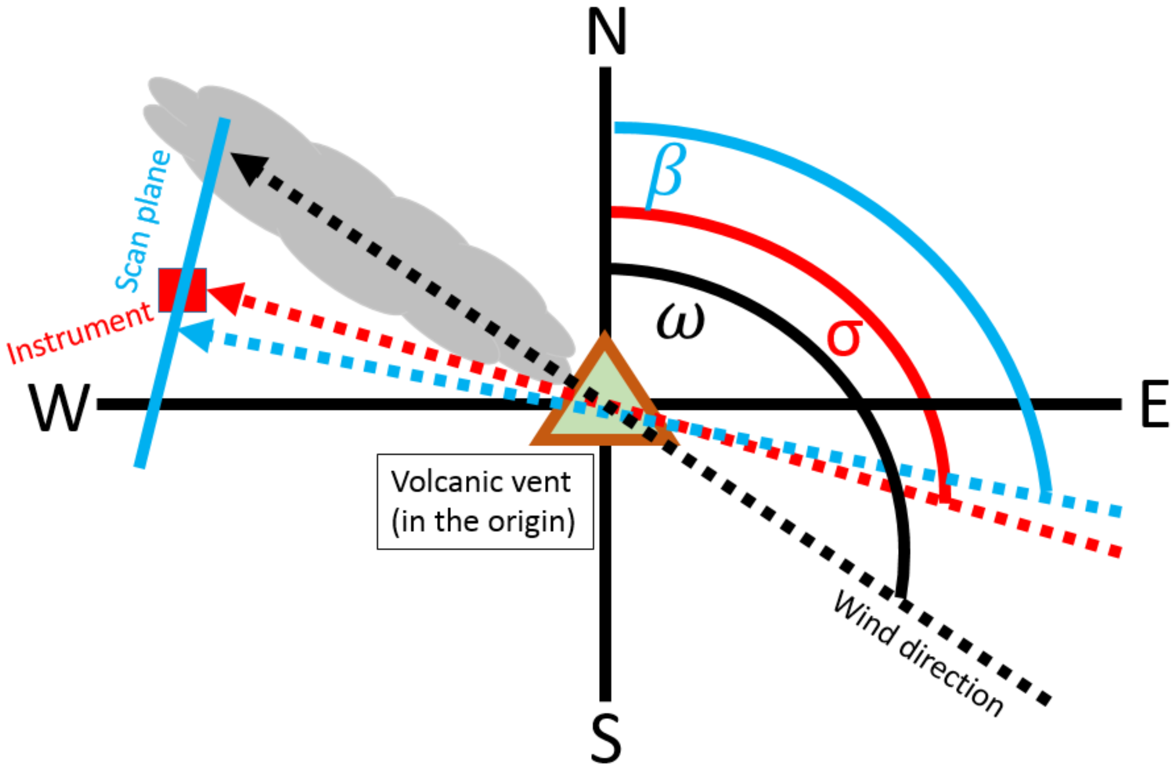

Figure 5.8: Sketch of the geometric conditions which are used to estimate the plume age of the observed volcanic gas plume.

the negative BrO SCDs (instead of regarding them as extreme outlier/artefacts of the DOAS fit): a BrO contamination of the reference region. [Lübcke et al., 2016] reported that the reference region of the Bruma station is relatively often contaminated with SO_2. Such a contamination may be accompanied by a contamination with BrO. If the young plume does not yet contain BrO, the NOVAC retrieval would find negative BrO in the plume region when compared with a contaminated reference region. An argument against this hypothesis is that Lübcke et al. [2016] reported contamination occurring predominantly for low wind speeds while the negative BrO SCDs coincided with high wind speeds. A detailed analysis of this contradiction is yet to be conducted.

Consequences of a correction of the plume age effects The quantitative impact of the plume age effect on the BrO/SO_2 time series is examined by a proposed correction of this effect. To keep the correction simple, a linear model is applied: Data with a $T_{plume} \geq 9\,\text{min}$ remains unaltered. Data with $T_{plume} < 9\,\text{min}$ are elevated either by

$$\mathrm{BrO/SO_2}^{corr} = \frac{\mathrm{BrO/SO_2}^{meas}}{1 - 0.11 \cdot (9\,\text{min} - T_{plume}[\text{min}])} \tag{5.2}$$

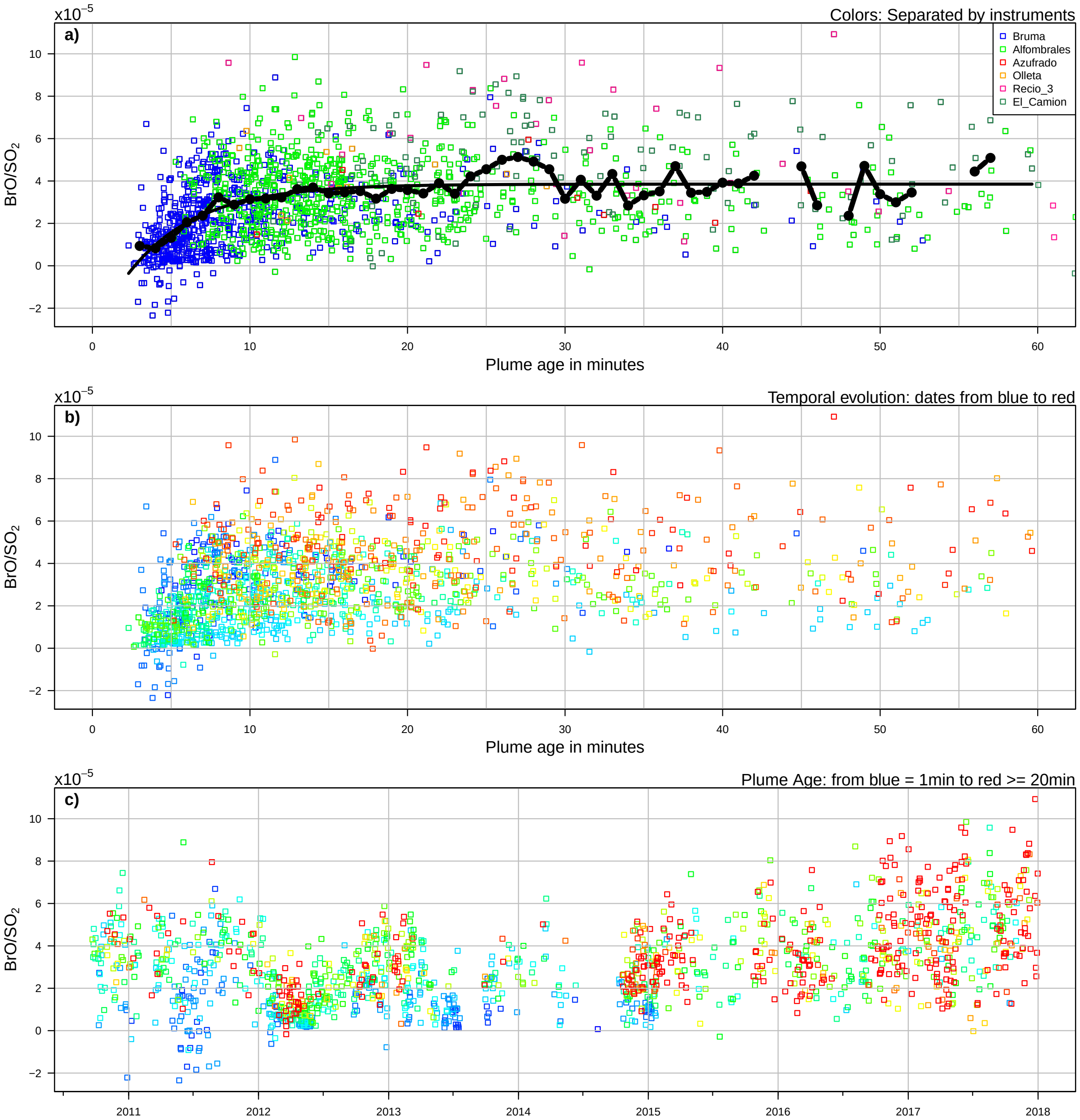

Figure 5.9: BrO/SO$_2$ molar ratios in the volcanic gas plume as function of the plume age. **a)** Comparison divided in subsets from the different stations (colour coded). Mean values of 1-mins (black dots) and best matching model $BrO(t) = BrO_{equil} \cdot (1 - e^{-\alpha\cdot(t-t_0)})$ (black line, 1-min bins and model calculated for the total data set). **b)** Same comparison but the colour code now indicates the absolute date. **c)** BrO/SO$_2$ time series with the plume age colour coded.

Table 5.4: Nevado del Ruiz: empirical BrO genesis rates for different subsets of the data. Applied model: $BrO(t) = BrO_{equil} \cdot (1 - e^{-\alpha \cdot (t - t_0)})$

BrO genesis (total time series)	
Mean equilibrium level BrO_{equil}	$(3.9 \pm 0.1) \cdot 10^{-5}$
Lifetime parameter α	$(0.23 \pm 0.03)\,\text{min}^{-1}$
Delay parameter t_0	$(2.7 \pm 0.3)\,\text{min}$
BrO genesis (until June 30 2012 only)	
Mean equilibrium level BrO_{equil}	$(2.8 \pm 0.1) \cdot 10^{-5}$
Lifetime parameter α	$(0.40 \pm 0.10)\,\text{min}^{-1}$
Delay parameter t_0	$(3.0 \pm 0.4)\,\text{min}$
BrO genesis (Bruma station only)	
Mean equilibrium level BrO_{equil}	$(3.1 \pm 0.1) \cdot 10^{-5}$
Lifetime parameter α	$(0.31 \pm 0.05)\,\text{min}^{-1}$
Delay parameter t_0	$(2.8 \pm 0.3)\,\text{min}$
BrO genesis (Bruma station until June 30 2012 only)	
Mean equilibrium level BrO_{equil}	$(3.5 \pm 0.2) \cdot 10^{-5}$
Lifetime parameter α	$(0.30 \pm 0.07)\,\text{min}^{-1}$
Delay parameter t_0	$(3.1 \pm 0.4)\,\text{min}$
BrO genesis (Bruma station only and BrO > 0)	
Mean equilibrium level BrO_{equil}	$(3.0 \pm 0.1) \cdot 10^{-5}$
Lifetime parameter α	$(0.30 \pm 0.06)\,\text{min}^{-1}$
Delay parameter t_0	$(2.3 \pm 0.4)\,\text{min}$

if the measured data has been positive or by

$$\text{BrO}/\text{SO}_2{}^{corr} = \text{BrO}/\text{SO}_2{}^{meas} + 0.4 \cdot 10^{-5} \cdot (9\,\text{min} - T_{plume}[\text{min}]) \tag{5.3}$$

if the measured data has been negative. The two major discrepancies between the such corrected data and the original data are (compare the Tables 5.3, 5.5 and the Figures 5.6, 5.10): (1) The negative linear trend in the BrO/SO_2 molar ratios in the first period has increased from $(-1.38) \cdot 10^{-5}$ year^{-1} to $(-1.68) \cdot 10^{-5}$ year^{-1}. (2) The second period of persistently low BrO/SO_2 molar ratios (May–December 2013) has disappeared. Remarkably, the amplitude of the annual cyclicity has hardly decreased (from $0.57 \cdot 10^{-5}$ to $0.51 \cdot 10^{-5}$) but the phase shift has changed such that the annual cycle is now maximum on November 30 instead of December 17. Accordingly, the annual periodicity is apparently not caused by variations of the wind conditions.

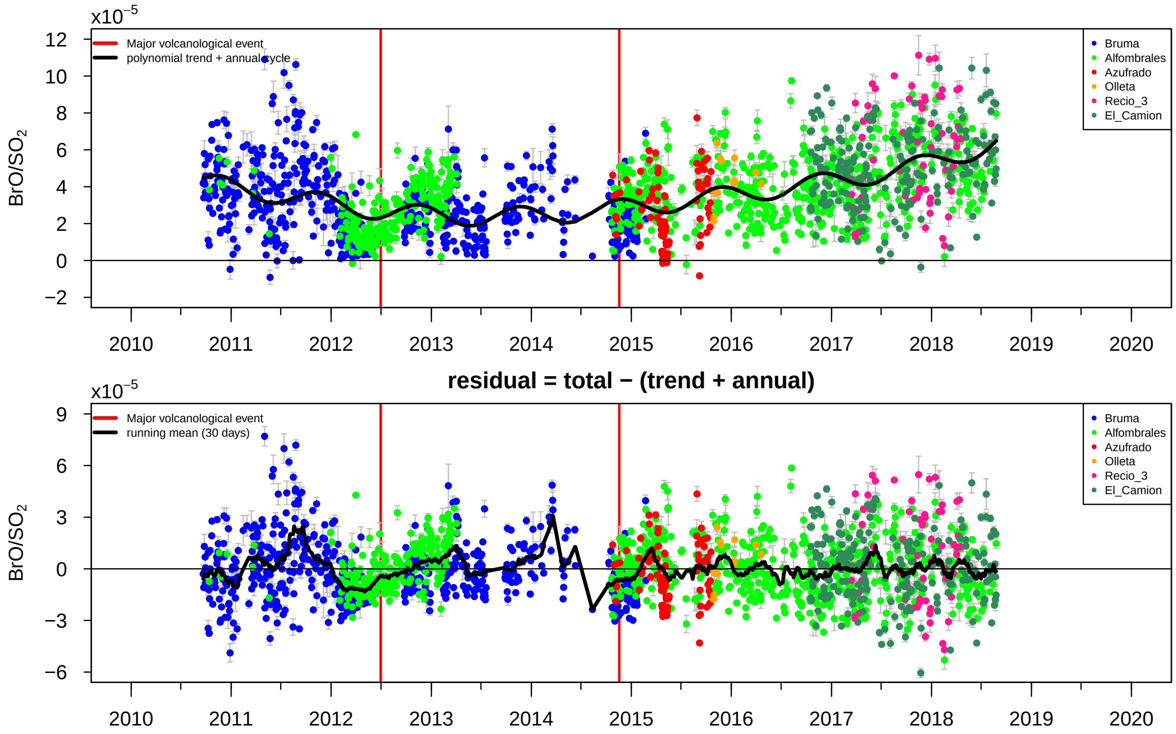

Figure 5.10: Like Figure 5.5 but with the proposed correction for young gas plumes applied. More negative linear trend until July 2012, but the amplitude of the annual cycle hardly decreased (see Table 5.5).

Table 5.5: Like Table 5.3 but for data which has been corrected for plume age effects.

General statistics of total time series	
Total standard deviation (of daily means)	$2.02 \cdot 10^{-5}$
Observed long-term pattern	
Linear trend until Jul 12	$(-1.68 \pm 0.12) \cdot 10^{-5}$ year^{-1}
Linear trend from Jul 12 to Nov 14	$(0.16 \pm 0.13) \cdot 10^{-5}$ year^{-1}
Linear trend from Jul 12 to Nov 14	$(0.84 \pm 0.05) \cdot 10^{-5}$ year^{-1}
Amplitude of annual component	$0.51 \cdot 10^{-5}$
Phase shift of annual component	maximum on November 30
General statistics of the residual time series	
Standard deviation of (total - trend)	$1.75 \cdot 10^{-5}$
Standard deviation of (total - trend - annual)	$1.72 \cdot 10^{-5}$

Variations of atmospheric pressure, temperature, humidity The variations of the atmospheric pressure by ± 1 mbar and of the temperature by ± 2 K are arguably too small to have a significant influence on the bromine chemistry in the volcanic plume. It should be nevertheless noted that the atmospheric pressure is the only presented ECMWF parameter whose annual cycle matches the annual cycle in the BrO/SO$_2$ molar ratios without a significant phase shift (with minimum pressure correlating with maximum BrO/SO$_2$ molar ratios). The specific and relative humidity (and also the rain fall rates) are both minimum in January/February and thus there is a phase shift of $1-3$ months between the annual cycles of the humidity and of the BrO/SO$_2$ molar ratios. Accordingly, no correlation could be found between these parameters. Furthermore, also a time-lag analysis of the correlation of the BrO/SO$_2$ molar ratios (where the polynomial long-term trend has been subtracted beforehand) and the relative humidity does not find a correlation coefficient above ± 0.1. Nevertheless, the rain fall pattern (not presented here) moderately correlate with the BrO/SO$_2$ molar ratios, see the discussion on the hydrothermal system in the next but one section.

Variations in the tropospheric ozone background Nevado del Ruiz is all of the year south of or within the ITCZ. In consequence, Nevado del Ruiz could be considered as a part of the climatological southern hemisphere although it is actually located on the geographically northern hemisphere. The seasonal cycles of the BrO/SO$_2$ time series and the tropospheric ozone background are in phase. The sign of this correlate is positive if Nevado del Ruiz is considered in the climatological southern hemisphere but negative if Nevado del Ruiz is considered in the climatological northern hemisphere. This question cannot yet be answered as no available tropospheric ozone data has been reported for Nevado del Ruiz. In contrast, the total ozone column around Nevado del Ruiz has an annual cycle with maxima of 274 Dobson units in August/September and minima of 243 Dobson units in December/January [IDEAM2, 2018].

Radiative transport effects and the cloud cover Variation of the radiative transport in the atmosphere could be another meteorological impact on the spectroscopic results. Such variations can be caused, e.g., by a variation of the cloud cover, of the cloud brightness, and of the aerosol load in the atmosphere. The cloud cover indeed shows an annual cyclicity (possibly with a semi-annual modulation), however, with a phase shift of $1-3$ month relative to the BrO/SO$_2$ molar ratios. Furthermore, while variations in the radiative transport can significantly affect the observed SCDs, such effects are expected to have only a weak impact on the BrO/SO$_2$ molar ratios because applying the ratio cancels most of the radiative transport effects on the individual SO$_2$ and BrO SCDs [Lübcke et al., 2014].

Possible origin (3): the melting glacier

All Columbian glaciers are continuously melting for decades due to the global warming (Figure 5.11). At Nevado del Ruiz, the melting is presumably further accelerated due to the additional heating by the underlying magmatic system. From $1960-1985$, the glacier on Nevado del Ruiz shrunk by $0.1\,\mathrm{km}^2$ of its extension per year to an extension of $21\,\mathrm{km}^2$ in 1985, before it lost $3\,\mathrm{km}^2$ at once during the eruption in 1985. Subsequently from $1985-2002$, the glacier shrunk with an accelerated rate of $0.3\,\mathrm{km}^2$ per year to an extension of $10.3\,\mathrm{km}^2$. From $2002-2010$, the glacier shrunk with a reduced rate of $0.1\,\mathrm{km}^2$ per year to an extension of $9.5\,\mathrm{km}^2$ in 2010. From $2010-2014$, the glacier shrunk with an accelerated rate of $0.5\,\mathrm{km}^2$ per year to an extension of about $7.5\,\mathrm{km}^2$ in 2014 [Ceballos et al., 2006, Huggel et al., 2007, Thouret et al., 2007, Monterroso-Tobar et al., 2018]. The turning point to an accelerated melting rate is in good agreement with the new phase of volcanic activity which started in 2010.
In 1999, the glacier had an average thickness of 47 m and an ice density (uppermost 3 m) of $680\,\mathrm{kg\,m^{-3}}$ [Ceballos et al., 2006]. Assuming that the mass loss is proportional to the loss in glacier extension (and assuming a constant ice density), the glacier lost from $2010-2014$ a mass of $\Delta m = 16\,\mathrm{Mt}$ per year. This appears to be a conservative estimate because a simultaneous reduction of the average ice thickness would cause an even larger mass loss rate. There are at least three plausible mechanisms how a variation of the glacier extend may influence the volcanic degassing signal:

1. The melt water is presumably an important inflow of water into the hydrothermal system. Possible consequences of melt water flow variations are discussed in the subsequent section on the "hydrothermal system as possible origin".

2. The mass loss implies a reduction in hydrostatic pressure on the volcanic edifice and may thus cause a reduction of the pressure in the shallow magma chamber. The relationship between a decreasing extended hydrostatic load and the stress fields in the volcanic conduit can be rather complex. Assuming for a first estimate that the pressure reduction is constant everywhere below the glacier area A (of that year), the annual decrease in the hydrostatic (magma) pressure is given by $\Delta p \approx \frac{g \cdot \Delta m}{A} \approx 14\,\mathrm{kPa}$. In comparison, the magma pressure is in the order of tens of Megapascals in the shallow system. Accordingly, the melting glacier may cause a pressure variation in the (sub-)permill range. This speculative decreasing trend in the magma pressure would coincide with a decreasing trend in the $\mathrm{BrO/SO_2}$ molar ratios implying a positive correlation between magma pressure and the $\mathrm{BrO/SO_2}$ molar ratio.

3. The decreasing glacier area may allow for new degassing pathways which have been blocked beforehand. These additional pathways for fumarolic side degassing may allow for a faster decompression rate of the shallow magma chamber. To my knowledge, no fumarolic degassing at formerly glacierised locations has

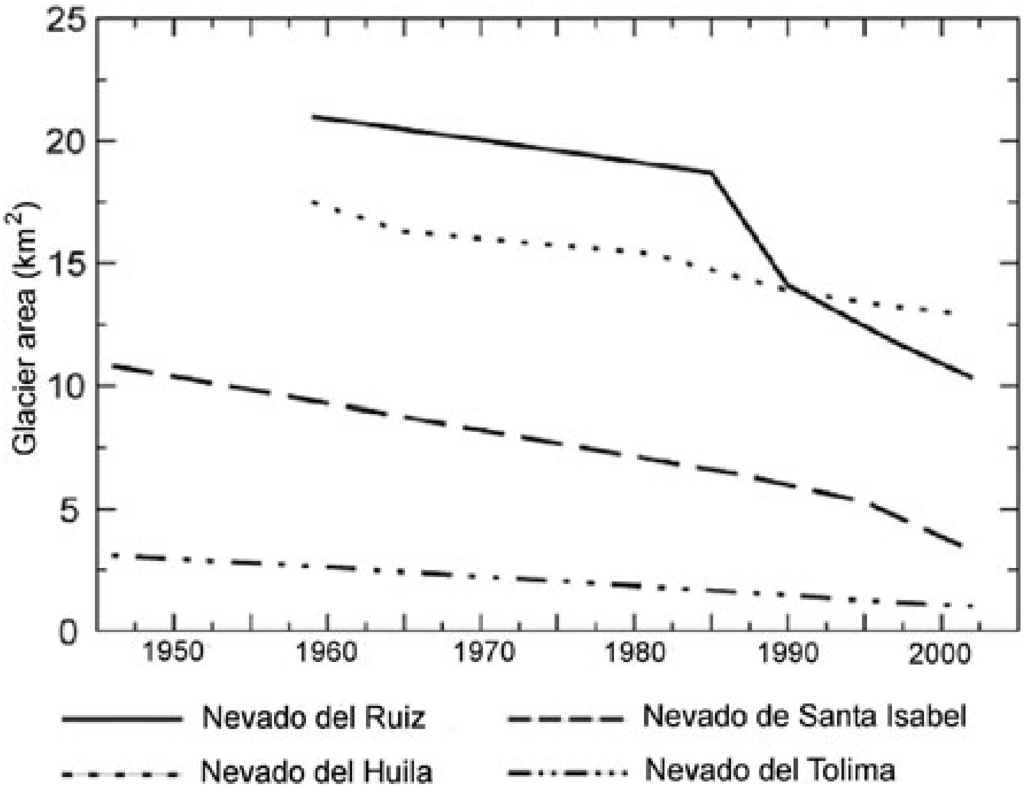

Figure 5.11: Melting of several Colombian glaciers. In 1985, the glacier on Nevado del Ruiz lost 16 % of its area due to the eruption. Since then the glacier is retreating even faster. Figure reprinted from [Huggel et al., 2007] with kind STM permission from CUP.

been reported thus this option can be ruled out as an origin of the observed patterns.

Possible origin (4): hydrothermal system

The hydrothermal system can scrub a part of a crossing flow of volcanic gases and thus reducing the magnitude of volcanic degassing. Furthermore, the scrubbing efficiency is in general different for the volcanic gas species and can thus alter the molar ratios of the crossing volcanic gas flow. Following the common hypothesis that bromine is more hydrophilic than sulphur, the larger a hydrothermal system the more bromine can be scrubbed from a crossing flow of volcanic gases and thus the smaller is the ultimate BrO/SO_2 molar ratio. Following this hypothesis, a net inflow of water in the hydrothermal system should cause a decrease of the BrO/SO_2 molar ratios and a net outflow from the hydrothermal system should cause an increase of the BrO/SO_2 molar ratios. Likewise a balanced water level but a higher exchange rate should decrease the BrO/SO_2 molar ratio as well. The two predominant sources of inflow are presumably melt water from the glacier and the heavy rain falls during the rain seasons.

The rain seasons in Manizales (major town closest to Nevado del Ruiz) spans from April to November and peaking in June with 346 mm and in August with 380 mm [IDEAM, 2018].The precipitation is lowest in January with only 37 mm. In contrast, the BrO/SO_2 molar ratios have been minimum in May and maximum in December (or possibly April/November when the plume age effects are considered). The above stated hypothesis would however let expect maximum BrO/SO_2 in January — when the precipitation is lowest — or even later because the rain water needs some time to infiltrate. The direct comparison would instead rather imply the opposite that strong past precipitation rates cause increased BrO/SO_2 molar ratios after a specific rain water infiltration time. This contradicts the above hypothesis. This contradiction could be solved when assuming an infiltration time of about 10 months. Another solution can be given by the interpretation that the precipitation rates not at all cause an annual variability in the hydrothermal system.

The accelerated glacier retreat rate between $2010 - 2014$ implies particularly strong melt water contributions to the hydrothermal system during this period. These extraordinary contributions may have caused a persistently rising water level during this period. This would imply a negative correlation between the water level an the BrO/SO_2 molar ratios. This would imply that the hydrothermal system at Nevado del Ruiz was more efficient in scrubbing sulphur than bromine from the volcanic gas flow during $2010 - 2014$.

In summary, the rain water pattern and the glacier melting rate both imply that the hydrothermal system could be the origin of the observed patterns if, and only if, it is more in scrubbing sulphur than bromine from the volcanic gas flow. This conditions is however rather unlikely and in consequence the hydrothermal system appears to be ruled out as an origin of the observed patterns.

Possible origin (5): magmatic/geological processes

The three periods of strongly different linear long-term BrO/SO_2 trends match perfectly the three distinct periods of magmatic activity proposed by Vargas et al. [2017]: (1) Influx of magma in the shallow system accompanied by decompression from $2011 - 2012$, (2) no magma influx in $2013 - 2014$, and (3) the evolution of a lava dome since 2015. Accordingly, the decreasing long-term BrO/SO_2 trend until early 2012 coincides with a decreasing trend in the magma pressure, the vanishing long-term BrO/SO_2 trend coincides with a relatively stable magmatic system, and the increasing long-term BrO/SO_2 trend coincides the evolution of the lava dome presumably accompanied by a pressure build-up in the shallow magma chamber. In consequence, the BrO/SO_2 molar ratios are apparently positively correlated with the magma pressure. This implies that bromine exsolves earlier from magma than sulphur, at least for the current conditions at Nevado del Ruiz.

No evidence for a long-term periodicity in the magmatic system or the magma supply rate is reported in the literature. Thus neither the annual pattern nor the hypothetical 440-days periodicity can be explained by a purely magmatic origin. In principle, an annual pattern could be plausibly driven by the response of the overall Earth mantle on the astronomic (radiative or tidal) forcing. The annual modulation of the tidal potential can be however expected to be rather insignificant already w.r.t. other hypothetical tidal effects.

The first (February–May 2012) and the third (April 2014 to January 2015) of the three periods of extraordinarily low BrO/SO_2 molar ratios (w.r.t. the long-term trend) occurred prior to peaks in the overall volcanic activity (while the second period has been identified to be caused by meteorological effects, see above). The first period has been accompanied by an extreme increase in volcanic SO_2 emissions. This could be caused either by an opening of the system or by a rapid ascent of gas-rich magma from greater depth. In both cases the magma pressure would decrease. This further supports the above hypothesis that BrO/SO_2 molar ratios positively correlated with the magma pressure. For the third period things are more ambiguous. Similarly to the first period, the low BrO/SO_2 molar ratios coincided with an extreme increase in SO_2 emissions presumably caused by the beginning of a new period of magma ascent. Less clear is however the interpretation of the drop in BrO/SO_2 molar ratios from May to October 2014, though the empirical evidence for this period is relatively weak.

5.4 Conclusions

The NOVAC data recorded at Nevado del Ruiz provides today's longest continuous time series of BrO/SO_2 molar ratios — or any molar ratio — in volcanic gas plumes. It spans at the day of writing over more than 10 years (since 2009 ongoing) and provides a daily mean in average all 0.6 days (after massive data filtering!). The long time span, the relatively good temporal resolution, and the strong and varying degassing behaviour of Nevado del Ruiz marks this time series an optimal data set to test our knowledge and models of volcanic bromine and sulphur degassing.

Observed pattern in the BrO/SO_2 molar ratios The general volcanic activity of Nevado del Ruiz during the recorded time series can be distinguished in (at least) three periods: (1) Prior to the phreatomagmatic explosions on June 30 2012, (2) between the phreatomagmatic explosions on June 30 2012 and enhanced general volcanic activity in November 2014, and (3) since November 2014. The evolution of the BrO/SO_2 molar ratios perfectly matches this division manifested most prominently in different about linear trends in these three periods. The linear annual trend has been $(-1.38 \pm 0.16) \cdot 10^{-5}$ in the first period, $(-0.10 \pm 0.13) \cdot 10^{-5}$ in the second period, and $(0.87 \pm 0.05) \cdot 10^{-5}$ in the third period. These different trends can be understand as manifestations of the different volcanological processes which took place [Vargas et al., 2017]: influx of magma in the shallow system accompanied by decompression from 2011 − 2012, no magma influx in 2013 − 2014, and the evolution of a lava dome since 2015. Besides the linear trends several persistent pattern have been observed in the BrO/SO_2 time series: (1) an annual periodicity with an amplitude of $0.57 \cdot 10^{-5}$, (2) another proposed periodicity with a period of about 440 days, (3) three time intervals of persistently low BrO/SO_2 molar ratios w.r.t. the long-term trend (lower by $0.42 - 0.95 \cdot 10^{-5}$) which lasted for at least half a year (February–May 2012, May–December 2013, and April 2014 to January 2015), (4) a time interval of 3 months with significantly negative BrO (and thus BrO/SO_2 molar ratios) which furthermore caused an apparent about semi-annual modulation in the beginning of the time series. Five possible origins of these patterns and the linear trends have been investigated, namely (1) instrumental drifts, (2) meteorological conditions and atmospheric chemistry, (3) the melting glacier, (4) the hydrothermal system, and (5) magmatic/geological processes.

Investigation of instrumental and meteorological effects No persistent patterns have been found for the instrumental drifts. In particular, the wavelength-to-pixel mapping of the detector stayed remarkably stable even without subsequent calibration. As expected, the instrument line function was subject to temperature-driven diurnal variations. Nevertheless, a first investigation of the time series of these variations did neither indicate an annual cycle nor other long-term trends. Furthermore, the expected

systematic offsets due to the diurnal variations are an order of magnitude smaller then the observed pattern in the BrO/SO_2 molar ratios.
A comparison of the BrO/SO_2 molar ratios with with wind conditions revealed that the HBr $\rightleftharpoons$ BrO conversion reach the equilibrium BrO level at around 9 min after the release of bromine to the atmosphere. This underestimation of the equilibrium BrO level for volcanic plumes younger than 9 min is the origin of the time interval of apparently low BrO/SO_2 molar ratios from May to December 2013. It does however neither alter the annual periodicity nor explain the other two periods of low BrO/SO_2 molar ratios. Furthermore, a plume age correction would imply an even steeper decreasing trend in the BrO/SO_2 molar ratios from late 2010 to July 2012. In addition, it has been observed that negative BrO values occurred exclusively for young plumes, thus possibly caused by a background BrO contamination. The atmospheric temperature, humidity, and cloud cover all show an annual cyclicity but all with a phase shift of $1-3$ months w.r.t. the BrO/SO_2 molar ratios. Only the variations in the atmospheric pressure coincide with the annual cycle in the BrO/SO_2 molar ratios, however the mean annual pressure variations of just ± 1 mbar are not expected to significantly influence the atmospheric chemistry.

Volcanological origin of the patterns The glacier melt water, the rain fall pattern, and the hydrothermal system could in principle cause an annual cycle and long-term trends in the BrO/SO_2 molar ratios. However, the direct comparison of the data would imply that the hydrothermal system scrubs sulphur from a crossing volcanic gas flow more efficiently than bromine. This contradicts the common assumption that bromine is more hydrophilic than sulphur. In consequence the hydrothermal system is expected to not cause the annual variations or long-term trends in the BrO/SO_2 molar ratios.
After having ruled out other origins for most of the observed pattern, the links of the BrO/SO_2 molar ratios to magmatic/geological processes have been investigated. As stated above, the linear long-term trend perfectly match the general volcanological periods of activity, implying a positive correlation between BrO/SO_2 molar ratios and the pressure in the magma. The two remaining periods of persistently low BrO/SO_2 molar ratios (February–May 2012 and April 2014 to January 2015) occurred some months ahead the volcanic crises. These two drops occurred as precursors of two major volcanological activity phases during the presented time period.

Summary The linear long-term BrO/SO_2 trends appear to be predominantly caused by variations in the magma pressure which varies the initial bromine to sulphur molar ratios in the magmatic gas phase. The two extraordinary drops in BrO/SO_2 molar ratios appear to be precursors of major changes in the volcanic activity. A correction for young plumes appears to be mandatory, however, it hardly affects NOVAC stations which are at a distance of at least 4 km w.r.t. the volcanic vent. The origin of the annual periodicity has not been found, though time series of many investigated parameters exhibited annual periodicities but also phase shifts relative to the periodic pattern in the BrO/SO_2 time series.

6 Cotopaxi

The content of this chapter has been published in [Dinger et al., 2018, submitted in August 2017]. This chapter is in large parts a literal reproduction of this publication in order to keep the high level of readability obtained by the peer-review process. This decision is further manifested in the text by keeping the "we"-narrator. This chapter nevertheless presents an updated version with respect to some editorial corrections and a formal harmonisation with this thesis but in particular also with respect to the latest version of the NOVAC retrieval and handling of the ECMWF data. The numerical SO_2 and BrO results have slightly changed but the major findings remained. In particular, the about two weekly signal in the BrO/SO_2 time series is still observed. The proposed value of maximum likelihood has slightly shifted from a periodicity of 13.7 days to 14.2 days accompanied by a slight enhancement of the false alarm probability from 0.9 % to 0.3 %. Both values are statistically in a good agreement. In contrast, the formerly reported weak correlation between the BrO/SO_2 molar ratios and the relative humidity is not further observed.

6.1 Volcanology and meteorology

Volcanology Cotopaxi (0.7°S, 78.4°W, 5897 m a.s.l.) is a glacier-capped stratovolcano located in the Ecuadorian inter-Andean valley, a N-S to NNE-SSW trending topographical depression. Volcanism in this area is caused by the oblique subduction of the Nazca plate beneath the South American plate, which experiences intense large-scale deformation leading to shortening of the lithosphere along the Andean orogeny [e.g., Trenkamp et al., 2002, Alvarado et al., 2016]. The volcano lies on a fault transfer zone [e.g., Gibbs, 1990] in which E-W striking normal faults and NNE-SSW-striking vertical, right-lateral oblique strike-slip faults accommodate the differential crustal shortening rates encountered North and South of Cotopaxi [Fiorini and Tibaldi, 2012]. Fiorini and Tibaldi [2012] thus proposed that the fault planes and restraining bends of this transfer zone act as the main magma pathways feeding the volcano. Observations of ground deformation and hypocenter distributions of volcanic earthquakes made in 2001/2002 [Hickey et al., 2015] and 2015 [Morales Rivera et al., 2017] suggest that Cotopaxi currently has a shallow magma reservoir beneath the southwestern flank, which is located at a depth of approximately $5 - 12$ km below the summit. Within the last 0.5 Ma, a rhyolitic and andesitic bimodal magmatism has occurred at Cotopaxi [Hall and Mothes, 2008]. The Smithonian Institution (http://volcano.si.edu/) lists 55 eruptions at Cotopaxi within the last 300 years, with the last confirmed eruption in 1940 (VEI 2) or, an unconfirmed eruption in 1942 (VEI 3), and the last major (VEI 4) eruption in 1877. The major hazard of an eruption from Cotopaxi consists in the generation of lahars as a consequence of melting the snow and ice of the summit glacier [Barberi et al., 1995]. During the 1877 eruption the glacier of Cotopaxi has completely been molten by the expelled pyroclastic flows, producing devastating lahars which traveled down the flanks of the volcano and destroyed e.g. the town of Latacunga located about 30 km South of the volcano [Aguilera et al., 2004]. Later activity of Cotopaxi did not involve melting of the glacier, which thus recovered since then.

Cotopaxi's recent unrest and eruption Around early April 2015 the seismic event rate started to increase and that marked the beginning of a new period of unrest. From mid May 2015 on, also the observed volcanic degassing of SO_2 and BrO increased to significant levels above the detection limit. On August 14 2015 several phreatomagmatic explosions opened the conduit resulting in continuous ash emissions and large gas emissions. The period of unrest and eruptions was monitored by the broad network of different sensors maintained by the local observatory IGEPN in Quito which published the accumulated data as well as interpretations in scientific papers. Those publications discussed the comparison of the temporal variations of magnitude [Bernard et al., 2016] and composition [Gaunt et al., 2016] of ash emissions as well as ground deformation [Morales Rivera et al., 2017] with seismic signals, SO_2 emission fluxes, and general visual observations. Morales Rivera et al. [2017] reported a maximum uplift of 3.4 cm at the western flank of Cotopaxi from April to August 2015 while they observed no further significant deformation after the eruption in August 2015. The authors explain the deformation by an inclined sheet intrusion located a few km southwest of the summit. Bernard et al. [2016] and Gaunt et al. [2016] agree in the division of the post-explosion dynamics in four phases: August 14 − 15 (phase 1), August 15 to October 2 (phase 2), October 2 to November 4 (phase 3), and November 4 − 11 (phase 4). In phase 1, several phreatomagmatic explosions occurred generating ash clouds reaching altitudes of 9.3 km above the crater and strong gas emissions. During phase 2, continuous but decreasing ash emissions were observed. In the first half of phase 2, the number of seismic long-period events as well as the amplitude of tremor was the highest of the overall period of unrest. In Phase 3, tremor and magnitude of ash emissions increased again and peaked in mid of October. In phase 4, only little ash was emitted and the ash plumes did not exceed 2.5 km above the crater.

Gaunt et al. [2016] suggest an intrusion of juvenile magma in a shallow reservoir (less then 3 km depth) since April 2015 as the reason for the reawakening of Cotopaxi, a suggestion backed by the findings of Morales Rivera et al. [2017]. The juvenile magma may have started to heat an overlying hydrothermal system which may ultimately resulted in dry degassing pathways, an interpretation which fits to the observation of shallow SO_2 degassing from May 2015 on. The phreatomagmatic explosions removed the plug which consisted of old, altered material. After the explosions, the magma ascent slowed down and/or the residence times at shallow levels increased. As the crystallinity increased, the magma stiffened and a new shallow plug was formed. The authors highlighted that the fragmentation mechanisms during phase 2 to 4 are not fully understood. Especially the continuous fine ash grain size distribution throughout all phases suggest that several fragmentations took place. As possible interpretation, the authors suggest a repetitive formation and destruction of shallow plugs.

Meteorological conditions during the Cotopaxi eruption The meteorological conditions at Cotopaxi have been accessed by the ECMWF model (Section 2.4). The presented data are interpolated to an altitude of 6000 m a.s.l., i.e. 100 m above the crater where we roughly expect the volcanic gas plume. For our comparison of gas and meteorological data we chose to focus on the data obtained at 18:00 UTC, i.e. 13:00 local time, which match the observation time of the DOAS measurement the best, especially when we compare with the daily averages of the BrO/SO_2 molar ratios which are centred around noon time.

During the period of unrest, some time series of the meteorological parameters show strong but apparently irregular variations (Figure 6.1). Most prominently, the total cloud, the specific humidity, and the relative humidity were on their half-year minima in mid September 2015. The total cloud cover increased about linearly to its half-year maximum in early November 2015, while the specific and relative humidity exhibited a strong step increase (almost doubling their values) in the second half of September 2015 and remained at these maximum values until late November 2015. Furthermore, the wind speeds have been persistently low at $(4 \pm 2)\ \frac{\mathrm{m}}{\mathrm{s}}$ from mid September 2015 to January 1 2016.

The meteorological times series have been checked for periodicities by a Lomb–Scargle analysis and an auto-correlation analysis applied on the de-trended about noon time series (trend removed from the time series by subtracting the best fit of a polynomial of 5th order but without a further annual cycle component). The analysis has been applied first on the total presented meteorological time series (July 1 2015 to January 1 2016) and then on the limited time interval of the BrO/SO_2 periodicity analysis (September 8 - December 15 2015). When applied to the total time series, the Lomb–Scargle analysis proposes some significant (here considered as signals with a false alarm probability of less than 1 %) periodicities in all meteorological parameters with periods of 11.6 days for the total cloud cover, 48.9 days for the atmospheric pressure, and 38.2 days for the wind speed. In contrast, the auto-correlation analysis does not confirm these or any significant periodicities in the meteorological time series. When applied to the limited time interval, both statistical methods confirm a periodicity of 11.6 days for the total cloud cover. In addition, both methods propose for this time interval a periodicity of 7 days in the air temperature. Furthermore, the Lomb–Scargle analysis proposes periodicities of 10.8 days, 18.2 days, and 45.9 days for

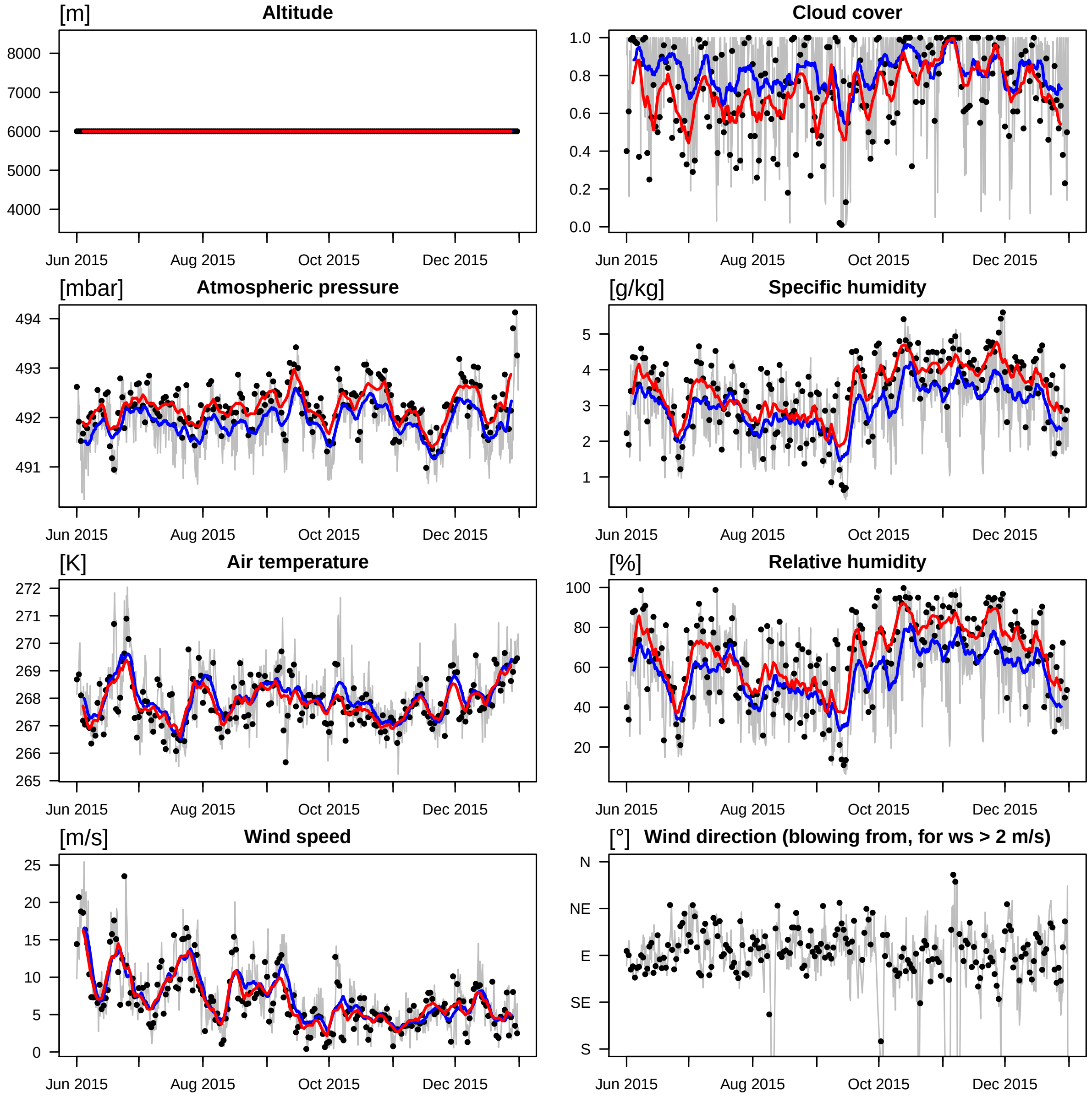

Figure 6.1: Meteorological conditions at Cotopaxi retrieved from ECMWF data with resolutions of 6 h and 0.14° x 0.14° and interpolated to an altitude of 6000 m a.s.l. **Grey lines:** 6-hourly data. **Blue lines:** weekly rolling average of the 6-hourly data (±3 days window). **Black dots:** around noon (18:00 UTC) data. **Red lines:** same rolling average but of the around noon data only.

the atmospheric pressure (though the latter is just half of the analysed time interval).

Predicted Earth tidal surface displacement at Cotopaxi location The tidal forces periodically displace the Earth's surface and interior, a summary of the theory of the Earth tides can be found in Section 2.4. The periodicities and magnitudes of the tide-induced surface displacement patterns at Cotopaxi are plotted in Figure 6.2 [predicted with the GNU R software using the package from Gama and Milbert, 2015].
The vertical surface displacements vary by up to ± 0.3 m within a day and follow a semi-diurnal periodicity (Figure 6.2, hourly-resolved data in the upper panel). The semi-diurnal peak-to-peak variation (calculated as the maximum difference within a sliding window of 13 h) of the vertical surface displacements varies between $0.15 - 0.55$ m with a maximum every 14.8 days (Figure 6.2, red line in upper panel). For ocean tides, this long-term periodicity is called spring–neap tidal cycle, a labelling which we adopt in this paper also for the Earth tides, i.e. maximum daily variations during a spring tide and minimum daily variations during a neap tide. Notably, each second spring tidal maximum slightly more pronounced, because the tide-inducing forces of Moon and Sun are slightly stronger during full moon, than they are during new moon. The Earth tides also result in horizontal displacements (see Figure 6.2 lower panel). Near the equator, where Cotopaxi is located, the East–West displacement is a factor of 5 and the North-South displacement is a factor of 10 smaller than the vertical displacement but for higher latitudes these ratios differ. The East–West component of the tide is in phase with the vertical component (Figure 6.5) while the North–South component has no strictly regular periodicity but reaches a maximum roughly every $13 - 14$ days. This is mainly due to the elliptic shape of the Moon orbit and the inclination of the Earth with respect to the ecliptic. Furthermore, due to the variation in the solar declination all tidal components display a semi-annual modulation of the mean displacement with maximum (for the vertical and East–West component) or minimum (for the North–South component) variation at the autumnal and vernal equinox (around September 23 and March 20, respectively).

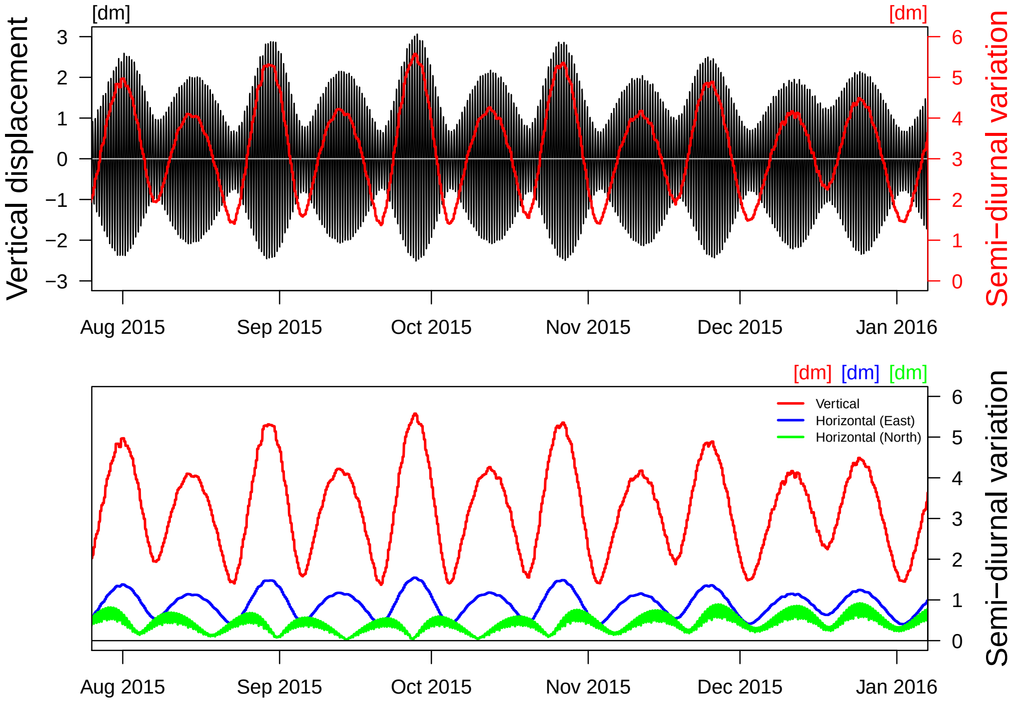

Figure 6.2: Time series of the vertical (top panel and red line in bottom panel) and horizontal (blue and green lines of the lower panel) components of the ground surface displacement at Cotopaxi due to the Earth tides. **Upper panel:** Hourly resolved vertical surface displacements (black, left ordinate axis) and its daily peak-to-peak variation (red, right ordinate axis). **Lower panel:** Time series of the daily peak-to-peak variation for all three spatial directions. Vertical and East-West components of the tide are in phase and have a periodicity of 14.8 days. The North–South component of the tide has no strictly regular periodicity but reaches a maximum roughly every 13 – 14 days and is increasing from September to December 2015. Figure reprinted from [Dinger et al., 2018].

6.2 DOAS measurements of SO_2 and BrO

NOVAC stations at Cotopaxi Today four NOVAC stations are installed around Cotopaxi at distances of 2 to 15 km, predominately downwind (Figure 6.3 and Table 6.1). The stations Refugio (instrument no.: D2J2160) and NASA (I2J4969) have operated since 2008. In August 2015, the instrument I2J4969 was relocated from NASA station to the more distantly located new San Joaquin station because the former became unsuitable due to increased ash precipitation. In October 2015, the stations Refugio Sur (D2J2815) and Cami (D2J2835) were additionally installed.

SO_2 and BrO time series during the Cotopaxi 2015 period of unrest We retrieved the time series of the SO_2 and BrO SCDs during the Cotopaxi 2015 period of unrest (May 2015 – April 2016, Figure 6.4). From August 2015 to February 2016, Cotopaxi also emitted large amounts of ash. These ash emissions can alter the atmospheric radiative transport and thus result in an underestimation of the retrieved SO_2 and BrO SCDs [e.g., Mori et al., 2006, Kern et al., 2010]. Nevertheless, those underestimations are approximately the same for both gas species thus their ratio is almost not affected by those ash emissions [Lübcke et al., 2014]. Further, it is under debate whether ash has a differential scavenging effect on sulphur and halogens, respectively [Bagnato et al., 2013, Delmelle et al., 2014].

Prior to May 2015, Cotopaxi was limited to fumarolic degassing and no significant gas plume was detected since the installation of the NOVAC instruments in 2008 (SO_2 SCDs $\leq 2 \cdot 10^{17} \frac{\text{molec}}{\text{cm}^2}$ and BrO SCDs were below the detection limit of $3 \cdot 10^{13} \frac{\text{molec}}{\text{cm}^2}$). Between mid May 2015 and the phreatomagmatic explosions on August 14 2015, the SO_2 SCDs increased up to $2 \cdot 10^{18} \frac{\text{molec}}{\text{cm}^2}$ and the BrO SCDs increased up to $5 \cdot 10^{13} \frac{\text{molec}}{\text{cm}^2}$. Within this period, the calculated BrO/SO_2 molar ratios were extremely low with an average of $(0.4 \pm 1.5) \cdot 10^{-5}$. No variations can be resolved because the BrO SCDs are close to the BrO detection limit. Within the week directly after the phreatomagmatic explosions on August 14 2015, mean SO_2 SCDs of $2 \cdot 10^{18} \frac{\text{molec}}{\text{cm}^2}$ were observed with a maximum value of $5 \cdot 10^{18} \frac{\text{molec}}{\text{cm}^2}$, the mean BrO SCDs increased from approximately 0 to $2 \cdot 10^{13} \frac{\text{molec}}{\text{cm}^2}$, to a maximum of $7 \cdot 10^{13} \frac{\text{molec}}{\text{cm}^2}$, and a mean BrO/SO_2 molar ratio of $(1.1 \pm 0.9) \cdot 10^{-5}$ was derived.

From August 22 to September 8 2015, there are only sparse plume data recorded because the solar panel at NASA station was temporarily covered by ash and the gas plume was apparently not transported through the field of view of the Refugio station during this period. Since September 8 2015, the I2J4969 instrument continued operation from the more distant San Joaquin station. Furthermore, two further NOVAC stations were installed in late September 2015. In consequence, the volcanic gas plume has then been observed from effectively three different distances to the volcanic vent: 2.6 km to Refugio station, $7.7 - 8.1$ km for Refugio Sur and Cami stations, and 16 km for San

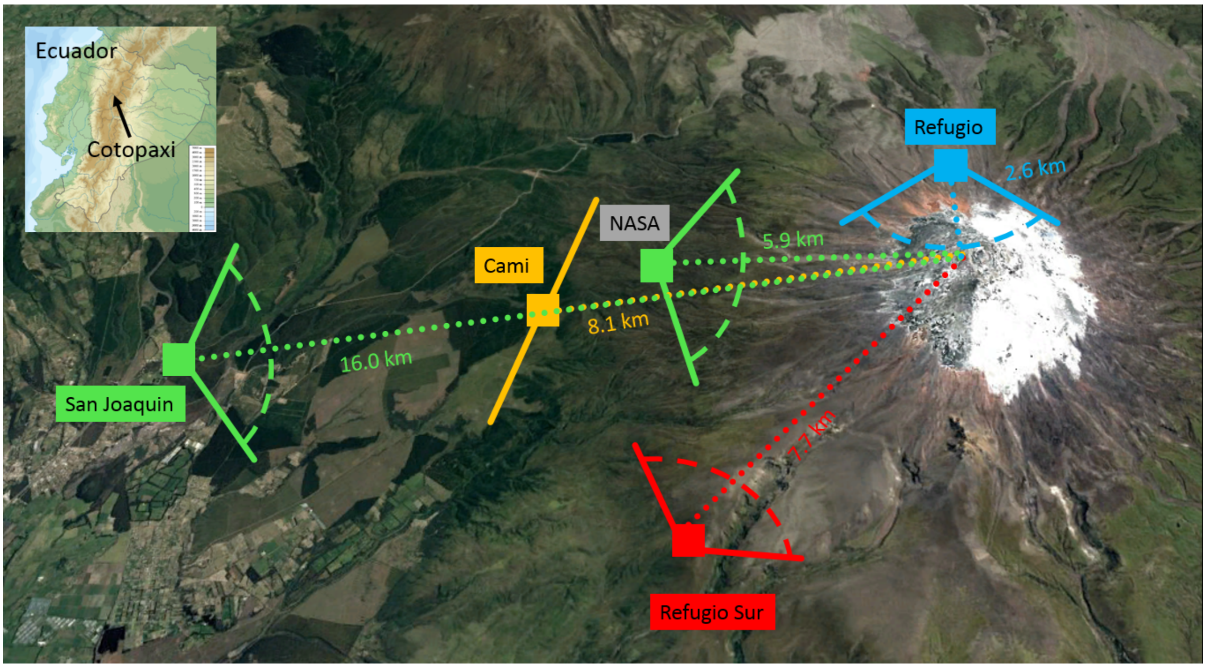

Figure 6.3: Location and scan geometries (see details in Galle et al. [2010]) of the four NOVAC stations at Cotopaxi volcano, the colours match to the time series in Figure 6.4. After the phreatomagmatic explosions on August 14 2015 the instrument I2J4969 was relocated from NASA station to San Joaquin station. The wind rose in the right bottom corner illustrates the typical wind conditions at an altitude of 100 m above the crater, i.e. 6000 m a.s.l. The map was created with graphical material from Google Earth and https://commons.wikimedia.org/wiki/File:Ecuador_relief_location_map.svg.

Table 6.1: Geometric properties of the NOVAC stations at Cotopaxi. See Table 5.1 for details. The cone angle on Refugio station has been changed on September 23 2015.

NOVAC station	coordinates	altitude A	distance D	angular position σ	scan plane angle β	cone angle
Refugio	-0.66, -78.44	4853 m	2.6 km	173°	200°	90°/60°
NASA	-0.68, -78.49	3959 m	5.9 km	98°	102°	60°
San Joaquin	-0.69, -78.58	3200 m	16.0 km	87°	85°	60°
Refugio Sur	-0.73, -78.49	4020 m	7.7 km	49°	35°	60°
Cami	-0.68, -78.51	3651 m	8.1 km	93°	115°	90°

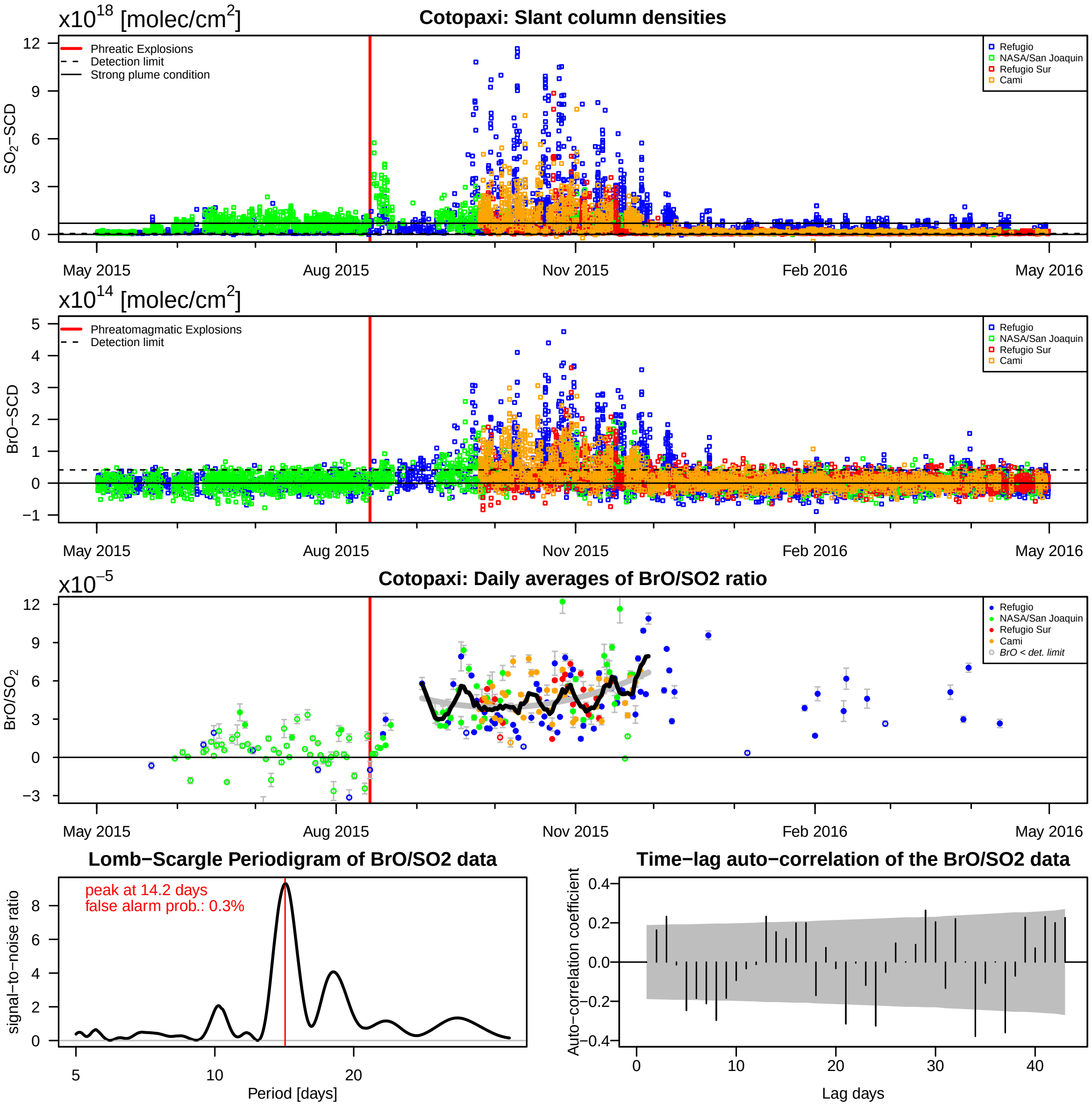

Figure 6.4: Three upper panels: Time series of the slant column densities of SO_2 and BrO and calculated BrO/SO_2 molar ratios in the gas plume emitted from Cotopaxi (tick marks indicate first day of the particular month). The NOVAC stations are indicated by the different colours. BrO data below the detection limit are highlighted by open circles. **Lowest panels:** Lomb–Scargle frequency component analysis and time-lag auto-correlation coefficients (dashed lines give 90 % confidence level) of the BrO/SO_2 molar ratio variations. Both analyses are based on the trend-corrected data acquired during the time interval from September 8 to December 1 2015 (see text).

Table 6.2: Typical SO_2 SCDs and BrO SCDs in the gas plume of Cotopaxi in the year 2015. Except for the first and the two last lines, the mean values refer to the data which are filtered for the strong plume threshold $S_{SO_2} > 7 \cdot 10^{17}\,\frac{\text{molec}}{\text{cm}^2}$.

Time period	mean SO_2	max SO_2	mean BrO	max BrO	mean BrO/SO_2
May 1 - May 22	$0.1 \cdot 10^{18}$	$0.2 \cdot 10^{18}$	≈ 0	$4 \cdot 10^{13}$	
May 22 - Aug 14	$1 \cdot 10^{18}$	$2 \cdot 10^{18}$	$0.4 \cdot 10^{13}$	$5 \cdot 10^{13}$	$(0.4 \pm 1.5) \cdot 10^{-5}$
Aug 14 - Aug 22	$2 \cdot 10^{18}$	$5 \cdot 10^{18}$	$2 \cdot 10^{13}$	$7 \cdot 10^{13}$	$(1.1 \pm 0.9) \cdot 10^{-5}$
Aug 22 - Sep 8			*(data gap)*		
Sep 8 - Dec 1					$(4.7 \pm 2.0) \cdot 10^{-5}$
Refugio	$3 \cdot 10^{18}$	$12 \cdot 10^{18}$	$11 \cdot 10^{13}$	$40 \cdot 10^{13}$	$(4.3 \pm 2.2) \cdot 10^{-5}$
Refugio Sur/Cami	$2 \cdot 10^{18}$	$6 \cdot 10^{18}$	$8 \cdot 10^{13}$	$30 \cdot 10^{13}$	$(4.7 \pm 1.5) \cdot 10^{-5}$
San Joaquin	$1 \cdot 10^{18}$	$3 \cdot 10^{18}$	$5 \cdot 10^{13}$	$20 \cdot 10^{13}$	$(5.0 \pm 2.5) \cdot 10^{-5}$
Dec 1 - May 1 '16					$(4.6 \pm 2.4) \cdot 10^{-5}$
Refugio	$1 \cdot 10^{18}$	$2 \cdot 10^{18}$	$5 \cdot 10^{13}$	$18 \cdot 10^{13}$	$(4.6 \pm 2.4) \cdot 10^{-5}$
Refugio Sur/Cami	$0.1 \cdot 10^{18}$	$0.8 \cdot 10^{18}$	≈ 0	$11 \cdot 10^{13}$	
San Joaquin	$0.1 \cdot 10^{18}$	$0.2 \cdot 10^{18}$	≈ 0	$8 \cdot 10^{13}$	

Joaquin station. Accordingly, the stations see different plumes with respect to the plume dispersion (which could effect in particular the plume region finder algorithm) and the atmospheric plume age (which could effect the bromine chemistry within the volcanic gas plume). The closer a NOVAC station is located to the volcanic vent the larger are the observed SO_2 and BrO SCDs are larger but the smaller are the observed BrO/SO_2 molar ratios (Table 6.2). Remarkably, the apparent drop in the (SO_2) SCD time series prior to September 8 retrieved from the NASA/San Joachin data (the green dots in the upper panels of Figure 6.4) is an artefact of the instrument relocation. For consistency, the following paragraph discusses the quantitative observation of the Refugio Sur and Cami stations which are both installed in about the same distance to the volcanic vent as the former NASA station. The observations of the other two NOVAC stations are compared in the subsequent paragraph.

From late September 2015 to late November 2015, the mean SO_2 SCDs observed by the Refugio Sur and Cami stations remained approximately on the same level as observed by the NASA station directly after the explosions (a significant amount of the data has been above $2 \cdot 10^{18}\,\frac{\text{molec}}{\text{cm}^2}$ but typically below $4 \cdot 10^{18}\,\frac{\text{molec}}{\text{cm}^2}$). In contrast, much higher BrO SCDs were observed in this period with daily maxima typically varying between $1 - 2 \cdot 10^{14}\,\frac{\text{molec}}{\text{cm}^2}$ but up to $4 \cdot 10^{14}\,\frac{\text{molec}}{\text{cm}^2}$. From late November 2015 to May 1 2016 (the end of the presented time series), the SO_2 and BrO SCDs dropped to levels below or close to the detection limits comparable with the situation prior to the start of the eruptive period in May 2016.

The SCD time series retrieved by the San Joaquin station have been similar to those of the Refugio Sur and Cami stations but with absolute levels of about half of their SCDs for both SO_2 and BrO. From September 8 and December 1, the SCD time series retrieved by the Refugio station show absolute values which are about 50 % larger than the values observed by the Refugio Sur and Cami stations. Furthermore, the Refugio station observed 8 extraordinary strong SO_2 peaks ($S_{SO_2} > 5 \cdot 10^{18} \, \frac{\text{molec}}{\text{cm}^2}$, namely on September 23, September 29, October 10/11, October 20/21, October $19 - 31$, November $9 - 12$, November 17/18, November 26) which were always also accompanied by strong peaks in the BrO SCDs. A comparison with the wind profile reveals that at least 4 (on September 23, September 29, October 10/11, October 20/21) of those 9 SO_2-peaks coincide with extremely low wind speeds ($< 2 \, \frac{\text{m}}{\text{s}}$, see Figure 6.1). From December 1 2015 to May 1 2016, the Refugio station persistently observed SO_2 SCDs above or close to the strong plume condition $S_{SO_2}^{thres} = 7 \cdot 10^{17} \, \frac{\text{molec}}{\text{cm}^2}$ and mean BrO SCDs of $5 \cdot 10^{13} \, \frac{\text{molec}}{\text{cm}^2}$. From September 8 to December 1 2015, the mean BrO/SO_2 molar ratios have been $(4.7 \pm 2.0) \cdot 10^{-5}$ when averaged over all stations and thus a factor of four larger than in the two weeks directly after the phreatomagmatic explosions. Furthermore, the BrO/SO_2 time series of this 3-monthly time interval indicates a linear trend of $(0.9 \pm 0.2) \cdot 10^{-5}$ per month (i.e. per 30.5 days).

An inter-comparison of the individual NOVAC stations reveals a positive correlation between the BrO/SO_2 molar ratios and the distance between the station to the volcanic vent from $(4.3 \pm 2.2) \cdot 10^{-5}$ observed by Refugio station, via $(4.7 \pm 1.5) \cdot 10^{-5}$ observed by Refugio Sur and Cami stations, to $(5.0 \pm 2.5) \cdot 10^{-5}$ observed by San Joaquin station. Although this systematic offset i significant and plausible, the BrO/SO_2 molar ratios retrieved at the different stations are nevertheless in good agreement within the overall natural variability. Furthermore, all individual stations observed at least qualitatively the same linear trend in the BrO/SO_2 time series

Periodic pattern in the BrO/SO_2 molar ratios after the explosions From early September 2015 to late November 2015, the BrO/SO_2 time series has an almost daily resolution. This extraordinary temporal resolution allows for a detection of possible "high-frequency" (with periods of weeks or months) variations in the BrO/SO_2 time series. And indeed, the maxima and minima of the BrO/SO_2 molar ratios apparently follow a periodic pattern with a period of about two weeks and an amplitude (of the smoothed data) of about $1 \cdot 10^{-5}$, i.e. a relative variation of about ±20 %, as illustrated by the rolling average over 7 days (thick black line in third panel in Figure 6.4).

The quantitative estimation for the reliability of this signal has been tested by a Lomb–Scargle analysis and a time-lag auto-correlation analysis (Section 4.2). Both methods were applied to the daily data (arithmetically averaged over all instruments when daily means were available for several instruments) for the time interval from September 8 2015 to December 1 2015. The first week of September 2015 and the first week of December 2015 were excluded from both analyses as the temporal resolution is much worse at those times. The trend was removed by subtracting a polynomial of 5th order

from the BrO/SO_2 time series.
The Lomb–Scargle analysis identifies a periodicity of 14.2 days and the auto-correlation analysis confirms the existence of a periodicity of $14 - 15$ days (lowest panels in Figure 6.4). For both methods, the results are highly significant (Lomb–Scargle false alarm probability of 0.3 % and an auto-correlation detection confidence of about 90 %, respectively) and thus the periodic signal is with high probability an observation of a natural process (or a series of those) rather than statistical noise. In addition, the Lomb–Scargle analysis proposes a further peak at a periodicity of 18.1 days, however, with a false alarm probability of 9 %.

6.3 Comparison of BrO/SO_2 with other data

Correlation analysis We observed three significant variations in the BrO/SO_2 time series: (1) an abrupt step increase in the BrO/SO_2 molar ratios within September 2015 (unfortunately the exact behaviour is hidden by the data gap), (2) an increasing trend from September to December 2015, and (3) the periodic pattern from September to December 2015. In the following we compare the variations in the volcanological, meteorological, and calculated tidal data with the variations in the BrO/SO_2 data. For the time interval from September 1 to December 1 2015, we performed a correlation analysis between the BrO/SO_2 data, the meteorological data, and the calculated tidal data. We compared the daily means of the gas data (calculated from data above the strong plume threshold), the noon data of the meteorological data, and the tidal data delayed in time (see below). All data sets were left with their long-term trends in order to compare the total variations (Figure 6.5). An analogue analysis with de-trend data leads to similar results but lower correlation coefficients.

Comparison of BrO/SO_2 time series with SCDs and meteorology The BrO/SO_2 molar ratios are not correlated with the daily means of the SO_2 SCDs but partially correlated with the daily means of the BrO SCDs, with correlation coefficients of $-3\,\%$ and 42 %, respectively. Furthermore, no significant correlation between the BrO/SO_2 molar ratios and any of the presented meteorological parameter has been observed. All recorded gas plumes had a plume age of at least 9 min. A comparison of the plume age versus the BrO/SO_2 molar ratios implies that the HBr $\rightleftharpoons$ BrO conversion had reached the equilibrium BrO level already prior to minute 9.

Comparison of the BrO/SO_2 time series with the Earth tides It should be kept in mind that one can expect a delay between a tide-driven process in the volcanic system and the finally observed volcanic gas emissions. We determined the delay by a cross-correlation analysis between the BrO/SO_2 molar ratios and the calculated tidal surface displacement. For this purpose, we shifted the time series of the Earth tide data variably by up to two week backwards in time and so manually maximised the cross-correlation coefficient between BrO/SO_2 and tide-induced surface displacement. However, the optimal delay is different when we optimise for the different components of the tidal signal: it is 98 h when we optimise with respect to the vertical component (or East–West component which is perfectly in phase with the vertical component) but 11 h when we optimise for the North–South component. As a result we derived correlation coefficients between the BrO/SO_2 molar ratios and the vertical component or the North–South component of $-41\,\%$ and 50 %, respectively (see Figure 6.5 where both optimisation scenarios are included). As last analysis step, we dropped the handy representation (vertical, North–South, East–West) of the tide-induced surface

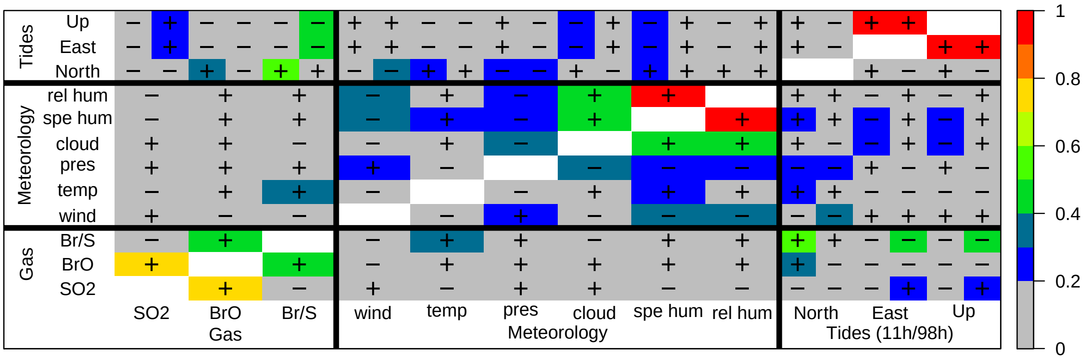

Figure 6.5: Correlation coefficients of the different data sets, where "Br/S" is used as abbreviation for BrO/SO_2 molar ratios. The colours indicate the absolute value of the coefficient binned in bins of 10 %. The signs of the correlations are indicated by the "+" and "-", respectively. The unity auto-correlations are omitted for better readability. In order to account for the delay between tidal forcing and atmospheric measurement, the time series of the tides was shifted backwards in time prior to the correlation analysis. The figure shows the correlation for a shift of 11 h (left column) and for a shift of 98 h (right column), see text for derivation of the shifts. For both shifts, the North–South component correlates the strongest with the BrO/SO_2 molar ratios.

displacement but correlated the displacement in variable directions (calculated as the component of the displacement vector in the chosen three-dimension direction) with the BrO/SO_2 molar ratios. The overall optimum was again found to be strictly horizontal and quite strictly to the North (optimum was 1° NNE but with similarly high correlation coefficients of above 50 % for a range of 1° NNE ±5°) and thus again with a delay of 11 h.

The tidal North–South displacement component fits extraordinarily well to both, the trend and the “skewed” periodic pattern in the BrO/SO_2 data (Figure 6.6a). Further, a scatter plot revealed a highly significant contrast in BrO/SO_2 data between small and large semi-diurnal tidal deviations (Figure 6.6b). For the tidal vertical displacement component, this contrast is not that obvious (Figure 6.7b)

Comparison of BrO/SO_2 time series with volcanological data During the first week after the explosions on August 14 2015, the BrO/SO_2 molar ratios remained on a similar low level ($\leq 1 \cdot 10^{-5}$) as prior to the explosions. The BrO/SO_2 molar ratios abruptly increased to a mean value of about $4 \cdot 10^{-5}$ during the next two subsequent weeks. Gaunt et al. [2016] mentioned that the hydrothermal system might have been drying during those weeks. Accordingly, at first bromine predominately partitioned in the hydrous fluid of the hydrothermal system, but after the hydrothermal system has been dried out the bromine has probably directly partitioned to the gas phase.

The increasing trend in BrO/SO_2 from mid of September 2015 to early December

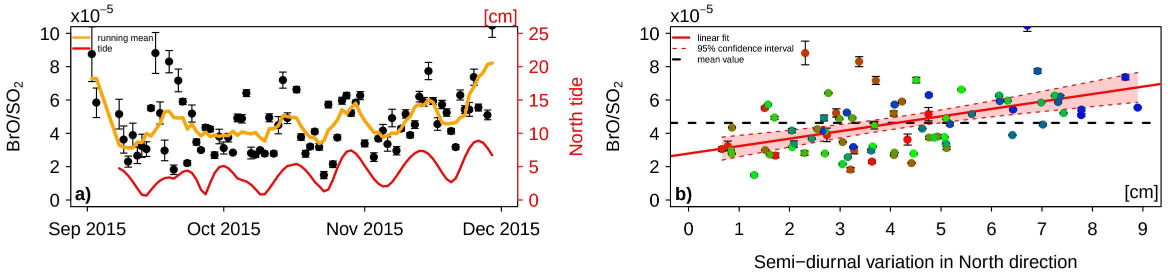

Figure 6.6: Graphical comparison of temporal variations of the BrO/SO$_2$ molar ratio and the predicted tide-induced surface displacement variation in North-South direction. **a:** Comparison of the time series. **b:** Scatterplot which illustrates the correlation coefficient of 50 % between both time series. The measurement date is given by the colour of the data points which is gradually changing from red (September 1 2015) to blue (December 1 2015).

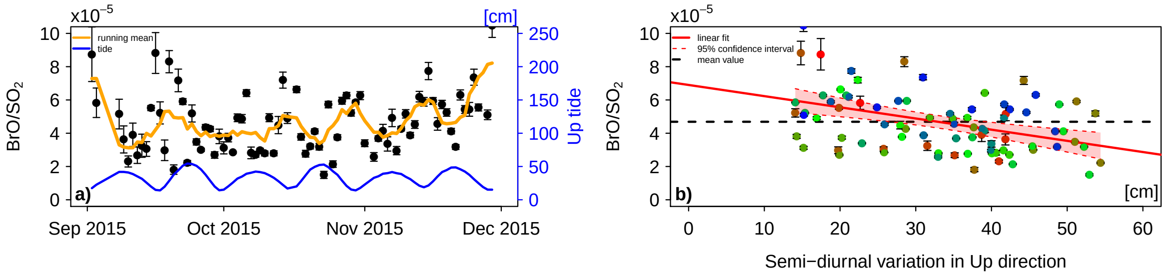

Figure 6.7: Graphical comparison of temporal variations of the BrO/SO$_2$ molar ratio and the predicted tide-induced surface displacement variation in vertical direction. **a:** Comparison of the time series. **b:** Scatterplot which illustrates the correlation coefficient of −41 % between both time series. The measurement date is given by the colour of the data points which is gradually changing from red (September 1 2015) to blue (December 1 2015).

2015 indicates a slow but continuous change in magma pressure, magma temperature, or composition of the degassing magma body. The possible reasons are manifold. Following Gaunt et al. [2016], the mingling of the old magma with juvenile magma could have continuously changed the effective magma composition. Furthermore, if HBr degasses at higher pressures than SO$_2$, a gradual pressure increase due to e.g. the formation of a new plug may have resulted in suppressed SO$_2$ degassing. If in contrast HBr is degassing at lower pressures than SO$_2$, the increasing trend may indicate that the magma has already degassed most SO$_2$ while the magma still holds significant amounts of HBr which yet has to degas. The latter interpretation would be supported by the relatively large BrO SCDs but rather small SO$_2$ SCDs since January 2016.

6.4 On the origin of the periodic BrO/SO_2 pattern

Plausible volcanological origins The volcanic unrest and in particular the explosions in August 2015 deflected the volcanic system from the equilibrium. Thus, the observed periodic pattern in the BrO/SO_2 data might be a manifestation of a damped and oscillating restoring process of the volcanic system to a new equilibrium. However, the damping of magma motion is rather high and thus a one-time excitement of the magma column, e.g. by the explosions on August 14 2015, is unlikely to cause an observable oscillation of six periods. As another possible explanation, the periodic pattern may have been caused by a chance repetition of six one-time events at equidistant time intervals, e.g. by a repetitive plug formation and destruction as suggested by Gaunt et al. [2016]. Anyway, even if the interpretation of a repetitive plug formation holds true, the probability that those events happened at equidistant timing is expected to be rather low unless the events are triggered by a periodic external forcing. The spring–neap tide cycle of the Earth tides is such a continuous periodic forcing which, at least in principle, is continuously varying the magmatic system. Finally, we can not exclude that the unrest or geometry itself might have led to an accidental periodicity in the activity of two weeks which was also completely independent from tidal influence, e.g. a periodic magma intrusion from the deep to the shallow reservoir due to tectonics. However, again, it appears to be unlikely that such an accidental periodicity has a period of just two weeks. Thus from all geological origins, the tidal forcing appears to be the best candidate to explain the observed periodic signal in the BrO/SO_2 data.

Possible tidal origin In this reasoning, the shallow emplacement of magma prior to the phreatomagmatic explosion in August 2015 may have (temporarily?) shifted the geometry of the Cotopaxi magma plumbing system from a non-excitable to an excitable state. Additionally, the explosive activity very likely gave rise to a transition from closed system to open system degassing, and thus made the volcano more perceptive to external influences. Further, combining our results and the interpretation from Gaunt et al. [2016] suggests a possible tide-induced repetitive plug formation and destruction, causing an alternation of "open and almost shut condition" as proposed by Fischer et al. [2002] for explosive activity at Karymsky volcano. All those effects can result in a periodic variation of the pressure regime in the shallow magmatic system, leading to a periodic variation of the volatile solubility in the magmatic melt, which in turn may vary the magnitude and/or composition of volcanic gas emissions.

North–South component and local fault system Tide-induced processes are intuitively expected to strictly follow the periodicity of the strongest tidal long-term pattern, that is the spring–neap tide cycle with period of 14.8 days. The observed periodic pattern of 14.2 days in our BrO/SO_2 data, however, correlates somewhat stronger with the temporal intraday amplitude variation of the North–South component of the tide-induced surface displacement, which follows a rather irregular pattern with maxima occurring roughly every $13 - 14$ days. Our results accordingly suggest that the volcanic system of Cotopaxi (currently?) is more sensitive to tide-induced stresses acting in the North-South direction, rather than to stresses in the vertical and East–West directions.

This interpretation is further supported by the orientation of the local fault system and associated ambient stress field at Cotopaxi, which is located in a transfer fault zone with greatest principal stress acting in the ENE–WSW direction and the weakest principal stress in the North–South, i.e. also in horizontal direction [Fiorini and Tibaldi, 2012]. Such a setting favours the intrusion and ascent of magma along East–West striking planar structures, which is further corroborated by the observation of the inclined sheet intrusion beneath the south-western flank of the volcano [Morales Rivera et al., 2017]. Thus, the additional tide-generated stresses probably have a much higher relative impact, when they act in the direction of weakest principle stress, i.e. normal to East-West striking compressible magma pathways, if compared to the other directions. Such a directional dependency is indeed well known for the tidal response of inclined planar aquifers, which cross-cut borehole wells. Bower [1983] e.g. reported oscillations of water levels in boreholes in Canada, which indicated a strong response to the horizontal component of the semi-diurnal M2 tide acting normal to the strike direction of the intersecting aquifers.

7 Masaya

7.1 Geology and Meteorology

Masaya (12.0°N, 86.2°W, 635 m a.s.l.) is located on the Nicaraguan portion of the Central American Volcanic Belt (CAVF). The Smithonian Institution lists 28 eruptions during the last 200 years (with mainly VEI1 and some VEI2). Since December 11 2015, Masaya hosts a shallow lava lake [Aiuppa et al., 2018]. Masaya has been in persistent contact with a hydrothermal system at least until 2010 [MacNeil et al., 2007, Pearson et al., 2012, Mauri et al., 2012]. The volcanic gas plume often hovers close to the ground causing serious issues to the local agriculture and health conditions of the local population [Baxter et al., 1982, Delmelle et al., 2002, van Manen, 2014].

The meteorological conditions are accessed by ECMWF model data for an altitude of 700 m a.s.l. (Figure 7.1) and by ground-based data from the Managua airport, which is located 15 km north of Masaya (Figure 7.2, data from https://mesonet.agron.iastate.edu). The ECMWF time series indicates for all presented parameters annual cycles, however, with different timing of their extrema. The barometric pressure varied between $931 - 937$ mbar, with maxima in January/February and minima in October/November. The ambient air temperature varied between $295 - 300$ K with maxima in March/April and minima in autumn. Masaya is within the ITCZ in May–June and in September–October and south of the ITCZ in July–August. The specific and relative humidity varied between $10 - 16 \, \frac{\mathrm{g\,H_2O}}{\mathrm{kg\,air}}$ and $50 - 90$ %, respectively, with maxima from June to October, with minima in February/March, and in some years with weaker secondary minimum in July/August. The cloud cover varied between two clearly distinguishable plateaus with values of (0.3 ± 0.1) from December to March and values of (0.7 ± 0.2) from May to October. The wind speed varied between $1 - 15 \, \frac{\mathrm{m}}{\mathrm{s}}$, with maxima in January/February, with weaker secondary in July, and with minima in October. The wind is blowing all the year from the East–Northeast, that is $(80 \pm 11)^\circ$. The around noon ground-based data in general agree with the pattern observed in the ECMWF data, with variations in the ambient temperature between $302 - 307$ K, variations in the relative humidity between $40 - 70$ %, variations in the wind speeds between $2 - 8 \, \frac{\mathrm{m}}{\mathrm{s}}$, and a mean wind direction of $(88 \pm 26)^\circ$. The latter differs significantly as $(103 \pm 29)^\circ$ when considering all times of the day. Furthermore, a tomography of the volcanic gas plume from March to October 2014 with two NOVAC instruments confirms a mean wind direction of $(83 \pm 4)^\circ$ (Figures 7.3 and 7.7).

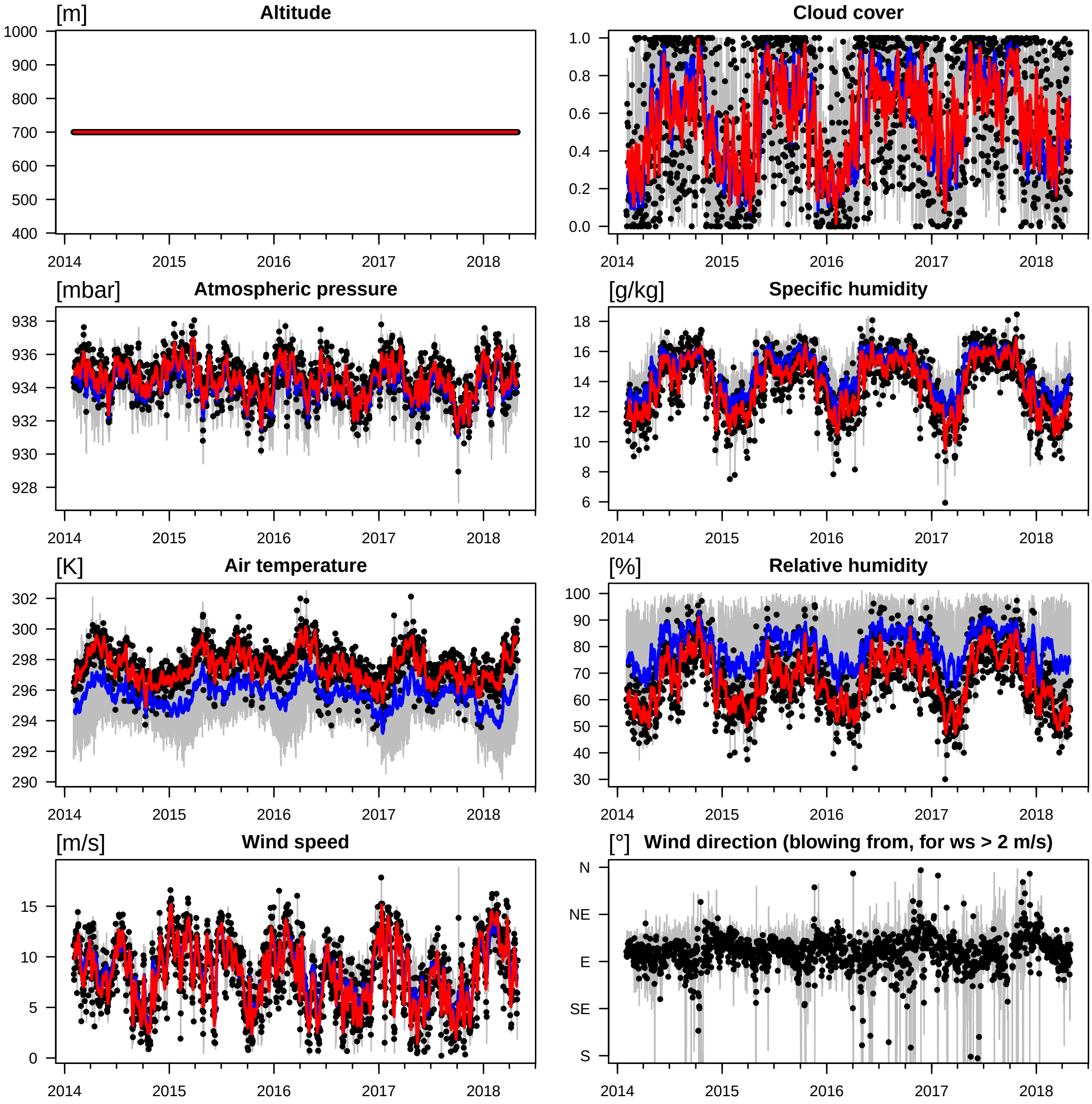

Figure 7.1: Meteorological conditions at Masaya volcano retrieved from ECMWF data with resolutions of 6 h and 0.14° x 0.14° and interpolated to an altitude of 700 m a.s.l.. **Grey lines:** 6-hourly data. **Blue lines:** weekly rolling average over the 6-hourly data (±3 days window). **Black dots:** around noon (18:00 UTC) data. **Red lines:** same rolling average but over the around noon data. Absolute variations are almost the same for the full data set and the around noon data only. The exceptions are the air temperature and the relative humidity. As expected, the air temperature is larger around noon which thus causes a smaller relative humidity around noon.

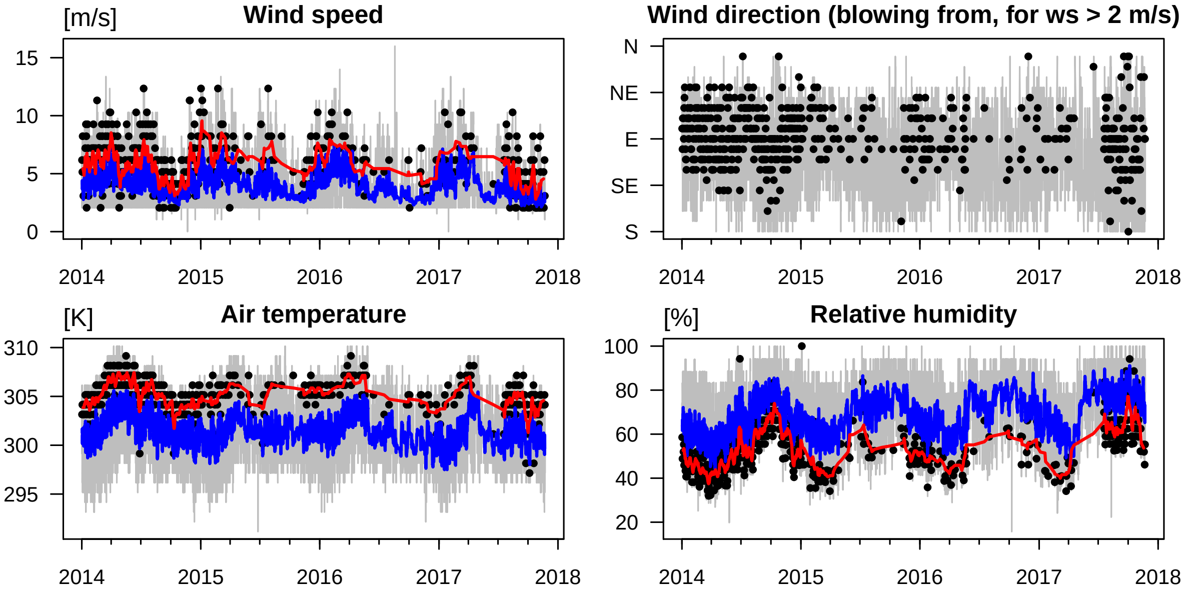

Figure 7.2: Meteorological conditions retrieved from a ground-based station at Managua airport (15 km north of Masaya volcano). **Grey lines:** hourly data. **Blue lines:** rolling average over the hourly data (±2 weeks window). **Black dots:** around noon (18:00 UTC) data. **Red lines:** same rolling average but over the around noon data.

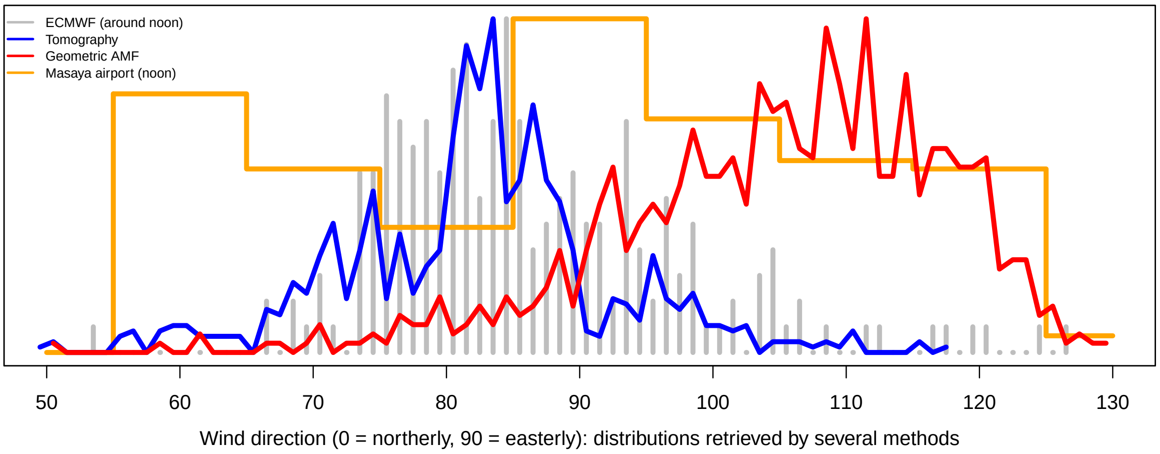

Figure 7.3: Wind direction at Masaya in March – October 2014 retrieved by several approaches. The results from ECMWF and the plume tomography are in good agreement. Managua airport station shows a stronger variability and in average more easterly/less northerly winds. The geometric Air Mass Factor (AMF) check strongly deviates from the other results, indicating that the persistent difference in SCDs observed between the two NOVAC stations is not caused by the wind direction.

7.2 DOAS measurements of SO_2 and BrO

NOVAC stations at Masaya First NOVAC measurements have been conducted at Masaya in 2007 and 2009 but with only little data recorded. From March 2014 to March 2018, the NOVAC station "Caracol" (instrument: D2J2124_0) operates continuously but with some data gaps of several months. From March to October 2014, a second NOVAC station "Nancipal" (D2J2375_0) operated quite close to Caracol (Figure 7.4). The Caracol stations stopped operating in March 2018. There is again Caracol data available since June 2018. A field campaign in January 2019 observed, however, that instead only the Nancital station is operating, there are thus doubts whether the data since June 2018 are indeed recorded at Caracol station. Until this has been clarified data after March 2018 is mostly excluded from the following analysis.
The following quantitative description of the time series refers to Caracol station. From March 2014 to March 2018, the SO_2 SCDs have varied between $1 - 5 \cdot 10^{18}\,\frac{\text{molec}}{\text{cm}^2}$, with maximum values of $9 \cdot 10^{18}\,\frac{\text{molec}}{\text{cm}^2}$, and a proposed linear trend of $(0.16 \pm 0.01) \cdot 10^{18}\,\frac{\text{molec}}{\text{cm}^2}$ per year. No significant differences have been observed for the SO_2 SCDs when comparing the time series prior and after December 2015. The SO_2 time series indicates an annual cyclicity with pronounced minima in every January, however, the maxima show no consistent timing.
The formation of the lava lake in December 2015 marks an important change in the volcanic system and a separation of the gas time series before and after December 2015 appears to be reasonable. In order to avoid contributions from the seasonal modulation, the long-term averages for both time series are retrieved for the two periods spanning over exact multiples of a year, namely from September 1 2014 to September 1 2015 ("prior to the lava lake formation") and from January 1 2016 to January 1 2018 ("after the lava lake formation"). From March 2014 to September 2015, the BrO SCDs had typical daily maxima of about $2 \cdot 10^{14}\,\frac{\text{molec}}{\text{cm}^2}$ and maxima of up to $4 \cdot 10^{14}\,\frac{\text{molec}}{\text{cm}^2}$. There is a data gap from September to December 2015. From December 2015 to March 2018, the BrO SCDs had typical daily maxima of about $3 \cdot 10^{14}\,\frac{\text{molec}}{\text{cm}^2}$ and maxima of up to $8 \cdot 10^{14}\,\frac{\text{molec}}{\text{cm}^2}$. The evolution of the lava lake coincides with an apparent step increase by $0.8 \cdot 10^{14}\,\frac{\text{molec}}{\text{cm}^2}$ in the mean BrO SCDs from $0.7 \cdot 10^{14}\,\frac{\text{molec}}{\text{cm}^2}$ prior to the lava lake

Table 7.1: Geometric properties of the NOVAC stations at Masaya. See Table 5.1 for details.

NOVAC station	coordinates	altitude A	distance D	angular position σ	scan plane angle β	cone angle
Caracol	11.98, -86.18	382 m a.s.l.	1.5 km	75°	54°	90°
Nancital	11.99, -86.18	340 m a.s.l.	1.7 km	95°	100°	90°

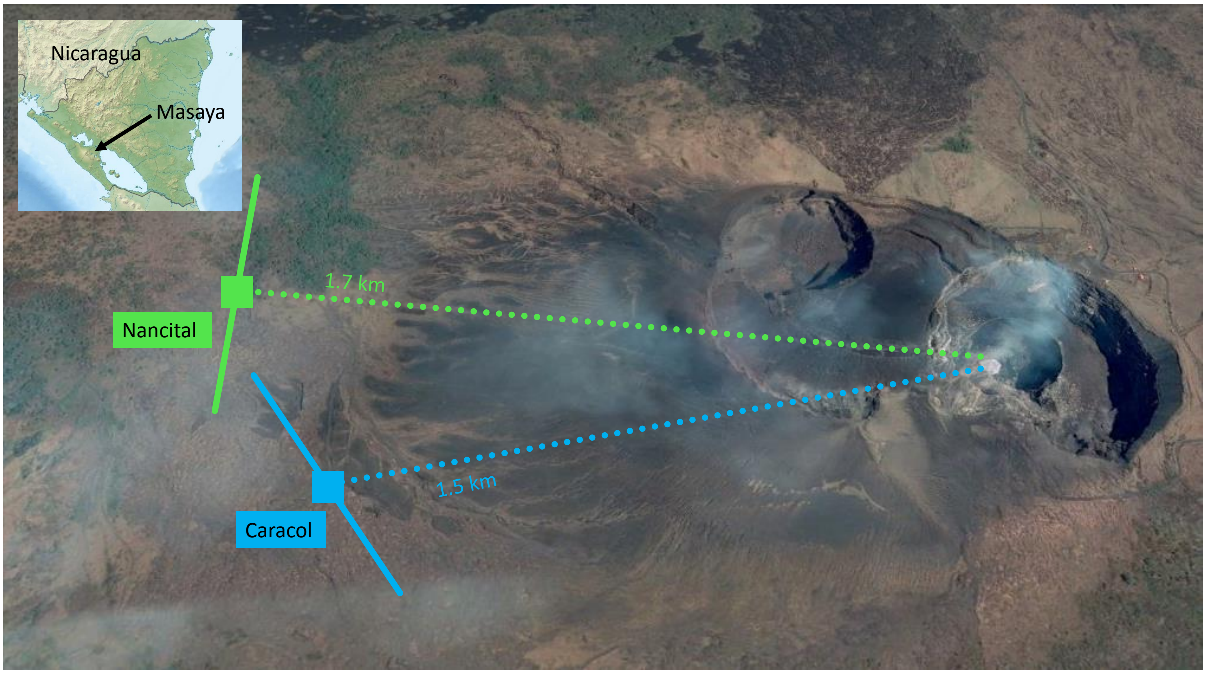

Figure 7.4: Location and scan geometries of the two NOVAC stations at Masaya volcano, the colours match to the time series in Figure 7.5. The map was created with graphical material from https://commons.wikimedia.org/wiki/File:Nicaragua_relief_location_map.jpg and Google Earth.

evolution to $1.5 \cdot 10^{14}\,\frac{\text{molec}}{\text{cm}^2}$ after the lava lake evolution. No significant linear trends have been observed for the separated time periods: $(-0.08 \pm 0.04) \cdot 10^{14}\,\frac{\text{molec}}{\text{cm}^2}$ per year prior to the lava lake evolution and $(0.01 \pm 0.02) \cdot 10^{14}\,\frac{\text{molec}}{\text{cm}^2}$ per year after the lava lake evolution. Considering the overall time series from March 2014 to March 2018, the BrO SCDs indicate a linear trend of $(0.31 \pm 0.01) \cdot 10^{14}\,\frac{\text{molec}}{\text{cm}^2}$ per year. The BrO time series does not indicate an obvious annual cycle.

Patterns in the BrO/SO_2 time series From March 2014 to March 2018, the BrO/SO_2 molar ratios have varied between $1 - 9 \cdot 10^{-5}$ but with some peaks of up to $14 \cdot 10^{-5}$. Considering the overall time series from March 2014 to March 2018, the mean BrO/SO_2 molar ratio has been $(3.7 \pm 1.8) \cdot 10^{-5}$. Prior to the lava lake evolution, the mean BrO/SO_2 molar ratio has been $(2.7 \pm 1.2) \cdot 10^{-5}$. After the lava lake evolution, the mean BrO/SO_2 molar ratio has been $(4.1 \pm 1.7) \cdot 10^{-5}$. This implies a step increase by $1.4 \cdot 10^{-5}$ in the mean BrO SCDs possibly caused by the lava lake evolution (see yellow bars in Figure 7.6). Furthermore, the BrO/SO_2 time series indicates an extremely significant annual cycle with an amplitude of $1.6 \cdot 10^{-5}$, i.e. about 50 % of the mean BrO/SO_2 molar ratio. For consistency with earlier chapters, a polynomial long-term

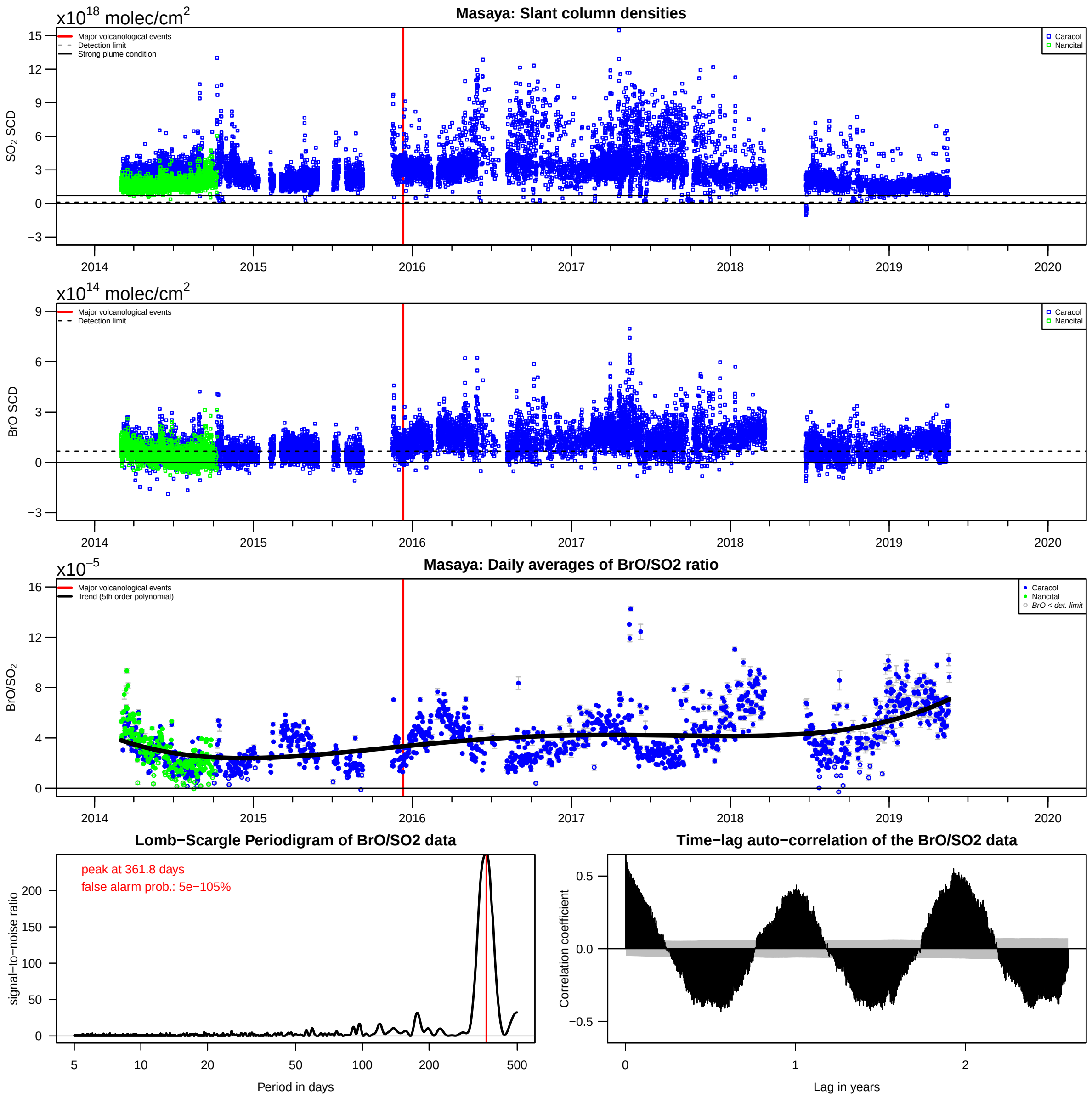

Figure 7.5: Three upper panels: Time series of the slant column densities of SO_2 and BrO and calculated BrO/SO_2 molar ratios in the gas plume emitted from Masaya (tick marks indicate first day of the particular month). The NOVAC stations are indicated by the different colours. BrO data below the detection limit are highlighted by open circles. **Lowest panels:** Lomb–Scargle frequency component analysis and time-lag auto-correlation coefficients (grey region gives the 90 % confidence interval) of the BrO/SO_2 molar ratio variations. Both analyses are based on the trend-corrected data acquired during the time interval indicated by the trend line in the BrO/SO_2 time series (see text).

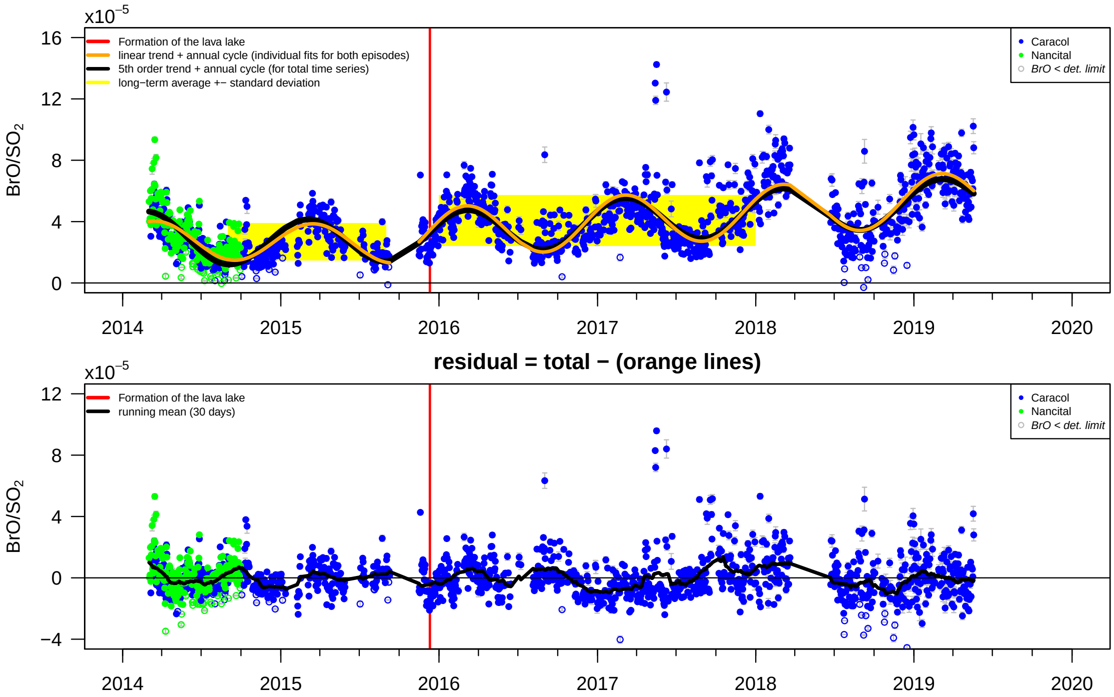

Figure 7.6: BrO/SO_2 molar ratios at Masaya. **Upper panel:** Best fit of the long-term pattern in the BrO/SO_2 time series prior and after the lava lake formation (orange lines) and for the total time series (black line). The proposed step increase caused by the lava lake formation is indicated by the yellow bands. **Lower panel:** Residual BrO/SO_2 time series when subtracting the best fit from the two parts of the time series.

trend of 5th order is subtracted from the original BrO/SO_2 time series prior to the Lomb–Scargle analysis and the time-lag auto-correlation analysis (Figure 7.5). The alternative of subtracting instead constant offset of $1.5 \cdot 10^{-5}$ from the data since December 2015 and the subtracting of a linear trend from such altered time series results in the detection of the very same annual periodicity. The Lomb–Scargle analysis proposes an additional semi-annual modulation of the BrO/SO_2 time series.

A linear trend plus a sinusoidal with annual frequency was fitted to the two time series prior and after the lava lake formation and the fit results were subsequently subtracted from the data in order to check for further residual pattern (Figure 7.6). The linear trends have been $(-0.17 \pm 0.10) \cdot 10^{-5}$ and $(0.70 \pm 0.04) \cdot 10^{-5}$ prior and after, respectively, the lava lake formation. The residual variations spans $\pm 2 \cdot 10^{-5}$ with a standard deviation of $1.3 \cdot 10^{-5}$ and some outliers of up to $9 \cdot 10^{-5}$. No semi-annual modulation of the dominant annual periodicity has been found in the residual time series. Nevertheless, an irregular cyclicity of plateaus with slightly enhanced or reduced BrO/SO_2 molar ratios is observed between 2014 and 2018.

7.3 Discussion

Deviating SCDs observed by the two NOVAC station From March 2014 to October 2014, the Nancital station was operating simultaneously with and in close spatial proximity to the Caracol station. Given the rather constant wind direction from East-Northeast, both NOVAC stations are expected to monitor the same plume with respect to the plume age and the degree of dilution. Both stations indeed perfectly agree in the resulting the BrO/SO_2 molar ratios and their temporal evolution (Figure 7.5c). In contrast, the Nancital station observed SO_2 and BrO SCDs which are a factor of $1.5 - 2$ smaller than the SCDs observed by the Caracol station (Figure 7.5 where this is not obvious in the BrO panel due to the large amount of data points scattering around zero). Differences in the SCDs can be caused by several effects. Obvious candidates are (1) a background contamination with volcanic gases, (2) different geometric light paths through the plume, (3) an asymmetric plume geometry, (4) radiative transport effects. All of these possible causes can be ruled out for these time series because the volcanic gas plume was most of the time closer to the Caracol station than to the Nancital stations. Accordingly, (1) a background contamination may cause an underestimation of the Caracol data rather than of the Nancital data, (2) the geometric light path is shorter for the Caracol station than for the Nancital station for a circular plume geometry (see Figure 7.3) and (3) much shorter if the plume geometry is horizontally extended, and (4) the sun was for the overall period during noon approximately in the zenith and propagating during the day in plume direction, thus radiative transport effects can be expected to be rather similar for both stations. Another possible origin could be the plume region algorithm which may less efficiently separate the central plume region from the reference/diluted region for the Nancital station because the (potentially flattend) plume occupies a smaller angular space in the scan plane. The plume finder algorithm gives estimates between $S_{mean} = S_{max} \cdot \mathrm{erf}(\sqrt{1/2}) \approx 0.68 \cdot S_{max}$ (if a well defined Gaussian distribution was detected) and $S_{mean} \approx S_{max}$ (if a rather broad Gaussian distribution was detected). Accordingly, if the plume finder algorithm would typically output S_{max} for Caracol station but $0.68 \cdot S_{max}$ for Nancital station, this could explain a difference in the SCD by up to 1.46. However, the plume finder algorithm finds for Caracol station in 25 % of the scans but for Nancital station in only 21 % of the scans well defined Gaussian distributions. Accordingly, also the plume finder algorithm may underestimate the Caracol data rather than the Nancital data. In conclusion, no explanation for the difference in the SCDs has been found. Vice versa, this findings demonstrates the strength of the BrO/SO_2 molar ratios compared to SO_2 emission fluxes because the BrO/SO_2 molar ratios are apparently unaffected by this non-understood discrepancy.

Plume tomography The NOVAC retrieval gives the central angular position of the detected volcanic gas plume (by means of the scan zenith angle ε). The relationship between the plume height (above ground) H and the wind directions ω is given by

$$H + A = D \cdot \left| \frac{\sin(\omega - \sigma)}{\cos(\omega - \beta) \cdot \tan(\varepsilon)} \right| \tag{7.1}$$

where the fixed station geometry parameters A, D, σ, β are summarised in Table 7.1 and the horizontal geometrical considerations are sketched in Figure 5.8. A simultaneous retrieval of the plume position by the Caracol and the Nancital stations then allows for a tomographic retrieval of the plume heights (above ground) H and the wind directions ω from March to October 2014, at least when assuming that the plume altitude $H + A$ and the wind direction are identical for both stations (two equations and two unknown parameters). If a NOVAC station i observes $\varepsilon_i = 0°$, eq. 7.1 gets invalid. In such a case, the wind direction is trivially given by $\omega = \sigma_i$ and the plume height can be retrieved by applying eq. 7.1 on the other station. The plume tomography algorithm proposes wind directions of $(83 \pm 4)°$ and a total plume altitude $H + A$ of (665 ± 166) m which implies a plume height H above the NOVAC station of (283 ± 166) m for the Caracol station and of (325 ± 166) m for the Nancital station (Figure 7.7).

Bromine chemistry in the volcanic gas plume of Masaya The NOVAC stations at Masaya are located in close proximity to the volcanic vent and thus they typically observe volcanic gas plumes with an atmospheric plume age between $2 - 5$ min. A comparison of the BrO/SO$_2$ time series with the plume ages (retrieved from the ECMWF wind data) indicates that the BrO genesis has reached the equilibrium already within the first 2 min (Figure 7.8a). In contrast, almost all outliers in the BrO/SO$_2$ molar ratios are observed for relatively large plume ages (which means at Masaya larger than 7 min, see Figure 7.8c). Furthermore, no significant correlation has been found between the BrO/SO$_2$ molar ratios and the plume altitude (as retrieved by the tomography from March to October 2014).

A correlation analysis with the other meteorological parameters at around noon time indicates rather large correlation coefficients between the BrO/SO$_2$ molar ratios with the specific and relative humidity of -39 % and -29 %, respectively. The bromine explosion works more efficiently for lower pH-value (it depends on the number density of protons H$^+$ and bromide ions Br$^-$ in the aerosol phase). Ceteris paribus, a larger humidity would result in more water in the aerosols and thus a larger pH-value or likewise a lower number density of H$^+$ and Br$^-$ ions. The observed correlation between the BrO/SO$_2$ molar ratios and the humidity thus implies a strongly impact of the humidity on the BrO explosion if the specific humidity is rather large. In contrast to Masaya, the volcanic gas plumes of Nevado del Ruiz and Cotopaxi are in released in an altitude of more than 5 km a.s.l. There the specific humidity is much lower (compare with Figure 5.1 and 6.1). Accordingly, variations in the specific humidity have a smaller

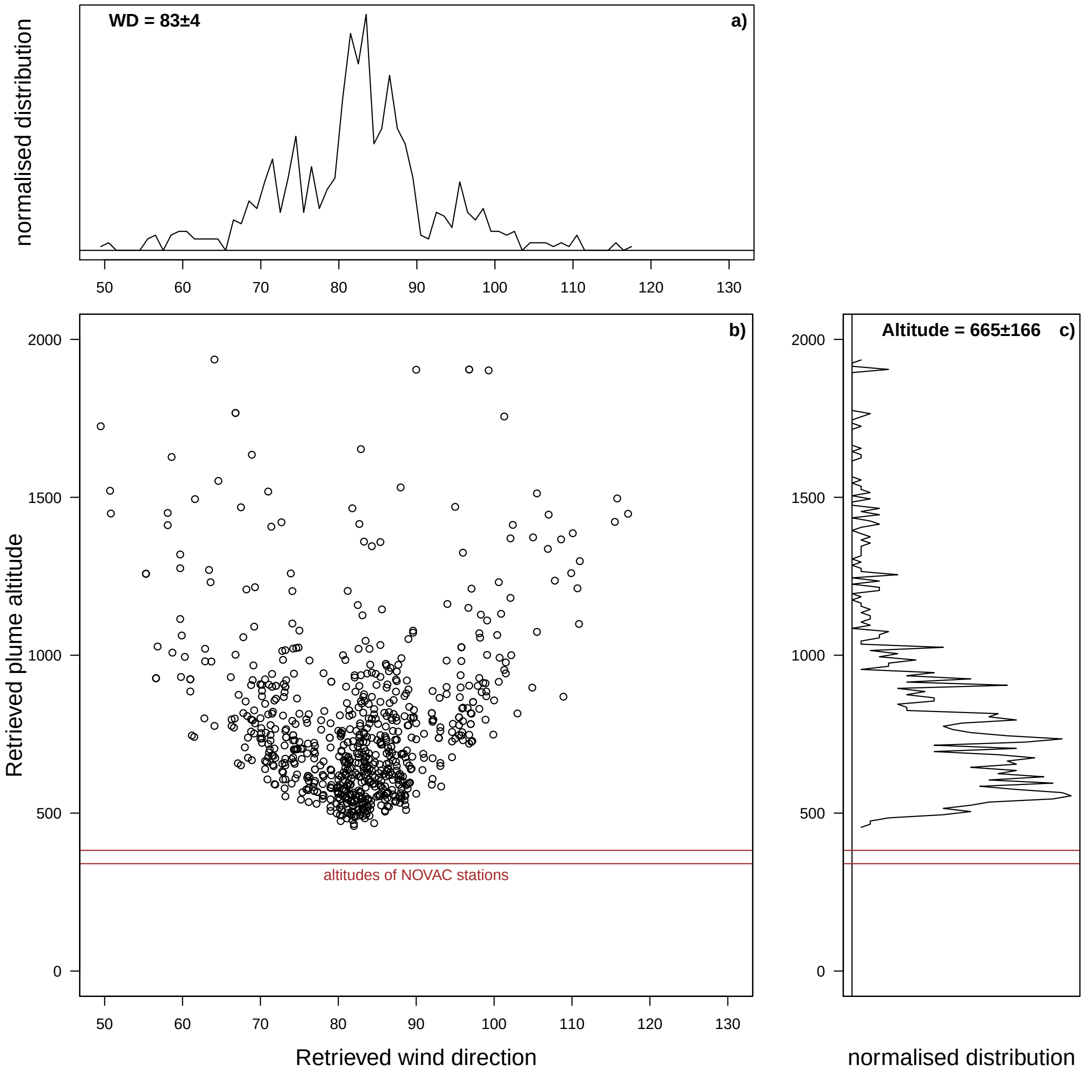

Figure 7.7: Results of plume tomography at Masaya, **a)** Histogram of the retrieved wind directions. **b)** Scatter plot of the retrieved plume altitude as a function of the wind direction. The upper brownish line marks The altitude of the Caracol and Nancital NOVAC stations are marked by the upper and the lower brownish lines. **c)** Histogram of the retrieved plume altitudes.

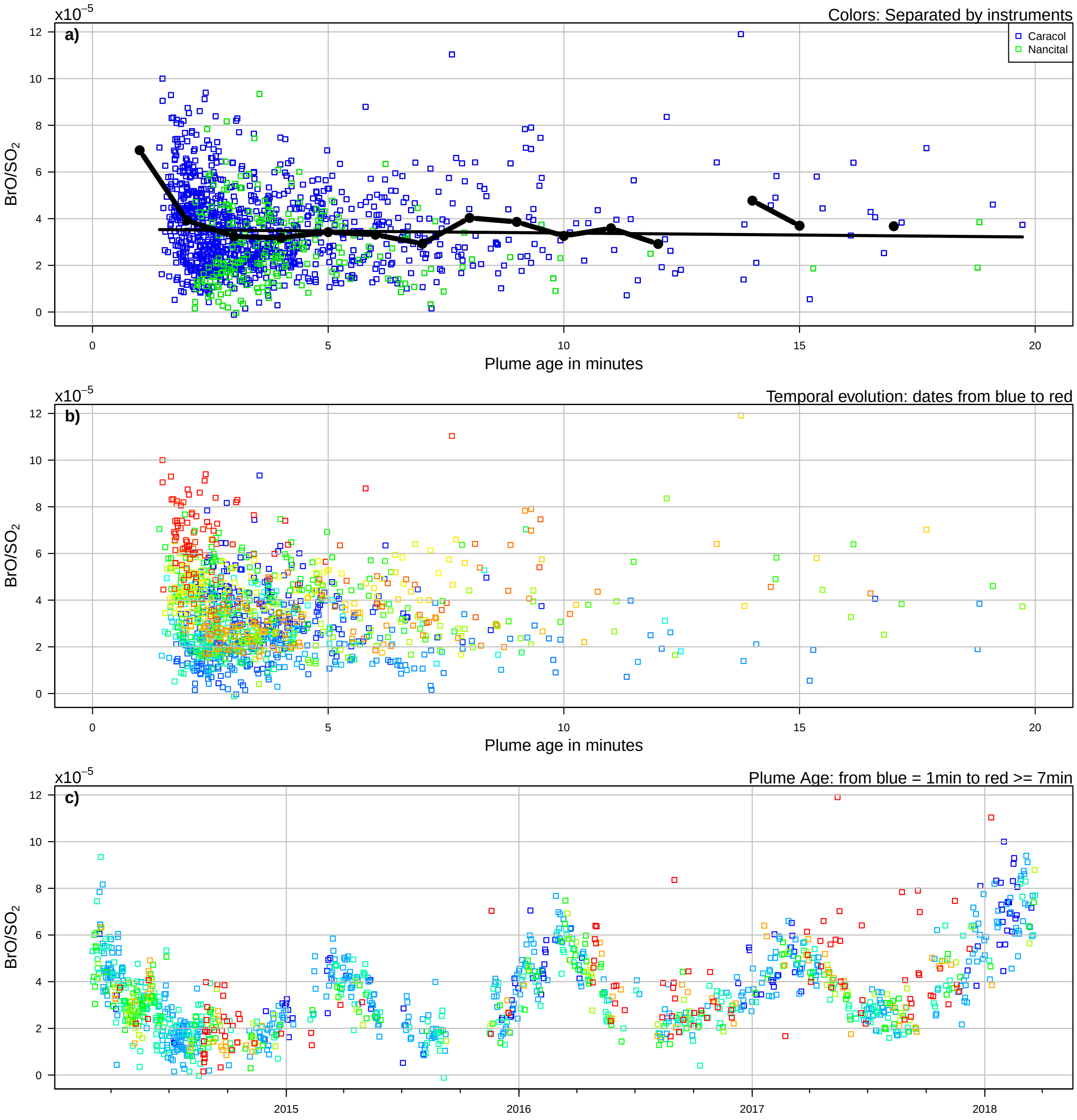

Figure 7.8: BrO/SO$_2$ molar ratio in the volcanic gas plume of Masaya as function of the plume age. **a)** Comparison divided in subsets from the different stations (colour coded). Mean values of 1-mins (black dots) and best matching model $BrO(t) = BrO_0 + const \cdot T_{plume}$. Some few data points with plume ages between $20 - 60$ min are not presented in order to have a better zoom on the first 5 min. **b)** Same comparison but the colour code now indicates the absolute date. **c)** Time series of the BrO/SO$_2$ molar ratios with the plume age colour coded.

impact there and the aerosol phase may in general be extremely acid anyway.
No data for the tropospheric ozone background have been found. On the hand, the maxima of the BrO/SO_2 molar ratios coincide with the expected maxima in northern hemispheric tropospheric background ozone levels (Section 2.3). On the other hand, Masaya is slightly south of the ITCZ in July and within the ITCZ during the summer and thus Masaya may not be considered to be part of the climatological northern hemisphere for most of the year. As a remark, the observed correlation between the BrO/SO_2 molar ratios and the humidity could be a manifestation of the position of the ITCZ instead of a causal link between enhanced humidity and decrease BrO concentrations.

Discussion of the BrO/SO_2 time series The following patterns have been observed in the BrO/SO_2 time series of Masaya's gas plume: (1) an extremely dominant annual periodicity with an amplitude of $1.5 \cdot 10^{-5}$ with maxima in March and minima in September (2) a step increase by $1.4 \cdot 10^{-5}$ in late 2015, and (3) a linear trend of $(0.70 \pm 0.04) \cdot 10^{-5}$ per year since late 2015.
As discussed above, the annual periodicity is most likely a manifestation of the seasonal humidity cycle and may furthermore be affected by the seasonal cycle in the tropospheric ozone background concentration. The step increase in late 2015 coincides with the formation of the current shallow lava lake. The step increase in BrO/SO_2 molar ratios could thus be cause (1) by the evasion of subsurface altering of the gas flow such as the magma-induced evaporation of the former hydrothermal system, (2) by the reduction of the hydrostatic pressure on the upper most magma/lava layers, or (3) by the arrival of juvenile bromine-rich magma in the shallow magmatic system. The linear trend since the formation of the lava lake could indicate the general degassing evolution of the hypothetical batch of juvenile magma since its arrival in the shallow magmatic system in 2015. Accordingly, increasing BrO/SO_2 molar ratios indicate that bromine degasses later than sulphur from (this) magma.

8 Comparison of six NOVAC volcanoes

This chapter presents the retrieved spectroscopic results for three further NOVAC volcanoes: Tungurahua, Galeras, and Villarrica. Finally the major findings of all six volcanoes are compared.

8.1 Tungurahua

Warnach er al. (2019) (including me as co-author) reported and discussed the BrO/SO_2 time series retrieved by the original BrO/SO_2 retrieval proposed by Lübcke et al. [2014]. This section presents the analogous time series when retrieved by the advanced BrO/SO_2 retrieval developed during this thesis. Both time series are compared to each other but no detailed interpretation of the data is aimed for.

Volcanology Tungurahua (1.5°S, 78.5°W, 5023 m a.s.l.) is located on the Eastern Cordillera of the Ecuadorian Andes. Tungurahua is Ecuador's most active volcano [Le Pennec et al., 2008, Bablon et al., 2018]. The last period of unrest ranged from 1999 to 2016. The activity was episodic, with periods of continuous explosions (up to VEI3) lasting for several months in alternation with periods of only little eruptions lasting as well for several months.

DOAS measurements Tungurahua is monitored by DOAS instruments since 2004 and became part of NOVAC as early as 2006 when the three stations Pillate (instrument(s): D2J2140), Bayushig (I2J8546, D2J2236), Huayrapata (I2J8548, D2J2235) have been installed. The fourth station Runtun (D2J2237, D2J2239) has been added in 2011 (Figure 8.1 and Table 8.1). The episodic activity is also observed in the volcanic SO_2 emission fluxes which varied from less than 100 to 35000 tonnes of SO_2 per day where the mean emission flux was about a factor of 1.75 greater during explosive phases compared to the intermediate more quiescent phases [Arellano et al., 2008, Hidalgo et al., 2015].
For the entire period from 2007 to 2016, the maximum SO_2 SCDs remained on the same

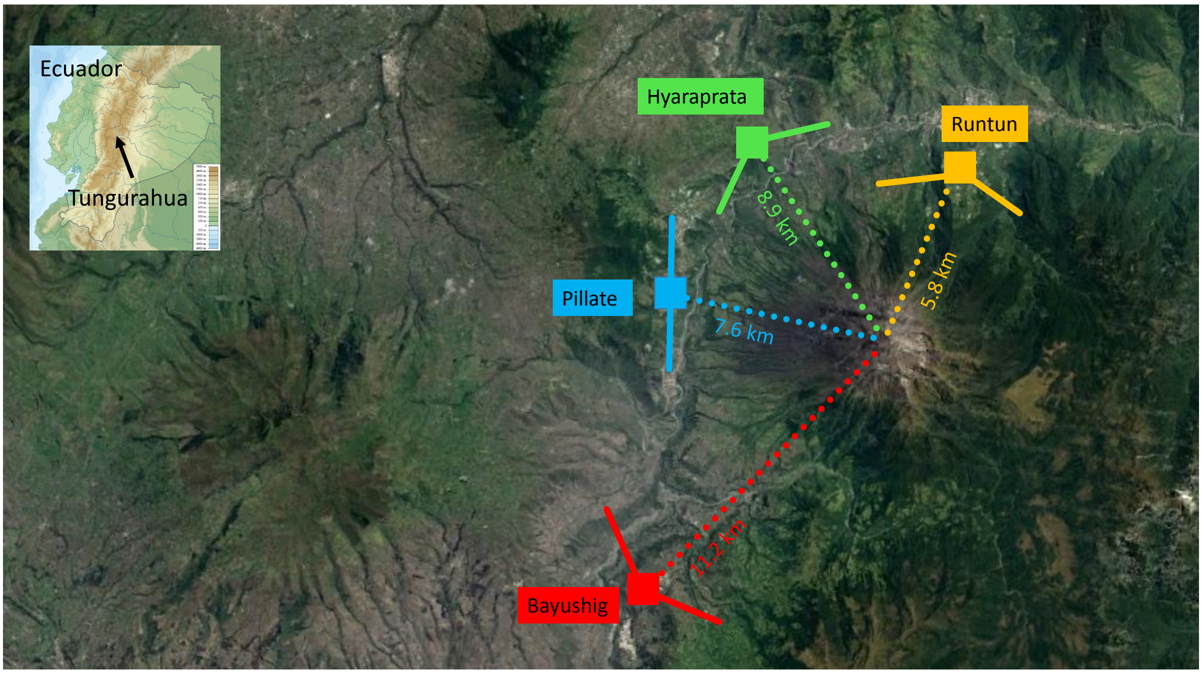

Figure 8.1: Location and scan geometries of the four NOVAC stations at Tungurahua volcano. The map was created with graphical material from Google Earth and https://commons.wikimedia.org/wiki/File:Ecuador_location_map.svg.

Table 8.1: Geometric properties of the NOVAC stations at Tungurahua. See Table 5.1 for details.

NOVAC station	coordinates	altitude	distance	angular position	scan plane angle	cone angle
		A	D	σ	β	
Pillate	-1.45, -78.51	2599 m	7.6 km	104°	90°	90°
Huayrapata	-1.40, -78.94	2911 m	8.9 km	143°	144°	60°
Bayushig	-1.54, -78.52	2783 m	11.2 km	44°	30°	60°
Runtun	-1.42, -78.43	2637 m	5.8 km	201°	202°	60°

level of about $3 \cdot 10^{18}\ \frac{\text{molec}}{\text{cm}^2}$ through the phases of high activity but almost exclusively below the strong plume condition of $7 \cdot 10^{17}\ \frac{\text{molec}}{\text{cm}^2}$ during phases of low activity. Therefore, effectively no BrO/SO_2 molar ratios have been calculated for phases of low activity and the presented BrO/SO_2 time series consequently shows a similar episodic activity pattern with $20 - 30$ separated high activity intervals from $2007 - 2016$ (Figure 8.2). Runtun station observed two exceptionally strong peaks in the SO_2 SCD which last about 2 weeks during the activity episodes in May 2011 and December 2011. Nevertheless, both times the BrO/SO_2 molar ratios retrieved from the Runtun stations are in good agreement with the observations from the other stations. The maxima of the BrO SCDs during the high activity phases varied between $1 - 2 \cdot 10^{14}\ \frac{\text{molec}}{\text{cm}^2}$ and close to the detection limit during low activity phases. The BrO/SO_2 molar ratios varied typically from below $1 \cdot 10^{-5}$ to $10 \cdot 10^{-5}$ and with some further peaks up to $20 \cdot 10^{-5}$.

The BrO/SO_2 time series indicates a step increase in the second half of 2010 between the activity episodes ending in June 2010 and starting in November 2010, respectively (see yellow bars in Figure 8.2c and Figure 8.3). The mean value and standard deviation of the BrO/SO_2 molar ratios has been $(2.5 \pm 1.7) \cdot 10^{-5}$ from April 2007 to June 2010 and $(4.5 \pm 2.3) \cdot 10^{-5}$ from December 2010 to March 2016. The step increase was preceded by an atypical behaviour in the latest activity phase in June/July 2010 where an extremely strong and distinguishable peak in the BrO/SO_2 molar ratios of $8 - 14 \cdot 10^{-5}$ occurred in the middle of the phase compared to the usual ratios of $1.5 - 4 \cdot 10^{-5}$ of at the start and end of this particular activity phase (Figure 8.3).

The Lomb–Scargle analysis proposes a weak periodicity of 282 days in the BrO/SO_2 time series. The origin of this signal is not yet clear. Besides, no other long-term patterns have been observed at Tungurahua neither for the SO_2 and BrO SCDs nor for the BrO/SO_2 molar ratios. It is worth to note that the BrO/SO_2 molar ratios apparently decreases exponentially within the activity phase in January 2008.

Comparison of the spectroscopic results with Warnach et al. [2019] The here presented spectroscopic results are in general in good agreement with the results presented by Warnach et al. [2019]. As expected, the Gaussian plume finder sometimes causes slightly higher SO_2 SCDs compared with the data from Warnach et al. [2019]. Remarkably, the discrepancy gets in the order of up to 30 % for the SO_2 peaks in 2015 and 2016 (while this is not the case for the years 2007 to 2014). Two BrO time series are rather similar. Some outliers are missing vice versa. If they are missing in the data from Warnach et al. [2019], this could be caused e.g. by a plume dilution. If they are missing in the here presented data, they could be filtered out by the additional quality filters. The only extreme discrepancy is again an activity peak in 2016. The BrO/SO_2 molar ratios are similar to the BrO/SO_2 molar ratios by Warnach et al. [2019] when retrieved via the daily mean approach.

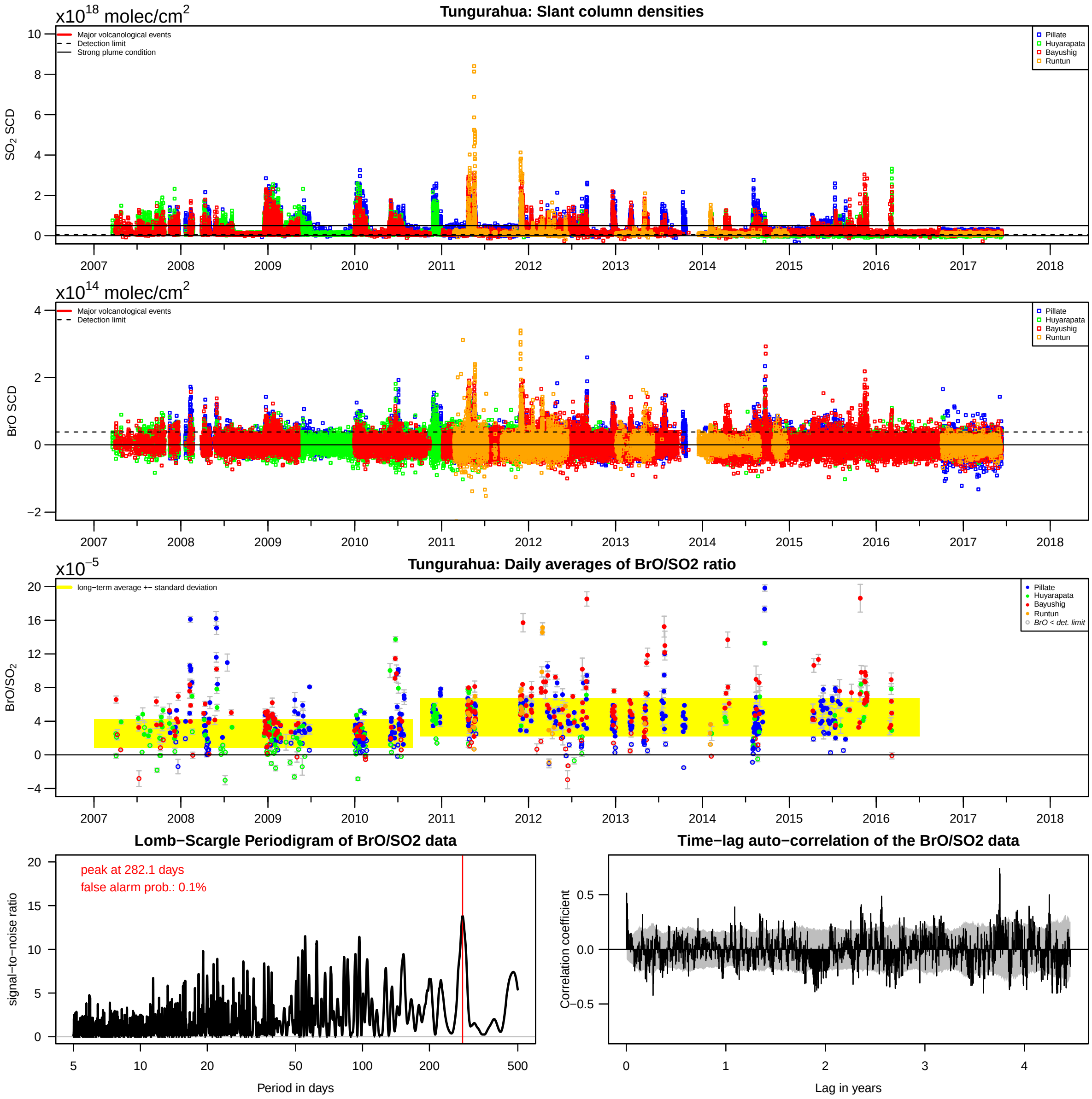

Figure 8.2: Three upper panels: Time series of the slant column densities of SO_2 and BrO and calculated BrO/SO_2 molar ratios in the gas plume emitted from Tungurahua (tick marks indicate first day of the particular (half-)year). The NOVAC stations are indicated by the different colours. BrO data below the detection limit are highlighted by open circles. **Lowest panels:** Lomb–Scargle frequency component analysis and time-lag auto-correlation coefficients (grey region gives 90 % confidence level) of the BrO/SO_2 molar ratio variations.

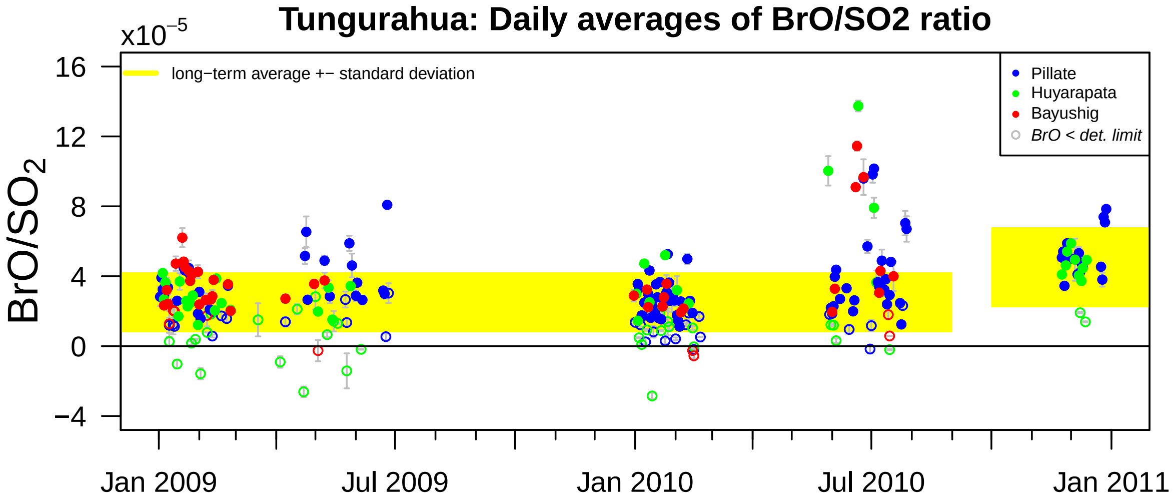

Figure 8.3: BrO/SO_2 molar ratios as Tungurahua in the years 2009 and 2010. The NOVAC instruments are indicated by the different colours. In late 2010, the base line of the BrO/SO_2 molar ratios shifted persistently from 2.5 to 4.5. The last activity episode prior to the step increase exhibited an atypical progress with an extreme BrO/SO_2 peak the the middle of the period.

Discussion of the BrO/SO_2 time series The step increase in late 2010 indicates a distinction of the BrO/SO_2 time series since 2007 in two fundamentally different time intervals (prior and after late 2010). Instrumental ageing can be ruled out as the origin of the step increase with reasonably high probability because it has been observed similarly by all three instruments. Also a persistent offset in the atmospheric chemistry/meteorology is not plausible. Furthermore, Bustillos et al. [2018] propose that the hydrothermal system started to refill beginning in early 2010 what would also rule out that the step increase is caused by less efficient hydrothermal bromine scrubbing after late 2010.

Rendered all other possible origins rather unlikely, the step increase in the BrO/SO_2 molar ratios accordingly indicates a fundamental change in the magmatic system in late 2010. The general volcanic activity indicates a phase shift in summer 2011 from an episodic activity behaviour to a more continuous activity behaviour since November 2011 [Hidalgo et al., 2015]. In contrast, no evidence of a particularly fundamental changed has been reported for late 2010. Accordingly, the step increase in BrO/SO_2 appears to be a precursor of the fundamental changes in 2011.

Warnach et al. [2019] reported a correlation between low BrO/SO_2 molar ratios and high volcanic activity and high BrO/SO_2 molar ratios and low volcanic activity based on the investigation of the individual activity episodes. What holds true for the individual episodes can also hold for the long-term behaviour. Accordingly, the step increase may indicate a step to a generally less active stage followed by the ultimate quiescence since March 2016. Whether this cooldown of the volcanic activity was caused by a degassing of the residual bromine or by a descent of the magma causing less sulphur degassing can however not be distinguished because of the yet limited knowledge on the bromine solubility.

8.2 Galeras

Volcanology Galeras (1.2°N, 77.4°W, 4276 m a.s.l.) is located in the Cordillera Central of the Colombian Andes near the Ecuadorian border. Galeras is the historically most active Colombian volcano (Smithonian Institution: 30 eruptions since 1500 with VEI $1-3$) and became re-actived in 1988 after 50 years of quiescence [Stix et al., 1997]. The reactivation was accompanied by large SO_2 emission fluxes from 1988 [e.g. Fischer et al., 1994, Zapata et al., 1997, Alfaro and Zapata, 1997] until 2009 (Figure 8.5).

DOAS measurements Since 2007, three NOVAC stations monitor Galeras in a distance of $8-13$ km (Figure 8.4 and Table 8.2). From the start of the NOVAC record in December 2007 until May 2009, enhanced SO_2 SCDs of $1-3\cdot 10^{18}\,\frac{\text{molec}}{\text{cm}^2}$ have been observed peaking in May/June 2008. Since May 2009 four further shorter and weaker periods of strong degassing have been detected (September 2009, September 2010, March 2011, February – July 2012) with SO_2 SCDs of up to $1.5\cdot 10^{18}\,\frac{\text{molec}}{\text{cm}^2}$. The mean BrO SCDs have been significantly above the detection limit from May 2008 to May 2009 with maximum values of up to $1.5\cdot 10^{14}\,\frac{\text{molec}}{\text{cm}^2}$. Besides the distinct activity episodes no (linear) trend or periodic pattern has been observed in the SO_2 and BrO SCDs.
From January 2008 to May 2009, the mean BrO/SO_2 molar ratios have been $(1.9\pm 1.5)\cdot 10^{-5}$ with some peaks of up to $6\cdot 10^{-5}$. Furthermore but with only limited statistical significance, the BrO/SO_2 molar ratios have been roughly $4\cdot 10^{-5}$ for the activity episode in September 2009, around or below $1\cdot 10^{-5}$ for the activity episodes in September 2010 and March 2011, and $(2.6\pm 1.9)\cdot 10^{-5}$ during the activity episode from February to July 2012. Accordingly, no persistent long-term trend of the base line has been observed for the BrO/SO_2 molar ratios between 2008 and 2013 and the indicated drop in BrO/SO_2 molar ratios in 2010 and 2011 has no reliable empirical backing.
A statistical analysis of the BrO/SO_2 molar ratios during the activity episode from April 2008 to April 2009 indicates a significant linear trend of $(1.4\pm 0.4)\cdot 10^{-5}$ per year with a proposed mean BrO/SO_2 molar ratio of $1.2\cdot 10^{-5}$ in April 2008 and $2.7\cdot 10^{-5}$ in April 2009. No periodicc patterns have been observed for the activity period (see lowest panels in Figure 8.5).

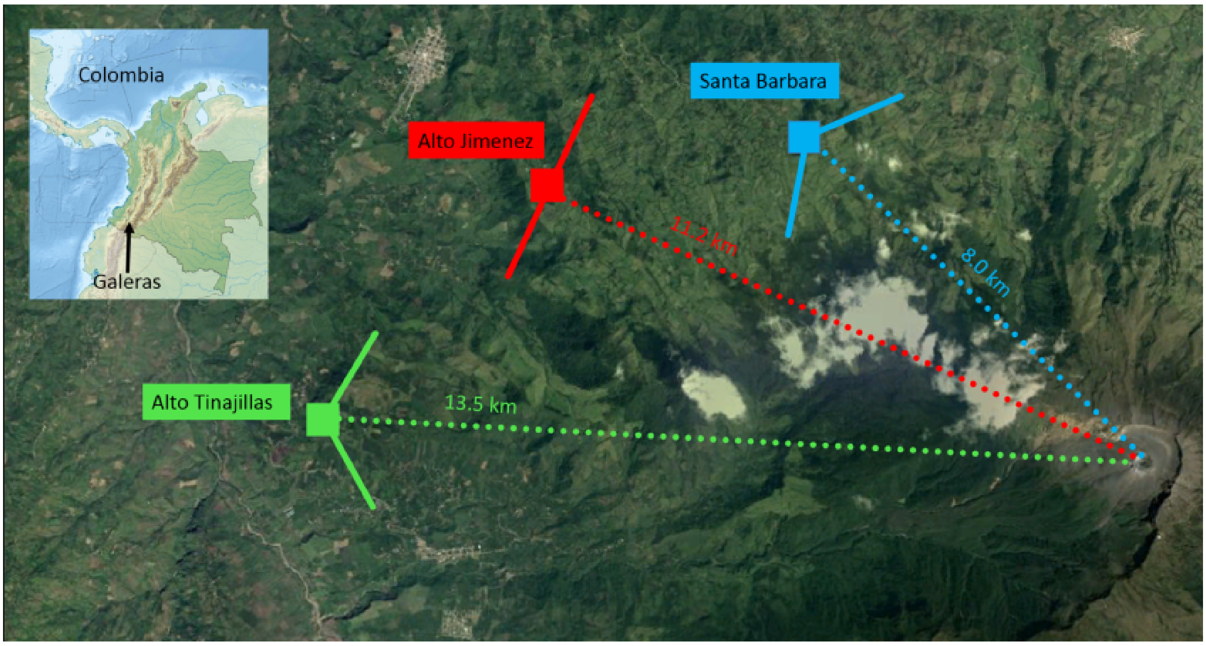

Figure 8.4: Location and scan geometries of the two NOVAC stations at Galeras volcano, the colours match to the time series in Figure 8.5. The map was created with graphical material from https://commons.wikimedia.org/wiki/File:Colombia_relief_location_map.jpg and Google Earth.

Table 8.2: Geometric properties of the NOVAC stations at Galeras. See Table 5.1 for details.

NOVAC station	coordinates	altitude	distance	angular position	scan plane angle	cone angle
		A	D	σ	β	
Santa Barbara	1.27, -77.41	2609 m	8000 m	135°	131°	60°
Alto Tinajillas	1.23, -77.48	2100 m	13500 m	94°	94°	60°
Alto Jimenez	1.26, -77.45	2410 m	11200 m	115°	115°	60°

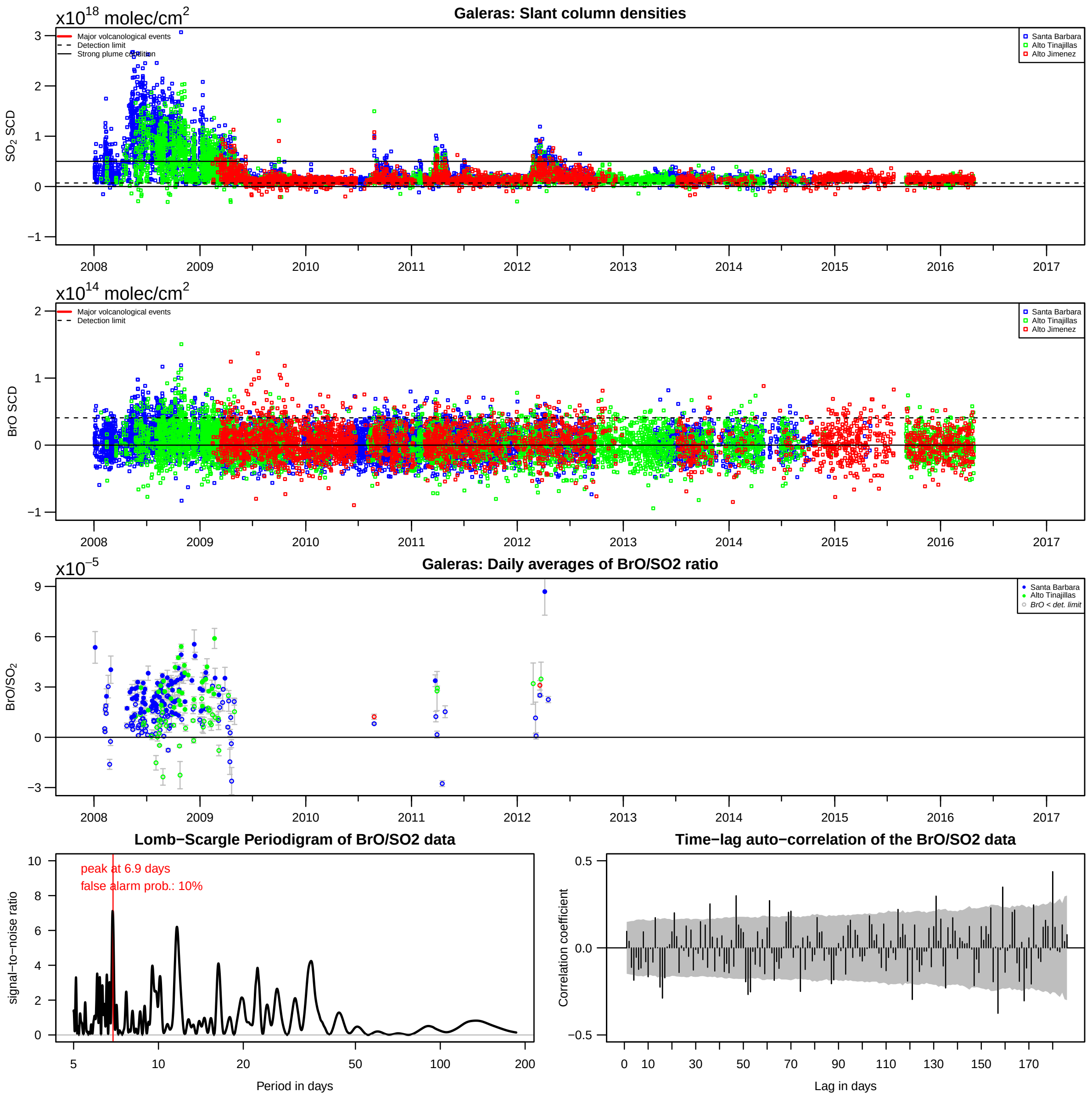

Figure 8.5: Three upper panels: Time series of the slant column densities of SO_2 and BrO and calculated BrO/SO_2 molar ratios in the gas plume emitted from Galeras (tick marks indicate first day of the particular month). The NOVAC stations are indicated by the different colours. BrO data below the detection limit are highlighted by open circles. **Lowest panels:** Lomb–Scargle frequency component analysis and time-lag auto-correlation coefficients (dashed lines give 90 % confidence level) of the BrO/SO_2 molar ratio variations.

8.3 Villarrica

Volcanology Villarrica (39.4°S, 71.9°W, 2860 m a.s.l.) is located in the southern part of the Chilean Andes. It hosts a lava lake since 1985 [Witter et al., 2004]. The hydrothermal system is virtually not existent. Villarrica is permanently active since at least the 14th century (the Smithonian Institution counts 139 individual eruptions since 1384) with a predominant activity of VEI 2 but only VEI 1 for the last 13 eruptions since 1992.

DOAS measurements From late 2009 to late 2013, three NOVAC stations have operated at Villarrica in distances of $7.0 - 9.7\,\mathrm{km}$. From November 2015 to March 2016, again three NOVAC stations have operated at Villarrica, however, the Pichillancahue station had been replaced by the Tralco station and the Las Cascadas station provided data only in December 2015 (Figure 8.6 and Table 8.3).
The observed SO_2 SCDs are in general much lower than for the other volcanoes discussed in this thesis. Only few SO_2 SCDs exceeds the usual "strong plume threshold" of $0.7 \cdot 10^{18}\,\frac{\mathrm{molec}}{\mathrm{cm}^2}$. From February 2010 to March 2012, the maximum daily SO_2 SCDs varied between $0.3 - 1.5 \cdot 10^{18}\,\frac{\mathrm{molec}}{\mathrm{cm}^2}$. After March 2012, virtually all observed SO_2 SCDs were below $0.3 \cdot 10^{18}\,\frac{\mathrm{molec}}{\mathrm{cm}^2}$. From February 2010 to December 2012, the maximum daily BrO SCDs varied between $5 - 10 \cdot 10^{13}\,\frac{\mathrm{molec}}{\mathrm{cm}^2}$ and were thus for most days above the detection limit. From November 2015 to March 2016, the spectroscopic analysis of the data from the new instrument at Los Nevados (D2J2563) results in BrO SCDs which extremely scattered around zero with values of $\pm 2 \cdot 10^{14}\,\frac{\mathrm{molec}}{\mathrm{cm}^2}$. These results appear to be obvious instrumental/spectroscopic artefacts. The presented spectra have nevertheless passed all of the rather conservative quality filters. A more detailed analysis of e.g. the ILS variations is required to understand the origin of these false results. It has to be highlighted that those results have been observed of times of insignificant degassing (as measured by the/any SO_2 threshold) and are thus routinely filtered from the BrO/SO_2 analysis anyway. In order to enhance the temporal resolution of the BrO/SO_2 time series, the SO_2 threshold has been lowered to $3 \cdot 10^{17}\,\frac{\mathrm{molec}}{\mathrm{cm}^2}$ for Villarrica (only). From February 2010 to March 2012, the BrO/SO_2 varied between $2 - 15 \cdot 10^{-5}$. The long-term mean for this period has been $(6.8 \pm 2.7) \cdot 10^{-5}$ which is in perfect agreement with the average BrO/SO_2 molar ratio of $6.9 \cdot 10^{-5}$ reported for Villarrica in November 2004 [Bobrowski and Platt, 2015].

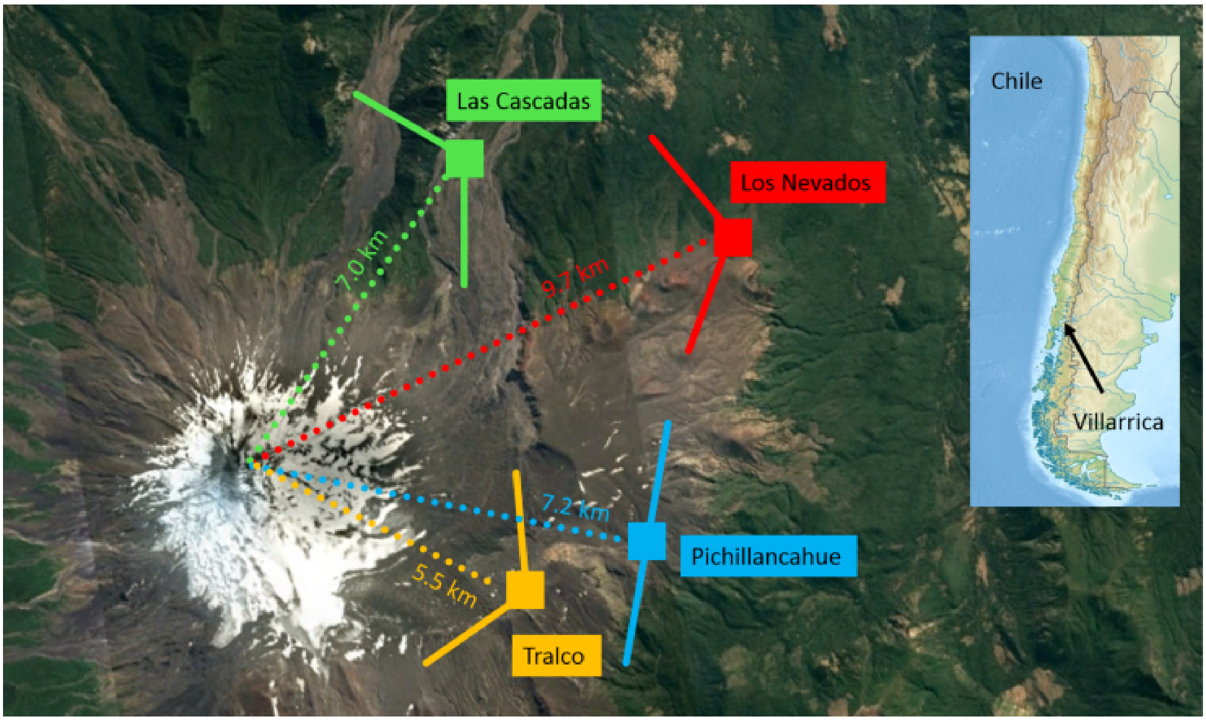

Figure 8.6: Location and scan geometries of the two NOVAC stations at Villarrica volcano, the colours match to the time series in Figure 8.7. The map was created with graphical material from https://commons.wikimedia.org/wiki/File:Relief_Map_of_Chile.jpg and Google Earth.

Table 8.3: Geometric properties of the NOVAC stations at Villarrica. See Table 5.1 for details.

NOVAC station	coordinates	altitude A	distance D	angular position σ	scan plane angle β	cone angle
Pichillancahue	-39.44, -71.86	1584 m	7.2 km	290°	280°	90°
Las Cascadas	-39.38, -71.88	993 m	7.0 km	228°	240°	60°
Los Nevados	-39.40, -71.83	1477 m	9.7 km	256°	260°	60°
Tralco	-39.45, -71.88	1910 m	5.5 km	302°	295°	60°

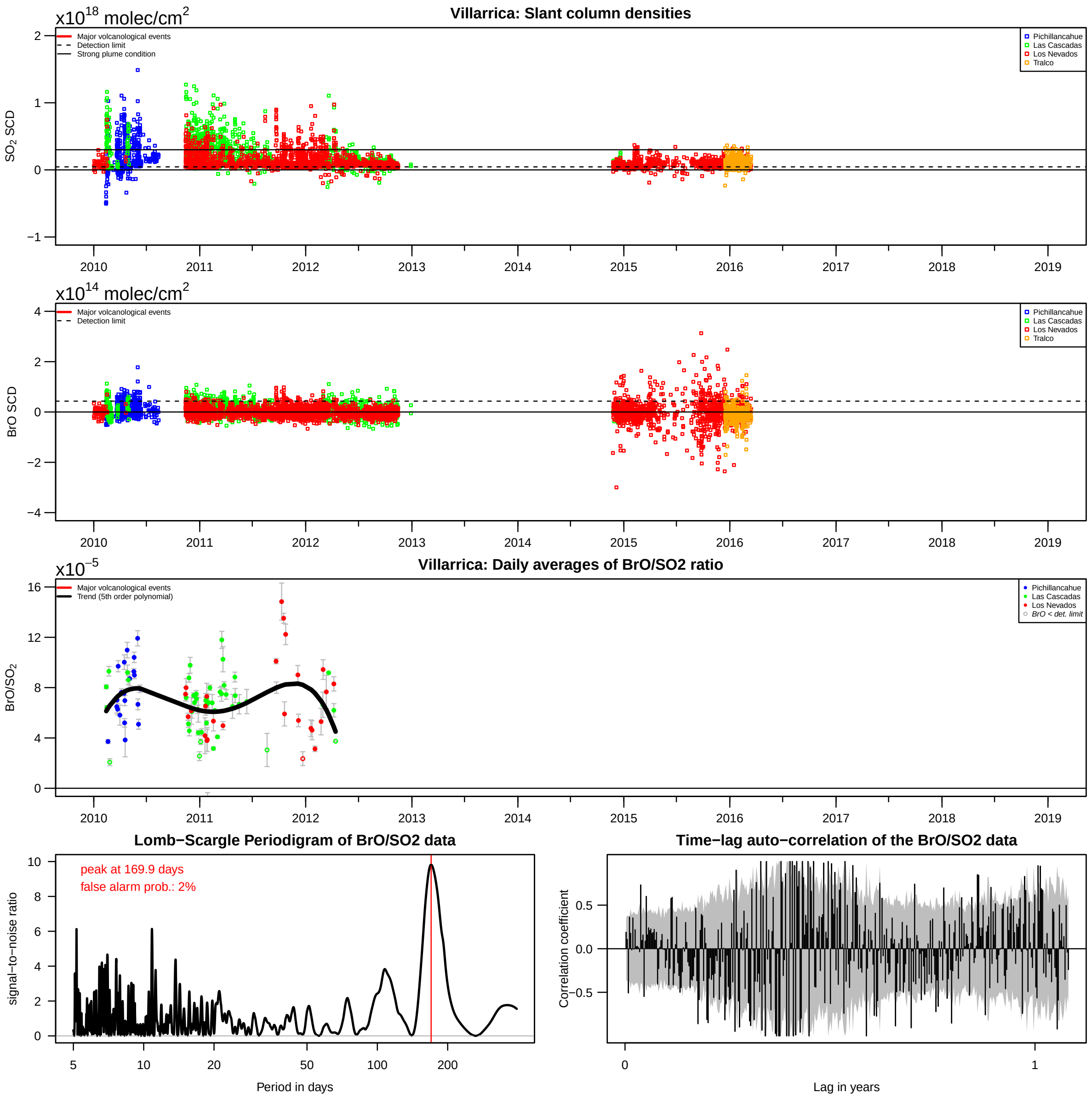

Figure 8.7: Three upper panels: Time series of the slant column densities of SO_2 and BrO and calculated BrO/SO_2 molar ratios in the gas plume emitted from Villarrica (tick marks indicate first day of the particular month). The NOVAC stations are indicated by the different colours. BrO data below the detection limit are highlighted by open circles. **Lowest panels:** Lomb–Scargle frequency component analysis and time-lag auto-correlation coefficients (grey region gives the 90 % confidence level) of the BrO/SO_2 molar ratio variations.

8.4 Intercomparison of NOVAC results

The core of the comparison are the four evaluated volcanoes in Ecuador and Colombia which are located in the same proximity (1.5°S – 4.9°N). These four volcanoes will be called the "central volcanoes" in the following comparison. The set is complemented by Masaya (12.0°N) somewhat above the northern edge of the Andes and Villarrica (39.4°S) at the southern part of the Andes. While the volcanic systems of the these six volcanoes are all fed by the subduction of the pacific plate(s), differences in their volatile budgets are nevertheless expectable. Although the volcanoes differ in their activity and eruption behaviour some global similarities have been observed.

Quantitative scale of the BrO/SO_2 molar ratios For the four central volcanoes and averaged over the entire time series, the daily means of the BrO/SO_2 molar ratios varied between $(1.8 - 4.2) \cdot 10^{-5}$ accompanied by an absolute and relative standard deviation of the daily means varying between $(1.4 - 3.2) \cdot 10^{-5}$ and $(50 - 78)\,\%$ (Figure 8.8). Ignoring Galeras, the other three volcanoes agree in a long-term BrO/SO_2 base line of $(3.3 - 4.0) \cdot 10^{-5}$. It has to be highlighted that the Galeras data have been observed exclusively during a phase of strong general volcanic activity. The long-term average of Galeras could thus been biased towards lower BrO/SO_2 molar ratios which is in good agreement with the general findings of this thesis that strong volcanic activity anti-correlates with the BrO/SO_2 molar ratio (see below).
For Masaya, the average daily mean of the BrO/SO_2 molar ratios is $4.0 \cdot 10^{-5}$ accompanied by an absolute and relative standard deviation of $2.0 \cdot 10^{-5}$ and 50 %. This overall average is in perfect agreement with the findings for the three/four central volcanoes. For Villarrica, the average daily mean of the BrO/SO_2 molar ratios is $6.9 \cdot 10^{-5}$ accompanied by an absolute and relative standard deviation of the daily means of $2.5 \cdot 10^{-5}$ and 36 %. Villarrica and Masaya (since 2015) host lava lakes. The lava lake formation at Masaya was accompanied by an apparent step increase in the BrO/SO_2 molar ratios by $2 \cdot 10^{-5}$. This observation together with the generally enhanced BrO/SO_2 molar ratios at Villarrica could indicate that the Br/S molar ratio directly released from a lava lake is more representative for the real Br/S molar ratio in the shallow magmatic gas phase while the real Br/S molar ratios gets systematically reduced during the degassing through the solid material in the volcanic vent of partially closed systems and/or through a hydrothermal system.
All 6 NOVAC volcanoes are in agreement with the global range of BrO/SO_2 molar ratios for South American volcanoes of $(1.1 - 6.9) \cdot 10^{-5}$ [Bobrowski and Platt, 2015].

Annual periodicities in the BrO/SO_2 molar ratios For Nevado del Ruiz and Masaya annual periodicities have been detected in the BrO/SO_2 time series. Plausible meteorological origins for this pattern in the BrO/SO_2 time series are (1) seasonal variations

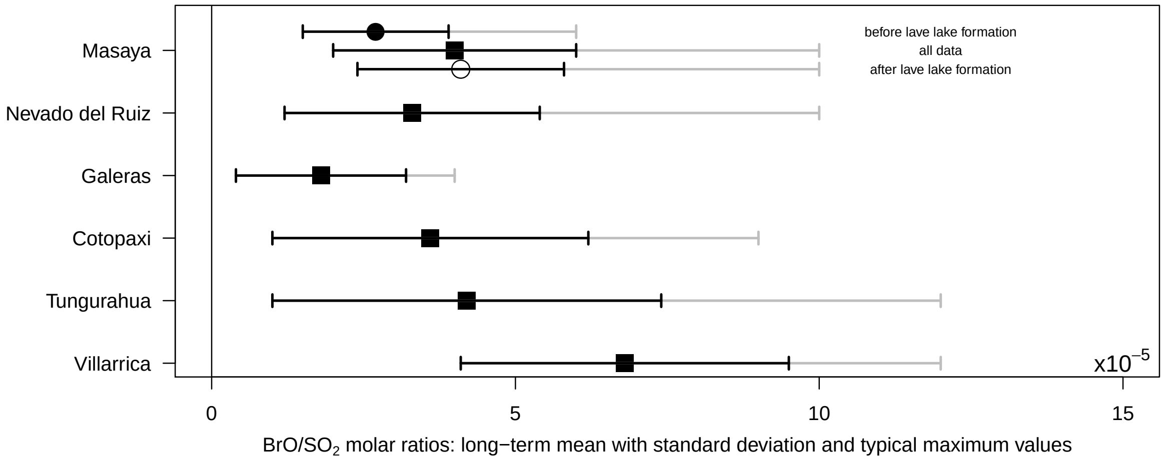

Figure 8.8: Comparison of the six presented NOVAC volcanoes: Long-term mean values of the BrO/SO_2 molar ratios with long-term standard deviation and the typical maximum values (neglecting some single outliers). The Masaya results are presented for three different time ranges.

of the ambient temperature variations which affect the instrumental line function, (2) seasonal variations in the wind field which affect the observed plume age, (3) seasonal variations of the humidity which affect the bromine chemistry in the volcanic gas plume, (4) seasonal variations in the tropospheric ozone background which affect the bromine chemistry in the volcanic gas plume, and (5) seasonal variations in the rainfalls which affect the hydrothermal system. In addition to these superficial mechanisms, (6) a magmatic origin of the seasonal variations appears to be unexpected. Further, while the semi-diurnal Earth tide or the spring-neap Earth tide cycle may have an impact on the magmatic system, (7) the annual modulation of the tidal potential is rather small and thus not expected to be significant.

(1) The instrumental variations have been examined in great detail for the predominant instrument at Nevado del Ruiz and to a lesser extent for the instruments at Masaya (in particular no manual modelling of the instrument line function has been conducted there). No seasonal patterns have been found for any of the investigated instrument properties. Accordingly, the seasonal BrO/SO_2 variations are not caused by instrument effects. (2) A correlation of the BrO/SO_2 molar ratios with the plume age of the observed volcanic gas plume has been found for Nevado del Ruiz (correlation coefficient of 0.31), however, a proposed correction of the plume age effects does not cause the annual cycle in the BrO/SO_2 molar ratios to vanish but rather shifts the cycle by about 1 month. No such correlation has been observed at Masaya. (3) Strong anti-correlations between the BrO/SO_2 molar ratios and the specific and relative humidity have been found for Masaya (correlation coefficients of $-42\,\%$ and $-32\,\%$) but no such correlations have been found for Nevado del Ruiz and Cotopaxi. (4) A qualitative comparison of the seasonal extrema of the BrO/SO_2 molar ratios and the tropospheric ozone back-

ground proposes a positive correlation for both volcanoes if Masaya is considered to be affected by the northern climatological hemisphere and Nevado del Ruiz to be affected of the southern climatological hemisphere. This is plausible because Nevado del Ruiz — although located at 4.9°N — is all the year south of the inner tropical convergence zone. (5) Masaya currently hosts no hydrothermal system and thus there the rainfall patterns can be assumed to have no impact on the volcanic gas emissions. For Nevado del Ruiz, the BrO/SO_2 molar ratios and the rainfall patterns correlates positively if a ground penetration time of about 4 months is assumed or negatively if a ground penetration time of about 10 months is assumed. The first — i.e. higher BrO/SO_2 after the rain season — would contradict the expectation that a larger hydrothermal system reduces the Br/S molar ratio of a crossing gas flow. The latter appears to be a rather long ground penetration time.
For all other volcanoes including Villarrica no such annual patterns have been observed, however, the episodic sampling rate or temporal range of their time series do not allow to rule out the possibility of an undetected annual cycles.

Fortnightly periodicity For Cotopaxi, a persistent fortnightly periodic pattern has been observed in the BrO/SO_2 time series. Several plausible causes for this signal have been assessed to be rather unlikely. The Earth tidal forcing has been discussed as the best candidate with an unexpected high correlation coefficients of 50 % when compared with the North–South displacement and −41 % when compared with the vertical displacement. For all other volcanoes, no persistent fortnightly periodicity has been observed. For Masaya such a pattern can be observed for limited time intervals. For Nevado del Ruiz some time intervals indicate a weak monthly periodic pattern. If the hypothesis of Earth tidal impact on Cotopaxi holds true, not detecting the Earth tidal impact indicated that the volcanic systems of the other volcanoes are temporarily not excitable by the Earth tides. Chapter 9 sets up a model on the link between Earth tides and volcanic degassing.

Extraordinary drops in the BrO/SO_2 time series For Nevado del Ruiz, two extraordinary drops by about $2 \cdot 10^{-5}$ have been observed which persisted for several months. Both drops have incided just several months ahead of the two major peaks in volcanic activity since 2010. This poses the BrO/SO_2 molar ratios as potential precursor for volcanic hazards at Nevado del Ruiz. No such extraordinary drops have been observed for the other volcanoes prior to major volcanic activity changes.

Long-term increase in BrO/SO_2 molar ratios during an eruption period For the four central volcanoes plus Masaya, the BrO/SO_2 molar ratios have been significant greater at the end of evaluated time series compared to the beginning of the evaluated time series. The increase either happened by a continuous approximately linear trend or a step increase (both usually superimposed by periodic patterns, extraordinary peaks, or natural short-term variability). For Nevado del Ruiz and Masaya the eruption period started prior to the NOVAC record and is still ongoing. For Tungurahua the eruption period has started prior to the NOVAC record but stopped in 2016. For Cotopaxi and Galeras the NOVAC record covers a complete period of prominent activity. Linear trends have been observed at least for subsets of the BrO/SO_2 time series for Nevado del Ruiz ($(-1.37 \pm 0.16) \cdot 10^{-5}$ per year from December 2010 until early 2012 and $(0.88 \pm 0.05) \cdot 10^{-5}$ per year from early 2015 until August 2018), Galeras ($1.1 \cdot 10^{-5}$ per year between 2008 and 2009), and Cotopaxi ($(2.4 \pm 1.4) \cdot 10^{-5}$ per year extrapolated from the trend from September 2015 to April 2016). Three persistent step increases have been observed in the BrO/SO_2 time series for Cotopaxi (from about $1 \cdot 10^{-5}$ to $4 \cdot 10^{-5}$), Masaya (from $2.7 \cdot 10^{-5}$ to $4.7 \cdot 10^{-5}$), and Tungurahua (from $2.5 \cdot 10^{-5}$ to $4.0 \cdot 10^{-5}$). For Villarrica, the larger part of the BrO/SO_2 data indicates a decrease in BrO/SO_2 molar ratios from $7.5 \cdot 10^{-5}$ in 2010 to $4.5 \cdot 10^{-5}$ in 2012. In September/October 2011, however, a persistent peak of about $13 \cdot 10^{-5}$ has been observed resulting in a rather constant BrO/SO_2 molar ratios from $2010 - 2012$ when the peak is not neglected from the averaging.

Instrumental artefacts or meteorological variations appear to be rather unlike explanations for these persistent increases, first of all because all instruments would had to have the same simultaneous one-time ageing effects and there is no meteorological mechanisms which let us expect such a significant and global change of the atmospheric chemistry. The only plausible monotonous meteorological trend would be the global warming and the accompanying climate change but it is not expected that it can cause such significant changes on time scales of years.

Anti-correlation between BrO/SO_2 molar ratios and volcanic activity With instrumental and atmospheric origins ruled out in particular as causes for the persistent long-term increases in the BrO/SO_2 molar ratios (see last paragraph), these increases have to be caused by volcanological origins, e.g. due to hydrothermal variations or magmatic variations. The first explanation follows the rational that the Br/S molar ratio should be the lower the stronger the hydrothermal system scrubs crossing gas flows released from the magmatic gas phase. Accordingly, then the long-term increase in BrO/SO_2 molar ratios indicates that with ongoing magmatic activity the hydrothermal system either shrinks continuously or gets increasingly saturated in bromine. A step increase may be caused by single strong evaporation events which transform the hydrothermal system to a state of negligible scrubbing potential and thus constant average BrO/SO_2 molar ratios afterwards.

If also a hydrothermal origin can be ruled out, the observed long-term Br/S increase have to be caused by a change in the magmatic gas source either by entry of juvenile magma in the shallow chamber with another bromine to sulphur molar ratio or by a change in the magma pressure e.g. due to cooling. The juvenile magma approach does not fit to the observation that the eruptive period general calms down. The decreasing pressure approach implies that bromine degasses predominately “later” than sulphur, either because then the pressure is lower or because the melt composition has further due to magma cooling.

Part III: Models

9 On the link between the Earth tides and volcanic degassing

This theoretical model has been published in [Dinger et al., 2019]. This chapter is in large parts a literal reproduction of this publication in order to keep the high level of readability obtained by the peer-review process. This decision is further manifested in the text by keeping the "we"-narrator.

Motivation In view of the growing number of studies revealing similar biweekly patterns in volcanic activity, this paper investigates whether a causality from the tidal potential to variations in the volcanic degassing is analytically traceable in a comprehensible way. High-temperature gas emissions of persistently strong passively degassing volcanic systems are commonly thought to be fed by sustained magma convection reaching the uppermost portions of the volcanic conduit, where volatile-rich low-viscous magma ascends through essentially degassed magma of higher viscosity, which in turn descends at the outer annulus of the conduit [Kazahaya et al., 1994, Palma et al., 2011, Beckett et al., 2014]. Magma ascent rates associated with such convective flow typically vary roughly between 1 and 100 $\mathrm{m\,h^{-1}}$ [Cassidy et al., 2015, 2018] and thus are orders of magnitudes larger than what we can derive for potentially tide-induced vertical magma displacement rates of at most 0.6 m within 6 h (if not further amplified). A comprehensive model of the tidal impact on the magma motion thus requires a coupling of the convective and the tide-induced transport mechanisms.
Our conceptual model aims to provide the first step by investigating the purely tide-induced transport mechanism acting on the low-viscous inner magma column neglecting any interferences between the magma ascent and the tidal mechanism, i.e. the model ignores the magma convection in the column. We model the response of such a quasi-static magmatic system (volcanic conduit connected to a laterally more extended deeper magma reservoir) to tide-induced gravity variations analogously to the response of a classical mercury thermometer to temperature variations: the tide drives a periodical expansion of the magma in the reservoir which leads to a periodical vertical displacement of the low-viscous magma column in the conduit.
We derive the temporal evolution and amplitude of the vertical magma displacement across the radial conduit profile and examine its impact on the bubble coalescence rate. In order to introduce our novel approach comprehensibly, the modelled processes and

conditions are as simplified as suitable; the major simplifications are listed in Appendix A. All findings in this paper are derived analytically. The quantitative model estimates are presented for two exemplary magmatic systems. These examples are intended to match simplified versions of the Villarrica (39.5°S) and Cotopaxi (0.7°S) volcanoes, where covariation between outgassing activity and Earth tidal movements has been observed previously [Bredemeyer and Hansteen, 2014, Dinger et al., 2018, or this thesis, respectively]. The associated model parameter sets are listed in Table 9.1. Further, all quantitative estimates are presented for the spring tide, and the consequences of the contrast between spring tide and neap tide are discussed in the last part of this chapter.

9.1 Tide-induced magma displacement in the conduit

Model set-up We model the magmatic system analogously to established convection models [Kazahaya et al., 1994, Palma et al., 2011, Beckett et al., 2014], with the exception that the descending high-viscous magma annulus is assumed to be not affected by the tide-induced dynamics and therefore is considered as an effective part of the host rock, while "conduit" refers in our model exclusively to the ascending low-viscous magma column. We assume the conduit to be a vertically oriented cylinder with length L_c, radius R_c, and cross-sectional area $A_c = \pi \cdot R_c^2$ which is confined by the penetrated host rock (and high-viscous magma annulus), connected to a deeper, laterally more extended magma reservoir with volume V_r and centre of mass at a depth D_r, and either exhibiting an open vent or capped by a gas-permeable solid plug (Figure 9.1). The magmatic melt in the conduit is modelled as a mixture of a liquid phase and a gas phase having a mean density ρ_{melt}, which varies with pressure and thus depth, a constant kinematic bulk viscosity ν, and homogeneous local flow properties. The magma compressibility $\beta(\phi)$ strongly depends on the gas volume fraction ϕ and lies between the compressibility $\beta(0) = 2 \cdot 10^{-10}\,\mathrm{Pa}^{-1}$ of volatile-rich rock and the compressibility $\beta_0(1) \approx p^{-1}$ of an ideal gas [see e.g. Tripoli et al., 2016]. The magmatic melt in the reservoir is modelled to be volatile-rich but hosting no gas phase of significant volume and thus having a constant compressibility $\beta_r \approx \beta(0)$. Further, the quasi-static condition implies a steady-state density stratification within the magma and also with respect to the host rock [no neutral buoyancy, Parfitt et al., 1993]. In this equilibrium, we assume a constant hydrostatic pressure gradient $(\nabla p)_{vert}$.

Response of the host rock on tidal stresses Magma pathways are often located at intersection points of large-scale fault systems [Nakamura, 1977, Takada, 1994], or in fault transfer zones [e.g., Gibbs, 1990], where the surrounding host rock geometry is relatively sensitive to directional changes in pressure. The vertical and horizontal

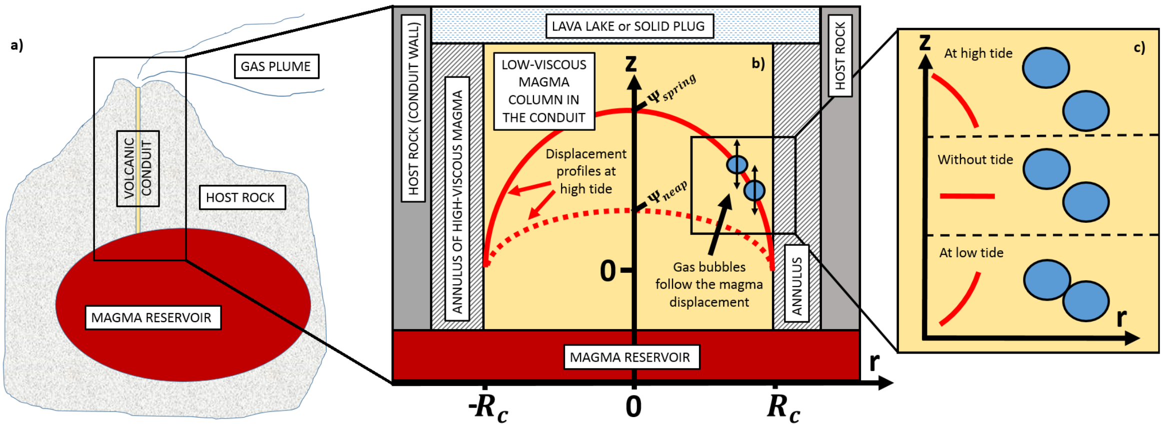

Figure 9.1: a)+b) Sketch of the model set-up. The model compartments are indicated by white boxes but not depicted to scale. **b)** The semi-diurnal tide causes a radial magma displacement profile in the conduit with different amplitudes during spring tide and neap tide. **c)** Concept of the tide-enhanced bubble coalescence: Two bubbles which are initially close to each other (see "without tide") exhibit differential vertical tide-induced displacements, which enhances the chance for bubble coalescence (here "at low tide").

components of the tidal force exert additive shear tension on the host rock, potentially causing a compression of the host rock [Sottili et al., 2007] or a differential slip between both sides of the fault system [Ide et al., 2016]. Both mechanisms can cause an increase in the areal conduit cross section. Connected to the magma reservoir, such an increasing conduit volume is accompanied by decompression and thus causes a magma to flow from the reservoir to the conduit which pushes the initial magma column in the conduit upwards until the initial hydrostatic pressure gradient is re-established. Vice versa a relative decrease in the areal conduit cross section leads to an effective descent of the initial magma column in the conduit. For a given periodic area increase ΔA_c, the amplitude Δz_{hr} of this additive elevation-descent cycle of the centre of mass of the initial magma column is given by

$$\Delta z_{hr} = \frac{L_c}{2} \cdot \frac{\Delta A_c}{A_c + \Delta A_c} \approx \frac{L_c}{2} \cdot \frac{\Delta A_c}{A_c} \tag{9.1}$$

The quantitative scale of tide-induced conduit cross section variations is presumably hardly accessible. The theoretical horizontal components of the tide-induced ground surface displacement are up to about ±7 cm [Baker, 1984]. Slip-induced dilation of faults with widths in the sub-centimetre range thus appear to be plausible. For illustration, a conduit radius increase by $\Delta R_c = 1\,\text{mm}$ would result in an additive vertical centre of mass displacement by $\Delta z_{hr} = 0.33\,\text{m}$ for Villarrica and $\Delta z_{hr} = 0.13\,\text{m}$ for Cotopaxi. As a remark, these mechanisms do not require a cylindrical conduit and fault-slip mechanisms would rather lead to an uni-directional area increase rather than a homogeneous radial increase. Furthermore, the tide could also cause a variation in the host rock permeability [Bower, 1983, Elkhoury et al., 2006, Manga et al., 2012]. This mechanism and its possible interference with the concept presented here are ignored in our model.

Tide-induced magma expansion in the reservoir The semi-diurnal tide causes a sinusoidal variation in the gravitational acceleration with angular frequency $\omega_{sd} = 1.5 \cdot 10^{-4}\,\mathrm{rad\,s^{-1}}$ and amplitude (equals the half peak-to-peak amplitude) $a_0^{st} = 1.4\,\mathrm{\mu m\,s^{-2}}$ during spring tide and $a_0^{nt} = 0.5\,\mathrm{\mu m\,s^{-2}}$ during neap tide. Besides those host rock mechanisms triggered by the tidal stresses, also these tide-induced gravity variations may cause a periodical elevation of the magma in the inner conduit. The compressible magma in the reservoir is pressurised by the hydrostatic load whose weight is proportional to the local gravitational acceleration g. A reduction in the local gravitational acceleration by a_0 leads to a decompression and thus expansion of the magma in the reservoir by $\Delta V_r = \frac{a_0}{g} \cdot (\nabla p)_{vert} \cdot D_r \cdot \beta_r \cdot V_r$. The tidal force can accordingly lead to a periodical magma expansion–shrinkage cycle in the reservoir with a semi-diurnal periodicity and an amplitude modulation within the spring–neap tidal cycle of up to $\Delta V_r \sim \mathcal{O}(100 - 1000\,\mathrm{m}^3)$.

The realisation of this additional magma volume implies a displacement and thus compression of the host rock at the location of maximum host rock compressibility. This is typically true for the conduit. Assuming that the magma expansion in the reservoir ultimately and exclusively causes an increase in the conduit volume, the volume increase causes an elevation of the centre of mass of the initial magma column in the conduit by

$$\Delta z_{dec} = \frac{\Delta V_r}{A_c} = \frac{a_0}{g} \cdot (\nabla p)_{vert} \cdot D_r \cdot \beta_r \cdot \frac{V_r}{\pi \cdot R_c^2} \tag{9.2}$$

In the general case, the additional volume could be realised by a slight increase in the conduit radius by $\Delta R_{dec} \approx \frac{R_c}{2} \cdot \frac{\Delta z_{dec}}{L_c} \sim \mathcal{O}(1\,\mathrm{mm})$ caused, for example, by the tidal stresses. If the magmatic system has an open vent, the additional volume can alternatively be realised by an elevation of the lava lake level and thus without a host rock compression.

Analogously, the tide-induced gravity variations result in an expansion of the initial magma column in the conduit. This effect is, however, typically negligible compared to the reservoir effect for sufficiently large reservoirs (volume contrast between reservoir and conduit of more than 1000; see Table 9.1); thus, for simplicity we neglect the effect of the expansion of the initial magma column in the conduit.

The responses of the overall magmatic system on the tidal stresses and tide-induced gravity variations act simultaneously and in phase with the tidal force. The overall vertical tide-induced magma displacement in the conduit Δz_{max} can thus be larger then the individual mechanisms, i.e. $\{\Delta z_{hr}, \Delta z_{dec}\} \leq \Delta z_{max} < \Delta z_{hr} + \Delta z_{dec}$. In the following we focus on the reservoir expansion mechanism only in order to keep the derivation of the model parameters strictly analytical. The host rock mechanism is therefore reduced to establishing the required areal conduit cross section increase of ΔR_{dec}.

Radial flow profile in the conduit The tide-induced vertical magma displacement in the conduit is delayed and extenuated by a viscosity-induced drag force. We access the temporal evolution and amplitude of the tide-induced displacement via the force (per unit mass) balance acting on the centre of mass of the magma column in the conduit

$$\underbrace{\overbrace{\gamma \cdot \dot{z}(t)}^{\text{inner force}}}_{\text{drag force}} = \overbrace{\underbrace{a_0 \cdot \sin(\omega_{sd} \cdot t)}_{\text{tidal force}} - \underbrace{\omega_0^2 \cdot z(t)}_{\text{restoring force}} - \underbrace{\ddot{z}(t)}_{\text{inertial force}}}^{\text{external force}} \tag{9.3}$$

where the two model parameters are the bulk damping rate γ and the eigenfrequency ω_0 of the magma column. The restoring force ensures that the centre of mass displacement tends towards the current "equilibrium" displacement associated with the current strength of the tidal force, i.e. $a_0 = \omega_0^2 \cdot \Delta z_{max}$. We further assume a Newtonian bulk drag force proportional to the flow velocity.

The continuity condition implies that the magma flows faster in the conduit centre than close to the boundary between the low-viscous and high-viscous magma/host rock. Accordingly, we assume a no-slip condition at the conduit boundary $r = R_c$ and derive the analytical solution of the tide-induced parabolic vertical displacement profile $z(r,t)$ in the conduit

$$\begin{cases} z(r,t) &= \Psi \cdot \left[1 - \left(\frac{r}{R_c}\right)^2\right] \cdot \sin(\omega_{sd} \cdot t - \varphi_0) \\ \Psi &= \dfrac{2 \cdot a_0}{\sqrt{(\omega_0^2 - \omega_{sd}^2)^2 + (\gamma \cdot \omega_{sd})^2}} \\ \varphi_0 &= \arctan\left(\dfrac{\gamma \cdot \omega_{sd}}{\omega_0^2 - \omega_{sd}^2}\right) \\ \gamma &= \dfrac{8 \cdot \nu}{R_c^2} \\ \omega_0^2 &= \dfrac{a_0}{\Delta z_{dec}} = \dfrac{g \cdot \pi \cdot R_c^2}{\beta_r \cdot V_r \cdot D_r \cdot (\nabla p)_{vert}} \end{cases} \tag{9.4}$$

with the radial coordinate $0 \leq r \leq R_c$, the maximum vertical magma displacement amplitude Ψ (which equals twice the centre of mass displacement) and the phase shift φ_0 between tidal force and magma displacement in the conduit (see Appendix C).

For Villarrica, the model implies a tidal displacement amplitude of $\Psi_{vill}^{st} = 0.45\,\text{m}$ which lags behind the tide by $\varphi_{0,vill} \cdot \omega_{sd}^{-1} = 2.0\,\text{h}$, where the displacement is predominantly limited by drag force. For Cotopaxi, the tidal displacement amplitude is $\Psi_{coto}^{st} = 0.09\,\text{m}$

and lags by $\varphi_{0,coto} \cdot \omega_{sd}^{-1} = 0.2\,\mathrm{h}$, where the displacement is predominantly limited by the restoring force. In comparison, the direct tide-induced gravity variations leads to a variation in the hydrostatic pressure of $10 - 100\,\mathrm{Pa}$. In the context of the hydrostatic pressure gradient this pressure variation has a similar effect as a vertical magma displacement by about 1 mm, thus rendering the direct tidal impact negligible compared to the indirect mechanism derived here.

Table 9.1: Choice of model parameters, motivated by conditions at (1) Villarrica volcano located at 39.5°S hosting a persistent lava lake of basaltic composition; and (2) Cotopaxi volcano located at 0.7°S which preferentially erupts andesitic magma and intermittently is capped by a solid plug. If not stated otherwise, all numerical values in this chapter are calculated with these parameters.

Model parameter			**Location-independent constants/assumptions**			
Physical parameter	Notation	Unit	Value	Literature		
pure spring tide amplitude	a_0^{st}	$\mathrm{m\,s^{-2}}$	$1.4 \cdot 10^{-6}$	Baker [1984], at the equator		
semi-diurnal periodicity	ω_{sd}	$\mathrm{rad\,s^{-1}}$	$1.5 \cdot 10^{-4}$	Baker [1984]		
hydrostatic pressure gradient	$(\nabla p)_{vert}$	$\mathrm{Pa\,m^{-1}}$	$2.7 \cdot 10^{4}$	for andesitic host rock		
solubility coefficient of water	K_{H_2O}	$\mathrm{Pa^{-1}}$	$1 \cdot 10^{-11}$	Zhang et al. [2007]		
magma compressibility	β_r	$\mathrm{Pa^{-1}}$	$2 \cdot 10^{-10}$	for the magma in the deep reservoir, see Appendix B		
(local) gas volume fraction	ϕ		$< \phi_{perc}$	$\phi_{perc} = 0.3 - 0.7$, Rust and Cashman [2011]		
			Villarrica		**Cotopaxi**	
conduit length	L_c	km	2	see Appendix B	4	see Appendix B
conduit radius	R_c	m	6	see Appendix B	40	see Appendix B
reservoir volume	V_r	$\mathrm{km^3}$	35	see Appendix B	35	see Appendix B
depth of reservoir (c.o.m.)	D_r	km	3	see Appendix B	8	see Appendix B
kinematic viscosity	ν	$\mathrm{m^2\,s^{-1}}$	0.1	Palma et al. [2011]	4	(andesitic melt)
melt density	ρ_{melt}	$\mathrm{kg\,m^{-3}}$	2600	Palma et al. [2011]	2500	(andesitic melt)
melt weight fraction of water	$C^0_{H_2O}$	%	2	Palma et al. [2011]	5	Martel et al. [2018]
max. vertical tidal acceleration	a_0	$\mathrm{m\,s^{-2}}$	$0.61 \cdot a_0^{st}$	Baker [1984], at 39.5°S	a_0^{st}	Baker [1984], at 0.7°S
gravitational acceleration	g	$\mathrm{m\,s^{-2}}$	9.81	at 39.5°S	9.78	at 0.7°S
magma temperature	T	°C	1200		1000	

9.2 Tide-enhanced bubble coalescence

Integrated over a semi-diurnal cycle, the tides do not result in a net magma displacement. A link from tides to degassing thus requires tide-enhanced mechanisms which irreversibly change the state of magmatic gas phase. Bubble growth constitutes a predominantly exergonic and thus irreversible mechanism because the bubble surface tension inhibits or at least damps bubble shrinkage and dissolution [Prousevitch et al., 1993]. Within a tide-induced radial displacement profile, neighbouring gas bubbles can exhibit differential tide-induced vertical displacements potentially enhancing the bubble coalescence rate (see Figure 9.1c and Appendix D). The variation in the bubble coalescence rate leads to bigger bubbles and thus the tide can indeed modify an irreversible mechanism.

In this section, we set up a simplified formalisation of the magmatic gas phase and the typically predominant mechanisms which govern the bubble coalescence rate, and estimate the relative tide-induced enhancement of the bubble coalescence by a comparison with these classical mechanisms. We consider a magma layer in the conduit at a particular depth, accordingly, the parameters discussed in the following describe the local conditions within a small volume of magma and should not be confused with the integrated bulk values for the total magma column. The variation in the tide-induced enhancement at different magma depths is discussed in the subsequent section.

Gas bubbles in magmatic melt The dominant part of the magmatic volatile content is typically water followed by carbon dioxide, sulphur compounds and minor contributions from a large number of trace gases such as halogen compounds [Oppenheimer et al., 2014]. For simplicity, we assume that all macroscopic properties of the gas phase are dominated by the degassing of water, in particular that the gas volume fraction ϕ exclusively consists of water vapour. The volatile solubility of magmatic melts is primarily pressure dependent with secondary dependencies on temperature, melt composition, and volatile speciation [Gonnermann and Manga, 2013]. The pressure dependency of the water solubility C_{H_2O} in magmatic melt is given in a first approximation by $C_{H_2O}(p) = \sqrt{K_{H_2O} \cdot p}$ with the corresponding solubility coefficients K_{H_2O} [find an empirical formulation in Zhang et al., 2007]. For the local gas volume fraction $\phi(p)$ at a depth associated with the pressure p, we obtain

$$\phi(p) = \frac{\rho_{melt}(p)}{\rho_{gas}(p)} \cdot \left(C^0_{H_2O} - \sqrt{K_{H_2O} \cdot p} \right) \tag{9.5}$$

with the total water weight fraction $C^0_{H_2O}$ of the magmatic melt and the mass densities of the gas phase ρ_{gas} and of the overall melt (liquid + gas) ρ_{melt}.

The gas phase consists of separated bubbles as long as the gas volume fraction is below the percolation threshold of $\phi_{perc} = 0.3 - 0.7$ [the variation is due to the range of different magmatic conditions, Rust and Cashman, 2011]. Bubbles typically vary in size following a power law [Cashman and Marsh, 1988, Blower et al., 2003] or a mixed power-law exponential distribution [Le Gall and Pichavant, 2016] and in shape from spherical to ellipsoidal [Rust et al., 2003, Moitra et al., 2013]. While models based on polydisperse bubble size distributions are available [Sahagian and Proussevitch, 1998, Huber et al., 2013, Mancini et al., 2016], a common starting point to analyse the temporal evolution of the bubbles is nevertheless the assumption of a monodisperse size distribution of spherical bubbles [Prousevitch et al., 1993, Lensky et al., 2004].

Simple polydisperse bubble size distribution We note the bubble size distribution $\delta_b^{size}(f \in \mathbb{R}^+)$ with respect to the bubble radius (rather than the volume), i.e. the bubble radius is given by $r_b = f \cdot R_b$ with the hypothetical bubble radius $R_b(p)$ of a monodisperse bubble size distribution. An estimate of a power-law bubble size distribution would require three parameters: the exponent and the lower and upper truncation cut-off [Lovejoy et al., 2004]. An estimate of a mixed power-law exponential bubble size distribution would require at least two further parameters. The following analysis is conducted for an arbitrary bubble size distribution, nevertheless, for a basic quantitative estimate, we mimic a proper polydisperse bubble size distribution by the simpler single-parametric

$$\tilde{\delta}_b^{size}(f;q) = \begin{cases} 1-q & : \ f = 1 \\ q & : \ f = \sqrt[3]{2} \end{cases} \tag{9.6}$$

with $0 \leq q < \frac{1}{2}$ which represents a monodisperse distribution except for a fraction of q bubbles which emerged from a past coalescence of two bubbles with $f = 1$.

Bubble motion and bubble coalescence Diffusion-driven volatile degassing can only take place in the immediate vicinity of a bubble and when the supersaturation pressure is larger than the bubble surface tension [Proussevitch and Sahagian, 2005]. The volatile degassing rate is thus controlled by the spatial bubble distribution as well as the bubble size distribution [Lensky et al., 2004]. Both distributions change during bubble rise which is caused by a vertical ascent of the overall magma column/parcel with velocity v_{melt} and a superimposed bubble buoyancy with a velocity v_{buoy} which reads for a bubble with radius r_b (Stoke's law)

$$v_{buoy}(r_b) = \frac{2 \cdot g \cdot r_b^2}{9 \cdot \nu} \cdot \left(1 - \frac{\rho_{gas}}{\rho_{melt}}\right) \approx \frac{2 \cdot g \cdot r_b^2}{9 \cdot \nu} \tag{9.7}$$

If the buoyancy velocity is negligible compared to the magma ascent, the bubble flow is called "dispersed"; if the bubble buoyancy velocity contributes significantly to the overall bubble ascent, the bubble flow is called "separated" [Gonnermann and Manga, 2013]. Rising bubbles grow continuously because of (1) decompression and (2) the increasing volatile degassing rate due to the associated decreases in the magmatic volatile solubility and of the bubble surface tension. Bubble coalescence accelerates the bubble growth.

Bubble coalescence requires two bubble walls to touch and ultimately to merge. Once two bubbles are sufficiently close to each other, near-field processes such as capillary and gravitational drainage cause a continuous reduction in the film thickness between the bubble walls until the bubbles merge after drainage times ranging from seconds to hours depending on the magmatic conditions [Herd and Pinkerton, 1997, Castro et al., 2012, Nguyen et al., 2013].

For small gas volume fractions, however, the initial distance between bubbles is large compared to the bubble dimensions and the coalescence rate is dominated by bubble transport mechanisms acting on longer length scales. Because bubble diffusion is typically negligibly small, bubble walls can only approach when a particular mechanism leads to differential bubble rise velocities or by bubble growth. In magmas with a sufficiently separated bubble flow, two neighbouring bubbles of different size can approach each other vertically due to the differential buoyancy velocities [Manga and Stone, 1994, Lovejoy et al., 2004]. In magmas with a dispersed bubble flow, in contrast, the relative position of bubble centres remains fixed thus bubble coalescence is controlled by the bubble expansion rate caused by the ascent of the overall magma column/parcel.

Comparison of bubble coalescence mechanism The proposed tide-induced bubble transport mechanism is compared in the following with the classically predominant bubble transport/approaching mechanisms in order to estimate the relative contribution of the tidal mechanism on the overall coalescence rate. We access the (absolute) strength of a particular transport mechanism by its "collision volume" H_i (see Appendix D). The tidal mechanism is noted by H_{tide}. For comprehensibility, we focus on a comparison of the tidal mechanisms with the two "end-member" scenarios of a purely separated (H_{buoy}) and a purely dispersed (H_{disp}) bubble flow, respectively. A more comprehensive formulation of the classically predominant bubble transport/approaching mechanisms has been proposed, e.g., by Mancini et al. [2016].

For a separated bubble flow, the relative tidal contribution on the bubble coalescence rate depends reciprocally on the reference bubble radius R_b and on the degree of polydispersivity q (Figure 9.2). For $q = 0.1 - 0.4$, the tidal mechanism contributes at least 10 % to the overall bubble coalescence rate for a range of reference bubble radii of $R_b = 32 - 65\,\mu\text{m}$ for Villarrica and $R_b = 37 - 78\,\mu\text{m}$ for Cotopaxi. For comparison, Le Gall and Pichavant [2016] obtained from basalt decompression experiments mean bubble radii of (at most, depending on the volatile content) 23 µm for a pressure of 100 MPa ($\sim$ depth of 3.7 km) and of 80 µm for a pressure of 50 MPa ($\sim$ depth of 1.9 km) and concluded an extensive bubble coalescence rate at depth associated with $50 - 100$ MPa. Similarly, Castro et al. [2012] obtained from rhyolite decompression

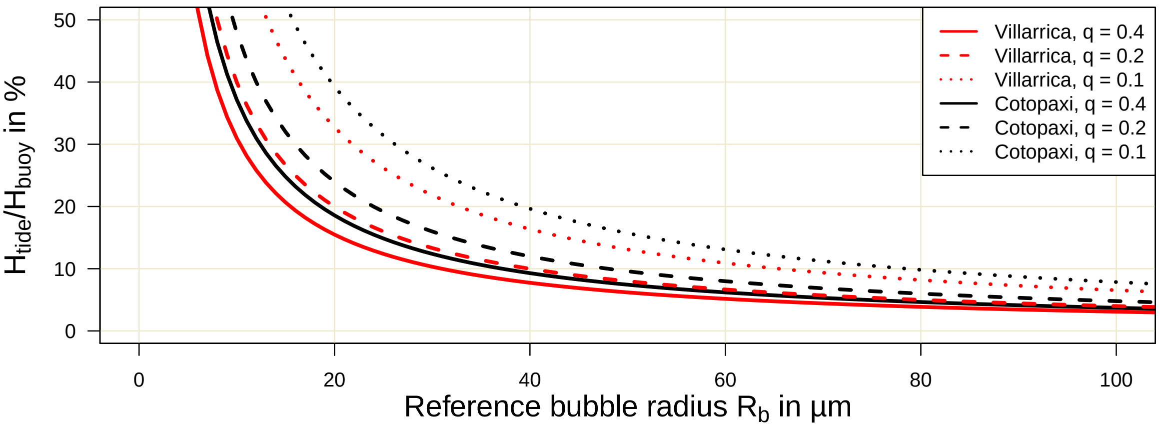

Figure 9.2: Relative contribution of the tidal mechanism (magnitude given by H_{tide}) on the bubble coalescence rate for a purely separated bubble flow (magnitude given by H_{buoy}) depending on the reference bubble radius R_b and the degree of polydispersity q. The reference bubble radius is reciprocally linked to the depth of the particular magma layer.

experiments mean bubble radii of 15 µm for a pressure of 100 MPa ($\sim$ depth of 3.7 km) and of 30 µm for a pressure of 40 MPa ($\sim$ depth of 1.5 km). For andesitic magma, the dependency of the bubble size on the pressure is presumably between the values for the basaltic and the rhyolitic magma. We conclude that the tidal mechanism can significantly contribute to the bubble coalescence rate in magma layers at a depth greater than 1 km, associated with bubble radii of $30 - 80$ µm. In contrast, the tidal contribution becomes negligible at shallow levels once the bubble radii are in the millimetre-range which corresponds to the bubble size range at which bubbles efficiently start to segregate from the surrounding melt.

For a dispersed bubble flow, the relative tidal contribution on the bubble coalescence rate depends reciprocally on the magma ascent rate, hardly on the gas volume fraction ϕ, but approximately linearly on the volatile content $C^0_{H_2O}$ of the magma (see Figure 9.3). The tidal contribution causes an enhancement of the bubble coalescence rate equivalent to the enhancement caused by an increase in the magma ascent velocity by about $0.5\,\mathrm{m\,h^{-1}}$ for Cotopaxi and $2.5\,\mathrm{m\,h^{-1}}$ for Villarrica for the $C^0_{H_2O}$ listed in Table 9.1. For comparison, the magma ascent velocities in passively degassing volcanic systems vary roughly between 1 and $100\,\mathrm{m\,h^{-1}}$ [Cassidy et al., 2015, 2018]. The tidal mechanism can accordingly contribute by at least several percent but potentially up to multiples of 10 % to the overall bubble coalescence rate. For gas volume fractions exceeding the minimum percolation threshold of $\phi_{perc} \approx 0.3$, the model assumption of independent spherical bubbles increasingly loses its validity.

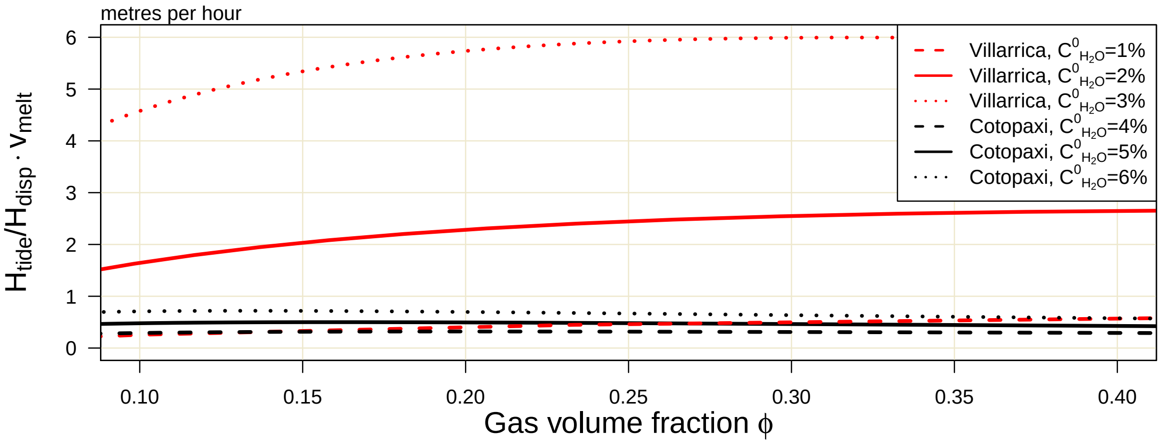

Figure 9.3: Relative contribution of the tidal mechanism (magnitude given by H_{tide}) on the bubble coalescence rate for a purely dispersed bubble flow (magnitude given by H_{disp}) depending on the gas volume fraction and the initial water weight fraction of the magmatic melt. The corresponding values for ϕ are calculated with equation (9.5) assuming an ideal gas and magma temperatures of 1200°C for Villarrica and 1000°C for Cotopaxi. The relative tidal contribution is displayed as the equivalent to an enhancement of the magma ascent rate which would have the same effect on the bubble coalescence rate. The model increasingly loses validity above the percolation threshold of $\phi_{perc} \approx 0.3$.

9.3 Discussion and Conclusions

Our model implies a tide-induced periodical vertical magma displacement in the conduit within every semi-diurnal cycle in the order of $0.1 - 1\,\mathrm{m}$ due to magma expansion in the reservoir. At Villarrica, the modelled vertical magma displacement of $0.45\,\mathrm{m}$ implies a periodic variation in the lava lake level [whose areal cross section is about 10 times larger than for the conduit, Goto and Johnson, 2011] of about $5\,\mathrm{cm}$. At Cotopaxi, the modelled vertical magma displacement of $0.09\,\mathrm{m}$ may apply additive stress on the solid plug.

We linked this magma displacement to bubble coalescence and compared the relative strength of the tide-induced bubble transport mechanism with respect to the classically predominant bubble transport mechanisms in magmas hosting a purely separated or a purely dispersed bubble flow. For both scenarios, we found that the tidal contributions to the overall bubble coalescence rate can be in the order of at least several percent up to multiples of $10\,\%$ at a depth of several kilometres. At shallower depth, the direct tide-induced contribution to the overall bubble coalescence rate is rather negligible because the classical transport mechanisms become more efficient.

The tide-enhanced bubble coalescence rate at greater depth can nevertheless affect the gas phase in the overlying shallower layer because the additionally coalesced bubbles have a larger buoyancy velocity as well as a reduced surface tension and can thus stimulate on the one hand enhanced volatile degassing from the melt phase to the gas phase and on the other hand enhanced bubble coalescence rates in overlying layers [Prousevitch et al., 1993]. These enhancements can ultimately cause the percolation of the gas phase at a somewhat greater depth compared to the tide-free scenario. In consequence, the magma becomes gas-permeable at this greater depth potentially causing enhanced volcanic gas emissions [Rust and Cashman, 2011, Gonnermann et al., 2017]. The additional contributions from this greater depth to the volcanic gas emissions may also slightly shift the chemical composition of the overall gas emissions towards the chemical composition of the gas phase at this greater depth when compared to the tide-free scenario [Burton et al., 2007].

The quantitative results have been derived for the tidal forcing during spring tide. In contrast, the amplitude of the tide-induced mechanism is smaller by a factor of 3 during neap tide. Accordingly, the amplitude of the additional tide-induced contributions to the coalescence rate varies within a spring–neap tide cycle entailing a periodical signal with a period of about 14.8 days superimposed on the (nevertheless potentially much stronger) tide-independent coalescence rate. For a dispersed bubble flow scenario with rather fast magma ascent, a propagation of this superimposed signal from the enhanced coalescence rate via a variation in the percolation depth to the volcanic gas emissions is comprehensible. For a separated bubble flow scenario, however, the gas bubbles may need much more time than one spring–neap tide cycle to rise from a depth of several kilometres to the percolation depth. Magmatic systems can, however, become permeable already in a depth of $1 - 3\,\mathrm{km}$ [Edmonds and Gerlach, 2007, Burton et al., 2007], i.e. where the derived tidal effects are the strongest. In such a scenario, the tide-enhanced bubble coalescence rate could accordingly cause enhanced degassing without a significant delay.

In a scenario with a shallower percolation depth, the periodic pattern could nevertheless propagate to the degassing signal because several crucial parameters such as the mean bubble radius R_b and the gas volume fraction ϕ typically vary rather monotonously with pressure and thus depth [Gonnermann and Manga, 2013], implying a depth dependency of the relative tidal contributions to the bubble coalescence rate. Convolved along the vertical conduit axis, the tide-enhanced coalescence rate may accordingly preserve an overall periodicity driven by the dominant contributions from those magma layers which are particularly sensitive to the tidal mechanism. Moreover, this pressure dependency implies that gas contributions originating from the particularly tide-sensitive depths are more pronounced in the subsequent volcanic gas emissions during spring tide. Therefore tide-induced variations in the chemical composition within the volcanic gas plumes may be particularly manifested in the relative molar degassing ratios [e.g. Burton et al., 2007, Bobrowski and Giuffrida, 2012, Balcone-Boissard et al., 2016] associated with these depths.

Conclusions We traced a possible tidal impact from the tidal potential to a magma expansion in the reservoir; to a vertical magma displacement profile in the conduit; to an enhanced bubble collision/coalescence rate; and ultimately motivated a link between the tide-enhanced bubble coalescence rate and the periodical signal in the observed volcanic gas emissions. Furthermore, illustrative quantitative calculations indicated that the proposed tide-induced mechanism could lead to an enhancement of the bubble coalescence rate by up to multiples of 10 %. If propagated from enhanced bubble coalescence to a variation in the magnitude or chemical composition of the volcanic gas emissions, a periodical spring tide signal would be large enough to explain the observed about 2-weekly variations in volcanic gas emissions.

Nevertheless, our conceptual model only aimed at a proof of concept. Future studies may increase the complexity of the model by e.g. (1) lifting several of our numerous simplifications (Appendix A), (2) incorporating macroscopic tidal mechanisms affecting the host rock explicitly, (3) adding several further microscopic mechanisms such as a tide-induced loosening of bubbles attached to the conduit walls or the tidal impact on crystal orientation, and (4) investigating possible non-linear interferences between the tide-induced dynamics and the tide-independent magma convection flow.

9.4 Appendix material

Appendix A: List of applied mayor simplifications

In our model we applied several simplifications regarding the shape and physical properties of the magma plumbing system. This we did for the sake of clarity and, even more importantly, in order to isolate the tide-induced effect on magma flow and degassing. To achieve this, we (1) modelled the tide-induced magma flow in the conduit neglecting any tide-independent magma dynamics such as magma convection, which implies an initial mechanical and thermodynamic equilibrium between magma and adjacent host rock. The only exception is the discussion of the impact of a constant magma ascent on the bubble coalescence rate. (2) The expansion of the initial conduit magma is neglected. We assume (3) a gas-tight host rock, (4) a cylindrical volcanic conduit, (5) a no-slip condition between the conduit wall and the magma, and (6) homogeneous magma flow properties. (7) The viscosity of the magma in the conduit is assessed by the effective bulk viscosity. (8) The radial tide-induced magma displacement is neglected. Moreover, (9) bubble coalescence is modelled by bubble collision, neglecting near-field drainage processes, bubble deformation processes, and post-collision coalescence processes. (10) Simple bubble size distributions are chosen, and (11) it is assumed that the volcanic gas phase exclusively consists of water vapour.

Appendix B: Quantitative estimates for the geometrical model parameters

The conduit radius is a crucial model parameter. The uppermost 200 m of Villarrica's conduit have frequently been exposed during the decades prior to the 2015 eruption due to pronounced oscillations of the lava lake level [Moussallam et al., 2016, Johnson et al., 2018b]. The cross-sectional area of the conduit has a radius of about 30 m [Goto and Johnson, 2011] which at greater depths, however, narrows down to a mean radius of the order of $R_c = 6\,\mathrm{m}$ as is implied by studies based on gas emission magnitudes [Palma et al., 2011] and seismoacoustic properties [Richardson et al., 2014]. The active vent of Cotopaxi was capped by an area of hot material with a diameter of 116-120 m during the eruption in 2015 [Johnson et al., 2018a]. Although missing an empirical evidence, it is plausible that the mean conduit radius is somewhat narrower and therefore we assume a (rather conservative) value of $R_c = 40\,\mathrm{m}$.
Depth and volume of the magma reservoir constitute further crucial model parameters whose empirical estimates come with an even larger uncertainty. Seismic observations conducted at Villarrica imply the existence of a shallow magma reservoir with a lateral diameter of at least 5 km and a vertical extent of about 2.5 km whose centre of mass

is located at a depth of around $D_r = 3\,\mathrm{km}$ below the summit [Mora-Stock, 2015], implying a conduit length of about $L_c = 2\,\mathrm{km}$. Assuming an ellipsoidal magma reservoir this implies a magma reservoir volume of $V_r = 35\,\mathrm{km}^3$ at Villarrica. The magmatic system of Cotopaxi in contrast seems to be more complex and hosts a rather small magma pocket ($2\,\mathrm{km}^3$) beneath the SW-flank and at a depth of about 4 km below the summit [Hickey et al., 2015]. Furthermore, seismic observations revealed fluid movements (magma and/or hydrothermal fluids) within a centrally located 85 km^3 column spanning 2 to 14 km depth below the summit [Ruiz et al., 1998]. This fluid column is assumed to connect the laterally offset shallow pocket with two much larger deeper magma reservoirs, which are situated between 7 and 11 km and somewhere at a depth greater than 16 km below the summit [Arias et al., 2015, Mothes et al., 2017, Martel et al., 2018]. For heating $85\,\mathrm{km}^3$ of rock, these deep-seated magma reservoirs may be rather large. Missing any accurate volume estimate, we estimate that the upper of the two deep-seated reservoirs hosts a magma volume of $V_r = 35\,\mathrm{km}^3$ with a centre of mass depth of $D_r = 8\,\mathrm{km}$. The choice of equal reservoir volumes for both Villarrica and Cotopaxi allows for a better comparison of the impact of varying the other volcanic parameters. Further, we assume the small magma pocket as the lower end of the conduit, i.e. with a conduit length of $L_c = 4\,\mathrm{km}$.

Appendix C: Calculation of tide-induced conduit flow

Oscillating centre of mass displacement After a negligible settling time, the driven oscillator described by eq. 9.3 oscillates with semi-diurnal periodicity and we obtain the general long-term solution

$$\begin{cases} z(t) = z_0 \cdot \sin(\omega_{sd} \cdot t - \varphi_0) \\ z_0 = \dfrac{a_0}{\sqrt{(\omega_0^2 - \omega_{sd}^2)^2 + (\gamma \cdot \omega_{sd})^2}} \\ \varphi_0 = \arctan\left(\dfrac{\gamma \cdot \omega_{sd}}{\omega_0^2 - \omega_{sd}^2}\right) \end{cases} \tag{9.8}$$

Navier–Stokes equation for periodical pipe flow When exposed to a constant force (per unit mass) f^0_{ext}, a viscous fluid in a cylindrical pipe with radius R_c flows with a parabolic velocity profile $v^0(r)$, $0 \le r \le R_c$:

$$v^0(r) = \frac{R_c^2 \cdot f^0_{ext}}{4 \cdot \nu}\left[1 - \left(\frac{r}{R_c}\right)^2\right] \tag{9.9}$$

When exposed to a periodically varying and thus time-dependent external force $f_{ext}(t) = f^0_{ext} \cdot e^{i\omega t}$, the analytical solution of the flow profile is more complicated [Spurk, 1997]:

$$v(r,t) = \overline{v^0(r)} \cdot \Re \left[-i \cdot \frac{8}{N^2} \cdot e^{i\omega t} \cdot \left(1 - \frac{J_0(\sqrt{-i}\, N \, \frac{r}{R_c})}{J_0(\sqrt{-i}\, N)} \right) \right] \tag{9.10}$$

with the centre of mass velocity $\overline{v^0(r)}$ of a constant forcing (see eq. 9.9), the real part $\Re[..]$, the imaginary unit i, the Bessel function $J_0(..)$, and the dimensionless parameter $N = \sqrt{\frac{\omega}{\nu}} \cdot R_c$. In the limit $N \to 0$, the velocity profile asymptotically adopts the time dependency as well as the magnitude of the external force. For $N = 1$ the exact magnitude is already $0.98 \cdot f^0_{ext}$ and the radial profile shows hardly any deviation from a parabolic profile. For the chosen model parameters (Table 9.1) and $\omega = \omega_{sd}$, we obtain $N \approx 0.2$ and thus eq. 9.10 reduces in very good approximation to the familiar

$$v(r,t) \approx \frac{R_c^2 \cdot f_{ext}(t)}{4 \cdot \nu} \left[1 - \left(\frac{r}{R_c} \right)^2 \right] \tag{9.11}$$

Derivation of the equation of motion (eq. 9.4) The vertical velocity of the centre of mass can be obtained as $\dot{z}(t) = z_0 \cdot \omega_{sd} \cdot \cos(\omega_{sd} \cdot t - \varphi_0)$ from eq. 9.8 and as $v(t) = (\pi \cdot R_c^2)^{-1} \cdot \int_0^{R_c} v(r,t) \cdot 2\,\pi\, r\, dr = \frac{R_c^2}{8 \cdot \nu} \cdot f_{ext}(t)$ from eq. 9.11. Further, we know $f_{ext}(t) = f_{int}(t) = \gamma \cdot \dot{z}(t)$ from eq. 9.3. Applying $f_{ext}(t)$ to eq. 9.11 reveals $\gamma = \frac{8 \cdot \nu}{R_c^2}$ and ultimately the fully parametrised equation of motion in eq. 9.4.

Appendix D: Calculation of the collision volumes

As is common for most coalescence models (including those cited above), we consider spherical bubbles only. Two spherical bubbles with radii $f_1 \cdot R_b$ and $f_2 \cdot R_b$ (f_1 and f_2 drawn from $\delta_b^{size}(f)$) collide as soon as the distance between their bubble centres is $r_{coal} = (f_1 + f_2) \cdot R_b$. We introduce the "collision volume" $H(f_1, f_2; \Delta t)$ associated with a bubble with radius $f_1 \cdot R_b$ as the volume enclosing all possible initial locations of the bubble centre of another bubble with radius $f_2 \cdot R_b$ such that both bubbles collide (and thus coalesce) at the latest after a time interval Δt. All bubble collision mechanisms are derived as enhancements of the initial static collision volume

$$H_0(f_1, f_2) = \frac{4\,\pi}{3} \cdot R_b^3 \cdot (f_1 + f_2)^3 \tag{9.12}$$

and we consider only those bubble pairs which have not collided already in the initial state. The absolute enhancement of the collision volume due to a particular bubble

collision mechanism divided by Δt thus gives the enhancement of the bubble collision rate contributed by the particular mechanism. Because the tide-induced mechanisms is derived for a semi-diurnal cycle, the relative strengths of all coalescence mechanisms are compared with respect to this time interval Δt_{sd}.
The collision volumes of the different collision mechanisms are all derived with the same approach: We fix the position of a bubble with arbitrary radius $f_1 \cdot R_b$ and derive $H(f_1, f_2; \Delta t)$ with respect to the relative motion of another bubble with arbitrary radius $f_2 \cdot R_b$. In each case the initial collision volume $H_0(f_1, f_2)$ is subtracted either already tacitly in the motivation or explicitly mathematically. Higher-order details such as the influence of a third bubble on the numeric results are ignored.

Tide-enhanced bubble collision volume We fix the horizontal coordinates $(r, \varphi)_{bubble1} = (r_0, 0), 0 \leq r_0 \leq R_c$, of the first bubble, where the cylindrical symmetry of the conduit allows to pick the azimuth angle without loss of generality, and vary the horizontal coordinates $(r, \varphi)_{bubble2} = (r, \varphi)$ of a second bubbles. The horizontal distance h between the two bubbles is thus given by $r^2 = r_0^2 - 2 \cdot r_0 \cdot h \cdot \cos(\varphi) + h^2$. Within a semi-diurnal cycle, the peak-to-peak differential tide-induced vertical displacement of two bubbles at the radial coordinates r and r_0 is given by $\Delta z_{tide}(r, r_0) = 2 \cdot |z_0(r) - z_0(r_0)|$ (see eq. 9.4). The tide-induced collision volume is then the integral of $\Delta z_{tide}(r, r_0)$ integrated over a circle with radius r_{coal}:

$$H_{tide}(r_0) = \int_0^{r_{coal}} dh\, h \int_0^{2\pi} d\varphi\, \Delta z_{tide}(r, r_0) \tag{9.13}$$

$$= \frac{4\,\Psi\, r_0}{R_c^2} \int_0^{r_{coal}} dh\, h^2 \int_0^{2\pi} d\varphi \left| \cos(\varphi) - \frac{h}{2\, r_0} \right| \tag{9.14}$$

This integral has to be split into two integrals at the angles where the sign of the absolute function changes, which is the case at $\pm\varphi' = \pm \arccos(\frac{h}{2 r_0}) \approx \pm\frac{\pi}{2}$:

$$H_{tide}(r_0) = \frac{16 \cdot \Psi \cdot r_0}{R_c^2} \int_0^{r_{coal}} dh\, h^2 \underbrace{[\sin(\varphi') - \cos(\varphi') \cdot \varphi']}_{\approx 1 \text{ for } h << r_0} \tag{9.15}$$

$$\approx \frac{16 \cdot \Psi \cdot r_0}{R_c^2} \cdot \frac{r_{coal}^3}{3} \tag{9.16}$$

$$= \frac{4 \cdot \Psi \cdot r_0}{\pi \cdot R_c^2} \cdot H_0(f_1, f_2) \tag{9.17}$$

We integrate $H_{tide}(r_0)$ over the local spatial bubble distribution in the conduit in order to obtain the average effect. We parametrise the (isotropic) spatial bubble distribution by the depth-independent $\delta_b^{spatial}(r_0) = (1 + \alpha) \cdot \frac{1}{R} \cdot (\frac{r_0}{R})^{\alpha}$, which is a homogeneous distribution for $\alpha = 1$ but with all bubbles at the conduit wall if $\alpha \to \infty$, respectively.

For the averaged tide-induced collision volume, we obtain

$$\begin{aligned} H_{tide} &= \int_0^R \sigma_{tide}(r_0) \cdot \delta_b^{spatial}(r_0) \cdot dr_0 && (9.18) \\ &= \underbrace{\left[\frac{1+\alpha}{2+\alpha}\right]}_{\text{distribution}} \cdot \underbrace{\left[\frac{4 \cdot \Psi}{\pi \cdot R_c}\right]}_{\text{tidal}} \cdot \underbrace{H_0(f_1, f_2)}_{\text{scale}} && (9.19) \end{aligned}$$

The "distribution term" is $\frac{2}{3}$ for an isotropic bubble distribution and approaches unity if all bubbles are close to the host rock. Arguably, the conditions for crystal nucleation and thus bubble nucleation are better close to the host rock where the magma is cooler and more crystals and thus nucleation possibilities are available. Following this reasoning but also because we want to examine the maximum possible tidal impact, we set the distribution term to unity. The "tidal term" contains the information on the scale of the effective tide-induced impact. The "scale term" contains the information on the actual bubble size distribution, highlighting that the relative tidal enhancement is identical for any bubble size distribution, at least in our simple model.

Buoyancy-induced bubble collision volume Two bubbles with radii $f_1 \cdot R_b \neq f_2 \cdot R_b$ have a differential rise velocity $\Delta v_{buoy} = |f_2^2 - f_1^2| \cdot v_{buoy}(R_b)$ and thus their relative distance changes during the rise. The two bubbles will collide if the larger bubble is below the smaller and if the horizontal distance between their bubble centres is at most r_{coal}. Accordingly, the buoyancy-induced collision volume H_{buoy} is a cylindrical volume with base area $\pi \cdot r_{coal}^2$ and cylinder length $\Delta v_{buoy} \cdot \Delta t_{sd}$:

$$\begin{aligned} H_{buoy}(f_1, f_2) &= \pi \cdot r_{coal}^2 \cdot |f_2^2 - f_1^2| \cdot v_{buoy}(R_b) \cdot \Delta t_{sd} && (9.20) \\ &= \frac{3 \cdot |f_2 - f_1|}{4 \cdot R_b} \cdot v_{buoy}(R_b) \cdot \Delta t_{sd} \cdot H_0(f_1, f_2) && (9.21) \end{aligned}$$

For a given pair of bubbles with radii $f_1 \cdot R_b \neq f_2 \cdot R_b$, f_1 and f_2 drawn from $\delta_b^{size}(f)$, the ratio of the contribution from the tide-induced and the buoyancy-induced collision mechanisms is

$$\frac{H_{tide}}{H_{buoy}} = \frac{24 \cdot \Psi \cdot \nu}{\pi \cdot R_c \cdot |f_1 - f_2| \cdot g \cdot R_b \cdot \Delta t_{sd}} \qquad (9.22)$$

The bulk ratio (with respect to the local magma layer) can be obtained by a previous and separate integration of H_{tide} and H_{buoy} over f_1 and f_2 with respect to the actual bubble size distribution $\delta_b^{size}(f)$ (rather than integrating eq. 9.22). For the explicit bubble size distribution $\tilde{\delta}_b^{size}$ from eq. 9.6, we obtain the bulk collision volumes $\tilde{H}_{tide}$ and $\tilde{H}_{buoy}$

$$\frac{\tilde{H}_{tide}(q)}{H_0(1,1)} = (1 + 0.89 \cdot q + 0.11 \cdot q^2) \cdot \frac{4 \cdot \Psi}{\pi \cdot R_c} \tag{9.23}$$

$$\frac{\tilde{H}_{buoy}(q)}{H_0(1,1)} = (q - q^2) \cdot \frac{9}{16 \cdot R_b} \cdot v_{buoy}(R_b) \cdot \Delta t_{sd} \tag{9.24}$$

and thus the bulk ratio (used for the calculation of Figure 9.2)

$$\frac{\tilde{H}_{tide}}{\tilde{H}_{buoy}} = 60 \cdot \left(0.9 + \frac{1 + q^2}{q - q^2}\right) \cdot \frac{\nu[\mathrm{m^2\,s^{-1}}] \cdot \Psi[\mathrm{m}]}{R_c[\mathrm{m}] \cdot R_b[\mathrm{\mu m}]} \tag{9.25}$$

Growth-induced bubble collision volume In magma with a dispersed bubble flow ($v_{buoy} << v_{melt}$), a rising bubble exhibits a pressure decrease rate of

$$\frac{\Delta p}{\Delta t} = v_{melt} \cdot (\nabla p)_{vert} \tag{9.26}$$

Ignoring accompanying changes in secondary parameters such as melt temperature and magma composition and assuming for simplicity a monodisperse bubble size distribution (thus $R_b^3 \propto \phi$), for the enhancement of the collision volume due to a rise-driven pressure decrease by $\Delta p << p_0$ (apply eq. 9.5 on eq. 9.12), we obtain

$$\begin{aligned} H_{disp}(\Delta p; p_0) &= H_0(R_b(p_0 - \Delta p)) - H_0(R_b(p_0)) \\ &= H_0(1,1) \cdot \frac{C^0_{H_2O} - \frac{1}{2}\sqrt{K_{H_2O} \cdot p_0}}{C^0_{H_2O} - \sqrt{K_{H_2O} \cdot p_0}} \cdot \frac{\Delta p}{p_0} + \mathcal{O}\left[\left(\frac{\Delta p}{p_0}\right)^2\right] \end{aligned} \tag{9.27}$$

where we assumed that ρ_{melt} is constant and ρ_{gas} follows the ideal gas law. Inserting eq. 9.26 in eq. 9.27, we obtain:

$$\frac{H_{disp}(p_0)}{H_0(1,1)} = \frac{C^0_{H_2O} - \frac{1}{2}\sqrt{K_{H_2O} \cdot p_0}}{C^0_{H_2O} - \sqrt{K_{H_2O} \cdot p_0}} \cdot v_{melt} \cdot \Delta t_{sd} \cdot \frac{(\nabla p)_{vert}}{p_0} \tag{9.28}$$

The ratio of the contribution from the tide-induced and the growth-induced collision mechanism (used for the calculation of Figure 9.3) is

$$\frac{H_{tide}}{H_{disp}} = \underbrace{\frac{C^0_{H_2O} - \sqrt{K_{H_2O} \cdot p_0}}{C^0_{H_2O} - \frac{1}{2}\sqrt{K_{H_2O} \cdot p_0}}}_{\approx 0.25-0.5} \cdot \frac{4 \cdot \Psi[\mathrm{m}] \cdot p_0\,[\mathrm{MPa}]}{R_c[\mathrm{m}] \cdot v_{melt}[\mathrm{m\,h^{-1}}]} \tag{9.29}$$

10 Mechanical interaction between gas bubbles and tilted crystals

The model introduced in this chapter arose from the idea to add crystals to the tidal model discussed in Chapter 9. The model faces some analytical limitations and it thus not yet comprehensive. This chapter can be considered to be entirely independent from the content discussed in the rest of this thesis. I decided to include this chapter nevertheless in order to save the advances for future continuations.

10.1 Motivation, model set-up, nomenclature

Motivation The degassing of volatiles exerts fundamental control on the properties of the shallow magmatic system. In particular, the expansion of gas bubbles govern the over-pressuring of the system and thus control the shallow volcanic activity [Oppenheimer et al., 2014]. The expansion rate of the gas phase is often linked predominately to a buoyancy-driven bubble rise [e.g. Sparks, 1978, Gonnermann and Manga, 2013]. Bubble coalescence accelerates the bubble rise velocity and thus potentially controls the shallow volcanic activity in low viscous magma. Bubble coalescence has been studied empirically [e.g. Sahagian et al., 1989, Herd and Pinkerton, 1997, Castro et al., 2012] and theoretically [e.g. Mancini et al., 2016, and the comprehensive literature review therein]. However, these models have not yet included the impact of the crystal orientation on bubbles coalescence.

The degree of crystallinity strongly influences the degassing behaviour of the magmatic melt on a macroscopic scale [e.g. by varying the melt viscosity Caricchi et al., 2007] as well as on a microscopic scale [e.g. by heterogeneous bubble nucleation Hurwitz and Navon, 1994]. The impact of crystals on bubble coalescence has been studied only recently. Bai et al. [2011] report from experiments that the volatile degassing correlates positively with the degree of crystallinity. Spina et al. [2016] confirms this experimental finding for low crystallinity regimes but also highlight that a crystal volume above 30 % results in an opposing dampening of several degassing processes because the viscosity of the melt increases significantly. Further, Spina et al. [2016] report that elongated crystals have a stronger positive impact on volatile degassing than spherical crystals. In contrast, Okumura et al. [2012] observed no dependency of the gas permeability on

the degree of crystallinity. In all here cited experiments, the size of the crystals were comparable in size or smaller than the bubble size. However, elongated crystals can grow to sizes of up to several millimetres [e.g. Armienti et al., 1994, Kent et al., 2010, Brugger and Hammer, 2010, Okumura et al., 2016], i.e. an order of magnitude more extended than gas bubbles. Models of the microscopic interaction between crystals and bubbles are solely focussing on the impact of crystals on bubble nucleation, the reduction in bubble surface tension [“wetting angle”, e.g. Okumura et al., 2012], and the bubble shape. Little attention has yet given to the role of crystals acting as obstacles which hinder bubbles in their buoyancy-driven rise except for the observation that bubbles can get totally trapped in a crystal mesh. In particular elongated, tilted crystals whose spatial dimensions are much larger than the bubbles should therefore have a significant impact on the bubble rise as well as on the spatial bubble distribution.
This chapter introduces a basic model on this interaction between gas bubbles and tilted crystals and calculate the quantitative magnitudes of their most obvious accompanying impacts. The required crystal properties (elongated crystals, very low wetting angle) can be found in nature in the form of feldspar.

Model set-up and nomenclature This mechanical interaction between gas bubbles and tilted crystals could lead on the one hand in a polydisperse buoyancy velocity distribution and on the other hand in a non-negligible horizontal bubble mobility and thus bubble accumulation. Most results are derived analytically. The model output will be illustrated at some quantitative scales. If not stated otherwise, those quantitative numbers are derived by the chosen set of parameters given for Cotopaxi in Table 9.1 plus the additional parameters given in Table 10.1.
For simplicity only tabular crystals are examined, but most of the following reasoning can be adopted for any elongated crystal as well. The crystals have a homogeneous mass density $\rho_c \approx \rho_{melt}$, number density n_c, length $l_c \approx 500\,\mu\mathrm{m} \approx \mathcal{O}(10\,r_b)$, width $b_c \approx l_c/2$, and rather negligible depth $d_c < b_c$ (Figure 10.1). This implies that the geometric crystal centre is also the centre of mass. We call the two largest surfaces $(l_c \cdot b_c)$ “crystal faces”, the two surfaces $(b_c \cdot d_c)$ “crystal edges”, and the two other surfaces $(l_c \cdot d_c)$ are not referred to explicitly in this manuscript. The crystal orientation is given by the angles (θ, φ, ψ) where the zenith angle θ is chosen such that $\theta = 0°$ indicates that both crystal edges are above each other; the azimuth angle φ is of no concern in our model; and the “yaw” angle ψ is chosen such that $\psi = 90°$ indicates that the first principal axis of the crystal edges has no vertical component. We allow for arbitrary distributions for all three angles and note the distribution of the zenith angle $\delta_c(\theta)$. The moment of inertia associated with a variation of θ is given by $I_\theta \approx \frac{1}{12} \cdot \rho_c \cdot l_c^3 \cdot b_c \cdot d_c$. For better notation, the first principal axis of the crystal is labelled as s-axis with the s-origin in the centre of mass, thus the crystal faces ranges from $s_0 = \lambda \cdot \frac{l_c}{2}$ with some dimensionless $-1 \leq \lambda \leq 1$ (Figure 10.1). Further, an isotropic spatial crystal distribution is assumed, thus the crystals are vertically spaced by $\Delta z_c = \sqrt[3]{1/n_c}$. Bubbles are at all times spherical and have a radius distribution $\delta_b(f)$.

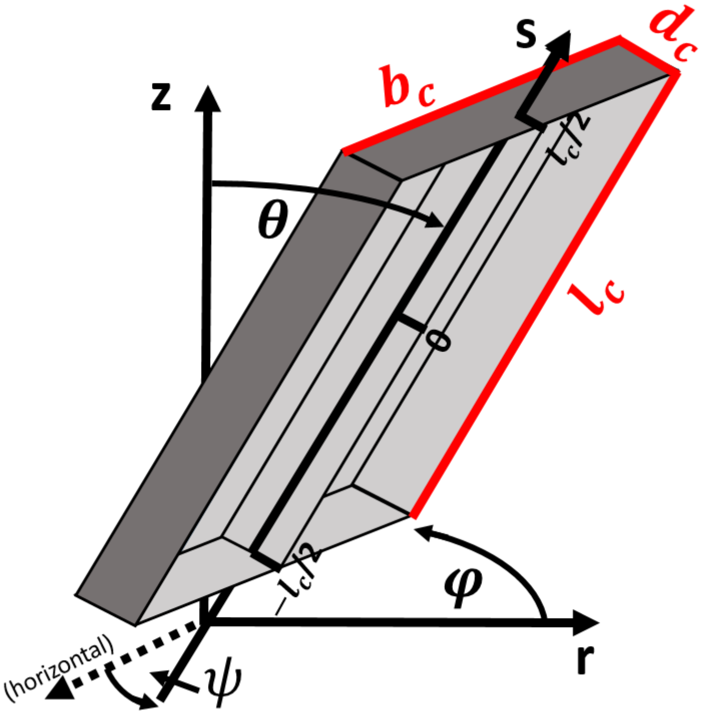

Figure 10.1: Nomenclature for the crystal dimensions and orientations: Zenith angle θ, yaw angle ψ, azimuth angle φ.

Table 10.1: Choice of model parameters. If not stated otherwise, all numerical values in this manuscript are calculated with these parameters.

Physical parameter	Notation	Unit	Value	Comment
initial pressure	p_0	MPa	70	
bubble radius	R	µm	25	@ 70 MPa
bas volume fraction	ϕ		0.15	up to 0.3 prior to percolation
crystal length	l_c	mm	0.5	
crystal width	b_c	mm	0.2	
crystal depth	d_c	mm	0.05	(no relevance for the model)
crystal number density	n_c	mm^{-3}	10	(elongated crystals only)

10.2 Simple scenario: 1 bubble and 1 crystal

The concept is introduced in the following for a particular bubble with radius r_b interacting with a single crystal with initial orientation θ_0 and yaw angle $\psi = 90°$. The bubble rises due to buoyancy with a vertical velocity $v_{buoy} = \frac{2\,g\,r_b^2}{9\,\nu}$ and hits the crystal centrally w.r.t. to b_c at some $s_0 = \lambda_0 \cdot \frac{l_c}{2}$ (furthermore, the following description sloppily assumes $d_c = 0$). After hitting the crystal, the bubble slides along the tilted crystal face but any rolling and sticking effects are neglected in this model. Until this slide ends, the bubble and the crystal interact with each other by the normal force

$$F_N(t) = \frac{4\,\pi}{3} \cdot r_b^3 \cdot \rho_{melt} \cdot g \cdot \sin(\theta(t)) \tag{10.1}$$

$$= 6\,\pi \cdot \nu \cdot r_b \cdot v_{buoy} \cdot \rho_{melt} \cdot \sin(\theta(t)) \tag{10.2}$$

which acts normal to the crystal face. This force simultaneously causes (1) a torque on the crystal resulting in a temporal variation of the crystal orientation $\theta(t)$ and (2) a deceleration and redirection of the bubble rise. The horizonal and vertical components of the rise velocity of the sliding bubble are

$$\begin{bmatrix} v_h(t) \\ v_z(t) \end{bmatrix}_{sliding} = \begin{bmatrix} \sin(\theta(t)) \cdot \cos(\theta(t)) \\ \cos^2(\theta(t)) \end{bmatrix} \cdot v_{buoy}(r_b) \tag{10.3}$$

and the absolute position of the bubble relative to the crystal centre is then

$$s(t) = s_0 + v_{buoy} \cdot \int_0^t \cos(\theta(t'))\,dt' \tag{10.4}$$

when measured in the s-axis frame. Depending on the current attachment location of the bubble with respect to the crystal centre, the torque results in general in two independent rotations, a rotation along the axis perpendicular to $(l_c \cdot d_c)$ (variation of the zenith angle θ) and a rotation along the s-axis (simultaneous variation of azimuth and yaw angle). For a yaw angle of 90°, the normal force is always perpendicular to the crystal face $(l_c \cdot b_c)$ implying that there is no torque component perpendicular to $(l_c \cdot b_c)$. Further because the bubble hits the crystal centrally, there is also no torque component perpendicular to $(l_c \cdot d_c)$. Thus, in this scenario there is only a rotation around the axis perpendicular to the $(l_c \cdot d_c)$.
The bubble-induced torque is countered by the a viscosity-induced drag force F_D. The magnitude of the rotation velocity $v_{rotation}(t) = |\frac{d\theta}{dt} \cdot s(t)|$ is rather small for any time t and thus also the Reynolds number ($Re = v_{rotation} \cdot b_c \cdot \nu^{-1} \ll 10^{-6}$) is extremely small for the overall interaction. In consequence, the drag force can be described by a laminar flow of viscous material. Assuming that it does not matter for such extremely laminar regimes whether the crystal is actually rotating or just moves transversally, the drag

force can be modelled by the generalised Stoke's law for a laminar flow

$$F_D = 6\,\pi \cdot \nu \cdot \rho_{melt} \cdot \tilde{r}_c \cdot \left| \frac{d\theta}{dt} \cdot s(t) \right| \tag{10.5}$$

with the equivalence radius $\tilde{r}_c \approx \frac{1+\sqrt{2}}{3} \sqrt{\frac{b_c \cdot l_c}{\pi}}$ of the crystal which is considered to be a flat plate with dimensions $l_c \geq b_c \gg d_c$ [Leith, 1987]. The drag-induced counter torque M_D then reads

$$M_D = 2 \cdot \int_0^{l_c/2} F_D \cdot ds = \underbrace{6\,\pi \cdot \nu \cdot \rho_{melt} \cdot \tilde{r} \cdot (l_c/2)^2}_{\equiv \alpha_D} \cdot \frac{d\theta}{dt} \tag{10.6}$$

Considering also the inertia term $I_\theta \cdot \frac{d^2\theta}{dt^2}$, the torque balance reads

$$I_\theta \cdot \frac{d^2\theta}{dt^2} + \alpha_D \cdot \frac{d\theta}{dt} = -s(t) \cdot \left[6\,\pi \cdot \nu \cdot \rho_{melt} \cdot r_b \cdot v_{buoy} \cdot \sin(\theta(t)) \right] \tag{10.7}$$

Divide for convenience by α_D gives

$$\beta \cdot \frac{d^2\theta}{dt^2} + \frac{d\theta}{dt} = -\gamma^2 \cdot \sin(\theta(t)) \cdot \left[\int_0^t \cos(\theta(t'))\, dt' + \frac{s_0}{v_b} \right] \tag{10.8}$$

with $\beta = \frac{l_c \cdot b_c \cdot d_c}{18\,\pi \cdot \tilde{r} \cdot \nu}$ and $\gamma = \sqrt{\frac{r_b}{\tilde{r}_c}} \cdot \frac{2 \cdot v_b}{l_c}$. A differentiation of eq. 10.8 by dt gives

$$\left(\frac{d\theta}{dt} \right)^2 = \gamma^2 \cdot \sin^2(\theta) + \left[\tan(\theta) - \beta \cdot \frac{d\theta}{dt} \right] \cdot \frac{d^2\theta}{dt^2} + \tan(\theta) \cdot \beta \cdot \frac{d^3\theta}{dt^3} \tag{10.9}$$

Remarkably, the differentiation neglected any information on the initial bubble position, i.e. eq. 10.9 does not depend explicitly on s_0. This information has to be re-introduced later by a proper constraint for the additional (third) integration constant (as the order of the differential equation changed from 2 to 3). No analytical solution/simplification has been found for eq. 10.9. A comparison of the magnitudes of the different terms however reveals that two terms can be neglected in good approximation. The magnitudes for β and γ^2 are both roughly $\mathcal{O}(10^{-11})$ and for any significant angle holds $\tan(\theta) = \mathcal{O}(0.1)$ and $\sin(\theta) = \mathcal{O}(0.1)$. Further, for any plausible rotation velocity holds $1 \gg \frac{d\theta}{dt} \gg \frac{d^2\theta}{dt^2} \gg \frac{d^3\theta}{dt^3}$. In consequence, (1) the term $\beta \cdot \frac{d\theta}{dt}$ can be dropped from the bracket term what (2) renders the term proportional in $\frac{d^3\theta}{dt^3}$ negligible compared to the term proportional to

$\frac{d^2\theta}{dt^2}$. Applying these simplifications, eq. 10.9 reduces to

$$\left(\frac{d\theta}{dt}\right)^2 = \gamma^2 \cdot \sin^2(\theta) + \tan(\theta) \cdot \frac{d^2\theta}{dt^2} \tag{10.10}$$

Remarkably, eq. 10.10 does not depend on β, that means no inertia effects are considered. Indeed, neglecting the inertial term already in eq. 10.8 (i.e. set $\beta = 0$) would directly result in eq. 10.10. Neglecting the third order term however also neglects the third integration constant. Thus, one of the initial condition has to be introduced as an additional constraint. Neglecting the inertia term implies that the actual process of initial acceleration from the rest position has been neglected. In consequence, it has to be assumed that the drag force always instantaneous adjusts to the normal force. This has to hold in particular at the initial conditions, i.e. the additional constraint reads $\frac{d\theta}{dt}|_{t=0} = \frac{d\theta}{dt}|_{\theta=\theta_0}$.

Analytical simplification of eq. 10.10 Eq. 10.10 can be reduced to a first order equation. Substituting $\psi = \frac{d\theta}{dt}$, thus $\frac{d^2\theta}{dt^2} = \psi \cdot \frac{d\psi}{d\theta}$, and rearranging of eq. 10.10 gives

$$\left[\psi^2 - \gamma^2 \cdot \sin^2(\theta)\right] d\theta + \left[-\tan(\theta) \cdot \psi\right] d\psi = 0 \tag{10.11}$$

By multiplying with $u(\theta) = \sin^{-3}(\theta) \cdot \cos(\theta)$, the resulting equation

$$\underbrace{\left[\sin^{-2}(\theta) \cdot \cot(\theta) \cdot \psi^2 - \gamma^2 \cdot \cot(\theta)\right]}_{A_\theta} d\theta + \underbrace{\left[-\sin^{-2}(\theta) \cdot \psi\right]}_{A_\psi} d\psi = 0 \tag{10.12}$$

has an exact solution (because $\frac{dA_\theta}{d\psi} = \frac{dA_\psi}{d\theta} = 2 \cdot u(\theta) \cdot \psi$), namely

$$\psi^2 = \gamma^2 \cdot \sin^2(\theta) \cdot \log[C \cdot \sin^{-2}(\theta)] \tag{10.13}$$

with an integration constant $C > 0$. Applying the initial conditions θ_0 and $\psi_0^2 = \gamma^2 \cdot \sin^2(\theta_0)$ implies $C = \exp(1) \cdot \sin^2(\theta_0)$. Re-substituting $\psi = \frac{d\theta}{dt}$ finally gives

$$\frac{d\theta}{dt} = -\text{sign}(s(t)) \cdot \gamma \cdot \sin(\theta) \cdot \sqrt{1 + 2 \cdot \log\left[\frac{\sin(\theta_0)}{\sin(\theta)}\right]} \tag{10.14}$$

where $-\text{sign}(s(t))$ assures that the physical constraint of a countering drag force is satisfied. No analytical solution of eq. 10.14 has been found. The following results for $\theta(t)$ and associated parameters are assessed instead by a numerical integration.

Retrieval of the total bubble slide time T and final crystal orientation $\theta(T)$ The bubble hits the crystal at $s_0 = \lambda \cdot \frac{l_c}{2}$. If $(0 < \lambda < 1)$, the bubble slides a distance of $(1-\lambda) \cdot \frac{l_c}{2}$ along the crystal face until it leaves the crystal independent on the particular model parameters. In this scenario the total slide time T can be obtained by solving

$$(1-\lambda) \cdot \frac{l_c}{2} = \int_0^T v_{buoy} \cdot \cos(\theta(t))\, dt \tag{10.15}$$

$$\Leftrightarrow (1-\lambda) \cdot A_{size} = \gamma \cdot \int_0^T \cos(\theta(t))\, dt \tag{10.16}$$

where the parametrisation of γ has been applied in the second step and $A_{size} = \sqrt{r_b/\tilde{r}_c}$. If $(-1 < \lambda < 0)$, the bubble slide can result in two distinguishable trajectories, depending on the model parameters: If the crystal orientation never exceeds $\theta < 90°$, the slide distance is $(1-\lambda) \cdot \frac{l_c}{2}$ and eq. 10.16 holds identically. If the crystal orientation at some time $T_{until\,turn}$ exceeds $\theta > 90°$ (i.e. $\theta(T_{until\,turn}) = 90°$), the total slide time $T = T_{until\,turn} + T_{after\,turn}$ can be obtained by

$$[1 + \lambda(T_{until\,turn})] \cdot A_{size} = \gamma \cdot \int_0^{T_{after\,turn}} \cos(\theta(t))\, dt \tag{10.17}$$

where $\lambda(T_{until\,turn}) < 0$ by construction.
The slide time T and the final zenith angle $\theta(T)$ can then be obtained by an iterative numerical integration of eq. 10.14. The numerical algorithm reads

$$\theta(t_{i+1}) = \lim_{\Delta t \to 0} \left[\theta(t_i) - \text{sign}(\lambda(t_i)) \cdot \gamma \cdot \sin(\theta(t_i)) \cdot \sqrt{1 + 2 \cdot \log\left[\frac{\sin(\theta_0)}{\sin(\theta(t_i))}\right]} \cdot \Delta t \right] \tag{10.18}$$

with the induction start $\theta(t_0) = \theta_0$.

Analytical estimation for T and $\theta(T)$ Before the quantitative results of the algorithm in eq. 10.18 are presented and discussed, some dependencies can be estimated analytically. Eq. 10.18 implies that θ can be decomposed as

$$\theta = \theta_0 + (\gamma \cdot t) \cdot f(\theta) + \mathcal{O}((\gamma \cdot t)^{>1}) \tag{10.19}$$

with a function $f(\theta)$ which is roughly proportional to $\sin(\theta)$ and in particular $|f(\theta)| < 1$ for most of all relevant scenarios. Thus for any times with $(\gamma \cdot t) < 0.1$ holds in good approximation

$$\frac{\cos(\theta)}{\cos(\theta_0)} = 1 - \tan(\theta_0) \cdot (\gamma \cdot t) \cdot f(\theta) + \mathcal{O}((\gamma \cdot t)^{>1}) \tag{10.20}$$

In consequence, if $\gamma \cdot T < 0.1$ and θ_0 not too large (this implies that there is no turning of the crystal), then holds approximately

$$\theta(T) > 0.9 \cdot \theta_0 \tag{10.21}$$

$$T \approx \frac{(1-\lambda) \cdot A_{size}}{\gamma \cdot \cos(\theta_0)} \tag{10.22}$$

Quantitative results of the numerical integration Eq.10.18 is a rather simple numerical algorithm compared, e.g., to more advanced algorithms which run several iterations. Its clear advantage is the relatively short run time and that the algorithm results are easily traceable. Its major drawback is its strict underestimation of $\theta(t_{i+1})$ because the $\frac{d\theta}{dt} \cdot \Delta t$ term is subtracting the previous — thus larger — $\theta(t_i)$ instead of an iteratively determined term which implicitly depends also on $\theta(t_i)$ (or likewise less than proportional on Δt). For sufficiently small Δt this underestimation nevertheless converges to zero (but increases the run time accordingly). Further, it is important to note that a variation of γ has an identical effect on the integration results as a variation of Δt. Setting a dynamic integration step size of $\gamma \cdot \Delta t = const$ thus results in exactly the same quantitative results for any γ. Physical-mathematically, eq. 10.18 nevertheless implies that there are residual dependencies on γ because $\sin(\theta(t_i))$ is implicitly depending on γ. Tests with a fixed $\Delta t = 10\,\mathrm{s}$ and varying γ by several orders of magnitude around $10^{-5}\,\mathrm{s}^{-1}$ indicate that these residual dependencies could cause quantitative effects on T and $\theta(T)$ of roughly $\log_{10}(10 \cdot \gamma)$, thus for most cases far below 1 %.

The following numerical results are calculated for $\gamma = 10^{-5}\,\mathrm{s}^{-1}$. Because the trajectory of θ is quasi independent on γ the quantitative finding holds true in very good approximation also for any $\gamma < 10^{-3}\,\mathrm{s}^{-1}$. The integration time interval has been set dynamical as $\Delta t = 10\,\mathrm{s} \cdot A_{size}$. The numerical results have been calculated for different sets $(\theta_0, \lambda, A_{size})$, namely $1° \leq \theta_0 \leq 89°$ in 1° steps, $-0.9 \leq \lambda \leq 0.9$ in 0.01 steps, and $A_{size} \in \{0.1, 1\}$ (Figures 10.2 and 10.3).

The numerical results revealed that A_{size} is the most crucial parameter. For $A_{size} = 0.1$ the numerical results are in good agreement with the approximated analytical derivations (Figure 10.2) for $\theta_0 < 50°$ and virtually any λ. For $\lambda < 0$ and $65° < \theta_0 < 75°$ the total slide time strongly increases because the crystal orientation come close to or even exceeds 90° what consequently slows th bubble rise. Further, the final crystal orientation here agrees almost perfectly with the analytical approximation of $0.9 \cdot \theta_0$ virtually independent on θ_0 or λ. This holds also for the absolute deviation from 90° if the crystal orientation turns.

Time scales The rising bubble with radius $r_b = f \cdot R_b$ covers in average a mean free path of $[n_c(\theta) \cdot l_c \cdot b_c \cdot \sin(\theta)]^{-1}$ until it hits a crystal with orientation θ after a time

$$\Delta t_{hit}^{BbyC} = \frac{1}{n_c(\theta) \cdot l_c \cdot b_c \cdot \sin(\theta) \cdot v_{buoy}(f \cdot R_b)} \tag{10.23}$$

Vice versa, a particular crystal with an initial orientation θ gets hit by a bubble with radius $r_b = f \cdot R_b$ in average every

$$\Delta t_{hit}^{CbyB} = \frac{1}{n_b(f) \cdot b_c \cdot l_c \cdot \sin(\theta) \cdot v_b} \tag{10.24}$$

When considering an explicit bubble size distribution $n_b(f)$ or an explicit crystal orientation distribution $n_c(\theta)$, the time scales for the bulk effects can be calculated by

$$(\Delta t_{hit}^{BbyC})_{bulk} = \frac{1}{l_c \cdot b_c \cdot v_{buoy}(R_b)} \cdot \frac{1}{f^2} \cdot \int_0^{\pi/2} \frac{d\theta}{n_c(\theta) \cdot \sin(\theta)} \tag{10.25}$$

$$(\Delta t_{hit}^{CbyB})_{bulk} = \frac{1}{l_c \cdot b_c \cdot v_{buoy}(R_b)} \cdot \frac{1}{\sin(\theta)} \cdot \int_0^{\infty} \frac{df}{n_b(f) \cdot f^2} \tag{10.26}$$

In the following, the ratio between the time scales will be used. In order to have some simple approximation, the time scales are compared with the analytical approximation of the slide time T:

$$\tau_{slide}^{BbyC} \equiv \frac{T}{\Delta t_{hit}^{BbyC}} = \frac{1}{2} \cdot n_c \cdot l_c^2 \cdot b_c \cdot \tan(\theta_0) \tag{10.27}$$

$$\tau_{slide}^{CbyB} \equiv \frac{T}{\Delta t_{hit}^{CbyB}} = \frac{1}{2} \cdot n_b \cdot l_c^2 \cdot b_c \cdot \tan(\theta_0) \tag{10.28}$$

but keep in mind under which conditions this approximation is valid!

Impact on crystal orientation The direct impact of one bubble slide event can be read of the Figures 10.2 and 10.3. The impact per time unit can be retrieved by multiplying with $\frac{\tau_{slide}^{CbyB}}{1+\tau_{slide}^{CbyB}}$. Besides this crystal erecting mechanism, the crystal orientation distribution is subject to further redistribution mechanisms such as the erection or shuffling of the crystal orientation by magma convection and the crystal nucleation. The latter is assumed to be isotropic in crystal orientation. The actual distribution is than controlled by the relative time scales of crystal erection and crystal nucleation.

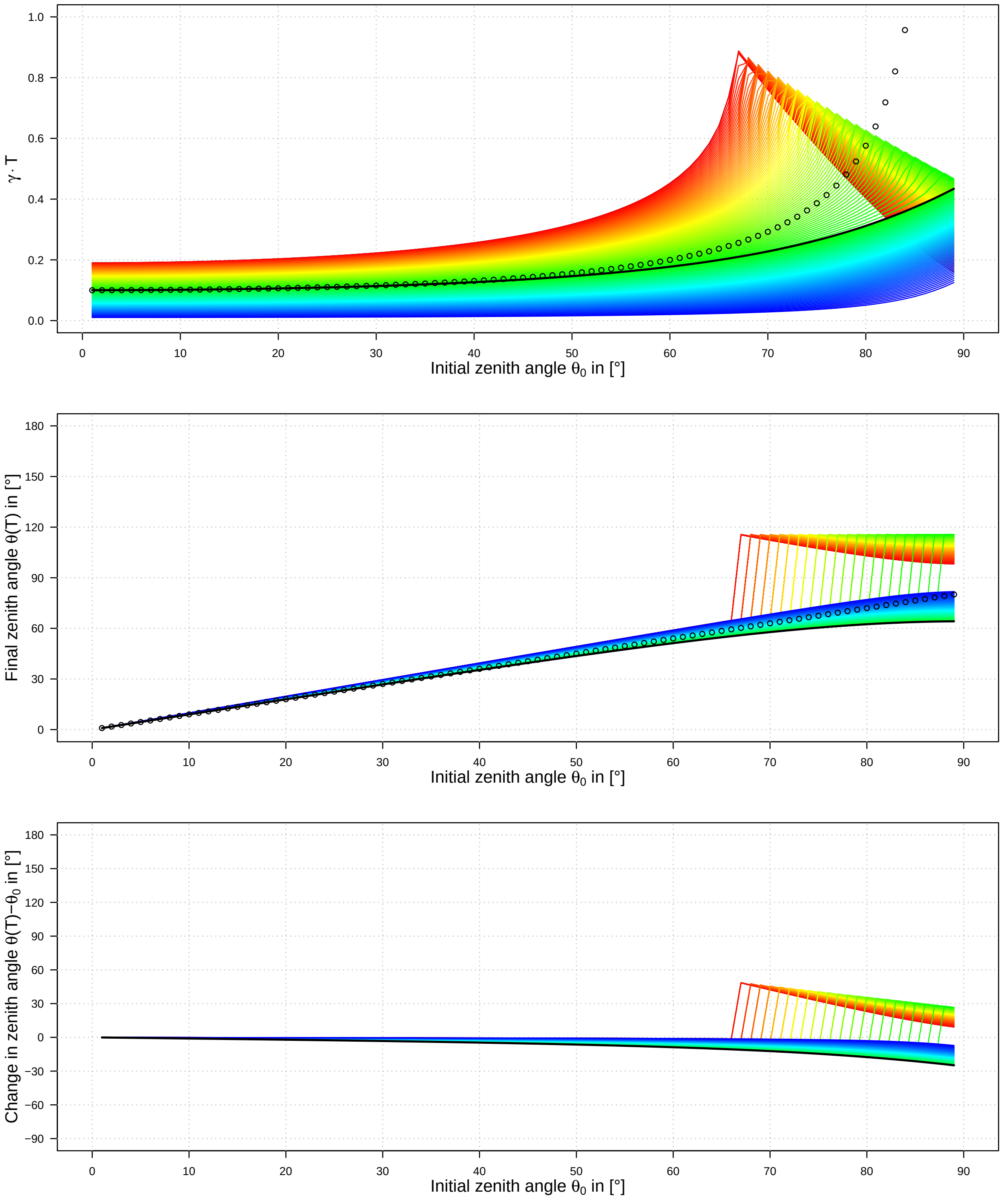

Figure 10.2: For $A_{size} = 0.1$, numerical solutions of the dimensionless slide time $\gamma \cdot T$ and the final zenith angle $\theta(T)$ depending on the initial zenith angle θ_0 and some chosen λ (colour-coded from red for $\lambda = -0.9$ to blue for $\lambda = 0.9$ and the black line indicates $\lambda = 0$). The open circles indicate the analytical approximation for $\lambda = 0$.

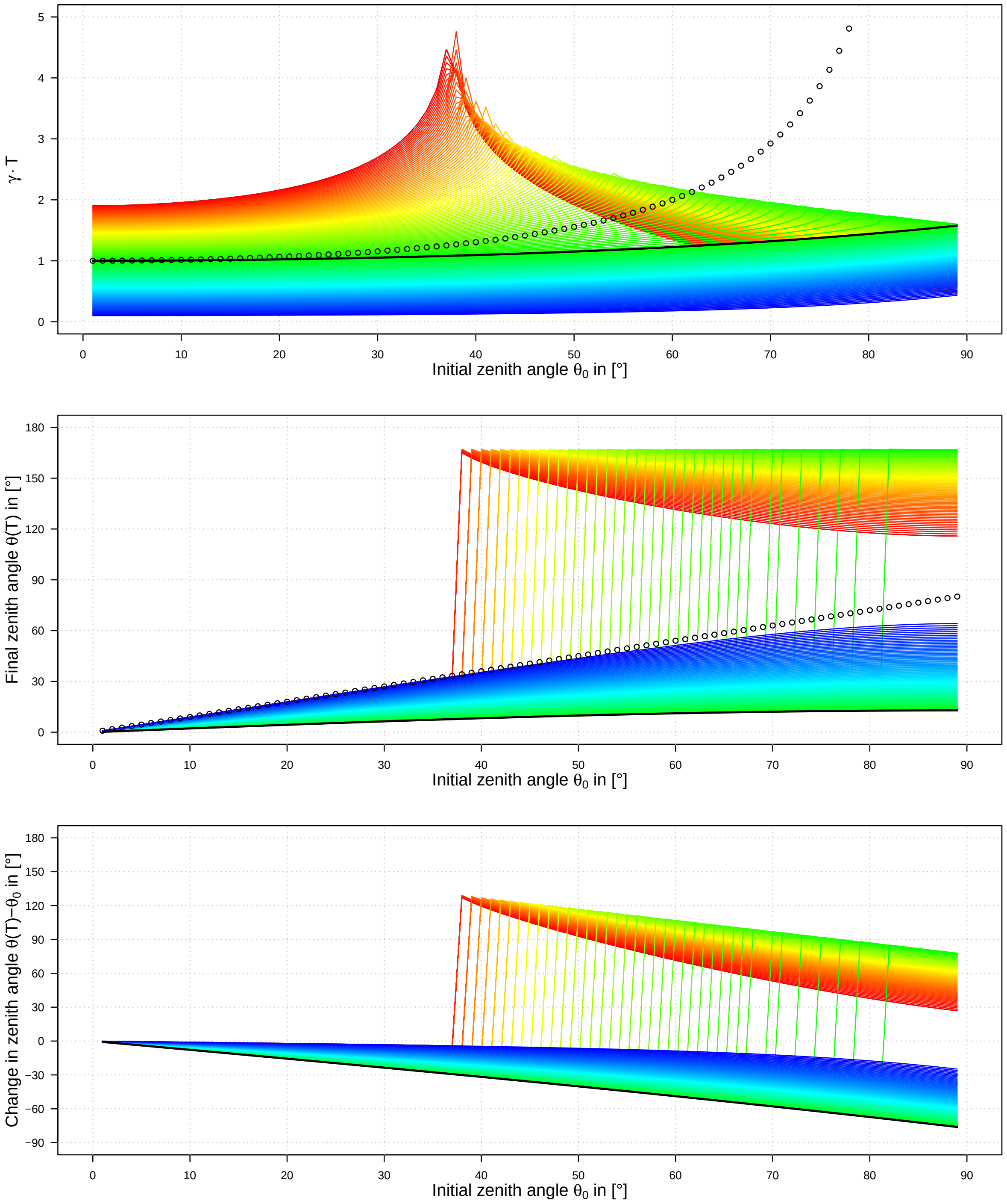

Figure 10.3: For $A_{size} = 1$, numerical solutions of the dimensionless slide time $\gamma \cdot T$ and the final zenith angle $\theta(T)$ depending on the initial zenith angle θ_0 and some chosen λ (colour-coded from red for $\lambda = -0.9$ to blue for $\lambda = 0.9$ and the black line indicates $\lambda = 0$). The open circles indicate the analytical approximation for $\lambda = 0$.

10.3 Crystal-orientation-induced enhancement of the bubble coalescence rate

The bubble slide results in a variation of the rise velocity during the slide as well as a horizontal redistribution (and accumulation) of the spatial bubble distribution in the magmatic melt. Both effects could independently result in an enhanced coalescence rate. On the other hand, the crystal-induced accumulation of bubbles could suppresses volatile degassing in the region above a crystal.

Crystal-orientation-induced collision volume H_{coi} The accumulation of bubbles on the crystal face is increasing the chance of coalescence. During the time interval T of the slide, the relative velocity between the attached bubble with radius $f_1 \cdot R_b$ and another non-attached bubble with radius $f_2 \cdot R_b$ is

$$\begin{bmatrix} v_h \\ v_z \end{bmatrix}_{relative} = \begin{bmatrix} -f_1^2 \cdot \sin(\theta) \cdot \cos(\theta) \\ f_2^2 - f_1^2 \cdot \cos^2(\theta) \end{bmatrix} \cdot v_{buoy}(R_b) \tag{10.29}$$

All non-attached bubbles with $f_2 > f_1 \cdot \cos(\theta)$ can approach the attached bubble. The corresponding collision volume (analogue to eq. 9.21, see Appendix of chapter 8) is the cylinder

$$\begin{aligned} H_{coi}(f_1, f_2, \theta(t)) &= \pi[(f_1 + f_2) \cdot R_b]^2 \cdot v_{buoy}(R_b) \cdot \int_0^T \max\Big(0, f_2^2 - f_1^2 \cdot \cos^2(\theta(t))\Big)\, dt \\ &= H_0 \cdot \frac{3 \cdot v_{buoy}}{4\,(f_1 + f_2)\,R_b} \cdot \int_0^T \max\Big(0, f_2^2 - f_1^2 \cdot \cos^2(\theta(t))\Big)\, dt \end{aligned} \tag{10.30}$$

where the max(..) operator implies that there may not be a crystal-orientation-induced effect on the coalescence rate for small θ will coalescent with the attached bubble.
In the following, we assume for the sake of simplicity (1) a constant $\theta(t) = \theta_0$ for the overall slide and (2) apply the analytical estimate $T = \frac{1-\lambda}{\cos(\theta_0)} \cdot \frac{l_c}{2\,v_{buoy}}$. Furthermore, then also λ is constant and in average vanishes. Thus eq. 10.30 reduces to

$$\begin{aligned} \frac{H_{coi}}{H_0}(f_1, f_2, \theta_0) &= \frac{3 \cdot l_c}{8 \cdot (f_1 + f_2) \cdot R_b \cdot \cos(\theta_0)} \cdot \max\Big(0, f_2^2 - f_1^2 \cdot \cos^2(\theta_0)\Big) \\ &= \frac{3\,v\,T}{4\,R_b} \cdot \Bigg[\frac{\sin^2(\theta)}{2}\Big((1-q)^2 + q^2 \cdot \sqrt[3]{2}\Big) + \\ &\qquad \frac{(1-q)\cdot q}{1+\sqrt[3]{2}}\Big(\sqrt[3]{4} - \cos^2(\theta) + \max(0, 1 - \sqrt[3]{4} \cdot \cos^2(\theta))\Big)\Bigg] \end{aligned} \tag{10.31}$$

Separated bubble flow For a significantly polydisperse bubble distribution, the crystal-orientation-induced coalescence has to be compared with the coalescence due to polydisperse rise velocities. For a given pair of bubbles, we obtain

$$\frac{H_{coi}}{H_{buoy}} = \frac{f_2^2 - f_1^2 \cdot \cos^2(\theta_0)}{|f_2^2 - f_1^2|} \cdot \frac{T}{T + \Delta t_{hit}^{BbyC}} \tag{10.32}$$

It has to be highlighted that the absolute value operator is only applied on the denominator. In order to calculate the overall ratio, both coalescence volumes have to be integrated separately over f_2 and f_1. Eq. 10.32 can however not be integrated directly due to the singularity. Instead eq. 9.21 and 10.31 are integrated separately for a given $\delta_b(f)$ and then their ratio is taken. For a first estimation, again

$$\tilde{\delta}_b^{size}(f;q) = \begin{cases} 1-q & : \ f = 1 \\ q & : \ f = \sqrt[3]{2} \end{cases} \tag{10.33}$$

with $0 \leq q < \frac{1}{2}$ is chosen (see eq. 9.6) which represents a monodisperse scenario except for a fraction q of bubbles which have coalescent once. Then, the integrals of eq. 9.21 and 10.31 reduce to simple sums. We obtain for the average $\tilde{H}_{buoy}$ and $\tilde{H}_{coi}$ and its ratio (see Appendix A2 for calculation)

$$\frac{\tilde{H}_{buoy}(q)}{H_0(1,1)} = (q - q^2) \cdot \frac{9}{16 \cdot R_b} \cdot v_{buoy}(R_b) \cdot (T + \Delta t_{hit}^{BbyC}) \tag{10.34}$$

$$\begin{aligned} \frac{\tilde{H}_{coi}(q)}{H_0(1,1)} = {} & \frac{3 \cdot v_{buoy} \cdot T \cdot \sin^2(\theta)}{8 \cdot R_b} \cdot \left[\left((1-q)^2 + q^2 \cdot \sqrt[3]{2} \right) + \right. \\ & \left. (q - q^2) \cdot \frac{2 \cdot (1 + \sqrt[3]{4})}{1 + \sqrt[3]{2}} \cdot \max\left(\frac{\sqrt[3]{4} - \cos^2(\theta)}{(1 + \sqrt[3]{4}) \cdot \sin^2(\theta)}, 1 \right) \right] \end{aligned} \tag{10.35}$$

$$\begin{aligned} \frac{\tilde{H}_{coi}}{\tilde{H}_{buoy}}(q,\theta) = {} & \frac{2}{3} \cdot \frac{T \cdot \sin^2(\theta)}{T + \Delta t_{hit}^{BbyC}} \cdot \left[\frac{1/q + \sqrt[3]{2} - 1}{1 - q} - (1 + \sqrt[3]{2}) + \right. \\ & \left. \frac{2 \cdot (1 + \sqrt[3]{4})}{1 + \sqrt[3]{2}} \cdot \max\left(\frac{\sqrt[3]{4} - \cos^2(\theta)}{(1 + \sqrt[3]{4}) \cdot \sin^2(\theta)}, 1 \right) \right] \end{aligned} \tag{10.36}$$

As a quantitative example, for $T = 1$, $\theta = 45°$, and $q = 0.1$ the ratio is 1.9 and thus twice as strong as the classical crystal-free end-member mechanism. In order to get the average impact of tilted crystals, eq. (10.36) has to be integrated over the actual distribution $\delta_c(\theta)$.

Disperse bubble flow The collision volume H_{disp} has been derived in Chapter 9. For the relative effect holds:

$$\frac{H_{coi}}{H_{disp}} = \sin(\theta_0) \cdot \tan(\theta_0) \cdot \frac{3\,l_c}{16\,R_b} \cdot \frac{H_0}{H_{disp}} \tag{10.37}$$

$$= \sin(\theta_0) \cdot \tan(\theta_0) \cdot \frac{3\,l_c}{16\,r_b} \cdot \frac{C^0_{H_2O} - \sqrt{K_{H2-O} \cdot p_0}}{C^0_{H2_O} - \frac{1}{2}\sqrt{K_{H_2O} \cdot p_0}} \cdot \frac{p_0}{(\nabla p)_{vert} \cdot v_{melt} \cdot \Delta t} \tag{10.38}$$

Concept of rise channel and crystal shadow

Besides the enhanced coalescence rate during the bubble slide, the crystal-induced bubble accumulation can have further effects on the bubble coalescence rate and on the total gas volume fraction. On the one hand, all bubbles leave the crystal at the upper crystal edge, aligning all bubbles in a "rise channel". There the bubble accumulation has a positive effect on bubble coalescence rate as well as on volatile degassing. On the other hand, no more bubble access the "crystal shadow" volume above the crystal (Figure 10.4).

Within the crystal shadow, the lack of bubbles suppresses the diffusion-driven short-distance volatile degassing. In order to investigate the relative impact of the crystal orientation on the overall volatile degassing and thus gas volume fraction, we set-up the following scenario: The investigated local magma volume contains isotropically distributed crystals of the same size and yaw angles of 90°, has a crystal number density n_c, and is supersaturated in volatiles. The volatile diffusion time scale compares to the rise velocity of the bubbles such that all volatiles within a horizontal spacing of $R_b + \delta$ from the bubble centre can and will degas in the bubble until the equilibrium saturation is reached. The magma volume is divided by the crystals in three kinds of regions (see right panel in Figure 10.4) which have different volatile weigh fractions C_i (for each particular volatile species) and volume fractions $\Omega_i < 1$ of the (local) magma volume ($\Sigma_{i=1}^{3}\Omega_i = 1$). The regions are (1) the background with C_{bg} and Ω_{bg}, (2) the rise channel which is depleted in volatiles with $C_{rc} \leq C_{bg}$ and Ω_{rc}, and (3) the crystal shadow with $C_{cs} \geq C_{bg}$ and Ω_{cs}. Accordingly, we obtain for the absolute change in the (local) gas volume fraction due to the existence of tilted crystals

$$\Delta\phi = \frac{\rho_{melt}}{\rho_{gas}} \cdot \left[\Omega_{rs} \cdot (C_{bg} - C_{rc}) + \Omega_{cs} \cdot (C_{bg} - C_{cs})\right] \tag{10.39}$$

The volume fractions of the rise channel and the crystal shadow can be parametrised. The volume fraction of the rise channel is constant for all crystal orientations

$$\Omega_{rc} = [2\,R + 2\,\delta] \cdot b_c \cdot \Delta z_c \cdot n_c = [2\,R_b + 2\,\delta] \cdot b_c \cdot n_c^{2/3} \tag{10.40}$$

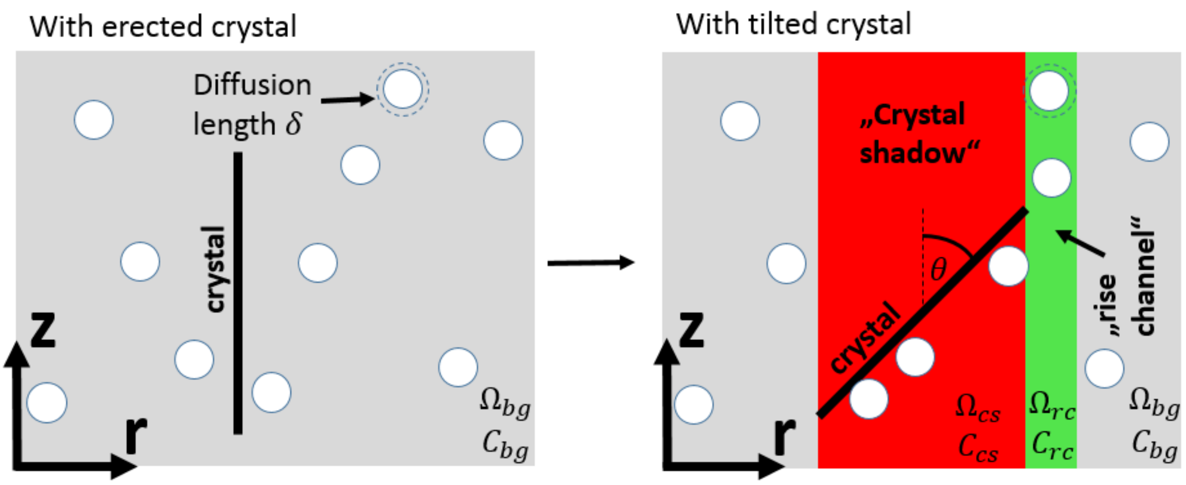

Figure 10.4: Concept of the crystal shadow and the rise channel. The positive vertical direction is denoted by the z-axis, both horizontal directions are denoted by the r-axis. Bubbles are ascending in positive z-direction. If the local magma patch is supersaturated in volatiles, the volatiles can diffuse into a bubble if they their distance to the bubble wall is at most δ. The crystal orientation is given by the zenith angle θ. When the crystal is not perfectly erected, it causes the constitution of three distinguishable spatial domains $i \in \{bg, cs, rc\}$: the unaltered background domain (bg, grey), the crystal shadow (cs, red), and the rise channel (rc, green). The both latter are actually located only above the crystal and the upper crystal edge, respectively. The volatile concentrations in the three domains are denoted by C_i and the volume fraction by Ω_i.

and the volume fraction of the crystal shadow is

$$\Omega_{cs} = [l_c \cdot \sin(\theta) - 2\,\delta] \cdot b_c \cdot \Delta z_c \cdot n_c = [l_c \cdot \sin(\theta) - 2\,\delta] \cdot b_c \cdot n_c^{2/3} \tag{10.41}$$

where the rather negligible cases of $\theta < \arcsin(2\,\delta / l_c)$ are ignored. Together, the equations 10.39, 10.40, and 10.41 give

$$\Delta\phi = \frac{\rho_{melt}}{\rho_{gas}} \cdot l_c \cdot b_c \cdot n_c^{2/3} \cdot \left[(C_{bg} - C_{rs}) \cdot \frac{2\,R_b + 2\,\delta}{l_c} + (C_{bg} - C_{cs}) \cdot \left(\sin(\theta) - \frac{2\,\delta}{l_c} \right) \right] \tag{10.42}$$

The volatile weight fraction C_{bg} of the background depends on the initial magma composition but also on the magma ascent rate and it thus not necessarily in equilibrium with the gas phase. In the rise channel, the bubble rate is enhanced by a factor of $1 + \frac{l_c \cdot \sin(\theta)}{2\,R_b}$ compared to the background. Thus, there the volatile weight fraction C_{rc} has to be lower than the background level, however, it can not be lower than the equilibrium level. In the crystal shadow, the volatile weight fraction C_{cs} is enhanced compared to the background. Potentially, the crystal shadow even holds the conserved volatile weight fraction as it was when the crystal formed, i.e. for some volatile species the initial weight fraction. For the order of magnitude of the diffusion length δ of water vapour holds approximately $\delta = \frac{2 \cdot D^{H_2O}}{v_{buoy}} \approx \nu \cdot D^{H_2O} << l_c$ with the H_2O diffusivity $D^{H_20} \approx 10^{-11} \mathrm{m}^2/\mathrm{s}$ [Gonnermann and Manga, 2013]. Following this reasoning, we can give an upper limit for the impact of crystal orientation. Fixing the maximum conditions (1) C_{bg} (and thus C_{rs}) is in equilibrium (e.g. due to a slow magma ascent), (2) $\delta << l_c$, and (3) $C_{cs} = C_0$ would give

$$\Delta\phi^{upper\ limit} = -l_c \cdot b_c \cdot n_c^{2/3} \cdot \ \sin\theta \cdot \frac{\rho_{melt}}{\rho_{gas}} \cdot (C_0 - C_{bg}) = -l_c \cdot b_c \cdot n_c^{2/3} \cdot \sin(\theta) \cdot \phi \tag{10.43}$$

For the chosen parameters and $\theta = 30°$, the gas volume fraction is reduced by 23 %, proposing a quite significant impact of the tilted crystals on the overall size of the gas phase. A smaller ϕ does not only mean less gas molecules which could constituted in the pressure build-up but also in a decreased coalescence rate because less bubbles or smaller bubbles are available. In particular in relatively great depth (e.g. when water vapour just starts to dissolve from the melt), this may significantly dampening the bubble rise.

Nevertheless, a non-vanishing δ and volatile diffusion from the crystal shadow to the rise channel counter this quantitative value. And the quantitative results are highly dependent on parameters of the particular magmatic melt.

10.4 Summary and outlook

The mechanical interaction of rising bubbles and tilted crystals has been investigated. It has been found that there is actually no literature on the most simple scenario, the bubble slide along the tilted crystal. The dynamics of such a process have been revealed to be rather complicated even on a simplified stage. Within this thesis the mathematical derivation for this rather general process is provided. A key finding is that crystals which have approximately the same extension as the gas bubbles get vertically aligned by the bubbles independently on parameters such as the magma viscosity. Another key finding is that bubbles which are much smaller than the particular crystal get redirected in their rise. In consequence, comparatively large crystals can enhance the bubble coalescence rate by a multiple when compared to exclusively vertically aligned crystals. Furthermore, the concept of the crystal shadow and the rise channel has been introduced. As a finding, tilted crystals could suppress volatile degassing in the domain above the crystals. As a maximum limit, a decrease of the overall magmatic gas volume fraction of −23 % has been proposed.
Originally, this model has been introduced in order to assess the tidal effect on volcanic degassing via the effect of the tide-induced displacement profile on the crystal orientation. When assuming an isotropic distribution of the crystal orientation, the effect of a tide-induced variation of the crystal orientation should more or less cancel w.r.t. to variations in the bubble slide mechanism. Though the crystal shadow effect could cause a persistently larger impact during a spring tide because then a larger magma domain potentially supersaturated in volatiles can degas (Figure 10.5).

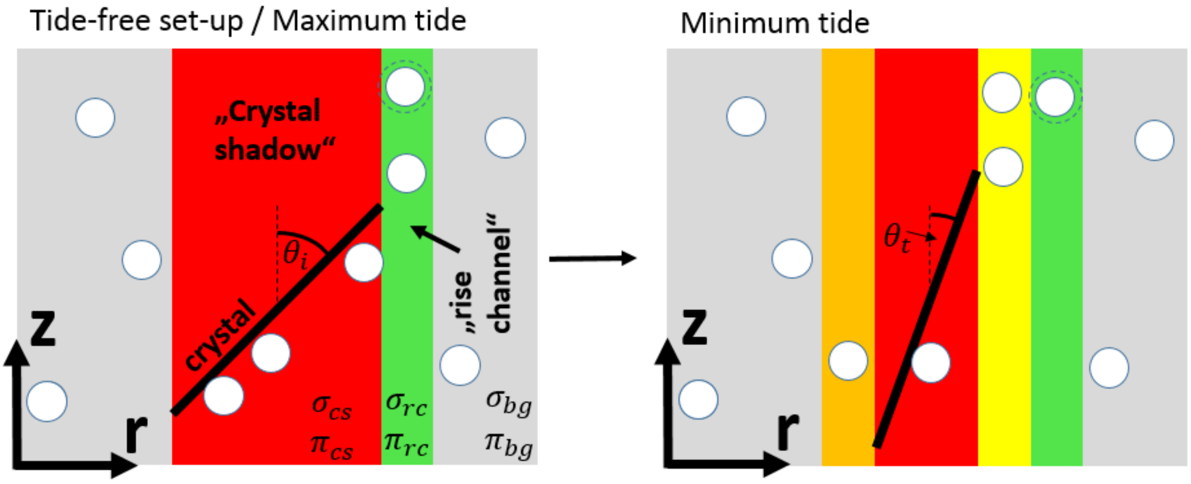

Figure 10.5: Concept of the tidal stirring. The tide-induced radial displacement profile (Chapter 9) could vary the orientation θ of the crystals. This allows for a periodical access to the crystal shadow (orange and yellow volumes) and thus to enhanced volatile degassing.

11 Conclusions

This thesis reports, analyses, and compares multi-year time series of SO_2 and BrO slant column densities as well as BrO/SO_2 molar ratios in the gas plumes emitted by 6 volcanoes in Central and South America (Nevado del Ruiz, Cotopaxi, Masaya, Tungurahua, Galeras, Villarrica). Its aim is to strengthen the understanding of variations in the BrO/SO_2 molar ratios in order to use this parameter as a tracer for magmatic processes. Particular emphasis has been risen in elucidation of different origins for the variations in the BrO/SO_2 molar ratios, namely a magmatic origin, a hydrothermal origin, a meteorological origin, an instrumental origin but also more specific origins such as a melting glacier or the Earth tides. Independent from — but motivated by — the empirical results, two fundamental models have been developed during this thesis; a model on the link between the Earth tides and volcanic degassing and a model on the mechanical interaction between gas bubbles and tilted crystals in magmatic melt. The major achievements and conclusions of this thesis are condensed in Figure 11.1 and summarised on the following pages.

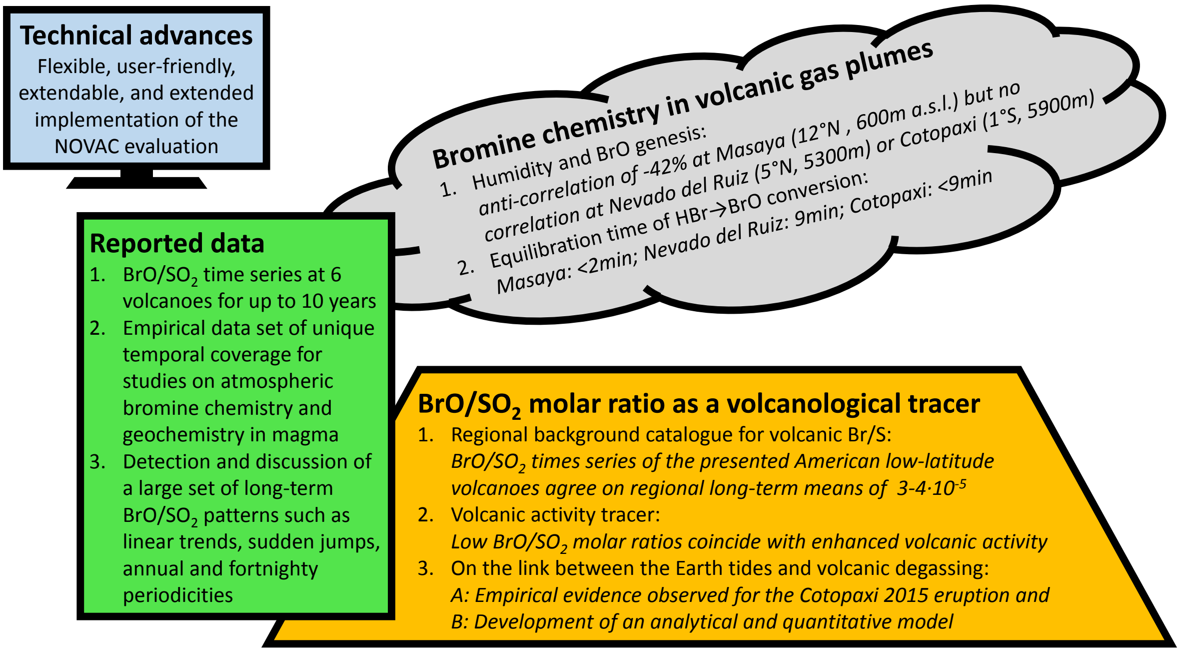

Technical advances
Flexible, user-friendly, extendable, and extended implementation of the NOVAC evaluation

Bromine chemistry in volcanic gas plumes
1. Humidity and BrO genesis:
   anti-correlation of -42% at Masaya (12°N , 600m a.s.l.) but no correlation at Nevado del Ruiz (5°N, 5300m) or Cotopaxi (1°S, 5900m)
2. Equilibration time of HBr→BrO conversion:
   Masaya: <2min; Nevado del Ruiz: 9min; Cotopaxi: <9min

Reported data
1. BrO/SO_2 time series at 6 volcanoes for up to 10 years
2. Empirical data set of unique temporal coverage for studies on atmospheric bromine chemistry and geochemistry in magma
3. Detection and discussion of a large set of long-term BrO/SO_2 patterns such as linear trends, sudden jumps, annual and fortnighty periodicities

BrO/SO_2 molar ratio as a volcanological tracer
1. Regional background catalogue for volcanic Br/S:
   BrO/SO_2 times series of the presented American low-latitude volcanoes agree on regional long-term means of $3\text{-}4\cdot10^{-5}$
2. Volcanic activity tracer:
   Low BrO/SO_2 molar ratios coincide with enhanced volcanic activity
3. On the link between the Earth tides and volcanic degassing:
   A: Empirical evidence observed for the Cotopaxi 2015 eruption and
   B: Development of an analytical and quantitative model

Figure 11.1: Major achievements and conclusions of this thesis.

Technical advances

Advances in the NOVAC BrO/SO_2 retrieval The already massive and yet continuously growing NOVAC data set makes an automatically retrieval algorithm inevitable. Lübcke [2014] provided a BrO/SO_2 retrieval algorithm tailored to single NOVAC instruments. Within this thesis, the implementation of his algorithm has been improved in particular with respect to flexibility, extensibility, and user-friendliness. Additionally, new functionalities have been developed: The accuracy of the final BrO/SO_2 results has been enhanced by a more sophisticated plume finder algorithm and the introduction of further data filters. The automatic detection and correction of a possible contamination of the background spectra with volcanic gases has been investigated together with co-workers but yet without concluding recommendations concerning the BrO/SO_2 retrieval [see Lübcke et al., 2016, Wilken, 2018]; thus this functionality is implemented but not yet routinely applied. Furthermore, the spectroscopic results are now semi-automatically assessed by a comprehensive statistical evaluation routine.
As an outlook, it has been agreed at the technical NOVAC meeting in February 2019 that the BrO/SO_2 evaluation presented here gets included in the official NOVAC routine (see http://novac-community.org/wp-content/uploads/2019/02/NOVAC-technical-meeting-2019_notes.pdf). Along with this update of the NOVAC routine, an automatic retrieval of the instrument line function should be included.

Additional parameters retrieved from NOVAC NOVAC has been designed in order to retrieve the SO_2 and BrO slant column densities in volcanic gas plumes, though several further parameters could be retrieved from the NOVAC spectra. This thesis explored on a basic level the possibilities to derive the differential O_4 slant column densities and the contrast in the colour index of the volcanic plume in order to, e.g., retrieve the effective light path lengths spectroscopically. Furthermore, a tomography with two NOVAC instruments allowed for a retrieval of the plume height and wind direction at Masaya. All these retrievals are implemented as optional modules in the evaluation routines.

Temporal variations of the instrument line function Temperature-induced variations of the instrument line function (ILF) could be the predominant source of systematic errors in the BrO and SO_2 retrieval from NOVAC spectra. These variations have been comprehensively investigated for a 9-year time series of the NOVAC instrument D2J2200_0. It has been confirmed that the additional Levenberg–Marquardt fit parameters can enhance the accuracy of the DOAS fit, in particular for large SCDs. Nevertheless, it is highly recommended to minimise the ILF-induced inaccuracies by improving the knowledge base on the ILF either by recording the temperature dependency of the ILF experimentally and/or by the application of an algorithm module which automatically retrieves the current ILF from the recorded NOVAC spectra.

Reported data

More than a decade of continuous BrO/SO_2 data Empirical time series of the BrO/SO_2 molar ratios in volcanic plumes have been typically recorded during field campaigns and are thus limited to a length of several weeks and to a particular location. In sharp contrast, the BrO/SO_2 time series reported here extend over 10 years and 6 locations spanning along the western American shore from 14°N to 39°S and thus allow for the detection of temporal cycles and regional–continental correlations in atmospheric bromine chemistry or volcanology.
This thesis focused on the temporal variations at the individual volcanoes. Future studies may use the massive data set and methods provided here to compile and compare all promising additional parameters with the BrO/SO_2 time series as well as the analysis of the spatial variations.

Detected long-term patterns in the BrO/SO_2 time series In terms of the long-term mean BrO/SO_2 molar ratios and for the range of the volcanoes presented here, the relative standard deviation of the BrO/SO_2 time series varied by $40 - 80\,\%$. The predominant part of this variation is caused by the relative mean diurnal BrO/SO_2 variability, which varied by $40 - 60\,\%$. Nevertheless, the lengths and relatively high resolution of these time series allowed for the detection of a diverse set of long-term patterns in the BrO/SO_2 molar ratios: linear long-term trends, persistent jumps, annual periodicities, and a fortnightly periodicity during the Cotopaxi eruption 2015. The annual cycles are found to be most likely induced by the seasonal cycles in the meteorology. The fortnightly periodicity are found to be most likely induced by the Earth tides. The other patterns are often found to coincide with volcanological changes.

Outlook With the NOVAC data base continuously increasing, conclusions drawn from BrO/SO_2 molar ratios can be expected to become more reliable with respect to the specific local volcanic system but also with respect to global links between deep magmatic processes and variations in the BrO/SO_2 ratios. The ongoing research of the atmospheric bromine chemistry will also help to separate atmospheric and magmatic origins for observed variations in the BrO data.
In particular: (1) The larger the time series the larger the chance to observe the behaviour of the volcanic gas emission in reaction to annual cycles and incidental events such as particularly strong rain events. (2) The empirical NOVAC BrO/SO_2 data combined with experiments and simulations could boost the understanding of the bromine chemistry in volcanic gas plumes. This enhanced knowledge can then be used to further improve the accuracy of the NOVAC data. (3) A robust knowledge on the long-term background BrO/SO_2 molar ratios allows for a faster detection of short-term variations in the BrO/SO_2 molar ratios which are linked to potential volcanic hazards such as it has been observed at Nevado del Ruiz.

Bromine chemistry in volcanic gas plumes

Massive empirical data set on atmospheric bromine chemistry Previous studies have examined the bromine chemistry in a volcanic gas plume by empirical observations, lab experiments, and model simulations. The evolution rate and equilibrium level of the HBr→BrO conversion are not yet fully understood but are expected to be potentially controlled by the rate of ozone in-mixing into the volcanic plume, the light intensity, and the chemical composition of the volcanic plume, e.g., the acidity of its aerosol phase.

In this thesis, a comparison of the BrO/SO_2 time series with the meteorological parameters has been conducted for Nevado del Ruiz (10 years of continuous data), Masaya (5 years), and Cotopaxi (1 year). No direct measurements on the meteorological parameters have been available for the proximity of the volcanoes and in particular not in the altitude of their volcanic gas plumes. As the best available proxy, simulation data from the ECMWF weather forecast model have been used. These simulations have however intrinsic problems at the mountainous topology of volcanoes and are of relatively poor spatial and temporal resolution.

Different observations on the impact of humidity At Masaya, a strong anti-correlation between the BrO/SO_2 molar ratios and the specific humidity has been observed (correlation coefficient of $-42\,\%$, average humidity of $14\,\frac{\mathrm{g\,H_2O}}{\mathrm{kg\,air}}$). No such significant correlation has however been observed for Nevado del Ruiz or Cotopaxi (both with an average humidity of about $4\,\frac{\mathrm{g\,H_2O}}{\mathrm{kg\,air}}$). This contrast may indicate that humidity variations impact the atmospheric bromine chemistry only at relatively large humidity levels/variations. Remarkably, the humidity variations at low latitudes are correlated to the position of the ITCZ and thus to a transition from one to the other climatological hemisphere. The correlation between the humidity and BrO/SO_2 molar ratios could thus be a manifestation of, for example, the impact of a change in the local ozone concentration on the bromine chemistry rather than of the humidity itself.

Retrieval of bromine conversion rate At Nevado del Ruiz, an asymptotic increase of the mean BrO/SO_2 molar ratios depending on the atmospheric age of the volcanic gas plumes (which is determined by the wind speed and direction) has been observed. The BrO/SO_2 molar ratios there reached an equilibrium around 9 min after the release to the atmosphere and remained at this level for at least 60 min. No such BrO/SO_2 evolution path has been observed at Masaya or Cotopaxi. Accordingly, at these volcanoes the BrO/SO_2 molar ratios reached the equilibrium prior to any NOVAC measurements, that is within the first 2 min and the first 9 min, respectively, after the release to the atmosphere, and remained on this level for at least 20 min and 60 min, respectively.

BrO/SO_2 molar ratios as a volcanological tracer

Towards a regional background catalogue for volcanic Br/S molar ratios The BrO/SO_2 times series at 4 of the 5 presented approximately equatorial American volcanoes (Masaya, Nevado del Ruiz, Cotopaxi, Tungurahua; 1.5°S – 12.0°N) agree in a regional long-term BrO/SO_2 level of $(3-4) \cdot 10^{-5}$. For Galeras, only data during a period of high activity were observed and thus the observed BrO/SO_2 molar ratios were lower (see below). For Villarrica (39.4°S), a long-term BrO/SO_2 molar ratio of $6.8 \cdot 10^{-5}$ was observed which agrees with the literature value of $6.9 \cdot 10^{-5}$. All here presented results are in good agreement with the literature which reports BrO/SO_2 molar ratios of Central and South American volcanoes spanning between $(1.1-6.9) \cdot 10^{-5}$.

Empirical evidence for lower BrO/SO_2 molar ratios at periods of enhanced general volcanic activity Decreased BrO/SO_2 molar ratios coincided with enhanced volcanic activity on several time scales, for example, persistently lower BrO/SO_2 molar ratios during multi-month phases of high activity at Nevado del Ruiz and Tungurahua and lower BrO/SO_2 molar ratios at the starts of multi-year eruption periods when compared to the long-term means. Furthermore, a comparison with the observed long-term pattern with other volcanological parameters indicates that bromine likely degasses later than sulphur from the magmatic system.

On the link between the Earth tides and volcanic degassing A persistent fortnightly periodicity has been observed in the BrO/SO_2 time series at Cotopaxi after its phreatomagmatic explosions on August 14 2015. Several possible meteorological and local volcanological origins for this pattern have been investigated but no plausible explanation has been found. In contrast, the spring–neap tide cycle is the only fundamental natural process with a fortnightly periodicity. A comparison of the BrO/SO_2 time series and the tide-induced ground surface displacements revealed unexpectedly high correlation coefficients of 50 % and 41 % for the displacement component in North–South direction or the synchronous components in vertical and East–West direction. The particularly large correlation with the North–South component can be explained by the fault geometry at Cotopaxi which is predominantly in ENE–WSW direction.
A quantitative model has been developed to investigate a possible causal link between the Earth tides and volcanic degassing. The model describes the impact of the tide-induced gravity variations on the bubble coalescence rate in magmatic melt and suggests a tide-induced enhancement by up to a multiple of 10 %. The theoretical framework of this model now allows for further advances on the tidal impact on volcanism. Another novel model investigates under which conditions the mechanical interaction between gas bubbles and tilted crystals in magmatic melt could cause an erection of the crystals or an enhanced bubble coalescence rate.

Acknowledgments

Not only for the sake of chronology, [redacted] and [redacted] have to be listed on the head of my acknowledgements. Their trust in my skills gave me the opportunity to start and complete the presented study on spectroscopy, atmospheric chemistry, and volcanology. The discussions with them taught me a deep understanding of spectroscopy. Their continuous support motivated me to pertinaciously pioneer the new terrain explored during this thesis. Many thanks to [redacted] and [redacted] whose supervision made it possible to me as an external doctoral candidate to submit this thesis to the Johannes Gutenberg University of Mainz.

I would like to thank many former and current members of the Atmospheric Science Group at the Institute for Environmental Physics at the University of Heidelberg. I equally enjoyed the high level of academic discussions and the always informal, open-minded, and cooperative atmosphere. Thank you [redacted] for explaining me so many things on volcanoes! Thank you [redacted] for introducing me comprehensively in the world of NOVAC evaluations (and also thank you for persisting on lunch at 12 sharp. ;-))

Thanks also to the many as kind and supportive members of the Satellite Remote Sensing group at the Max-Planck Institute for Chemistry in Mainz who became my second scientific home.

An extraordinary big thank you goes to [redacted] to [redacted] for our joint journey in the world of the Earth tides! Also, you are the greatest co-author I could imagine! This said, working together with [redacted] from [redacted] and [redacted] from [redacted] was definitively as pleasant and fruitful! :-)

Last but not least, I want to thank [redacted] for their manifold support for the last twenty nine years and for arousing my curiosity for sciences from the early beginning on. Aaand: Thank you [redacted], [redacted], and [redacted] for babysitting, camping, board game playing, reliable Vienna opera company, thesis proof-reading, ... you got it, right? ;-)

Personal data of third parties have to be made irrecognisable in the electronic version, see EU Regulation 2016/679 (GDPR).

Curriculum Vitae

March 20 1990
Born in Aalen, Germany

2000 – 2008
Hellenstein Gymnasium in Heidenheim, Germany

2008 – 2011
Bachelor of Science in PHYSICS at the University of Heidelberg, Germany
Thesis: *Osmotic power plants and their potential*

August 2011
IAESTE Internship at the Institute of High-precision measurements, Kiev, Ukraine

2011 – 2014
Master of Science in PHYSICS at the University of Heidelberg, Germany

- Thesis: *Characterisation of a Cavity Ring-Down Spectrometer for measuring* CO_2, CH_4, $\delta^{13}CO_2$, *and* $\delta^{13}CH_4$ *in ambient air*
- Marsilius Certificate for interdisciplinary studies
- Teaching Assistant in *Physics for natural scientists*, for 5 terms

March 2013
Internship at RWE Innogy (Dept. for Risk Controlling and Evaluation), Essen, Germany

2014 – 2019
Doctoral studies in PHYSICS at the University of Mainz, Germany — including

- Teaching Assistant/Presentation Coach in *Introduction in meteorology*, for 3 terms
- Field experience: CCVG Workshop 2014 in Chile, CCVG Workshop 2017 in Ecuador (and Colombia), Etna Int. Training School of Geochemistry 2018

2017 – 2019 (anticipated)
Master of Science in ECONOMICS at the University of Heidelberg, Germany

List of Abbreviations

- **Chemical compounds**
  BrO: Bromine Monoxide, **CO_2:** Carbon Dioxide, **HBr:** Hydrogen Bromine, **H_2O:** Water, **H_2S:** Hydrogen Sulfide, **O_3:** Ozone, **O_4:** Oxygen Dimer, **OClO:** Chlorine Dioxide, **SiO_2:** Silicon Dioxide (Quartz), **SO_2:** Sulphur Dioxide
- **COSPEC:** Correlation Spectroscopy
- **DOAS:** Differential Optical Absorption Spectroscopy
- **ECMWF:** European Centre for Medium-Range Weather Forecasts
- **FTIR:** Fourier Transform InfraRed spectroscopy
- **ILF:** Instrument Line Function
- **ITCZ:** Inner-Tropical Convergence Zone
- **MAX-DOAS:** Multi-AXis DOAS
- **NOVAC:** Network for Observation of Volcanic and Atmospheric Change
- **OMI:** Ozone Monitoring Instrument
- **PCA:** Principal Component Analysis
- **SCD:** Slant Column Density
- **TROPOMI:** TROPOspheric Monitoring Instrument
- **UV:** Ultra-Violet
- **VEI:** Volcanic Explosivity Index
- **WPM:** Wavelength-to-Pixel Mapping

List of Figures

List of Tables

Bibliography

Agnew, D. C.: Earth Tides, in: Treatise on Geophysics and Geodesy, Elsevier, 2007.

Aguilera, E., Pareschi, M. T., Rosi, M., and Zanchetta, G.: Risk from Lahars in the Northern Valleys of Cotopaxi Volcano (Ecuador), Natural Hazards, 33, 161–189, doi:10.1023/B:NHAZ.0000037037.03155.23, URL `https://doi.org/10.1023/B:NHAZ.0000037037.03155.23`, 2004.

Aiuppa, A.: Degassing of halogens from basaltic volcanism: Insights from volcanic gas observations, Chemical Geology, 263, 99 – 109, doi:http://dx.doi.org/10.1016/j.chemgeo.2008.08.022, URL `http://www.sciencedirect.com/science/article/pii/S0009254108003781`, halogens in Volcanic Systems and Their Environmental Impacts, 2009.

Aiuppa, A., Federico, C., Franco, A., Giudice, G., Gurrieri, S., Inguaggiato, S., Liuzzo, M., McGonigle, A. J. S., and Valenza, M.: Emission of bromine and iodine from Mount Etna volcano, Geochemistry, Geophysics, Geosystems, 6, doi:10.1029/2005GC000965, URL `https://agupubs.onlinelibrary.wiley.com/doi/abs/10.1029/2005GC000965`, 2005a.

Aiuppa, A., Federico, C., Giudice, G., and Gurrieri, S.: Chemical mapping of a fumarolic field: La Fossa Crater, Vulcano Island (Aeolian Islands, Italy), Geophysical Research Letters, 32, doi:10.1029/2005GL023207, URL `https://agupubs.onlinelibrary.wiley.com/doi/abs/10.1029/2005GL023207`, 2005b.

Aiuppa, A., Baker, D., and Webster, J.: Halogens in volcanic systems, Chemical Geology, 263, 1 – 18, doi:https://doi.org/10.1016/j.chemgeo.2008.10.005, URL `http://www.sciencedirect.com/science/article/pii/S0009254108004658`, halogens in Volcanic Systems and Their Environmental Impacts, 2009.

Aiuppa, A., de Moor, J. M., Arellano, S., Coppola, D., Francofonte, V., Galle, B., Giudice, G., Liuzzo, M., Mendoza, E., Saballos, A., Tamburello, G., Battaglia, A., Bitetto, M., Gurrieri, S., Laiolo, M., Mastrolia, A., and Moretti, R.: Tracking Formation of a Lava Lake From Ground and Space: Masaya Volcano (Nicaragua), 2014–2017, Geochemistry, Geophysics, Geosystems, 19, 496–515, doi:10.1002/2017GC007227, URL `https://agupubs.onlinelibrary.wiley.com/doi/abs/10.1002/2017GC007227`, 2018.

Alfaro, C. M. and Zapata, J. A.: Acid gas emissions from Galeras Volcano, Colombia, 1989–1994, Journal of Volcanology and Geothermal Research, 77, 209 – 228, doi:https://doi.org/10.1016/S0377-0273(96)00095-9, URL `http://www.sciencedirect.com/science/article/pii/S0377027396000959`, galeras Volcano, Colombia: Interdisciplinary Study of a Decade Volcano, 1997.

Aliwell, S. R., Van Roozendael, M., Johnston, P. V., Richter, A., Wagner, T., Arlander, D. W., Burrows, J. P., Fish, D. J., Jones, R. L., Tørnkvist, K. K., Lambert, J.-C., Pfeilsticker, K., and Pundt, I.: Analysis for BrO in zenith-sky spectra: An intercomparison exercise for analysis improvement, Journal of Geophysical Research: Atmospheres, 107, ACH 10–1–ACH 10–20, doi:10.1029/2001JD000329, URL `https://doi.org/10.1029/2001JD000329`, 2002.

Allard, P., Burton, M., and Muré, F.: Spectroscopic evidence for a lava fountain driven by previously accumulated magmatic gas, Nature, 433, 407 EP –, URL `http://dx.doi.org/10.1038/nature03246`, 2005.

Alvarado, A., Audin, L., Nocquet, J. M., Jaillard, E., Mothes, P., Jarrín, P., Segovia, M., Rolandone, F., and Cisneros, D.: Partitioning of oblique convergence in the Northern Andes subduction zone: Migration history and the present-day boundary of the North Andean Sliver in Ecuador, Tectonics, 35, 1048–1065, doi:10.1002/2016TC004117, URL `http://dx.doi.org/10.1002/2016TC004117`, 2016TC004117, 2016.

Andres, R. and Kasgnoc, A.: A time-averaged inventory of subaerial volcanic sulfur emissions, Journal of Geophysical Research: Atmospheres, 103, 25 251–25 261, doi:10.1029/98JD02091, URL `https://agupubs.onlinelibrary.wiley.com/doi/abs/10.1029/98JD02091`, 1998.

Arellano, S., Hall, M., Samaniego, P., Pennec, J.-L. L., Ruiz, A., Molina, I., and Yepes, H.: Degassing patterns of Tungurahua volcano (Ecuador) during the 1999–2006 eruptive period, inferred from remote spectroscopic measurements of SO2 emissions, Journal of Volcanology and Geothermal Research, 176, 151 – 162, doi:https://doi.org/10.1016/j.jvolgeores.2008.07.007, URL `http://www.sciencedirect.com/science/article/pii/S0377027308004198`, recent and active volcanism in the Ecuadorian Andes, 2008.

Arias, G., Molina Polania, C., Ruiz, M., Kumagai, H., Hernandez, S., Plain, M., Mothes, P., Yepez, M., Barrington, C., and Hidalgo, S.: Very Long Period Seismicity Accompanying Increasing Shallower Activity at Cotopaxi Volcano, 2015.

Armienti, P., Pareschi, M. T., Innocenti, F., and Pompilio, M.: Effects of magma storage and ascent on the kinetics of crystal growth, Contributions to Mineralogy and Petrology, 115, 402–414, doi:10.1007/BF00320974, URL `https://doi.org/10.1007/BF00320974`, 1994.

Aumento, F.: Radon tides on an active volcanic island: Terceira, Azores, Geofísica Internacional, 41, 499–505, URL `http://www.geofisica.unam.mx/unid_apoyo/editorial/publicaciones/investigacion/geofisica_internacional/anteriores/2002/04/aumento.pdf`, 2002.

Bablon, M., Quidelleur, X., Samaniego, P., Pennec, J.-L. L., Lahitte, P., Liorzou, C., Bustillos, J. E., and Hidalgo, S.: Eruptive chronology of Tungurahua volcano (Ecuador) revisited based on new K-Ar ages and geomorphological reconstructions, Journal of Volcanology and Geothermal Research, 357, 378 – 398, doi:https://doi.org/10.1016/j.jvolgeores.2018.05.007, URL `http://www.sciencedirect.com/science/article/pii/S0377027317303992`, 2018.

Bagnato, E., Aiuppa, A., Bertagnini, A., Bonadonna, C., Cioni, R., Pistolesi, M., Pedone, M., and Hoskuldsson, A.: Scavenging of sulphur, halogens and trace metals by volcanic ash: The 2010 Eyjafjallajökull eruption, Geochimica et Cosmochimica Acta, 103, 138 – 160, doi:https://doi.org/10.1016/j.gca.2012.10.048, URL `http://www.sciencedirect.com/science/article/pii/S0016703712006369`, 2013.

Bai, L., Baker, D. R., Polacci, M., and Hill, R. J.: In-situ degassing study on crystal-bearing Stromboli basaltic magmas: Implications for Stromboli explosions, Geophysical Research Letters, 38, n/a–n/a, doi:10.1029/2011GL048540, URL `http://dx.doi.org/10.1029/2011GL048540`, l17309, 2011.

Baker, T. F.: Tidal deformations of the Earth, Science Progress (1933-), 69, 197–233, URL `http://www.jstor.org/stable/43420600`, 1984.

Balcone-Boissard, H., Boudon, G., Cioni, R., Webster, J. D., Zdanowicz, G., Orsi, G., and Civetta, L.: Chlorine as a geobarometer for alkaline magmas: Evidence from a systematic study of the eruptions of Mount Somma-Vesuvius, Sci Rep, 6, 21 726, doi:10.1038/srep21726, URL `http://www.ncbi.nlm.nih.gov/pmc/articles/PMC4757863/`, 26888358[pmid], 2016.

Bani, P., Tamburello, G., Rose-Koga, E. F., Liuzzo, M., Aiuppa, A., Cluzel, N., Amat, I., Syahbana, D. K., Gunawan, H., and Bitetto, M.: Dukono, the predominant source of volcanic degassing in Indonesia, sustained by a depleted Indian-MORB, Bulletin of Volcanology, 80, 5, doi:10.1007/s00445-017-1178-9, URL `https://doi.org/10.1007/s00445-017-1178-9`, 2017.

Barberi, F., Coltelli, M., Frullani, A., Rosi, M., and Almeida, E.: Chronology and dispersal characteristics of recently (last 5000 years) erupted tephra of Cotopaxi (Ecuador): implications for long-term eruptive forecasting, Journal of Volcanology and Geothermal Research, 69, 217 – 239, doi:http://dx.doi.org/10.1016/0377-0273(95)00017-8, URL `http://www.sciencedirect.com/science/article/pii/0377027395000178`, 1995.

Baxter, P., Stoiber, R., and Williams, S.: VOLCANIC GASES AND HEALTH: MASAYA VOLCANO, NICARAGUA, The Lancet, 320, 150–151, URL `http://www.sciencedirect.com/science/article/pii/S0140673682911096`, 1982.

Bebbington, M. S.: Long-term forecasting of volcanic explosivity, Geophysical Journal International, 197, 1500–1515, doi:10.1093/gji/ggu078, URL `http://dx.doi.org/10.1093/gji/ggu078`, 2014.

Beckett, F., Burton, M., Mader, H., Phillips, J., Polacci, M., Rust, A., and Witham, F.: Conduit convection driving persistent degassing at basaltic volcanoes, Journal of Volcanology and Geothermal Research, 283, 19 – 35, doi:https://doi.org/10.1016/j.jvolgeores.2014.06.006, URL `http://www.sciencedirect.com/science/article/pii/S0377027314001814`, 2014.

Beirle, S., Hörmann, C., Penning de Vries, M., Dörner, S., Kern, C., and Wagner, T.: Estimating the volcanic emission rate and atmospheric lifetime of SO2 from space: a case study for Kilauea volcano, Hawaii, Atmospheric Chemistry and Physics, 14, 8309–8322, doi:10.5194/acp-14-8309-2014, URL `http://www.atmos-chem-phys.net/14/8309/2014/`, 2014.

Bernard, B., Battaglia, J., Proaño, A., Hidalgo, S., Vásconez, F., Hernandez, S., and Ruiz, M.: Relationship between volcanic ash fallouts and seismic tremor: quantitative assessment of the 2015 eruptive period at Cotopaxi volcano, Ecuador, Bulletin of Volcanology, 78, 80, doi:10.1007/s00445-016-1077-5, URL `http://dx.doi.org/10.1007/s00445-016-1077-5`, 2016.

Berrino, G. and Corrado, G.: Tidal signal in the recent dynamics of Campi Flegrei caldera (Italy), Journal of Volcanology and Geothermal Research, 48, 93 – 101, doi:https://doi.org/10.1016/0377-0273(91)90035-X, URL `http://www.sciencedirect.com/science/article/pii/037702739190035X`, 1991.

Blower, J., Keating, J., Mader, H., and Phillips, J.: The evolution of bubble size distributions in volcanic eruptions, Journal of Volcanology and Geothermal Research, 120, 1 – 23, doi:https://doi.org/10.1016/S0377-0273(02)00404-3, URL `http://www.sciencedirect.com/science/article/pii/S0377027302004043`, 2003.

Bobrowski, N. and Giuffrida, G.: Bromine monoxide / sulphur dioxide ratios in relation to volcanological observations at Mt. Etna 2006–2009, Solid Earth, 3, 433–445, doi:10.5194/se-3-433-2012, URL `http://www.solid-earth.net/3/433/2012/`, 2012.

Bobrowski, N. and Platt, U.: Quantification of volcanic reactive halogen emissions, chap. 24, Cambridge University Press, 2015.

Bobrowski, N., von Glasow, R., Aiuppa, A., Inguaggiato, S., Louban, I., Ibrahim, O. W., and Platt, U.: Reactive halogen chemistry in volcanic plumes, Journal of Geophysical Research: Atmospheres, 112, n/a–n/a, doi:10.1029/2006JD007206, URL `http://dx.doi.org/10.1029/2006JD007206`, d06311, 2007.

Bobrowski, N., Glasow, R., Giuffrida, G. B., Tedesco, D., Aiuppa, A., Yalire, M., Arellano, S., Johansson, M., and Galle, B.: Gas emission strength and evolution of the molar ratio of BrO/SO2 in the plume of Nyiragongo in comparison to Etna, Journal of Geophysical Research: Atmospheres, 120, 277–291, doi:10.1002/2013JD021069, URL `https://agupubs.onlinelibrary.wiley.com/doi/abs/10.1002/2013JD021069`, 2015.

Boichu, M., Oppenheimer, C., Tsanev, V., and Kyle, P. R.: High temporal resolution SO2 flux measurements at Erebus volcano, Antarctica, Journal of Volcanology and Geothermal Research, 190, 325 – 336, doi:https://doi.org/10.1016/j.jvolgeores.2009.11.020, URL `http://www.sciencedirect.com/science/article/pii/S0377027309004569`, 2010.

Bower, D. R.: Bedrock fracture parameters from the interpretation of well tides, Journal of Geophysical Research: Solid Earth, 88, 5025–5035, doi:10.1029/JB088iB06p05025, URL `http://dx.doi.org/10.1029/JB088iB06p05025`, 1983.

Bredemeyer, S. and Hansteen, T. H.: Synchronous degassing patterns of the neighbouring volcanoes Llaima and Villarrica in south-central Chile: the influence of tidal forces, International Journal of Earth Sciences, 103, 1999–2012, doi:10.1007/s00531-014-1029-2, URL `http://dx.doi.org/10.1007/s00531-014-1029-2`, 2014.

Brönnimann, S., Schuepbach, E., Zanis, P., Buchmann, B., and Wanner, H.: A climatology of regional background ozone at different elevations in Switzerland (1992–1998), Atmospheric Environment, 34, 5191 – 5198, doi:https://doi.org/10.1016/S1352-2310(00)00193-X, URL `http://www.sciencedirect.com/science/article/pii/S135223100000193X`, sixth Scientific Conference of the International Global Atmospheric, 2000.

Brugger, C. R. and Hammer, J. E.: Crystal size distribution analysis of plagioclase in experimentally decompressed hydrous rhyodacite magma, Earth and Planetary Science Letters, 300, 246 – 254, doi:https://doi.org/10.1016/j.epsl.2010.09.046, URL `http://www.sciencedirect.com/science/article/pii/S0012821X10006333`, 2010.

Bureau, H. and Métrich, N.: An experimental study of bromine behaviour in water-saturated silicic melts, Geochimica et Cosmochimica Acta, 67, 1689 – 1697, doi:https://doi.org/10.1016/S0016-7037(02)01339-X, URL `http://www.sciencedirect.com/science/article/pii/S001670370201339X`, 2003.

Bureau, H., Keppler, H., and Métrich, N.: Volcanic degassing of bromine and iodine: experimental fluid/melt partitioning data and applications to stratospheric chemistry, Earth and Planetary Science Letters, 183, 51 – 60, doi:https://doi.org/10.1016/S0012-821X(00)00258-2, URL `http://www.sciencedirect.com/science/article/pii/S0012821X00002582`, 2000.

Bureau, H., Foy, E., Raepsaet, C., Somogyi, A., Munsch, P., Simon, G., and Kubsky, S.: Bromine cycle in subduction zones through in situ Br monitoring in diamond anvil cells, Geochimica et Cosmochimica Acta, 74, 3839 – 3850, doi:https://doi.org/10.1016/j.gca.2010.04.001, URL `http://www.sciencedirect.com/science/article/pii/S0016703710001754`, 2010.

Bureau, H., Auzende, A.-L., Marocchi, M., Raepsaet, C., Munsch, P., Testemale, D., Mézouar, M., Kubsky, S., Carrière, M., Ricolleau, A., and Fiquet, G.: Modern and past volcanic degassing of iodine, Geochimica et Cosmochimica Acta, 173, 114 – 125, doi:https://doi.org/10.1016/j.gca.2015.10.017, URL `http://www.sciencedirect.com/science/article/pii/S0016703715005992`, 2016.

Burrows, J. P., Richter, A., Dehn, A., Deters, B., Himmelmann, S., Voigt, S., and Orphal, J.: Atmospheric remote-sensing reference data from GOME. 2. Temperature dependent absorption cross sections of O_3 in the 231-794 nm range., Journal of Quantitative Spectroscopy and Radiative Transfer, 61, 509–517, doi:10.1016/S0022-4073(98)00037-5, 1999.

Burton, M., Allard, P., Muré, F., and La Spina, A.: Magmatic Gas Composition Reveals the Source Depth of Slug-Driven Strombolian Explosive Activity, Science, 317, 227–230, doi:10.1126/science.1141900, URL `http://science.sciencemag.org/content/317/5835/227`, 2007.

Burton, M., Caltabiano, T., Murè, F., Salerno, G., and Randazzo, D.: SO2 flux from Stromboli during the 2007 eruption: Results from the FLAME network and traverse measurements, Journal of Volcanology and Geothermal Research, 182, 214 – 220, doi:http://dx.doi.org/10.1016/j.jvolgeores.2008.11.025, URL `http://www.sciencedirect.com/science/article/pii/S0377027308006240`, the 2007 Eruption of Stromboli, 2009.

Businger, S., Huff, R., Pattantyus, A., Horton, K., Sutton, A. J., Elias, T., and Cherubini, T.: Observing and Forecasting Vog Dispersion from Kilauea Volcano, Hawaii, Bulletin of the American Meteorological Society, 96, 1667–1686, doi:10.1175/BAMS-D-14-00150.1, URL `http://dx.doi.org/10.1175/BAMS-D-14-00150.1`, 2015.

Bussemer, M.: Der Ring-Effekt: Ursache und Einfluß auf die spektroskopische Messung stratosphärischer Spurenstoffe, Master's thesis, Ruperto Carola University of Heidelberg, Germany, 1993.

Bustillos, J. E., Romero, J. E., Guevara, A., and Díaz-Alvarado, J.: Tephra fallout from the long-lasting Tungurahua eruptive cycle (1999-2014): Variations through eruptive style transition and deposition processes, Andean Geology, 45, 47–77, doi:http://dx.doi.org/10.5027/andgeoV45n1-3036, 2018.

Büttner, R., Dellino, P., and Zimanowski, B.: Identifying magma-water interaction from the surface features of ash particles, Nature, 401, 688 EP –, URL `http://dx.doi.org/10.1038/44364`, 1999.

Butz, A., Dinger, A. S., Bobrowski, N., Kostinek, J., Fieber, L., Fischerkeller, C., Giuffrida, G. B., Hase, F., Klappenbach, F., Kuhn, J., Lübcke, P., Tirpitz, L., and Tu, Q.: Remote sensing of volcanic CO_2, HF, HCl, SO_2, and BrO in the downwind plume of Mt. Etna, Atmospheric Measurement Techniques, 10, 1–14, doi:10.5194/amt-10-1-2017, URL `https://www.atmos-meas-tech.net/10/1/2017/`, 2017.

Cadoux, A., Iacono-Marziano, G., Scaillet, B., Aiuppa, A., Mather, T. A., Pyle, D. M., Deloule, E., Gennaro, E., and Paonita, A.: The role of melt composition on aqueous fluid vs. silicate melt partitioning of bromine in magmas, Earth and Planetary Science Letters, 498, 450 – 463, doi:https://doi.org/10.1016/j.epsl.2018.06.038, URL `http://www.sciencedirect.com/science/article/pii/S0012821X18303893`, 2018.

Campion, R., Martinez-Cruz, M., Lecocq, T., Caudron, C., Pacheco, J., Pinardi, G., Hermans, C., Carn, S., and Bernard, A.: Space- and ground-based measurements of sulphur dioxide emissions from Turrialba Volcano (Costa Rica), Bulletin of Volcanology, 74, 1757–1770, doi:10.1007/s00445-012-0631-z, URL `https://doi.org/10.1007/s00445-012-0631-z`, 2012.

Campion, R., Delgado-Granados, H., Legrand, D., Taquet, N., Boulesteix, T., Pedraza-Espitía, S., and Lecocq, T.: Breathing and Coughing: The Extraordinarily High Degassing of Popocatépetl Volcano Investigated With an SO2 Camera, Frontiers in Earth Science, 6, 163, doi:10.3389/feart.2018.00163, URL `https://www.frontiersin.org/article/10.3389/feart.2018.00163`, 2018.

Caricchi, L., Burlini, L., Ulmer, P., Gerya, T., Vassalli, M., and Papale, P.: Non-Newtonian rheology of crystal-bearing magmas and implications for magma ascent dynamics, Earth and Planetary Science Letters, 264, 402 – 419, doi:https://doi.org/10.1016/j.epsl.2007.09.032, URL `http://www.sciencedirect.com/science/article/pii/S0012821X07005985`, 2007.

Carn, S. A., Fioletov, V. E., McLinden, C. A., Li, C., and Krotkov, N. A.: A decade of global volcanic SO2 emissions measured from space, Scientific Reports, 7, 44 095 EP –, URL `http://dx.doi.org/10.1038/srep44095`, article, 2017.

Carroll, M. R.: Chlorine solubility in evolved alkaline magmas, Annals of Geophysics, 48, doi:10.4401/ag-3223, URL `http://www.annalsofgeophysics.eu/index.php/annals/article/view/3223`, 2005.

Cashman, K. V. and Marsh, B. D.: Crystal size distribution (CSD) in rocks and the kinetics and dynamics of crystallization II: Makaopuhi lava lake, Contributions to Mineralogy and Petrology, 99, 292–305, doi:10.1007/BF00375363, URL `https://doi.org/10.1007/BF00375363`, 1988.

Cassidy, M., Cole, P., Hicks, K. E., Varley, N. R., Peters, N., and Lerner, A. H.: Rapid and slow: Varying magma ascent rates as a mechanism for Vulcanian explosions, Earth and Planetary Science Letters, 420, 73 – 84, doi:https://doi.org/10.1016/j.epsl.2015.03.025, URL `http://www.sciencedirect.com/science/article/pii/S0012821X15001685`, 2015.

Cassidy, M., Manga, M., Cashman, K., and Bachmann, O.: Controls on explosive-effusive volcanic eruption styles, Nature Communications, 9, 2839, doi:10.1038/s41467-018-05293-3, URL `https://doi.org/10.1038/s41467-018-05293-3`, 2018.

Castro, J. M., Burgisser, A., Schipper, C. I., and Mancini, S.: Mechanisms of bubble coalescence in silicic magmas, Bulletin of Volcanology, 74, 2339–2352, doi:10.1007/s00445-012-0666-1, URL `http://dx.doi.org/10.1007/s00445-012-0666-1`, 2012.

Ceballos, J. L., Euscátegui, C., Ramírez, J., Cañon, M., Huggel, C., Haeberli, W., and Machguth, H.: Fast shrinkage of tropical glaciers in Colombia, Annals of Glaciology, 43, 194–201, doi:10.3189/172756406781812429, 2006.

Chance, K. and Kurucz, R.: An improved high-resolution solar reference spectrum for earth's atmosphere measurements in the ultraviolet, visible, and near infrared, Journal of Quantitative Spectroscopy and Radiative Transfer, 111, 1289 – 1295, doi:http://dx.doi.org/10.1016/j.jqsrt.2010.01.036, URL `http://www.sciencedirect.com/science/article/pii/S0022407310000610`, special Issue Dedicated to Laurence S. Rothman on the Occasion of his 70th Birthday., 2010.

Chiodini, G., Paonita, A., Aiuppa, A., Costa, A., Caliro, S., De Martino, P., Acocella, V., and Vandemeulebrouck, J.: Magmas near the critical degassing pressure drive volcanic unrest towards a critical state, Nat Commun, 7, 13712, doi:10.1038/ncomms13712, URL `http://www.ncbi.nlm.nih.gov/pmc/articles/PMC5187427/`, 27996976[pmid], 2016.

Cigolini, C., Poggi, P., Ripepe, M., Laiolo, M., Ciamberlini, C., Donne, D. D., Ulivieri, G., Coppola, D., Lacanna, G., Marchetti, E., Piscopo, D., and Genco, R.: Radon surveys and real-time monitoring at Stromboli volcano: Influence of soil temperature, atmospheric pressure and tidal forces on 222Rn degassing, Journal of Volcanology and Geothermal Research, 184, 381 – 388, doi:https://doi.org/10.1016/j.jvolgeores.2009.04.019, URL `http://www.sciencedirect.com/science/article/pii/S0377027309002078`, 2009.

Clauser, C.: Einführung in die Geophysik, Springer Spektrum, doi:DOI 10.1007/978-3-642-04496-0, 2014.

Conde, V., Bredemeyer, S., Duarte, E., Pacheco, J. F., Miranda, S., Galle, B., and Hansteen, T. H.: SO2 degassing from Turrialba Volcano linked to seismic signatures during the period 2008–2012, International Journal of Earth Sciences, 103, 1983–1998, doi:10.1007/s00531-013-0958-5, URL `http://dx.doi.org/10.1007/s00531-013-0958-5`, 2014.

Condon, E. U.: Intensity-dependent absorption of light, Proceedings of the National Academy of Sciences of the United States of America, 52, 635–637, doi:10.1073/pnas.52.3.635, URL `https://www.ncbi.nlm.nih.gov/pubmed/16591212`, 16591212[pmid], 1964.

Connor, C. B., Stoiber, R. E., and Malinconico, L. L.: Variation in sulfur dioxide emissions related to earth tides, Halemaumau Crater, Kilauea Volcano, Hawaii, Journal of Geophysical Research: Solid Earth, 93, 14 867–14 871, doi:10.1029/JB093iB12p14867, URL `http://dx.doi.org/10.1029/JB093iB12p14867`, 1988.

Conrad, C. P. and Lithgow-Bertelloni, C.: How Mantle Slabs Drive Plate Tectonics, Science, 298, 207–209, doi:10.1126/science.1074161, URL `http://science.sciencemag.org/content/298/5591/207`, 2002.

Cooper, O., Parrish, D., Ziemke, J., Balashov, N., Cupeiro, M., Galbally, I., Gilge, S., Horowitz, L., Jensen, N., Lamarque, J.-F., Naik, V., Oltmans, S., Schwab, J., Shindell, D., Thompson, A., Thouret, V., Wang, Y., and Zbinden, R.: Global distribution and trends of tropospheric ozone: An observation-based review, Elementa Science of the Antropocene, doi:http://doi.org/10.12952/journal.elementa.000029, URL `https://www.elementascience.org/articles/10.12952/journal.elementa.000029/#`, 2014.

Custodio, S. I. S., Fonseca, J. F. B. D., d'Oreye, N. F., Faria, B. V. E., and Bandomo, Z.: Tidal modulation of seismic noise and volcanic tremor, Geophysical Research Letters, 30, n/a–n/a, doi:10.1029/2003GL016991, URL `http://dx.doi.org/10.1029/2003GL016991`, 1816, 2003.

Darwin, G.: Report of a committee for the harmonic analysis of tidal observations, in: Report of the British Association for the Advancement of Science, p. 49-117, 1883.

De Mendoca Dias, A.: The volcano of Capelinhos (Azores), the solar activity and the earth-tide, Bulletin Volcanologique, 24, 211–221, doi:10.1007/BF02599348, URL `http://dx.doi.org/10.1007/BF02599348`, 1962.

De Paolo, E., Walter, T., Zorn, E., Coppola, D., Laiolo, M., Massimetti, F., and Battaglia, M.: Lateral lava dome growth monitoring at Nevado del Ruiz Arenas craterusing TerraSAR-X amplitude Imagery, in: EGU General Assembly, URL `https://meetingorganizer.copernicus.org/EGU2019/EGU2019-9502-1.pdf`, 2019.

Delmelle, P., Stix, J., Baxter, P., Garcia-Alvarez, J., and Barquero, J.: Atmospheric dispersion, environmental effects and potential health hazard associated with the low-altitude gas plume of Masaya volcano, Nicaragua, Bulletin of Volcanology, 64, 423–434, doi:10.1007/s00445-002-0221-6, URL `https://doi.org/10.1007/s00445-002-0221-6`, 2002.

Delmelle, P., Ayris, P., and Maters, E.: Comment on "Scavenging of sulfur, halogens and trace metals by volcanic ash: The 2010 Eyjafjallajökull eruption" by Bagnato et al. (2013), Geochimica et Cosmochimica Acta, 127, 381 – 384, doi:https://doi.org/10.1016/j.gca.2013.07.021, URL `http://www.sciencedirect.com/science/article/pii/S0016703713004018`, 2014.

Di Napoli, R., Aiuppa, A., Bergsson, B., Ilyinskaya, E., Pfeffer, M. A., Guðjónsdóttir, S. R., and Valenza, M.: Reaction path models of magmatic gas scrubbing, Chemical Geology, 420, 251 – 269, doi:https://doi.org/10.1016/j.chemgeo.2015.11.024, URL `http://www.sciencedirect.com/science/article/pii/S0009254115301157`, 2016.

Dinger, F., Bobrowski, N., Warnach, S., Bredemeyer, S., Hidalgo, S., Arellano, S., Galle, B., Platt, U., and Wagner, T.: Periodicity in the BrO/SO_2 molar ratios in the volcanic gas plume of Cotopaxi and its correlation with the Earth tides during the eruption in 2015, Solid Earth, 9, 247–266, doi:10.5194/se-9-247-2018, URL `https://www.solid-earth.net/9/247/2018/`, 2018.

Dinger, F., Bredemeyer, S., Arellano, S., Bobrowski, N., Platt, U., and Wagner, T.: On the link between Earth tides and volcanic degassing, Solid Earth, 10, 725–740, doi:10.5194/se-10-725-2019, URL `https://www.solid-earth.net/10/725/2019/`, 2019.

Doodson, A. T.: The Harmonic Development of the Tide-Generating Potential, in: Proceedings of the Royal Society of London. Series A, Containing Paper of a Mathematical and Physical Character, Volume 100, Issue 704, doi:https://doi.org/10.1098/rspa.1921.0088, URL `https://royalsocietypublishing.org/doi/abs/10.1098/rspa.1921.0088`, 1921.

Dzurisin, D.: Influence of fortnightly Earth tides at Kilauea Volcano, Hawaii, Geophysical Research Letters, 7, 925–928, doi:10.1029/GL007i011p00925, URL `http://dx.doi.org/10.1029/GL007i011p00925`, 1980.

Edmonds, M. and Gerlach, T. M.: Vapor segregation and loss in basaltic melts, Geology, 35, 751, doi:10.1130/G23464A.1, URL `http://dx.doi.org/10.1130/G23464A.1`, 2007.

Edmonds, M., Pyle, D., and Oppenheimer, C.: A model for degassing at the Soufrière Hills Volcano, Montserrat, West Indies, based on geochemical data, Earth and Planetary Science Letters, 186, 159 – 173, doi:http://dx.doi.org/10.1016/S0012-821X(01)00242-4, URL `http://www.sciencedirect.com/science/article/pii/S0012821X01002424`, 2001.

Edmonds, M., Herd, R. A., Galle, B., and Oppenheimer, C. M.: Automated, high time-resolution measurements of SO2 flux at Soufrière Hills Volcano, Montserrat, Bulletin of Volcanology, 65, 578–586, doi:10.1007/s00445-003-0286-x, URL `http://dx.doi.org/10.1007/s00445-003-0286-x`, 2003.

Edmonds, M., Gerlach, T. M., and Herd, R. A.: Halogen degassing during ascent and eruption of water-poor basaltic magma, Chemical Geology, 263, 122 – 130, doi:https://doi.org/10.1016/j.chemgeo.2008.09.022, URL `http://www.sciencedirect.com/science/article/pii/S0009254108004361`, halogens in Volcanic Systems and Their Environmental Impacts, 2009.

Eisinger, M. and Burrows, J. P.: Tropospheric sulfur dioxide observed by the ERS-2 GOME instrument, Geophysical Research Letters, 25, 4177–4180, doi:10.1029/1998GL900128, URL `https://doi.org/10.1029/1998GL900128`, 1998.

Elias, T., Sutton, A. J., Oppenheimer, C., Horton, K. A., Garbeil, H., Tsanev, V., McGonigle, A. J. S., and Williams-Jones, G.: Comparison of COSPEC and two miniature ultraviolet spectrometer systems for SO2 measurements using scattered sunlight, Bulletin of Volcanology, 68, 313–322, doi:10.1007/s00445-005-0026-5, URL `https://doi.org/10.1007/s00445-005-0026-5`, 2006.

Elkhoury, J. E., Brodsky, E. E., and Agnew, D. C.: Seismic waves increase permeability, Nature, 441, 1135–1138, doi:10.1038/nature04798, URL `https://doi.org/10.1038/nature04798`, 2006.

Emter, D.: Tidal triggering of earthquakes and volcanic events, pp. 293–309, Springer Berlin Heidelberg, Berlin, Heidelberg, doi:10.1007/BFb0011468, URL `https://doi.org/10.1007/BFb0011468`, 1997.

Fagents, S., Gregg, T., and Lopes, R., eds.: Modeling Volcanic Processes: The Physics and Mathematics of Volcanism, Cambridge University Press, doi:10.1017/CBO9781139021562, 2013.

Fioletov, V. E., McLinden, C. A., Krotkov, N., and Li, C.: Lifetimes and emissions of SO2 from point sources estimated from OMI, Geophysical Research Letters, 42, 1969–1976, doi:10.1002/2015GL063148, URL `http://dx.doi.org/10.1002/2015GL063148`, 2015GL063148, 2015.

Fiorini, E. and Tibaldi, A.: Quaternary tectonics in the central Interandean Valley, Ecuador: Fault-propagation folds, transfer faults and the Cotopaxi Volcano, Global and Planetary Change, 90–91, 87 – 103, doi:http://dx.doi.org/10.1016/j.gloplacha.2011.06.002, URL `http://www.sciencedirect.com/science/article/pii/S0921818111000944`, coupled deep Earth and surface processes in System Earth: monitoring, reconstruction and process modeling, 2012.

Fischer, T. P., Morrissey, M. M., Marta Lucía Calvache, V., Diego Gòmez, M., Roberto Torres, C., Stix, J., and Williams, S. N.: Correlations between SO2 flux and long-period seismicity at Galeras volcano, Nature, 368, 135 EP –, URL `http://dx.doi.org/10.1038/368135a0`, 1994.

Fischer, T. P., Roggensack, K., and Kyle, P. R.: Open and almost shut case for explosive eruptions: Vent processes determined by SO2 emission rates at Karymsky volcano, Kamchatka, Geology, 30, 1059, doi:10.1130/0091-7613(2002)030<1059:OAASCF>2.0.CO;2, URL `http://dx.doi.org/10.1130/0091-7613(2002)030<1059:OAASCF>2.0.CO;2`, 2002.

Fleischmann, O. C., Hartmann, M., Burrows, J. P., and Orphal, J.: New ultraviolet absorption cross-sections of BrO at atmospheric temperatures measured by time-windowing Fourier transform spectroscopy, Journal of Photochemistry and Photobiology A: Chemistry, 168, 117 – 132, doi:http://dx.doi.org/10.1016/j.jphotochem.2004.03.026, URL `http://www.sciencedirect.com/science/article/pii/S1010603004001522`, 2004.

Fu, Q. and Sun, W.: Mie theory for light scattering by a spherical particle in an absorbing medium, Appl. Opt., 40, 1354–1361, doi:10.1364/AO.40.001354, URL `http://ao.osa.org/abstract.cfm?URI=ao-40-9-1354`, 2001.

Galle, B.: NOVAC: Second Year Activity Report, Tech. rep., NOVAC Consortium, 2008.

Galle, B., Oppenheimer, C., Geyer, A., McGonigle, A. J., Edmonds, M., and Horrocks, L.: A miniaturised ultraviolet spectrometer for remote sensing of SO2 fluxes: a new tool for volcano surveillance, Journal of Volcanology and Geothermal Research, 119, 241 – 254, doi:https://doi.org/10.1016/S0377-0273(02)00356-6, URL `http://www.sciencedirect.com/science/article/pii/S0377027302003566`, 2003.

Galle, B., Johansson, M., Rivera, C., Zhang, Y., Kihlman, M., Kern, C., Lehmann, T., Platt, U., Arellano, S., and Hidalgo, S.: Network for Observation of Volcanic and Atmospheric Change (NOVAC)—A global network for volcanic gas monitoring: Network layout and instrument description, Journal of Geophysical Research: Atmospheres, 115, n/a–n/a, doi:10.1029/2009JD011823, URL `http://dx.doi.org/10.1029/2009JD011823`, d05304, 2010.

Gama, J. and Milbert, D.: GNU R package "solidearthtides", version 1.0.2, https://cran.r-project.org/web/packages/solidearthtide/index.html, Tech. rep., 2015.

Gaunt, H. E., Bernard, B., Hidalgo, S., Proaño, A., Wright, H., Mothes, P., Criollo, E., and Kueppers, U.: Juvenile magma recognition and eruptive dynamics inferred from the analysis of ash time series: The 2015 reawakening of Cotopaxi volcano, Journal of Volcanology and Geothermal Research, 328, 134 – 146, doi:http://dx.doi.org/10.1016/j.jvolgeores.2016.10.013, URL `http://www.sciencedirect.com/science/article/pii/S0377027316301858`, 2016.

Gerlach, T.: Volcanic versus anthropogenic carbon dioxide, Eos, Transactions American Geophysical Union, 92, 201–202, doi:10.1029/2011EO240001, URL `https://agupubs.onlinelibrary.wiley.com/doi/abs/10.1029/2011EO240001`, 2011.

Gerlach, T. M.: Volcanic sources of tropospheric ozone-depleting trace gases, Geochemistry, Geophysics, Geosystems, 5, doi:10.1029/2004GC000747, URL `https://agupubs.onlinelibrary.wiley.com/doi/abs/10.1029/2004GC000747`, 2004.

Gerlach, T. M., McGee, K. A., Sutton, A. J., and Elias, T.: Rates of volcanic CO2 degassing from airborne determinations of SO2 Emission rates and plume CO2/SO2: test study at Pu'u 'O'o Cone, Kilauea Volcano, Hawaii, Geophysical Research Letters, 25, 2675–2678, doi:10.1029/98GL02030, URL `https://agupubs.onlinelibrary.wiley.com/doi/abs/10.1029/98GL02030`, 1998.

Germanovich, L. N. and Lowell, R. P.: The mechanism of phreatic eruptions, Journal of Geophysical Research: Solid Earth, 100, 8417–8434, doi:10.1029/94JB03096, URL `https://agupubs.onlinelibrary.wiley.com/doi/abs/10.1029/94JB03096`, 1995.

Gibbs, A. D.: Linked fault families in basin formation, Journal of Structural Geology, 12, 795 – 803, doi:http://dx.doi.org/10.1016/0191-8141(90)90090-L, URL `http://www.sciencedirect.com/science/article/pii/019181419090090L`, 1990.

Giggenbach, W. F.: Chemical Composition of Volcanic Gases, pp. 221–256, Springer Berlin Heidelberg, Berlin, Heidelberg, doi:10.1007/978-3-642-80087-0_7, URL `https://doi.org/10.1007/978-3-642-80087-0_7`, 1996.

Girona, T., Huber, C., and Caudron, C.: Sensitivity to lunar cycles prior to the 2007 eruption of Ruapehu volcano, Scientific Reports, 8, 1476, doi:10.1038/s41598-018-19307-z, URL `https://doi.org/10.1038/s41598-018-19307-z`, 2018.

Gliß, J., Bobrowski, N., Vogel, L., Pöhler, D., and Platt, U.: OClO and BrO observations in the volcanic plume of Mt. Etna – implications on the chemistry of chlorine and bromine species in volcanic plumes, Atmospheric Chemistry and Physics, 15, 5659–5681, doi:10.5194/acp-15-5659-2015, URL `http://www.atmos-chem-phys.net/15/5659/2015/`, 2015.

Global Volcanism Program: Report on Nevado del Ruiz (Colombia), in: Bulletin of the Global Volcanism Network, 42:6, Smithsonian Institution., 2017.

Gonnermann, H. M. and Manga, M.: Dynamics of magma ascent in the volcanic conduit, in: Modeling Volcanic Processes: The Physics and Mathematics of Volcanism, edited by Fagents, S. A., Gregg, T. K. P., and Lopes, R. M. C., pp. 55–84, Cambridge University Press, Cambridge, doi:10.1017/CBO9781139021562.004, URL `https://www.cambridge.org/core/books/modeling-volcanic-processes/dynamics-of-magma-ascent-in-the-volcanic-conduit/8B8F375FB8709B62A6C917BEE97C0007`, 2013.

Gonnermann, H. M., Giachetti, T., Fliedner, C., Nguyen, C. T., Houghton, B. F., Crozier, J. A., and Carey, R. J.: Permeability During Magma Expansion and Compaction, Journal of Geophysical Research: Solid Earth, 122, 9825–9848, doi:10.1002/2017JB014783, URL `https://agupubs.onlinelibrary.wiley.com/doi/abs/10.1002/2017JB014783`, 2017.

Goto, A. and Johnson, J. B.: Monotonic infrasound and Helmholtz resonance at Volcan Villarrica (Chile), Geophysical Research Letters, 38, doi:10.1029/2011GL046858, URL `https://agupubs.onlinelibrary.wiley.com/doi/abs/10.1029/2011GL046858`, 2011.

Grainer, J. F. and Ring, J.: Anomalous Fraunhofer Line Profiles, Nature, 193, 762–762, doi:10.1038/193762a0, URL `http://dx.doi.org/10.1038/193762a0`, 1962.

Gudmundsson, G.: Respiratory health effects of volcanic ash with special reference to Iceland. A review, The Clinical Respiratory Journal, 5, 2–9, doi:10.1111/j.1752-699X.2010.00231.x, URL `https://onlinelibrary.wiley.com/doi/abs/10.1111/j.1752-699X.2010.00231.x`, 2010.

Gutmann, A., Bobrowski, N., Roberts, T. J., Rüdiger, J., and Hoffmann, T.: Advances in Bromine Speciation in Volcanic Plumes, Frontiers in Earth Science, 6, 213, doi:10.3389/feart.2018.00213, URL `https://www.frontiersin.org/article/10.3389/feart.2018.00213`, 2018.

Hall, M. and Mothes, P.: The rhyolitic–andesitic eruptive history of Cotopaxi volcano, Ecuador, Bulletin of Volcanology, 70, 675–702, doi:10.1007/s00445-007-0161-2, URL `http://dx.doi.org/10.1007/s00445-007-0161-2`, 2008.

Halmer, M., Schmincke, H.-U., and Graf, H.-F.: The annual volcanic gas input into the atmosphere, in particular into the stratosphere: a global data set for the past 100 years, Journal of Volcanology and Geothermal Research, 115, 511 – 528, doi:https://doi.org/10.1016/S0377-0273(01)00318-3, URL `http://www.sciencedirect.com/science/article/pii/S0377027301003183`, 2002.

Hamilton, W. L.: Tidal cycles of volcanic eruptions: fortnightly to 19 yearly periods, Journal of Geophysical Research, 78, 3363–3375, doi:10.1029/JB078i017p03363, URL `http://dx.doi.org/10.1029/JB078i017p03363`, 1973.

Harrison, J. C., Ness, N. F., Longman, I. M., Forbes, R. F. S., Kraut, E. A., and Slichter, L. B.: Earth-tide observations made during the international geophysical year, Journal of Geophysical Research, 68, 1497–1516, doi:10.1029/JZ068i005p01497, URL `http://dx.doi.org/10.1029/JZ068i005p01497`, 1963.

Herd, R. A. and Pinkerton, H.: Bubble coalescence in basaltic lava: Its impact on the evolution of bubble populations, Journal of Volcanology and Geothermal Research, 75, 137 – 157, doi:https://doi.org/10.1016/S0377-0273(96)00039-X, URL `http://www.sciencedirect.com/science/article/pii/S037702739600039X`, 1997.

Hermans, C., Vandaele, A. C., Fally, S., Carleer, M., Colin, R., Coquart, B., Jenouvrier, A., and Merienne, M.-F.: Absorption Cross-section of the Collision-Induced Bands of Oxygen from the UV to the NIR, pp. 193–202, Springer Netherlands, Dordrecht, doi:10.1007/978-94-010-0025-3_16, URL `http://dx.doi.org/10.1007/978-94-010-0025-3_16`, 2003.

Hervo, M., Quennehen, B., Kristiansen, N. I., Boulon, J., Stohl, A., Fréville, P., Pichon, J.-M., Picard, D., Labazuy, P., Gouhier, M., Roger, J.-C., Colomb, A., Schwarzenboeck, A., and Sellegri, K.: Physical and optical properties of 2010 Eyjafjallajökull volcanic eruption aerosol: ground-based, Lidar and airborne measurements in France, Atmospheric Chemistry and Physics, 12, 1721–1736, doi:10.5194/acp-12-1721-2012, URL `https://www.atmos-chem-phys.net/12/1721/2012/`, 2012.

Hickey, J., Gottsmann, J., and Mothes, P.: Estimating volcanic deformation source parameters with a finite element inversion: The 2001-2002 unrest at Cotopaxi volcano, Ecuador, Journal of Geophysical Research: Solid Earth, 120, 1473–1486, doi:10.1002/2014JB011731, URL `http://dx.doi.org/10.1002/2014JB011731`, 2014JB011731, 2015.

Hidalgo, S., Battaglia, J., Arellano, S., Steele, A., Bernard, B., Bourquin, J., Galle, B., Arrais, S., and Vásconez, F.: SO2 degassing at Tungurahua volcano (Ecuador) between 2007 and 2013: Transition from continuous to episodic activity, Journal of Volcanology and Geothermal Research, 298, 1 – 14, doi:https://doi.org/10.1016/j.jvolgeores.2015.03.022, URL `http://www.sciencedirect.com/science/article/pii/S0377027315000980`, 2015.

Hidalgo, S., Battaglia, J., Arellano, S., Sierra, D., Bernard, B., Parra, R., Kelly, P., Dinger, F., Barrington, C., and Samaniego, P.: Evolution of the 2015 Cotopaxi Eruption Revealed by Combined Geochemical & Seismic Observations, Geochemistry, Geophysics, Geosystems, 0, doi:10.1029/2018GC007514, URL `https://agupubs.onlinelibrary.wiley.com/doi/abs/10.1029/2018GC007514`, 2018.

Hoheisel, A., Yeman, C., Dinger, F., Eckhardt, H., and Schmidt, M.: An improved method for mobile characterisation of $\delta^{13}CH_4$ source signatures and its application in Germany, Atmospheric Measurement Techniques, 12, 1123–1139, doi:10.5194/amt-12-1123-2019, URL `https://www.atmos-meas-tech.net/12/1123/2019/`, 2019.

Hörmann, C., Sihler, H., Bobrowski, N., Beirle, S., Penning de Vries, M., Platt, U., and Wagner, T.: Systematic investigation of bromine monoxide in volcanic plumes from space by using the GOME-2 instrument, Atmospheric Chemistry and Physics, 13, 4749–4781, doi:10.5194/acp-13-4749-2013, URL `http://www.atmos-chem-phys.net/13/4749/2013/`, 2013.

Huber, C., Su, Y., Nguyen, C. T., Parmigiani, A., Gonnermann, H. M., and Dufek, J.: A new bubble dynamics model to study bubble growth, deformation, and coalescence, Journal of Geophysical Research: Solid Earth, 119, 216–239, doi:10.1002/2013JB010419, URL `https://agupubs.onlinelibrary.wiley.com/doi/abs/10.1002/2013JB010419`, 2013.

Huggel, C., Ceballos, J. L., Pulgarln, B., Ramírez, J., and Thouret, J.-C.: Review and reassessment of hazards owing to volcano-glacier interactions in Colombia, Annals of Glaciology, 45, 128–136, doi:10.3189/172756407782282408, 2007.

Hurwitz, S. and Navon, O.: Bubble nucleation in rhyolitic melts: Experiments at high pressure, temperature, and water content, Earth and Planetary Science Letters, 122, 267 – 280, doi:https://doi.org/10.1016/0012-821X(94)90001-9, URL `http://www.sciencedirect.com/science/article/pii/0012821X94900019`, 1994.

Ide, S., Yabe, S., and Tanaka, Y.: Earthquake potential revealed by tidal influence on earthquake size-frequency statistics, Nature Geosci, 9, 834–837, URL `http://dx.doi.org/10.1038/ngeo2796`, letter, 2016.

IDEAM: Promedios Climatologicos 1981-2010, Institute of Hydrology, Meteorology and Environmental Studies (Colombia), URL `http://www.ideam.gov.co/web/tiempo-y-clima/clima`, 2018.

IDEAM2: MAPAS DE OZONO PROMEDIO EN COLOMBIAEN COLOMBIA, Institute of Hydrology, Meteorology and Environmental Studies (Colombia), URL `http://www.ideam.gov.co/documents/21021/418894/Ozono.pdf/8bb47148-739b-478b-88f6-13ec080e889d`, 2018.

Ilanko, T., Oppenheimer, C., Burgisser, A., and Kyle, P.: Cyclic degassing of Erebus volcano, Antarctica, Bulletin of Volcanology, 77, 56, doi:10.1007/s00445-015-0941-z, URL `https://doi.org/10.1007/s00445-015-0941-z`, 2015.

Jackson, E. L.: The Laki Eruption of 1783: impacts on population and settlement in Iceland, Geography, 67, 42–50, URL `http://www.jstor.org/stable/40570468`, 1982.

Johnson, J. B., Ruiz, M. C., Ortiz, H. D., Watson, L. M., Viracucha, G., Ramon, P., and Almeida, M.: Infrasound Tornillos Produced by Volcán Cotopaxi's Deep Crater, Geophysical Research Letters, 45, 5436–5444, doi:10.1029/2018GL077766, URL `https://doi.org/10.1029/2018GL077766`, 2018a.

Johnson, J. B., Watson, L. M., Palma, J. L., Dunham, E. M., and Anderson, J. F.: Forecasting the Eruption of an Open-Vent Volcano Using Resonant Infrasound Tones, Geophysical Research Letters, 45, 2213–2220, doi:10.1002/2017GL076506, URL `https://agupubs.onlinelibrary.wiley.com/doi/abs/10.1002/2017GL076506`, 2018b.

Johnston, M. J. S. and Mauk, F. J.: Earth Tides and the Triggering of Eruptions from Mt Stromboli, Italy, Nature, 239, 266–267, doi:10.1038/239266b0, URL `http://dx.doi.org/10.1038/239266b0`, 1972.

Kanamori, H. and Press, F.: How Thick is the Lithosphere ?, Nature, 226, 330 EP –, URL `http://dx.doi.org/10.1038/226330a0`, 1970.

Katragkou, E., Zanis, P., Tsikerdekis, A., Kapsomenakis, J., Melas, D., Eskes, H., Flemming, J., Huijnen, V., Inness, A., Schultz, M. G., Stein, O., and Zerefos, C. S.: Evaluation of near-surface ozone over Europe from the MACC reanalysis, Geoscientific Model Development, 8, 2299–2314, doi:10.5194/gmd-8-2299-2015, URL `https://www.geosci-model-dev.net/8/2299/2015/`, 2015.

Kazahaya, K., Shinohara, H., and Saito, G.: Excessive degassing of Izu-Oshima volcano: magma convection in a conduit, Bulletin of Volcanology, 56, 207–216, doi:10.1007/BF00279605, URL `https://doi.org/10.1007/BF00279605`, 1994.

Kendrick, M. A., Arculus, R. J., Danyushevsky, L. V., Kamenetsky, V. S., Woodhead, J. D., and Honda, M.: Subduction-related halogens (Cl, Br and I) and H2O in magmatic glasses from Southwest Pacific Backarc Basins, Earth and Planetary Science Letters, 400, 165 – 176, doi:https://doi.org/10.1016/j.epsl.2014.05.021, URL `http://www.sciencedirect.com/science/article/pii/S0012821X14003239`, 2014.

Kent, A. J. R., Darr, C., Koleszar, A. M., Salisbury, M. J., and Cooper, K. M.: Preferential eruption of andesitic magmas through recharge filtering, 3, 631 EP –, URL `http://dx.doi.org/10.1038/ngeo924`, 2010.

Kern, C.: Spectroscopic measurements of volcanic gas emissions in the ultra-violet wavelength region, Ph.D. thesis, Ruperto Carola University of Heidelberg, Germany, 2009.

Kern, C., Deutschmann, T., Vogel, L., Wöhrbach, M., Wagner, T., and Platt, U.: Radiative transfer corrections for accurate spectroscopic measurements of volcanic gas emissions, Bulletin of Volcanology, 72, 233–247, doi:10.1007/s00445-009-0313-7, URL `https://doi.org/10.1007/s00445-009-0313-7`, 2010.

Kern, C., Masias, P., Apaza, F., Reath, K. A., and Platt, U.: Remote measurement of high preeruptive water vapor emissions at Sabancaya volcano by passive differential optical absorption spectroscopy, Journal of Geophysical Research: Solid Earth, 122, 3540–3564, doi:10.1002/2017JB014020, URL `https://agupubs.onlinelibrary.wiley.com/doi/abs/10.1002/2017JB014020`, 2017.

Kraus, S.: DOASIS, A Framework Design for DOAS, Ph.D. thesis, University of Mannheim, 2006.

Kutterolf, S., Hansteen, T. H., Freundt, A., Wehrmann, H., Appel, K., Krüger, K., and Pérez, W.: Bromine and chlorine emissions from Plinian eruptions along the Central American Volcanic Arc: From source to atmosphere, Earth and Planetary Science Letters, 429, 234 – 246, doi:http://doi.org/10.1016/j.epsl.2015.07.064, URL `http://www.sciencedirect.com/science/article/pii/S0012821X15005075`, 2015.

La Spina, A., Burton, M., Harig, R., Mure, F., Rusch, P., Jordan, M., and Caltabiano, T.: New insights into volcanic processes at Stromboli from Cerberus, a remote-controlled open-path FTIR scanner system, Journal of Volcanology and Geothermal Research, 249, 66 – 76, doi:https://doi.org/10.1016/j.jvolgeores.2012.09.004, URL `http://www.sciencedirect.com/science/article/pii/S0377027312002806`, 2013.

Lampel, J.: Measurements of reactive trace gases in the marine boundary layerusing novel DOAS methods, Ph.D. thesis, Ruperto Carola University of Heidelberg, Germany, URL `https://archiv.ub.uni-heidelberg.de/volltextserver/17394/1/Dissertation%20Johannes%20Lampel.pdf`, 2014.

Lampel, J., Wang, Y., Hilboll, A., Beirle, S., Sihler, H., Pukite, J., Platt, U., and Wagner, T.: The tilt effect in DOAS observations, Atmospheric Measurement Techniques, 10, 4819–4831, doi:10.5194/amt-10-4819-2017, URL `https://www.atmos-meas-tech.net/10/4819/2017/`, 2017.

Larsen, L. B., Vinther, B. M., Briffa, K. R., Melvin, T. M., Clausen, H. B., Jones, P. D., Siggaard-Andersen, M.-L., Hammer, C. U., Eronen, M., Grudd, H., Gunnarson, B. E., Hantemirov, R. M., Naurzbaev, M. M., and Nicolussi, K.: New ice core evidence for a volcanic cause of the A.D. 536 dust veil, Geophysical Research Letters, 35, doi:10.1029/2007GL032450, URL `https://agupubs.onlinelibrary.wiley.com/doi/abs/10.1029/2007GL032450`, 2007.

Le Gall, N. and Pichavant, M.: Homogeneous bubble nucleation in H2O- and H2O-CO2-bearing basaltic melts: Results of high temperature decompression experiments, Journal of Volcanology and Geothermal Research, 327, 604–621, URL `http://www.sciencedirect.com/science/article/pii/S037702731630381X`, 2016.

Le Pennec, J.-L., Jaya, D., Samaniego, P., Ramón, P., Yánez, S. M., Egred, J., and van der Plicht, J.: The AD 1300–1700 eruptive periods at Tungurahua volcano, Ecuador, revealed by historical narratives, stratigraphy and radiocarbon dating, Journal of Volcanology and Geothermal Research, 176, 70 – 81, doi:https://doi.org/10.1016/j.jvolgeores.2008.05.019, URL `http://www.sciencedirect.com/science/article/pii/S0377027308002850`, recent and active volcanism in the Ecuadorian Andes, 2008.

Leith, D.: Drag on Nonspherical Objects, Aerosol Science and Technology, 6, 153–161, doi:10.1080/02786828708959128, URL `http://dx.doi.org/10.1080/02786828708959128`, 1987.

Lensky, N., Navon, O., and Lyakhovsky, V.: Bubble growth during decompression of magma: experimental and theoretical investigation, Journal of Volcanology and Geothermal Research, 129, 7 – 22, doi:https://doi.org/10.1016/S0377-0273(03)00229-4, URL `http:`

//www.sciencedirect.com/science/article/pii/S0377027303002294, the role of laboratory experiments in volcanology, 2004.

Lesne, P., Kohn, S. C., Blundy, J., Witham, F., Botcharnikov, R. E., and Behrens, H.: Experimental Simulation of Closed-System Degassing in the System Basalt–H2O–CO2–S–Cl, Journal of Petrology, 52, 1737, doi:10.1093/petrology/egr027, URL +http://dx.doi.org/10.1093/petrology/egr027, 2011.

Lomb, N. R.: Least-squares frequency analysis of unequally spaced data, Astrophysics and Space Science, 39, 447–462, doi:10.1007/BF00648343, URL http://dx.doi.org/10.1007/BF00648343, 1976.

Londono, J. M.: Evidence of recent deep magmatic activity at Cerro Bravo-Cerro Machín volcanic complex, central Colombia. Implications for future volcanic activity at Nevado del Ruiz, Cerro Machín and other volcanoes, Journal of Volcanology and Geothermal Research, 324, 156 – 168, doi:https://doi.org/10.1016/j.jvolgeores.2016.06.003, URL http://www.sciencedirect.com/science/article/pii/S0377027316301299, 2016.

Londono, J. M. and Galvis, B.: Seismic Data, Photographic Images and Physical Modeling of Volcanic Plumes as a Tool for Monitoring the Activity of Nevado del Ruiz Volcano, Colombia, Frontiers in Earth Science, 6, 162, doi:10.3389/feart.2018.00162, URL https://www.frontiersin.org/article/10.3389/feart.2018.00162, 2018.

Londoño, J. M. and Kumagai, H.: 4D seismic tomography of Nevado del Ruiz Volcano, Colombia, 2000–2016, Journal of Volcanology and Geothermal Research, 358, 105 – 123, doi:https://doi.org/10.1016/j.jvolgeores.2018.02.015, URL http://www.sciencedirect.com/science/article/pii/S0377027317305693, 2018.

Lopez, T., Carn, S., Werner, C., Fee, D., Kelly, P., Doukas, M., Pfeffer, M., Webley, P., Cahill, C., and Schneider, D.: Evaluation of Redoubt Volcano's sulfur dioxide emissions by the Ozone Monitoring Instrument, Journal of Volcanology and Geothermal Research, 259, 290 – 307, doi:https://doi.org/10.1016/j.jvolgeores.2012.03.002, URL http://www.sciencedirect.com/science/article/pii/S0377027312000650, the 2009 Eruption of Redoubt Volcano, Alaska, 2013.

Lovejoy, S., Gaonac'h, H., and Schertzer, D.: Bubble distributions and dynamics: The expansion-coalescence equation, Journal of Geophysical Research: Solid Earth, 109, n/a–n/a, doi:10.1029/2003JB002823, URL http://dx.doi.org/10.1029/2003JB002823, b11203, 2004.

Lowenstern, J. B.: Carbon dioxide in magmas and implications for hydrothermal systems, Mineralium Deposita, 36, 490–502, doi:10.1007/s001260100185, URL https://doi.org/10.1007/s001260100185, 2001.

Lübcke, P.: Optical remote sensing measurements of bromine and sulphur emissions: Investigating their potential as tracers of volcanic activity, Ph.D. thesis, Ruperto Carola University of Heidelberg, Germany, 2014.

Lübcke, P., Bobrowski, N., Arellano, S., Galle, B., Garzón, G., Vogel, L., and Platt, U.: BrO/SO_2 molar ratios from scanning DOAS measurements in the NOVAC network, Solid Earth, 5, 409–424, doi:10.5194/se-5-409-2014, URL `http://www.solid-earth.net/5/409/2014/`, 2014.

Lübcke, P., Lampel, J., Arellano, S., Bobrowski, N., Dinger, F., Galle, B., Garzón, G., Hidalgo, S., Chacón Ortiz, Z., Vogel, L., Warnach, S., and Platt, U.: Retrieval of absolute SO_2 column amounts from scattered-light spectra: implications for the evaluation of data from automated DOAS networks, Atmospheric Measurement Techniques, 9, 5677–5698, doi:10.5194/amt-9-5677-2016, URL `https://www.atmos-meas-tech.net/9/5677/2016/`, 2016.

Lundgren, P., Samsonov, S. V., López Velez, C. M., and Ordoñez, M.: Deep source model for Nevado del Ruiz Volcano, Colombia, constrained by interferometric synthetic aperture radar observations, Geophysical Research Letters, 42, 4816–4823, doi:10.1002/2015GL063858, URL `https://agupubs.onlinelibrary.wiley.com/doi/abs/10.1002/2015GL063858`, 2015.

MacNeil, R. E., Sanford, W. E., Connor, C. B., Sandberg, S. K., and Diez, M.: Investigation of the groundwater system at Masaya Caldera, Nicaragua, using transient electromagnetics and numerical simulation, Journal of Volcanology and Geothermal Research, 166, 217 – 232, doi:https://doi.org/10.1016/j.jvolgeores.2007.07.016, URL `http://www.sciencedirect.com/science/article/pii/S0377027307002454`, 2007.

Malinconico, J. and Lawrence, L.: Fluctuations in SO2 emission during recent eruptions of Etna, Nature, 278, 43 EP –, URL `http://dx.doi.org/10.1038/278043a0`, 1979.

Mancini, S., Forestier-Coste, L., Burgisser, A., James, F., and Castro, J.: An expansion–coalescence model to track gas bubble populations in magmas, Journal of Volcanology and Geothermal Research, 313, 44 – 58, doi:https://doi.org/10.1016/j.jvolgeores.2016.01.016, URL `http://www.sciencedirect.com/science/article/pii/S0377027316000263`, 2016.

Manga, M. and Stone, H.: Interactions between bubbles in magmas and lavas: effects of bubble deformation, Journal of Volcanology and Geothermal Research, 63, 267 – 279, doi:https://doi.org/10.1016/0377-0273(94)90079-5, URL `http://www.sciencedirect.com/science/article/pii/0377027394900795`, 1994.

Manga, M., Beresnev, I., Brodsky, E. E., Elkhoury, J. E., Elsworth, D., Ingebritsen, S. E., Mays, D. C., and Wang, C.-Y.: Changes in permeability caused by transient stresses: Field observations, experiments, and mechanisms, Reviews of Geophysics, 50, doi:10.1029/2011RG000382, URL `https://doi.org/10.1029/2011RG000382`, 2012.

Martel, C., Andújar, J., Mothes, P., Scaillet, B., Pichavant, M., and Molina, I.: Storage conditions of the mafic and silicic magmas at Cotopaxi, Ecuador, Journal of Volcanology and Geothermal Research, 354, 74 – 86, doi:https://doi.org/10.1016/j.jvolgeores.2018.02.006, URL `http://www.sciencedirect.com/science/article/pii/S0377027317306248`, 2018.

Mauri, G., Williams-Jones, G., Saracco, G., and Zurek, J. M.: A geochemical and geophysical investigation of the hydrothermal complex of Masaya volcano, Nicaragua, Journal of Volcanology and Geothermal Research, 227-228, 15 – 31, doi:https://doi.org/10.1016/j.jvolgeores.2012.02.003, URL `http://www.sciencedirect.com/science/article/pii/S0377027312000339`, 2012.

McKenzie, D. and Bickle, M. J.: The Volume and Composition of Melt Generated by Extension of the Lithosphere, Journal of Petrology, 29, 625–679, doi:10.1093/petrology/29.3.625, URL http://dx.doi.org/10.1093/petrology/29.3.625, 1988.

McNutt, S. R.: Eruptions of Pavlof Volcano, Alaska, and their Possible Modulation by Ocean Load and Tectonic Stresses: Re-evaluation of the Hypothesis Based on New Data from 1984–1998, pure and applied geophysics, 155, 701–712, doi:10.1007/s000240050284, URL https://doi.org/10.1007/s000240050284, 1999.

McNutt, S. R. and Beavan, R. J.: Volcanic earthquakes at Pavlof Volcano correlated with the solid earth tide, Nature, 294, 615–618, doi:10.1038/294615a0, URL http://dx.doi.org/10.1038/294615a0, 1981.

McNutt, S. R. and Beavan, R. J.: Patterns of earthquakes and the effect of solid earth and ocean load tides at Mount St. Helens prior to the May 18, 1980, eruption, Journal of Geophysical Research: Solid Earth, 89, 3075–3086, doi:10.1029/JB089iB05p03075, URL http://dx.doi.org/10.1029/JB089iB05p03075, 1984.

Meller, R. and Moortgat, G. K.: Temperature dependence of the absorption cross sections of formaldehyde between 223 and 323 K in the wavelength range 225–375 nm, Journal of Geophysical Research: Atmospheres, 105, 7089–7101, doi:10.1029/1999JD901074, URL http://dx.doi.org/10.1029/1999JD901074, 2000.

Mie, G.: Beiträge zur Optik trüber Medien, speziell kolloidaler Metallösungen, Annalen der Physik, 330, 377–445, doi:10.1002/andp.19083300302, URL https://onlinelibrary.wiley.com/doi/abs/10.1002/andp.19083300302, 1908.

Miller, C. A., Werner, C. A., Herd, R., and Edmonds, M.: A Remotely Operated, Automatic Scanning DOAS System at White Island, New Zealand., AGU Fall Meeting Abstracts, 2006.

Minnis, P., Harrison, E. F., Stowe, L. L., Gibson, G. G., Denn, F. M., Doelling, D. R., and Smith, W. L.: Radiative Climate Forcing by the Mount Pinatubo Eruption, Science, 259, 1411–1415, doi:10.1126/science.259.5100.1411, URL http://science.sciencemag.org/content/259/5100/1411, 1993.

Moffat, A. J. and Millan, M. M.: The applications of optical correlation techniques to the remote sensing of SO2 plumes using sky light, Atmospheric Environment (1967), 5, 677 – 690, doi:https://doi.org/10.1016/0004-6981(71)90125-9, URL http://www.sciencedirect.com/science/article/pii/0004698171901259, 1971.

Moitra, P., Gonnermann, H. M., Houghton, B. F., and Giachetti, T.: Relating vesicle shapes in pyroclasts to eruption styles, Bulletin of Volcanology, 75, 691, doi:10.1007/s00445-013-0691-8, URL https://doi.org/10.1007/s00445-013-0691-8, 2013.

Monks, P. S.: A review of the observations and origins of the spring ozone maximum, Atmospheric Environment, 34, 3545 – 3561, doi:https://doi.org/10.1016/S1352-2310(00)00129-1, URL http://www.sciencedirect.com/science/article/pii/S1352231000001291, 2000.

Monterroso-Tobar, M. F., Londoño-Bonilla, J. M., and Sansonov, S.: Determination of glacier retreat at Nevado del Ruiz, Santa Isabel and Tolima volcanoes, Colombia through optical image and Din-SAR, DYNA, 85, 329–337, doi:https://doi.org/10.15446/dyna.v85n206.66570, URL `https://revistas.unal.edu.co/index.php/dyna/article/view/66570`, 2018.

Mora-Stock, C. N.: Seismic Structure and Seismicity of Villarrica Volcano (Southern Central Chile), Ph.D. thesis, University of Kiel (Germany), 2015.

Morales Rivera, A. M., Amelung, F., Mothes, P., Hong, S.-H., Nocquet, J.-M., and Jarrin, P.: Ground deformation before the 2015 eruptions of Cotopaxi volcano detected by InSAR, Geophysical Research Letters, 44, 6607–6615, doi:10.1002/2017GL073720, URL `http://dx.doi.org/10.1002/2017GL073720`, 2017GL073720, 2017.

Moretti, R. and Ottonello, G.: Solubility and speciation of sulfur in silicate melts: The Conjugated Toop-Samis-Flood-Grjotheim (CTSFG) model, Geochimica et Cosmochimica Acta, 69, 801 – 823, doi:https://doi.org/10.1016/j.gca.2004.09.006, URL `http://www.sciencedirect.com/science/article/pii/S0016703704006933`, 2005.

Morgan, W. J.: Convection Plumes in the Lower Mantle, Nature, 230, 42 EP –, URL `http://dx.doi.org/10.1038/230042a0`, 1971.

Mori, T. and Notsu, K.: Remote CO, COS, CO2, SO2, HCl detection and temperature estimation of volcanic gas, Geophysical Research Letters, 24, 2047–2050, doi:10.1029/97GL52058, URL `https://agupubs.onlinelibrary.wiley.com/doi/abs/10.1029/97GL52058`, 1997.

Mori, T., Sato, M., Shimoike, Y., and Notsu, K.: High SiF4/HF ratio detected in Satsuma-Iwojima volcano's plume by remote FT-IR observation, Earth, Planets and Space, 54, 249–256, doi:10.1186/BF03353024, URL `https://doi.org/10.1186/BF03353024`, 2002.

Mori, T., Mori, T., Kazahaya, K., Ohwada, M., Hirabayashi, J., and Yoshikawa, S.: Effect of UV scattering on SO2 emission rate measurements, Geophysical Research Letters, 33, n/a–n/a, doi:10.1029/2006GL026285, URL `http://dx.doi.org/10.1029/2006GL026285`, l17315, 2006.

Mothes, P. A., Ruiz, M. C., Viracucha, E. G., Ramón, P. A., Hernández, S., Hidalgo, S., Bernard, B., Gaunt, E. H., Jarrín, P., Yépez, M. A., and Espín, P. A.: Geophysical Footprints of Cotopaxi's Unrest and Minor Eruptions in 2015: An Opportunity to Test Scientific and Community Preparedness, in: Advances in Volcanology, pp. 1–30, Springer Berlin Heidelberg, Berlin, Heidelberg, doi:10.1007/11157_2017_10, URL `https://doi.org/10.1007/11157_2017_10`, 2017.

Moussallam, Y., Bani, P., Curtis, A., Barnie, T., Moussallam, M., Peters, N., Schipper, C. I., Aiuppa, A., Giudice, G., Álvaro Amigo, Velasquez, G., and Cardona, C.: Sustaining persistent lava lakes: Observations from high-resolution gas measurements at Villarrica volcano, Chile, Earth and Planetary Science Letters, 454, 237 – 247, doi:https://doi.org/10.1016/j.epsl.2016.09.012, URL `http://www.sciencedirect.com/science/article/pii/S0012821X16304927`, 2016.

Moussallam, Y., Tamburello, G., Peters, N., Apaza, F., Schipper, C. I., Curtis, A., Aiuppa, A., Masias, P., Boichu, M., Bauduin, S., Barnie, T., Bani, P., Giudice, G., and Moussallam, M.: Volcanic gas emissions and degassing dynamics at Ubinas and Sabancaya volcanoes; implications for the volatile budget of the central volcanic zone, Journal of Volcanology and Geothermal Research, 343, 181 – 191, doi:https://doi.org/10.1016/j.jvolgeores.2017.06.027, URL `http://www.sciencedirect.com/science/article/pii/S0377027317301944`, 2017.

Métrich, N., Allard, P., Spilliaert, N., Andronico, D., and Burton, M.: 2001 flank eruption of the alkali- and volatile-rich primitive basalt responsible for Mount Etna's evolution in the last three decades, Earth and Planetary Science Letters, 228, 1 – 17, doi:https://doi.org/10.1016/j.epsl.2004.09.036, URL `http://www.sciencedirect.com/science/article/pii/S0012821X04005916`, 2004.

Nakamura, K.: Volcanoes as possible indicators of tectonic stress orientation — principle and proposal, Journal of Volcanology and Geothermal Research, 2, 1 – 16, doi:https://doi.org/10.1016/0377-0273(77)90012-9, URL `http://www.sciencedirect.com/science/article/pii/0377027377900129`, 1977.

Naranjo, J. L., Sigurdsson, H., N., C. S., and Fritz, W.: Eruption of the Nevado del Ruiz Volcano, Colombia, On 13 November 1985: Tephra Fall and Lahars, Science, 233, 961–963, doi:10.1126/science.233.4767.961, URL `http://science.sciencemag.org/content/233/4767/961`, 1986.

Newcomb, G. S. and Millan, M. M.: Theory, Applications, and Results of the Long-Line Correlation Spectrometer, IEEE Transactions on Geoscience Electronics, 8, 149–157, doi:10.1109/TGE.1970.271410, 1970.

Newhall, C. G. and Self, S.: The volcanic explosivity index (VEI) an estimate of explosive magnitude for historical volcanism, Journal of Geophysical Research: Oceans, 87, 1231–1238, doi:10.1029/JC087iC02p01231, URL `https://agupubs.onlinelibrary.wiley.com/doi/abs/10.1029/JC087iC02p01231`, 1982.

Ångström, A.: On the Atmospheric Transmission of Sun Radiation and on Dust in the Air, Geografiska Annaler, 11, 156–166, URL `http://www.jstor.org/stable/519399`, 1929.

Nguyen, C. T., Gonnermann, H. M., Chen, Y., Huber, C., Maiorano, A. A., Gouldstone, A., and Dufek, J.: Film drainage and the lifetime of bubbles, Geochemistry, Geophysics, Geosystems, 14, 3616–3631, doi:10.1002/ggge.20198, URL `https://agupubs.onlinelibrary.wiley.com/doi/abs/10.1002/ggge.20198`, 2013.

Nicholson, E., Mather, T., Pyle, D., Odbert, H., and Christopher, T.: Cyclical patterns in volcanic degassing revealed by SO2 flux timeseries analysis: An application to Soufrière Hills Volcano, Montserrat, Earth and Planetary Science Letters, 375, 209 – 221, doi:https://doi.org/10.1016/j.epsl.2013.05.032, URL `http://www.sciencedirect.com/science/article/pii/S0012821X1300277X`, 2013.

Nicolet, M.: On the molecular scattering in the terrestrial atmosphere : An empirical formula for its calculation in the homosphere, Planetary and Space Science, 32, 1467 – 1468, doi:https://doi.org/10.1016/0032-0633(84)90089-8, URL `http://www.sciencedirect.com/science/article/pii/0032063384900898`, 1984.

Okumura, S., Nakamura, M., Nakano, T., Uesugi, K., and Tsuchiyama, A.: Experimental constraints on permeable gas transport in crystalline silicic magmas, Contributions to Mineralogy and Petrology, 164, 493–504, doi:10.1007/s00410-012-0750-8, URL `https://doi.org/10.1007/s00410-012-0750-8`, 2012.

Okumura, S., Kushnir, A. R., Martel, C., Champallier, R., Thibault, Q., and Takeuchi, S.: Rheology of crystal-bearing natural magmas: Torsional deformation experiments at 800°C and 100MPa, Journal of Volcanology and Geothermal Research, 328, 237 – 246, doi:https://doi.org/10.1016/j.jvolgeores.2016.11.009, URL `http://www.sciencedirect.com/science/article/pii/S0377027316304589`, 2016.

Oppenheimer, C.: Climatic, environmental and human consequences of the largest known historic eruption: Tambora volcano (Indonesia) 1815, Progress in Physical Geography: Earth and Environment, 27, 230–259, doi:10.1191/0309133303pp379ra, URL `https://doi.org/10.1191/0309133303pp379ra`, 2003.

Oppenheimer, C., Scaillet, B., and Martin, R. S.: Sulfur Degassing From Volcanoes: Source Conditions, Surveillance, Plume Chemistry and Earth System Impacts, Reviews in Mineralogy and Geochemistry, 73, 363, doi:10.2138/rmg.2011.73.13, URL `http://dx.doi.org/10.2138/rmg.2011.73.13`, 2011.

Oppenheimer, C., Fischer, T., and Scaillet, B.: Volcanic Degassing: Process and Impact, in: Treatise on Geochemistry (Second Edition), pp. 111–179, Elsevier, doi:10.1016/B978-0-08-095975-7.00304-1, URL `https://hal-insu.archives-ouvertes.fr/insu-00904186`, 2014.

Pagé, L. and Hattori, K.: Tracing halogen and B cycling in subduction zones based on obducted, subducted and forearc serpentinites of the Dominican Republic, Scientific Reports, 7, 17 776, doi:10.1038/s41598-017-18139-7, URL `https://doi.org/10.1038/s41598-017-18139-7`, 2017.

Palma, J. L., Blake, S., and Calder, E. S.: Constraints on the rates of degassing and convection in basaltic open-vent volcanoes, Geochemistry, Geophysics, Geosystems, 12, doi:10.1029/2011GC003715, URL `https://agupubs.onlinelibrary.wiley.com/doi/abs/10.1029/2011GC003715`, 2011.

Parfitt, E., Wilson, L., and Head, J.: Basaltic magma reservoirs: factors controlling their rupture characteristics and evolution, Journal of Volcanology and Geothermal Research, 55, 1 – 14, doi:https://doi.org/10.1016/0377-0273(93)90086-7, URL `http://www.sciencedirect.com/science/article/pii/0377027393900867`, 1993.

Patanè, G., Frasca, A., Agodi, A., and Imposa, S.: Earth tides and Etnean volcanic eruptions: an attempt at correlation of the two phenomena during the 1983, 1985 and 1986 eruptions, Physics of the Earth and Planetary Interiors, 87, 123 – 135, doi:https://doi.org/10.1016/0031-9201(94)90026-4, URL `http://www.sciencedirect.com/science/article/pii/0031920194900264`, 1994.

Pearson, K.: LIII. On lines and planes of closest fit to systems of points in space, The London, Edinburgh, and Dublin Philosophical Magazine and Journal of Science, 2, 559–572, doi:10.1080/14786440109462720, URL `https://doi.org/10.1080/14786440109462720`, 1901.

Pearson, S. C. P., Kiyosugi, K., Lehto, H. L., Saballos, J. A., Connor, C. B., and Sanford, W. E.: Integrated geophysical and hydrothermal models of flank degassing and fluid flow at Masaya volcano, Nicaragua, Geochemistry, Geophysics, Geosystems, 13, doi:10.1029/2012GC004117, URL `https://agupubs.onlinelibrary.wiley.com/doi/abs/10.1029/2012GC004117`, 2012.

Pering, T., Tamburello, G., McGonigle, A., Aiuppa, A., Cannata, A., Giudice, G., and Patanè, D.: High time resolution fluctuations in volcanic carbon dioxide degassing from Mount Etna, Journal of Volcanology and Geothermal Research, 270, 115 – 121, doi:https://doi.org/10.1016/j.jvolgeores.2013.11.014, URL `http://www.sciencedirect.com/science/article/pii/S0377027313003508`, 2014.

Petrosino, S., Cusano, P., and Madonia, P.: Tidal and hydrological periodicities of seismicity reveal new risk scenarios at Campi Flegrei caldera, Sci Rep, 8, 13 808–13 808, doi:10.1038/s41598-018-31760-4, URL `https://www.ncbi.nlm.nih.gov/pubmed/30217987`, 30217987[pmid], 2018.

Pfeilsticker, K., Erie, F., Funk, O., Marquard, L., Wagner, T., and Platt, U.: Optical path modifications due to tropospheric clouds: Implications for zenith sky measurements of stratospheric gases, Journal of Geophysical Research: Atmospheres, 103, 25 323–25 335, doi:10.1029/98JD01803, URL `https://agupubs.onlinelibrary.wiley.com/doi/abs/10.1029/98JD01803`, 1998.

Platt, U. and Bobrowski, N.: Quantification of volcanic reactive halogen emissions, in: Volcanism and Global Environmental Change, edited by Schmidt, A., Fristad, K. E., and Elkins-Tanton, L. T., Cambridge University Press, doi:10.1017/CBO9781107415683.011, 2015.

Platt, U. and Lehrer, E.: ARCTOC final report, Tech. rep., European Union, 1997.

Platt, U. and Stutz, J.: Differential Optical Absorption Spectroscopy, Springer Berlin Heidelberg, 2008.

Platt, U., Perner, D., Harris, G. W., Winer, A. M., and Pitts, J. N.: Observations of nitrous acid in an urban atmosphere by differential optical absorption, Nature, 285, 312–314, doi:10.1038/285312a0, URL `http://dx.doi.org/10.1038/285312a0`, 1980.

Platt, U., Marquard, L., Wagner, T., and Perner, D.: Corrections for zenith scattered light DOAS, Geophysical Research Letters, 24, 1759–1762, doi:10.1029/97GL01693, URL `https://agupubs.onlinelibrary.wiley.com/doi/abs/10.1029/97GL01693`, 1997.

Platt, U., Bobrowski, N., and Butz, A.: Ground-Based Remote Sensing and Imaging of Volcanic Gases and Quantitative Determination of Multi-Species Emission Fluxes, Geosciences, 8, doi:10.3390/geosciences8020044, URL `http://www.mdpi.com/2076-3263/8/2/44`, 2018.

Pochanart, P., Akimoto, H., Kajii, Y., Potemkin, V. M., and Khodzher, T. V.: Regional background ozone and carbon monoxide variations in remote Siberia/East Asia, Journal of Geophysical Research: Atmospheres, 108, ACH 7–1–ACH 7–18, doi:10.1029/2001JD001412, URL `https://doi.org/10.1029/2001JD001412`, 2003.

Ponchaut, F., Lyard, F., and Provost, C. L.: An Analysis of the Tidal Signal in the WOCE Sea Level Dataset, Journal of Atmospheric and Oceanic Technology, 18, 77–91, 2001.

Press, W. H., Teukolsky, S. A., Vetterling, W. T., and Flannery, B. P.: Numerical Recipes in C (2Nd Ed.): The Art of Scientific Computing, Cambridge University Press, New York, NY, USA, 1992.

Prousevitch, A. A., Sahagian, D. L., and Anderson, A. T.: Dynamics of diffusive bubble growth in magmas: Isothermal case, Journal of Geophysical Research: Solid Earth, 98, 22 283–22 307, doi:10.1029/93JB02027, URL `http://dx.doi.org/10.1029/93JB02027`, 1993.

Proussevitch, A. and Sahagian, D.: Bubbledrive-1: A numerical model of volcanic eruption mechanisms driven by disequilibrium magma degassing, Journal of Volcanology and Geothermal Research, 143, 89 – 111, doi:https://doi.org/10.1016/j.jvolgeores.2004.09.012, URL `http://www.sciencedirect.com/science/article/pii/S0377027305000375`, volcanic Eruption Mechanisms, 2005.

Rampino, M. R. and Self, S.: Historic Eruptions of Tambora (1815), Krakatau (1883), and Agung (1963), their Stratospheric Aerosols, and Climatic Impact, Quaternary Research, 18, 127–143, doi:10.1016/0033-5894(82)90065-5, 1982.

Rüdiger, J., Gutmann, A., and Bobrowski, N.: Halogen activation in the plume of Masaya volcano: field observations and box model investigations, NN, 2019.

Richardson, J. P., Waite, G. P., and Palma, J. L.: Varying seismic-acoustic properties of the fluctuating lava lake at Villarrica volcano, Chile, Journal of Geophysical Research: Solid Earth, 119, 5560–5573, doi:10.1002/2014JB011002, URL `https://agupubs.onlinelibrary.wiley.com/doi/abs/10.1002/2014JB011002`, 2014.

Roberts, T., Braban, C., Martin, R., Oppenheimer, C., Adams, J., Cox, R., Jones, R., and Griffiths, P.: Modelling reactive halogen formation and ozone depletion in volcanic plumes, Chemical Geology, 263, 151 – 163, doi:https://doi.org/10.1016/j.chemgeo.2008.11.012, URL `http://www.sciencedirect.com/science/article/pii/S0009254108005366`, halogens in Volcanic Systems and Their Environmental Impacts, 2009.

Roberts, T. J.: Ozone Depletion in Tropospheric Volcanic Plumes: From Halogen-Poor to Halogen-Rich Emissions, Geosciences, 8, doi:10.3390/geosciences8020068, URL `http://www.mdpi.com/2076-3263/8/2/68`, 2018.

Roberts, T. J., Martin, R. S., and Jourdain, L.: Reactive bromine chemistry in Mount Etna's volcanic plume: the influence of total Br, high-temperature processing, aerosol loading and plume–air mixing, Atmospheric Chemistry and Physics, 14, 11 201–11 219, doi:10.5194/acp-14-11201-2014, URL `http://www.atmos-chem-phys.net/14/11201/2014/`, 2014.

Roberts, T. J., Lurton, T., Giudice, G., Liuzzo, M., Aiuppa, A., Coltelli, M., Vignelles, D., Salerno, G., Couté, B., Chartier, M., Baron, R., Saffell, J. R., and Scaillet, B.: Validation of a novel Multi-Gas sensor for volcanic HCl alongside H2S and SO2 at Mt. Etna, Bulletin of Volcanology, 79, 36, doi:10.1007/s00445-017-1114-z, URL `https://doi.org/10.1007/s00445-017-1114-z`, 2017.

Rüdiger, J., Schmitt, S., Pitton, D., Tirpitz, J.-L., Gutmann, A., Gutiérrez, X., Pöhler, D., Lampel, J., Horbanski, M., Sander, R., Zetzsch, C., Hoffmann, T., Held, A., Platt, U., and Bobrowski, N.: HALVIRE: HALogen activation in Volcanic plumes In Reaction chamber Experiments, in: EGU General Assembly Conference Abstracts, vol. 20 of *EGU General Assembly Conference Abstracts*, p. 14827, 2018.

Ruiz, M., Guillier, B., Chatelain, J.-L., Yepes, H., Hall, M., and Ramon, P.: Possible causes for the seismic activity observed in Cotopaxi Volcano, Ecuador, Geophysical Research Letters, 25, 2305–2308, doi:10.1029/98GL01689, URL `https://agupubs.onlinelibrary.wiley.com/doi/abs/10.1029/98GL01689`, 1998.

Rust, A., Manga, M., and Cashman, K.: Determining flow type, shear rate and shear stress in magmas from bubble shapes and orientations, Journal of Volcanology and Geothermal Research, 122, 111 – 132, doi:https://doi.org/10.1016/S0377-0273(02)00487-0, URL `http://www.sciencedirect.com/science/article/pii/S0377027302004870`, 2003.

Rust, A. C. and Cashman, K. V.: Permeability controls on expansion and size distributions of pyroclasts, Journal of Geophysical Research: Solid Earth, 116, doi:10.1029/2011JB008494, URL `https://agupubs.onlinelibrary.wiley.com/doi/abs/10.1029/2011JB008494`, 2011.

Rydelek, P. A., Davis, P. M., and Koyanagi, R. Y.: Tidal triggering of earthquake swarms at Kilauea Volcano, Hawaii, Journal of Geophysical Research: Solid Earth, 93, 4401–4411, doi:10.1029/JB093iB05p04401, URL `http://dx.doi.org/10.1029/JB093iB05p04401`, 1988.

Sahagian, D. L. and Proussevitch, A. A.: 3D particle size distributions from 2D observations: stereology for natural applications, Journal of Volcanology and Geothermal Research, 84, 173 – 196, doi:https://doi.org/10.1016/S0377-0273(98)00043-2, URL `http://www.sciencedirect.com/science/article/pii/S0377027398000432`, 1998.

Sahagian, D. L., Anderson, A. T., and Ward, B.: Bubble coalescence in basalt flows: comparison of a numerical model with natural examples, Bulletin of Volcanology, 52, 49–56, doi:10.1007/BF00641386, URL `https://doi.org/10.1007/BF00641386`, 1989.

Salerno, G., Burton, M., Oppenheimer, C., Caltabiano, T., Randazzo, D., Bruno, N., and Longo, V.: Three-years of SO2 flux measurements of Mt. Etna using an automated UV scanner array: Comparison with conventional traverses and uncertainties in flux retrieval, Journal of Volcanology and Geothermal Research, 183, 76 – 83, doi:http://dx.doi.org/10.1016/j.jvolgeores.2009.02.013, URL http://www.sciencedirect.com/science/article/pii/S0377027309000791, 2009.

Scaillet, B. and Pichavant, M.: A model of sulphur solubility for hydrous mafic melts: application to the determination of magmatic fluid compositions of Italian volcanoes, Annals of Geophysics, 48, doi:10.4401/ag-3226, URL http://www.annalsofgeophysics.eu/index.php/annals/article/view/3226, 2005.

Scargle, J. D.: Studies in astronomical time series analysis. II - Statistical aspects of spectral analysis of unevenly spaced data, Astrophysical Journal, 263, 835–853, doi:10.1086/160554, 1982.

Schmincke, H.-U.: Vulkanismus, 2014.

Sellitto, P., Spampinato, L., Salerno, G. G., and La Spina, A.: Aerosol Optical Properties of Pacaya Volcano Plume Measured with a Portable Sun-Photometer, Geosciences, 8, doi:10.3390/geosciences8020036, 2018.

Seo, S., Richter, A., Blechschmidt, A.-M., Bougoudis, I., and Burrows, J. P.: First high resolution BrO column retrievals from TROPOMI, Atmospheric Measurement Techniques Discussions, 2018, 1–26, doi:10.5194/amt-2018-365, URL https://www.atmos-meas-tech-discuss.net/amt-2018-365/, 2018.

Solomon, S., Schmeltekopf, A. L., and Sanders, R. W.: On the interpretation of zenith sky absorption measurements, Journal of Geophysical Research: Atmospheres, 92, 8311–8319, doi:10.1029/JD092iD07p08311, URL https://agupubs.onlinelibrary.wiley.com/doi/abs/10.1029/JD092iD07p08311, 1987.

Sottili, G. and Palladino, D. M.: Tidal modulation of eruptive activity at open-vent volcanoes: evidence from Stromboli, Italy, Terra Nova, 24, 233–237, doi:10.1111/j.1365-3121.2012.01059.x, URL http://dx.doi.org/10.1111/j.1365-3121.2012.01059.x, 2012.

Sottili, G., Martino, S., Palladino, D. M., Paciello, A., and Bozzano, F.: Effects of tidal stresses on volcanic activity at Mount Etna, Italy, Geophysical Research Letters, 34, n/a–n/a, doi:10.1029/2006GL028190, URL http://dx.doi.org/10.1029/2006GL028190, l01311, 2007.

Sparks, R.: The dynamics of bubble formation and growth in magmas: A review and analysis, Journal of Volcanology and Geothermal Research, 3, 1 – 37, doi:https://doi.org/10.1016/0377-0273(78)90002-1, URL http://www.sciencedirect.com/science/article/pii/0377027378900021, 1978.

Sparks, R. S. J.: Triggering of volcanic eruptions by Earth tides, Nature, 290, 448 EP –, URL http://dx.doi.org/10.1038/290448a0, 1981.

Spina, L., Cimarelli, C., Scheu, B., Genova, D. D., and Dingwell, D. B.: On the slow decompressive response of volatile- and crystal-bearing magmas: An analogue experimental investigation, Earth and Planetary Science Letters, 433, 44 – 53, doi:https://doi.org/10.1016/j.epsl.2015.10.029, URL http://www.sciencedirect.com/science/article/pii/S0012821X15006640, 2016.

Spinetti, C. and Buongiorno, M.: Volcanic aerosol optical characteristics of Mt. Etna tropospheric plume retrieved by means of airborne multispectral images, Journal of Atmospheric and Solar-Terrestrial Physics, 69, 981 – 994, doi:https://doi.org/10.1016/j.jastp.2007.03.014, URL `http://www.sciencedirect.com/science/article/pii/S1364682607000855`, 2007.

Spurk, J. H.: Fluid Mechanics, Springer, 1997.

Stix, J., Torres, R. C., M, L. N., J, G. P. C., Raigosa, J. A., M, D. G., and Castonguay, R.: A model of vulcanian eruptions at Galeras volcano, Colombia, Journal of Volcanology and Geothermal Research, 77, 285 – 303, doi:https://doi.org/10.1016/S0377-0273(96)00100-X, URL `http://www.sciencedirect.com/science/article/pii/S037702739600100X`, galeras Volcano, Colombia: Interdisciplinary Study of a Decade Volcano, 1997.

Stoiber, R. E., Williams, S. N., and Huebert, B. J.: Sulfur and halogen gases at Masaya Caldera Complex, Nicaragua: Total flux and variations with time, Journal of Geophysical Research: Solid Earth, 91, 12 215–12 231, doi:10.1029/JB091iB12p12215, URL `http://dx.doi.org/10.1029/JB091iB12p12215`, 1986.

Stutz, J. and Platt, U.: Numerical analysis and estimation of the statistical error of differential optical absorption spectroscopy measurements with least-squares methods, Applied Optics, 35, 6041–6053, doi:10.1364/AO.35.006041, 1996.

Symonds, R., Gerlach, T., and Reed, M.: Magmatic gas scrubbing: implications for volcano monitoring, Journal of Volcanology and Geothermal Research, 108, 303 – 341, doi:https://doi.org/10.1016/S0377-0273(00)00292-4, URL `http://www.sciencedirect.com/science/article/pii/S0377027300002924`, 2001.

Takada, A.: The influence of regional stress and magmatic input on styles of monogenetic and polygenetic volcanism, Journal of Geophysical Research: Solid Earth, 99, 13 563–13 573, doi:10.1029/94JB00494, URL `http://dx.doi.org/10.1029/94JB00494`, 1994.

Tamburello, G., Aiuppa, A., McGonigle, A. J. S., Allard, P., Cannata, A., Giudice, G., Kantzas, E. P., and Pering, T. D.: Periodic volcanic degassing behavior: The Mount Etna example, Geophysical Research Letters, 40, 4818–4822, doi:10.1002/grl.50924, URL `https://doi.org/10.1002/grl.50924`, 2013.

Telling, J., Flower, V., and Carn, S.: A multi-sensor satellite assessment of SO2 emissions from the 2012–13 eruption of Plosky Tolbachik volcano, Kamchatka, Journal of Volcanology and Geothermal Research, 307, 98 – 106, doi:https://doi.org/10.1016/j.jvolgeores.2015.07.010, URL `http://www.sciencedirect.com/science/article/pii/S0377027315002188`, sI: 2012-13 Tolbachik eruption, 2015.

Theys, N., Van Roozendael, M., Dils, B., Hendrick, F., Hao, N., and De Mazière, M.: First satellite detection of volcanic bromine monoxide emission after the Kasatochi eruption, Geophysical Research Letters, 36, doi:10.1029/2008GL036552, URL `https://agupubs.onlinelibrary.wiley.com/doi/abs/10.1029/2008GL036552`, 2009.

Theys, N., Hedelt, P., De Smedt, I., Lerot, C., Yu, H., Vlietinck, J., Pedergnana, M., Arellano, S., Galle, B., Fernandez, D., Carlito, C. J. M., Barrington, C., Taisne, B., Delgado-Granados, H., Loyola, D., and Van Roozendael, M.: Global monitoring of volcanic SO2 degassing with unprecedented resolution from TROPOMI onboard Sentinel-5 Precursor, Scientific Reports, 9, 2643, doi:10.1038/s41598-019-39279-y, URL `https://doi.org/10.1038/s41598-019-39279-y`, 2019.

Thouret, J. C., Ramírez C., J., Gibert-Malengreau, B., Vargas, C. A., Naranjo, J. L., Vandemeulebrouck, J., Valla, F., and Funk, M.: Volcano-glacier interactions on composite cones and lahar generation: Nevado del Ruiz, Colombia, case study, Annals of Glaciology, 45, 115–127, doi:10.3189/172756407782282589, 2007.

Timmreck, C.: Climatic effects of large volcanic eruptions, Ph.D. thesis, Max-Planck Institute for Meteorology, 2018.

Trenkamp, R., Kellogg, J. N., Freymueller, J. T., and Mora, H. P.: Wide plate margin deformation, southern Central America and northwestern South America, CASA GPS observations, Journal of South American Earth Sciences, 15, 157–171, doi:10.1016/S0895-9811(02)00018-4, 2002.

Tripoli, B. A., Cordonnier, B., Zappone, A., and Ulmer, P.: Effects of crystallization and bubble nucleation on the seismic properties of magmas, Geochemistry, Geophysics, Geosystems, 17, 602–615, doi:10.1002/2015GC006123, URL `http://dx.doi.org/10.1002/2015GC006123`, 2016.

Ulfarsson, G. F. and Unger, E. A.: Impacts and Responses of Icelandic Aviation to the 2010 Eyjafjallajökull Volcanic Eruption: Case Study, Transportation Research Record, 2214, 144–151, doi:10.3141/2214-18, URL `https://doi.org/10.3141/2214-18`, 2011.

van Manen, S.: Perception of a chronic volcanic hazard: persistent degassing at Masaya volcano, Nicaragua, Journal of Applied Volcanology, 3, 9, doi:10.1186/s13617-014-0009-3, URL `https://doi.org/10.1186/s13617-014-0009-3`, 2014.

Vandaele, A., Hermans, C., Simon, P., Carleer, M., Colin, R., Fally, S., Mérienne, M., Jenouvrier, A., and Coquart, B.: Measurements of the NO2 absorption cross-section from 42 000 cm-1 to 10 000 cm-1 (238-1000 nm) at 220 K and 294 K, Journal of Quantitative Spectroscopy and Radiative Transfer, 59, 171 – 184, doi:http://dx.doi.org/10.1016/S0022-4073(97)00168-4, URL `http://www.sciencedirect.com/science/article/pii/S0022407397001684`, 1998.

Vandaele, A., Hermans, C., and Fally, S.: Fourier transform measurements of {SO2} absorption cross sections: II.: Temperature dependence in the 29 000-44 000 cm-1 (227–345 nm) region, Journal of Quantitative Spectroscopy and Radiative Transfer, 110, 2115 – 2126, doi:http://dx.doi.org/10.1016/j.jqsrt.2009.05.006, URL `http://www.sciencedirect.com/science/article/pii/S0022407309001800`, 2009.

Vargas, C. A., Koulakov, I., Jaupart, C., Gladkov, V., Gomez, E., El Khrepy, S., and Al-Arifi, N.: Breathing of the Nevado del Ruiz volcano reservoir, Colombia, inferred from repeated seismic tomography, Sci Rep, 7, 46 094, doi:10.1038/srep46094, URL `http://www.ncbi.nlm.nih.gov/pmc/articles/PMC5385870/`, 28393851[pmid], 2017.

Villemant, B., Hammouya, G., Michel, A., Semet, M. P., Komorowski, J.-C., Boudon, G., and Cheminée, J.-L.: The memory of volcanic waters: Shallow magma degassing revealed by halogen monitoring in thermal springs of La Soufrière volcano (Guadeloupe, Lesser Antilles), Earth and Planetary Science Letters, 237, 710 – 728, doi:http://dx.doi.org/10.1016/j.epsl.2005.05.013, URL `http://www.sciencedirect.com/science/article/pii/S0012821X05003249`, 2005.

Vogel, L.: Volcanic plumes: Evaluation of spectroscopic measurements, early detection and bromine chemistry, Ph.D. thesis, Ruperto Carola University of Heidelberg, Germany, available at: http://www.ub.uni-heidelberg.de/archiv/13219, 2011.

Vogel, L., Sihler, H., Lampel, J., Wagner, T., and Platt, U.: Retrieval interval mapping: a tool to visualize the impact of the spectral retrieval range on differential optical absorption spectroscopy evaluations, Atmospheric Measurement Techniques, 6, 275–299, doi:10.5194/amt-6-275-2013, URL `http://www.atmos-meas-tech.net/6/275/2013/`, 2013.

Voight, B.: The 1985 Nevado del Ruiz volcano catastrophe: anatomy and retrospection, Journal of Volcanology and Geothermal Research, 44, 349 – 386, doi:https://doi.org/10.1016/0377-0273(90)90027-D, URL `http://www.sciencedirect.com/science/article/pii/037702739090027D`, 1990.

von Glasow, R.: Atmospheric chemistry in volcanic plumes, Proceedings of the National Academy of Sciences of the United States of America, 107, 6594–6599, URL `http://www.jstor.org/stable/25665222`, 2010.

von Glasow, R., Bobrowski, N., and Kern, C.: The effects of volcanic eruptions on atmospheric chemistry, Chemical Geology, 263, 131 – 142, doi:https://doi.org/10.1016/j.chemgeo.2008.08.020, URL `http://www.sciencedirect.com/science/article/pii/S0009254108003756`, halogens in Volcanic Systems and Their Environmental Impacts, 2009.

Vukovich, F. M., Brackett, V., Fishman, J., and Sickles II, J. E.: A 5-year evaluation of the representativeness of the tropospheric ozone residual at nonclimatological periods, Journal of Geophysical Research: Atmospheres, 102, 15 927–15 932, doi:10.1029/97JD00455, URL `https://doi.org/10.1029/97JD00455`, 1997.

Wagner, T., Chance, K., Frieß, U., Gil, M., Goutail, F., Hönninger, G., Johnson, P., Karlson-Tornkvist, K., Konstandinov, I., Leser, H., Petritoli, A., Richter, A., Roozendael, M. V., and Platt, U.: Correction of the Ring effect and I0-effect for DOAS observations of scattered sunlight, in: ESA Technical Report, 2002.

Wagner, T., Beirle, S., and Deutschmann, T.: Three-dimensional simulation of the Ring effect in observations of scattered sun light using Monte Carlo radiative transfer models, Atmospheric Measurement Techniques, 2, 113–124, doi:10.5194/amt-2-113-2009, URL `http://www.atmos-meas-tech.net/2/113/2009/`, 2009.

Wagner, T., Apituley, A., Beirle, S., Dörner, S., Friess, U., Remmers, J., and Shaiganfar, R.: Cloud detection and classification based on MAX-DOAS observations, Atmospheric Measurement Techniques, 7, 1289–1320, doi:10.5194/amt-7-1289-2014, URL `http://www.atmos-meas-tech.net/7/1289/2014/`, 2014.

Wagner, T., Beirle, S., Remmers, J., Shaiganfar, R., and Wang, Y.: Absolute calibration of the colour index and O_4 absorption derived from Multi AXis (MAX-)DOAS measurements and their application to a standardised cloud classification algorithm, Atmospheric Measurement Techniques, 9, 4803–4823, doi:10.5194/amt-9-4803-2016, URL `https://www.atmos-meas-tech.net/9/4803/2016/`, 2016.

Warnach, S.: Improvements of BrO and SO2 retrievals of NOVAC data - Tungurahua volcano as a case study, Master's thesis, Ruperto Carola University of Heidelberg, Germany, 2015.

Warnach, S., Sihler, H., Borger, C., Bobrowski, N., Hörmann, C., Beirle, S., Schöne, M., Platt, U., and Wagner, T.: Bromine monoxide measurements in volcanic plumes from S5-P/Tropomi, in: EGU General Assembly Conference Abstracts, vol. 20 of *EGU General Assembly Conference Abstracts*, p. 15519, 2018.

Warnach, S., Bobrowski, N., Hidalgo, S., Battaglia, J., Dinger, F., Lübcke, P., Arellano, S., Galle, B., Steele, A., Platt, U., and Wagner, T.: Variation of the BrO/SO2 molar ratio in the plume of Tungurahua volcano between 2007 and 2017 and its relationship to seismic data, frontiers, doi:doi: 10.3389/feart.2019.00132, URL `https://www.frontiersin.org/articles/10.3389/feart.2019.00132/abstract`, 2019.

Watson, E. B. and Harrison, T. M.: Zircon saturation revisited: temperature and composition effects in a variety of crustal magma types, Earth and Planetary Science Letters, 64, 295 – 304, doi:https://doi.org/10.1016/0012-821X(83)90211-X, URL `http://www.sciencedirect.com/science/article/pii/0012821X8390211X`, 1983.

Wennberg, P.: Atmospheric chemistry: Bromine explosion, Nature, 397, 299–301, doi:10.1038/16805, URL `http://dx.doi.org/10.1038/16805`, 1999.

Wilken, E.: Retrieval Advances of BrO/SO2 Molar Ratios from NOVAC, Master's thesis, Ruperto Carola University of Heidelberg, Germany, 2018.

Witham, F., Blundy, J., Kohn, S. C., Lesne, P., Dixon, J., Churakov, S. V., and Botcharnikov, R.: SolEx: A model for mixed COHSCl-volatile solubilities and exsolved gas compositions in basalt, Computers & Geosciences, 45, 87 – 97, doi:https://doi.org/10.1016/j.cageo.2011.09.021, URL `http://www.sciencedirect.com/science/article/pii/S0098300411003554`, 2012.

Witter, J. B., Kress, V. C., Delmelle, P., and Stix, J.: Volatile degassing, petrology, and magma dynamics of the Villarrica Lava Lake, Southern Chile, Journal of Volcanology and Geothermal Research, 134, 303 – 337, doi:https://doi.org/10.1016/j.jvolgeores.2004.03.002, URL `http://www.sciencedirect.com/science/article/pii/S0377027304000630`, 2004.

Wohletz, K. H.: Explosive magma-water interactions: Thermodynamics, explosion mechanisms, and field studies, Bulletin of Volcanology, 48, 245–264, doi:10.1007/BF01081754, URL `https://doi.org/10.1007/BF01081754`, 1986.

Zapata, J. A., Calvache, M., Cortes, G. P., Fischer, T., Garzon, G., Gomez, D., Narváez, L., Ordonez, M., Ortega, A., Stix, J., Torres, R., and Williams, S.: SO2 fluxes from Galeras Volcano, Colombia, 1989–1995: Progressive degassing and conduit obstruction of a Decade Volcano, Journal of Volcanology and Geothermal Research, 77, 195 – 208, doi:https://doi.org/10.1016/S0377-0273(96)00094-7, URL `http://www.sciencedirect.com/science/article/pii/S0377027396000947`, galeras Volcano, Colombia: Interdisciplinary Study of a Decade Volcano, 1997.

Zhang, Y., Xu, Z., Zhu, M., and Wang, H.: Silicate melt properties and volcanic eruptions, Reviews of Geophysics, 45, doi:10.1029/2006RG000216, URL `https://doi.org/10.1029/2006RG000216`, 2007.